

TECHNISCHE MECHANIK

40 years

Editor:
Magdeburger Verein für Technische Mechanik e.V.
und Otto-von-Guericke-Universität Magdeburg

Editorial Board:

Holm Altenbach (Magdeburg)

Albrecht Bertram (Magdeburg)

Daniel Balzani (Bochum)

Stefan Diebels (Saarbrücken)

Paweł Dłużewski (Warsaw)

Sascha Duczec (Sydney)

Christoph Egbers (Cottbus)

Victor Eremeyev (Gdansk)

Samuel Forest (Paris)

Michael I. Friswell (Bristol)

Ulrich Gabbert (Magdeburg)

Daniel Juhre (Magdeburg), editor-in-chief

Richard Markert (Darmstadt)

Reinaldo Rodriguez (Havanna)

Miroslav Šilhavý (Prague)

Paul Steinmann (Erlangen-Nuremberg)

Jens Strackeljan (Magdeburg)

Bob Svendsen (Aachen)

Dominique Thévenin (Magdeburg)

Kerstin Weinberg (Siegen)

Elmar Woschke (Magdeburg)

TECHNISCHE MECHANIK

Wissenschaftliche Zeitschrift für Grundlagen und Anwendungen der Technischen Mechanik
Scientific Journal for Fundamentals and Applications of Engineering Mechanics

The journal **Technische Mechanik** publishes refereed original articles on Engineering Mechanics in its broadest sense. It is intended to provide a forum for a rapid transfer of research results to industry and science. In that sense contributions are encouraged which demonstrate the practical application of new results and scientific findings.

In der **Technischen Mechanik** werden begutachtete Beiträge aus allen Gebieten der Mechanik publiziert. Ein Hauptanliegen besteht in der raschen Verfügbarmachung von Forschungsergebnissen für Industrie und Wissenschaft. In diesem Sinne werden vor allem auch solche Beiträge bevorzugt, die neben neuen Ergebnissen und Erkenntnissen auch deren praktische Anwendung beinhalten.

Copyright

Submission of a manuscript implies that the work described has not been published before (except in the form of an abstract or as part of a published lecture, review, or thesis); that it is not under consideration for publication elsewhere; that its publication has been approved by all co-authors, if any, as well as by the responsible authorities at the institute where the work has been carried out. The authors hold and retain the copyright of their papers. They grant the journal the non-exclusive right to publish the papers.

All articles published in this journal are protected by copyright. No material may be reproduced or copied without prior written permission of the copyright holder, except for personal use only.

Urheberrecht

Voraussetzung für die Einreichung eines Manuskriptes an die Redaktion der Zeitschrift ist, dass die Arbeit noch nicht publiziert oder an anderer Stelle zur Publikation eingereicht wurde. Ferner wird vorausgesetzt, dass die Publikation von allen beteiligten Autoren einer Arbeitsgruppe genehmigt ist und dass die Arbeit, wenn sie zur Publikation angenommen wurde, nicht an anderer Stelle in gleicher Form publiziert wird.

Die Urheberrechte für die Artikel liegen bei den jeweiligen Autoren. Sie gewähren der Zeitschrift das nicht-exklusive Recht der Veröffentlichung.

Die Zeitschrift sowie alle in ihr enthaltenen einzelnen Beiträge und Abbildungen sind urheberrechtlich geschützt. Jede Verwertung, die nicht ausdrücklich vom Urheberrechtsgesetz zugelassen ist, bedarf der vorherigen schriftlichen Zustimmung der Rechteinhaber. Ausgenommen sind Kopien für den persönlichen Gebrauch.

Editorial Board / Herausgeberkollegium:

Holm Altenbach (Magdeburg)
Albrecht Bertram (Magdeburg)
Daniel Balzani (Bochum)
Stefan Diebels (Saarbrücken)
Paweł Dłużewski (Warsaw)
Sascha Duczak (Sydney)
Christoph Egbers (Cottbus)
Victor Eremeyev (Gdansk)
Samuel Forest (Paris)
Michael I. Friswell (Bristol)
Ulrich Gabbert (Magdeburg)
Daniel Juhre (Magdeburg), editor-in-chief
Richard Markert (Darmstadt)
Reinaldo Rodriguez (Havanna)
Miroslav Šilhavý (Prague)
Paul Steinmann (Erlangen-Nuremberg)
Jens Strackeljan (Magdeburg)
Bob Svendsen (Aachen)
Dominique Thévenin (Magdeburg)
Kerstin Weinberg (Siegen)
Elmar Woschke (Magdeburg)

Redaktion/Editorial Office

W. Lenz (Chefredakteur)

Bezugsmöglichkeiten

Die Zeitschrift Technische Mechanik erscheint ab dem Jahr 2019 ausschließlich in elektronischer Form. Die Zeitschrift Technische Mechanik ist ein Open Access Journal. Alle Artikel können kostenfrei von unserer Webseite herunter geladen werden.

Für Veröffentlichungen fallen für die Autoren keine Kosten an. Alle Artikel werden einem standardmäßigen Begutachtungsprozess unterzogen.

The journal Technische Mechanik is distributed only electronically with the beginning of 2019. The journal Technische Mechanik is an Open Access journal. All papers are available free of charge for download. Publishing of papers is free of any costs for the authors. Each submitted paper runs through a standard peer review process.

Anschrift der Redaktion/Editorial Office

Redaktion Technische Mechanik
Institut für Mechanik
Otto-von-Guericke-Universität
Postfach 4120
D-39016 Magdeburg
Telefon: +49 391 67-52 459
Telefax: +49 391 67-12 439/-12 863
e-mail: Technische.Mechanik@ovgu.de
<http://journals.ub.uni-magdeburg.de/ubjournals/index.php/techmech>
<http://www.ovgu.de/techmech/>

Herausgeber/Publisher

Magdeburger Verein für Technische Mechanik e.V.
und Otto-von-Guericke-Universität Magdeburg
Geschäftsführender Herausgeber: D. Juhre
Stellvertr. geschäftsführender Herausgeber: E. Woschke

Inhalt / Contents

Preface	40 Jahre Zeitschrift Technische Mechanik 40th anniversary of the journal Technische Mechanik	109
M.-U. Noll, L. Lentz, U. von Wagner	Comparison of the dynamics of a Duffing equation model and experimental results for a bistable cantilever beam in magnetoelastic energy harvesting	111
M. Aßmus, R. Glüge, H. Altenbach	On the Analytical Estimation for Isotropic Approximation of Elastic Properties applied to Polycrystalline Cubic Silicon used at Solar Cells ...	120
L. Spannan, F. Duvigneau, M. Gavila Lloret, C. Daniel, D. Juhre, E. Woschke	A study on harmonic excitation based experimental characterization of damping materials for acoustic simulations	134
V. Rizov, H. Altenbach	Longitudinal Fracture Analysis of an Inhomogeneous Stepped Rod with Two Concentric Cracks in Torsion	149
J. Nordmann, M. Aßmus, R. Glüge, H. Altenbach	On the Derivation of Hooke's Law for Plane State Conditions	160
F. Scherff, J. Gola, S. Scholl, K. Srivastava, T. Staudt, D. Britz, F. Mücklich, S. Diebels	RVE-size Estimation and Efficient Microstructure-based Simulation of Dual-Phase Steel	175
S. Bergmann, F. Hassani, Z. Javanbakht, M. Aßmus	On a Fast Analytical Approximation of Natural Frequencies for Photovoltaic Modules	191
		204

40 Jahre Zeitschrift Technische Mechanik

In diesem Jahr begehen wir das 40-jährige Bestehen der Zeitschrift "Technische Mechanik".

Gegründet im Jahr 1980 mit dem Bestreben, den wissenschaftlichen Austausch zu den theoretischen Grundlagen und Anwendungen der Technischen Mechanik und verwandter Gebiete zu fördern, hat sich die Zeitschrift in den zurückliegenden vier Jahrzehnten international etabliert. Anfangs als reines Printmedium in deutscher Sprache konzipiert, führte uns die Entwicklung über die gedruckte und elektronische Version hin zum rein elektronisch verfügbaren Open-Access-Medium in englischer Sprache.

Besonderer Dank gilt dem Gründungsvater und den geschäftsführenden Herausgebern der zurückliegenden Jahre. Dies waren Professor Johannes Altenbach, Professor Ulrich Gabbert, Professor Friedrich Rimrott, Professor Siegfried Koczyk sowie Professor Albrecht Bertram. Ebenso danken wir allen am Zustandekommen der Ausgaben der Zeitschrift in den zurückliegenden Jahren beteiligten Mitarbeitern sowie natürlich allen Autoren und Gutachtern ohne deren Beiträge diese Zeitschrift nicht möglich wäre.

Von großer Bedeutung ist ebenfalls die Unterstützung durch den Magdeburger Verein für Technische Mechanik e.V. sowie durch die Otto-von-Guericke-Universität Magdeburg.

Wir hoffen auch in der Zukunft auf ein reges Interesse an unserer Open-Access-Zeitschrift "Technische Mechanik" sowie auf eine weite Verbreitung der wissenschaftlichen Beiträge.

Magdeburg, 2020

Die Herausgeber

40th anniversary of the journal Technische Mechanik

This year we are celebrating the 40th anniversary of the journal "Technische Mechanik".

Founded in 1980 with the aim of promoting scientific exchange on the theoretical foundations and applications of engineering mechanics and related fields, the journal has become internationally established over the past four decades. Initially conceived as a pure print medium in German language, the development led us through the printed and electronic version to the purely electronically available Open Access medium in English language.

Special thanks go to the founding father and the managing editors of the past years. These were Professor Johannes Altenbach, Professor Ulrich Gabbert, Professor Friedrich Rimrott, Professor Siegfried Koczyk and Professor Albrecht Bertram. We would also like to thank all employees involved in the issues of the journal in the past years and of course all authors and reviewers without whose contributions this magazine would not be possible.

The support given by the Magdeburger Verein für Technische Mechanik e.V. and the Otto-von-Guericke-University Magdeburg is also of great importance.

We hope that there will be also in future a keen interest in our Open Access journal "Technische Mechanik" and that the scientific articles will be widely distributed.

Magdeburg, 2020

The Editors

Comparison of the dynamics of a Duffing equation model and experimental results for a bistable cantilever beam in magnetoelastic energy harvesting

Max-Uwe Noll^{1*}, Lukas Lentz¹, and Utz von Wagner¹

¹ Technische Universität Berlin, Institut für Mechanik, Einsteinufer 5, 10587 Berlin, Germany

Abstract: Nonlinear energy harvesting systems, consisting of a piezo cantilever beam with two additional magnets placed near the beam’s free end, have received a lot of attention in the past decade. The most common approach to model this system is to discretize the beam in space with one modal ansatz function and to assume a cubic restoring force caused by the magnetic field. The magnets are positioned so that two stable equilibrium positions exist in addition to the unstable undeflected beam tip displacement, i.e. the system is bistable. This modeling procedure results in a Duffing equation with a negative linear and a positive cubic restoring term, which is capable to represent the bistability. However, its sufficiency is often just assumed without thorough experimental validation of the mentioned presumptions.

In this paper the authors present the results of broad experimental investigations into the sufficiency of the Duffing equation as the underlying model of the mechanical subsystem (beam and magnets, but for the sake of simplicity without piezos). Therefore, a model is developed accordingly, following the approach of most publications, where a heuristic method is used to determine the cubic restoring force of the system. The theoretical predictions of the Duffing like model concerning the dynamical response to different harmonic base excitations are compared to experimental measurements done on a physical setup of the investigated system. The results are generally in good agreement, however particular limitations regarding the model are observed, as there is a shift of the occurring solutions to higher frequencies in the theoretical model compared to the experiments.

Keywords: nonlinear dynamics, energy harvesting, bistable oscillator, Duffing equation, cubic restoring force

1 Introduction

The term energy harvesting describes specific strategies to derive small amounts of available energy from external sources, which would be otherwise lost. More specifically, vibrational energy harvesting systems use ambient vibrations to generate electric energy [Priya (2007), Kim et al. (2011), Erturk and Inman (2011b)]. Commonly, the mechanical energy is transferred into electric energy by the use of piezoceramics fixed on the corresponding bending structure. The tuning of such vibrating systems, as well as other strategies to increase their efficiency, have been addressed in many publications, e.g. [Adhikari et al. (2009), Erturk et al. (2009)]. Particularly due to the nature of real-world excitation processes [Lentz et al. (2017)], which can be partly stochastic or have broadband frequencies, approaches have been made to use more than the discrete base frequency of any foremost linear system [Pellegrini et al. (2013), Harné and Wang (2013), Daqaq et al. (2014), Wei and Jing (2017)]. About a decade ago [Erturk et al. (2009)] has proposed the setup in figure 1, which has received great attention.

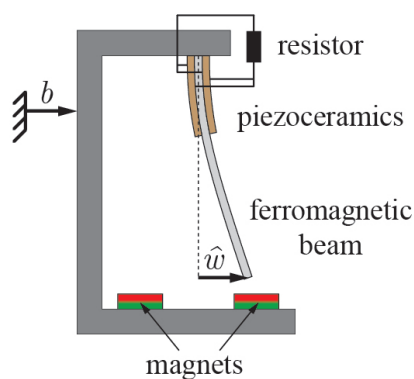


Fig. 1: Energy harvesting system. Modified figure of [Noll (2018)] with added coordinate b for the base excitation.

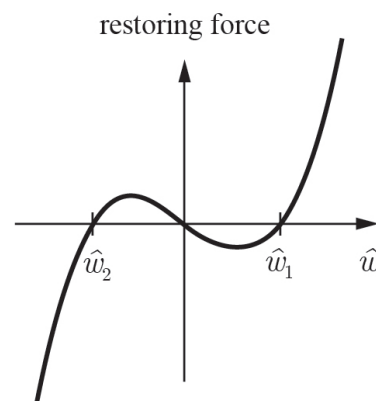


Fig. 2: Nonlinear restoring force with unstable trivial solution and two stable equilibria $\hat{w}_{1/2}$.

It consists of a base frame and a ferromagnetic cantilever beam that bends under base excitation b , with attached piezoceramic patches. The beam is clamped to an external structure, which excites the system by its motion. A characteristic feature of this particular system is its nonlinear behavior due to the magnets near the free end of the beam. In figure 2 the nonlinear restoring force is shown with its three equilibrium positions, at which the restoring force vanishes. Only the two non-zero equilibrium positions $\hat{w}_{1/2}$ are stable, which is the reason for the system to be called bistable. It has shown, as many other nonlinear systems, to be superior in efficiency to its linear counterpart when the excitation is not mono frequent but somehow distributed around the system's base frequency and when the beam orbits both stable positions ([Erturk and Inman (2011a), De Paula et al. (2015)]).

In order to model this energy harvesting system, it can be divided into three subsystems which are the bending beam structure, the restoring force caused by the magnetic field induced by the permanent magnets and the electrical part, which consists of the piezoceramics and the connected electrical circuit. The basic structure of the bistable cantilever beam with magnets, but without piezoceramics, was already described in [Moon and Holmes (1979)]. This part will be referred to as the mechanical subsystem in this paper. Hence, for the sake of simplicity, no piezoceramics are considered in the modeling and in the experiment in order to have the focus on the nonlinear magnetic restoring forces.

The key component of this mechanical subsystem is the cantilever beam, which is regularly modeled as an Euler-Bernoulli beam. The beam is discretized by its first linear eigenfunction (without magnets). This modeling has become the standard approach to describe its dynamics by a single second order ordinary differential equation, which has been applied many times (as in [Litak et al. (2010), Tam and Holmes (2014), De Paula et al. (2015), Noll et al. (2019a)]). The question if more than one ansatz function is necessary, is addressed in another paper by the authors [Noll et al. (2019b)]. Its conclusions are that the use of the first linear eigenfunction of the beam is suitable in most cases and the second linear ansatz function only has a small geometric share in cases of super harmonic responses. Following the standard modeling procedure, the magnets are replaced by a single transverse force that is applied at the tip of the beam and is assumed to be of a cubic polynomial type with vanishing quadratic term. This results in the Duffing equation with negative linear and positive cubic restoring force (see e.g. [Lentz (2018)]), which is a minimal model to describe bistability. A lot of varied systems with different arrangements of magnets (see e.g. Westermann et al. (2013); Lan and Qin (2017)) or even other nonlinear mechanisms finally end in a Duffing equation. Most of the publications about comparable bistable configurations follow this approach, or simply state a Duffing equation as the underlying model, as in [Litak et al. (2010)] or [Lentz and von Wagner (2015)]. The model parameters are then found heuristically in a manner described in the following. The displacement of the nontrivial equilibrium positions and the corresponding frequency of free vibration of small amplitude are needed. They provide the necessary information to determine the restoring parameters. This can (only) be done when an experimental setup exists, or corresponding assumptions regarding the system are made.

In [Noll et al. (2019a)] the authors have tried to apply an alternative procedure, where no existing experimental setup would be needed to determine a model by a direct computation of the restoring force. Therefore, the magnetic field was simulated by a two-dimensional FEM-approach with subsequent numeric force computation, where linear magnetic material behavior (i.e. constant permeability) is assumed. However, the resulting model in that case could not satisfyingly meet the conditions of matching equilibrium positions and corresponding frequencies. In contrast, the agreement of the equilibrium positions and frequencies are always achieved when using the aforementioned heuristic method. It yields a model that is a good approximation when the beam tip is in the vicinity of the stable equilibrium positions. However, in other ranges of the beam tip displacement, as for example the unstable equilibrium with zero displacement, this might not be a good approximation.

In this paper, dynamic experiments are described, investigating the system's steady state response for different harmonic base excitations with varying frequency and amplitude. In the following section, the experimental setup is introduced. The results will be compared to predictions of a model that is found according to the heuristic method, described in the second next section.

2 Experimental setup

The main focus is on the mechanical subsystem (figure 3) of the energy harvesting system, that consists of a cantilever beam (dimensions: $250 \times 20 \times 1$ mm) and permanent magnets (dimensions: $5 \times 20 \times 10$ mm). No piezoceramics are considered in the presented investigations, as mentioned in the introduction. The distance between the beam tip in the undeflected state and the top side of the magnets is about 6 mm and the gap between the magnets is 12.7 mm. The beam made of ferromagnetic steel is modeled according to section 3 as an Euler-Bernoulli beam and therefore mechanically characterized by its mass per length μ and bending stiffness EI . Further it is magnetically characterized by its relative permeability. There are some indications that the material of the beam is not linear regarding its magnetic properties, i.e. it shows a distinct hysteresis depending on the strength of the applied external magnetic field [Noll et al. (2019a)]. The magnets are made of NdFeB (Neodymium) with remanence $B_r = 1.35$ T. The overall system has the physical properties given in table 1.

Tab. 1: Physical properties of the experimental setup (cf. figure 3).

property	value
first circular eigenfrequency of the beam when no magnets are present ω_0	2π 13.4 Hz
displacement of the nonzero equilibrium positions $\hat{w}_{1/2}$ (distance from the undeflected position when permanent magnets are present)	+6.97 mm −6.97 mm
circular frequency of the oscillation in equilibrium positions with small amplitude ω	2π 14.9 Hz 2π 14.6 Hz
damping ration with magnets in equilibrium positions D	0.0013 0.0019

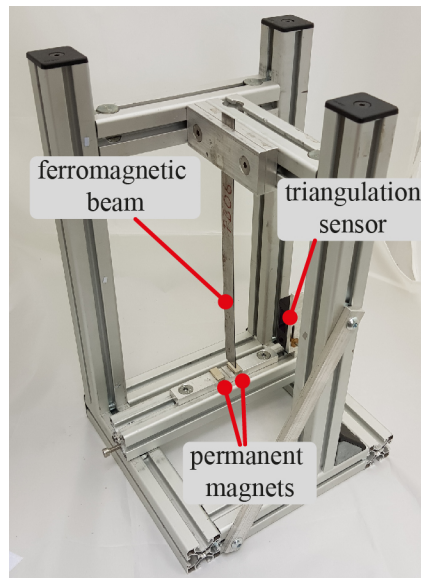


Fig. 3: Mechanical subsystem of the investigated energy harvesting system.

Note that in general there are two different circular frequencies ω for small vibrations in each stable equilibrium, due to an undesired but unavoidable asymmetry of the experimental setup. For the heuristic modeling later, the average will be taken. Same applies to the damping ratios D that are found by determining the logarithmic decrement from time signals of free beam vibrations. In order to measure the quantities in table 1, the setup shown in figure 4 is used. It consists of several devices to realize a harmonic base excitation and devices to measure the beam's response in form of its beam tip displacement. Also, the actual base excitation occurring at the base frame is measured. To determine the static (and later dynamic) displacement of the beam tip a laser triangulation sensor (ALLSENSE AM500-50) is used. It is attached to the moving base frame (cf. figure 3), hence directly provides the relative displacement of the beam tip with respect to the permanent magnets, which are fixed within the moving aluminum framework. The harmonic signal of the base excitation is generated by MATLAB R2018a and further processed by a measurement box (Datatranslation DT9837A) that provides the desired voltage signal for a shaker (LDS V406/8-PA100E) after amplification (LDS PA 100E Power Amplifier). The shaker is attached to a vibration table, containing four leaf springs as support, on which the system in figure 3 is placed. The vibration table has a notable dynamic of its own, which has an influence on the base excitation. The base frequency of the vibration table is about 6 Hz, which is not very far from the considered range of frequencies in experiments later. The range will be 7 Hz to 18 Hz and is chosen around the first eigenfrequency of the beam of 13.4 Hz. Hence, the transfer function of the vibration table is not constant within the considered range of frequencies and needs to be regarded. The measurement box provides a voltage signal that is amplified and provided to the shaker.

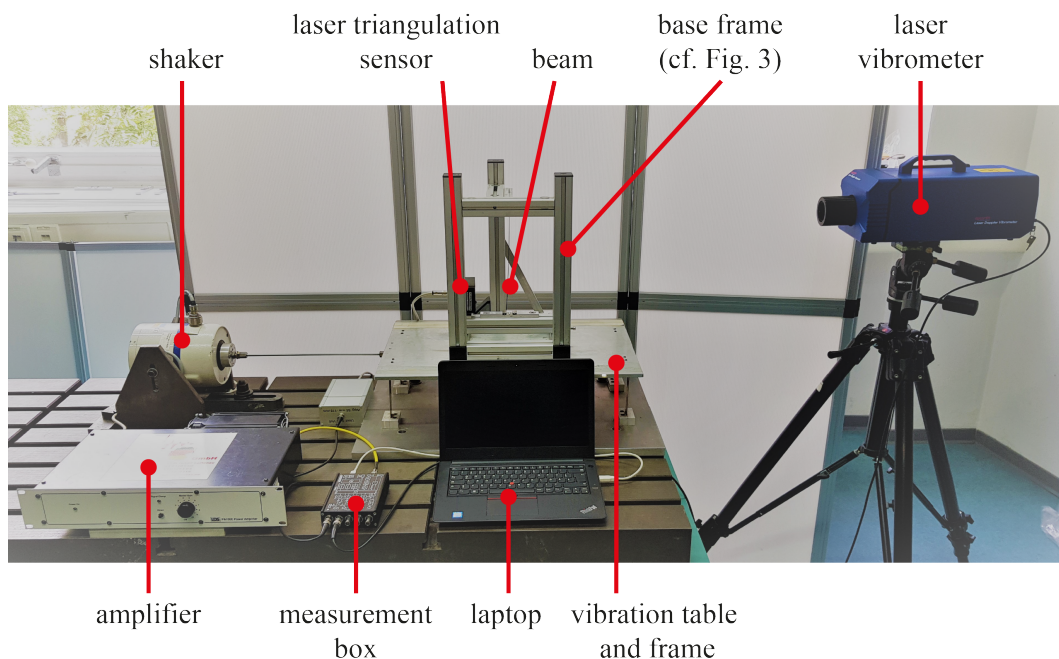


Fig. 4: Experimental setup of the energy harvesting system placed on a vibration table excited by a shaker, with measurement devices and related data acquisition tools.

The shaker generates a force proportional to this signal, to excite the vibrating table. Since a harmonic base excitation of a certain amplitude A is desired, that is independent of the circular excitation frequency Ω , the signal provided by the measurement box needs to regard the dynamics of the vibration table. To confirm that the specified signal of the excitation concurs with the actual base motion it is measured by a laser vibrometer (OptoMET Nova Basis), that determines the velocity \dot{b} of the base frame. The base excitation, that is proportional to the acceleration \ddot{b} , is then found from this measurement by a numerical differentiation of the time signal of the discrete velocity values. The reason it is measured is that the base excitation occurring at the base frame is not always concurring with the specified signal generated in MATLAB. There is a bias in magnitude and a phase shift of roughly π rad originating from the dynamics of the vibration table. Also, the authors have observed that there are cases in which the beam, due to its inertia, has a retroactive effect on the actual base excitation. Especially when the beam tip exhibits large orbits around both of its stable equilibrium positions, deviations of the actual base excitation from the desired specified signal are probable. The measurements later to be shown in detail are chosen due to their fairly harmonic base motion.

All measurements are done in the steady state of the system, which is assumed to be reached after a 60 seconds transient response of the system. Subsequently the measurements are done for 10 seconds with a sample rate of 10 kHz. The sampling is performed after a suitable lowpass filter applied by the measurement box.

3 Modeling of the mechanical subsystem

The different aspects of the overall system can be, to a certain extent, modeled separately and in different levels of complexity. Two existing publications of the authors deal with particular parts of the energy harvesting system which are: first, the magnetic field, the thereby caused magnetic restoring force and the resulting corresponding stationary behavior of the system (equilibrium positions and corresponding frequencies of small free vibrations) in [Noll et al. (2019a)] and second, the spatial discretization of the beam using only the first linear eigenfunction of the beam in [Noll et al. (2019b)]. In both publications the beam has been modeled as an Euler-Bernoulli beam structure, that bends under excitation. The beam displacement is described by a partial differential equation for the beam displacement w depending on the beam coordinate ξ and time t as given in many continuum dynamics textbooks. Following the classical discretization process as in [Noll et al. (2019a)], the mixed Ritz ansatz

$$w(\xi, t) = x(t) \phi(\xi), \quad (1)$$

where x is the time dependent modal coordinate. ϕ is the first eigenfunction of the linear beam, $\xi \in [0, L]$ the beam coordinate and L the total length of the beam. ϕ is chosen to be 1 at $\xi = L$, hence x concurs with the beam tip displacement $\hat{w} = w(L, t)$ (cf. figure 1). It yields the ordinary differential equation of motion given by

$$\ddot{x}(t) + 2D\omega\dot{x}(t) - \alpha x(t) + \beta x^3(t) = g\ddot{b}(t). \quad (2)$$

Compared to [Noll et al. (2019a)] the term on the right-hand side is added, since in this paper dynamic experiments of the driven Duffing oscillator are performed considering a base excitation, while in [Noll et al. (2019a)] the static behavior and free vibrations were investigated. The coefficient g is determined accordingly and given by

$$g = - \frac{\int_0^L \phi(\xi) d\xi}{\int_0^L \phi^2(\xi) d\xi}. \quad (3)$$

The excitation is chosen to be a base excitation of a constant amplitude A of the form $\ddot{b}(t) = A \cos \Omega t$.

In order to get the specific kind of restoring term, that is $-\alpha x(t) + \beta x^3(t)$, the assumption has been made that the magnetic force is a cubic polynomial of the beam tip displacement. Further, a linear modal damping has been inserted with the damping ratio D . In cases where α and β are both positive, bistability is existent with the two nontrivial equilibrium positions $x_{1/2}$ on each side of the undeflected beam position

$$x_{1/2} = \pm \sqrt{\frac{\alpha}{\beta}}. \quad (4)$$

Further, if considering oscillations within these two equilibrium positions with small amplitude the circular frequency for free vibrations in each of the stable equilibrium position can be determined after linearization by

$$\omega = \sqrt{2\alpha}. \quad (5)$$

When a physical setup is available the model parameters can be determined and are given in table 2 for the setup in figure 3.

Tab. 2: Model parameters of corresponding experimental setup given table 1.

parameter	ω [1/s]	D [-]	α [1/s ²]	β [1/s ²]	g [1/m]
value	92.7	0.0016	4275.6	$8.8 \cdot 10^7$	-1.57

The parameter ω and D are found as the average of their values from an analysis of the time signals of free beam vibrations in each stable equilibrium when the magnets are applied. Even though the beams's circular eigenfrequency $\omega_0 = 2\pi 13.4$ 1/s has no direct significance for the setup with magnets, it is taken to define the frequency ratio η as

$$\eta = \frac{\Omega}{\omega_0}, \quad (6)$$

which is used later. α and β are found according to (4), (5) and g by equation (3). This approach is of a heuristic nature and therefore an experimental setup needs to be present first to find the according model parameters. This is an essential drawback of this approach, since these quantities need to be measured every time the setup is changed (e.g. the distance between the magnets). On the other hand, an advantage is that the model gives a good approximation of the physical setup when the beam tip is near one of the stable equilibrium positions. The approach ensures, that the equilibrium as well as the corresponding frequency of the model concur with those of the setup (except for possible asymmetries which cannot be covered by an uneven cubic force model). In the next section the experimental results are presented, and a comparison is done to the predictions of the Duffing model.

4 Experimental results and comparison to theory

In this section experimental results are shown and compared to the predictions provided by the corresponding Duffing model equation (2) with parameters in table 2. The setup is excited by different harmonic base excitations, which differ in acceleration amplitude and frequency. The beam tip displacement is measured, as well as the actual excitation. It is common to look at the phase diagram of the solution, which is a trajectory in the state space, that shows the velocity of the beam tip over the beam tip displacement (see figure 5). For that, the beam's velocity is to be determined from the measurement of the beam tip displacement, which is achieved by a numerical differentiation done using the central difference quotient. Since the signal of the beam tip displacement is noisy and a numerical differentiation increases noise, it is necessary to lowpass filter the signals. This is done using a Butterworth lowpass filter with cut-off frequency of 90 Hz (5 times the largest excitation frequency). This frequency is chosen as a compromise between a low cut-off frequency to get smooth results and a high cut-off frequency to remain the characteristics of the phase trajectory. Also, sub and super harmonics are to be expected. The super harmonics, which can be several multiples of the excitation frequency, could be eliminated by a filter with a too low cut-off frequency.

The solution that occurs depends on the initial conditions since the system is nonlinear, what means that for one excitation different types of solutions are possible. One approach to distinguish different solutions is to consider the turning points of the beam tip throughout the measurement time. In figure 5 the turning points are marked. More specifically: when the velocity changes in sign, the beam is changing the direction it travels. If all those occurring turning points (and therefore all beam tip displacements also) have the same sign (either all exclusively positive or negative) the solution is called intrawell (in blue). If the sign switches periodically with a period not being larger than a defined threshold, the solution is labeled as interwell solution (red). If there is a very large number of turning points (in this work set to be greater than 25) with positive and negative signs the solution is considered to be chaotic, even though it might be possible it is a periodic solution with a very large period.

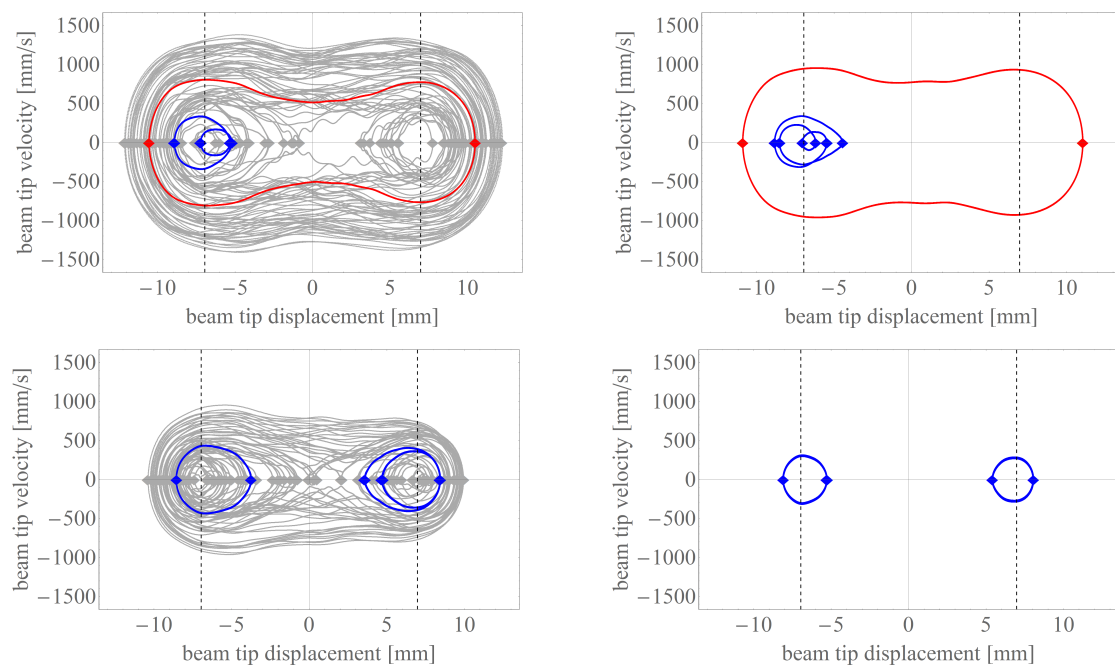


Fig. 5: Experimental phase diagrams and turning points (marker) of different solutions for a harmonic acceleration of amplitude $A = 3.81$ m/s² and different excitation frequencies. Upper left: 7 Hz / $\eta \approx 0.52$; upper right: 8.5 Hz / $\eta \approx 0.64$; lower left: 14 Hz / $\eta \approx 1.05$; lower right: 17 Hz / $\eta \approx 1.27$. Color code refers to the type of solution: intrawell solutions in blue, interwell solutions in red and chaotic solutions in gray.

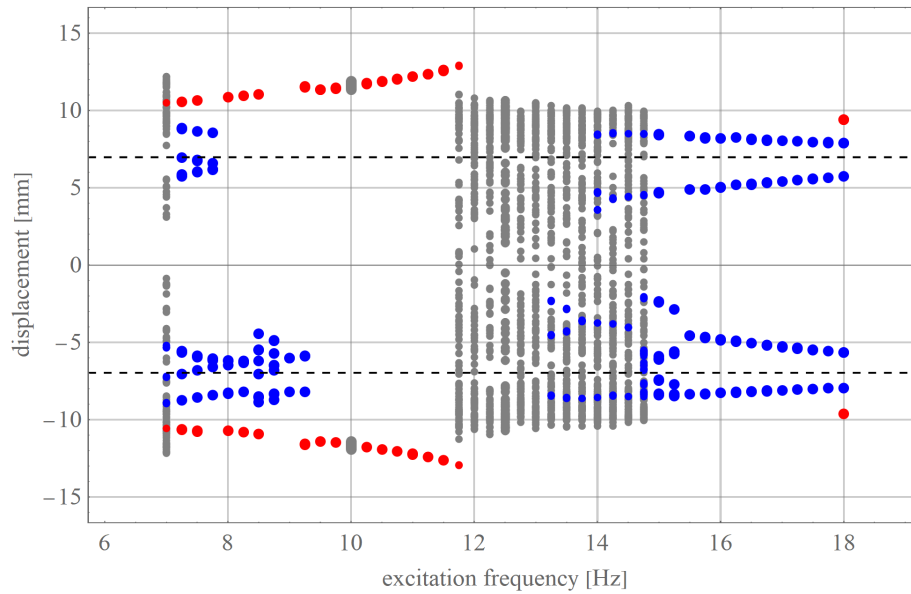


Fig. 6: Experimental results: turning points of the beam tip for parallel existing steady state solutions for harmonic acceleration of constant amplitude $A = 3.81 \text{ m/s}^2$ and different excitation frequencies. Color code corresponding to figure 5.

Another possible way of displaying the occurring types of solutions is the system response diagram in figure 6, which is especially suitable to show the influence of the excitation frequency and is also used e.g. in [Lentz (2018)]. It shows all turning points of different solutions that exist in parallel for excitations of different frequency but constant amplitude. As it can be seen, there are different frequency ranges where more than one solution exists and some ranges, where only one solution has occurred during the different experimental repetitions. For each frequency ten experiments have been made, sometimes having the same final steady state and sometimes having different final steady states. The initial conditions of each experiment are not known nor reproducible, which means they cannot be controlled. Hence, it is not possible to directly reproduce each experiment numerically, making a comparison of the experiment to the Duffing model difficult. To deal with the lack of controllability of the entirety of the occurring solutions in the experiments (and also numerics), many trials with different initial conditions are done to increase the chances of various solutions, to allow a comparison between experimental and numerical results.

In figure 7, the results of numerical simulations of the model in equation (2) can be seen. It is found by a numerical integration using the NDSolve-function of MATHEMATICA 11 with no changes of the default settings with respect e.g. to the integration scheme, step size and precision goal. To get a better numerical conditioning, the differential equation for the modal coordinate x is transformed to be in the magnitude of millimeter $\tilde{x} = 10^{-3}x$ before solving for \tilde{x} and transforming back. The sets of initial conditions in this case need to be chosen and are set to be 126 different equidistant values for \tilde{x} for $t = 0$ between -15 and 15 and zero velocity. The integration time is 1000 seconds and the last ten seconds are used to be analyzed for their turning points analogous to the experimental data. For avoiding large arguments in the periodic cosine function and corresponding errors, the values are set back in the range between 0 and 2π when exceeding this range.

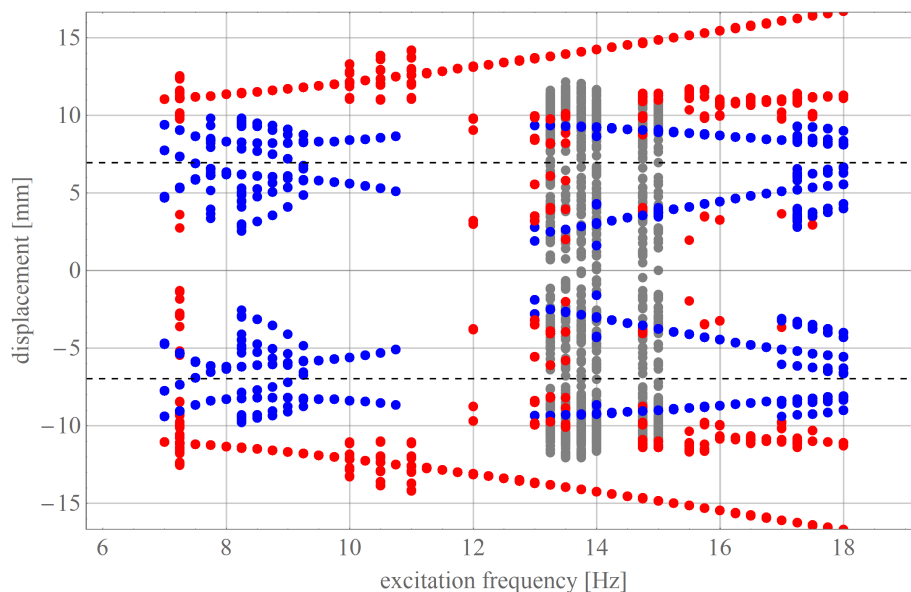


Fig. 7: Numerical results: system response diagram in Fig. 6 found by numerical integration of the Duffing model. Color code corresponding to figure 5.

When comparing both outcomes in figure 6 and 7 similar characteristics can be seen. In both diagrams, there are three main frequency ranges distinguishable: one at lower frequencies, where mostly intra- and interwell solutions (blue and red) occur in parallel, another range, where interwell solutions (only red) exist solely and a third where chaotic solutions are probable and also intrawell and interwell occur again. A difference between both diagrams is that in theory those three regions are shifted to higher frequencies. In the experiment lower excitation frequencies (around about 10 Hz / $\eta \approx 0.75$) lead to the preferred large interwell solutions and in theory, this range is slightly shifted to larger frequencies (around about 12 Hz / $\eta \approx 0.9$). The position of this range is of high interest due to its high potential for energy harvesting purposes since the beam undergoes large periodic deformations that cause high energy outputs. It is also noteworthy that the biggest region, where chaotic solutions were observed, in experiment is around the eigenfrequency of the beam (13.4 Hz / $\eta = 1$) and in theory again shifted to the right for larger frequencies (14 Hz / $\eta \approx 1.05$). Another difference is that in theory large interwell solutions occur for every considered frequency but do not occur as often in the experiments. It shall be noted that the experimentally realized base excitation may differ from a harmonic excitation due to different reasons explained in section 2. A measure of the amplitude of each actual base acceleration is given by the Root Mean Square (RMS) value. The mean value of the acceleration amplitude A for all experiments (ten repetitions for each of the 45 frequencies) in figure 6 is 3.81 m/s^2 and the standard deviation of all values is 0.086 m/s^2 .

The results shown so far were generated for one specific amplitude of the base excitation. In the next step, different amplitudes are considered. A map of the type of the solution (color code consistent to the figures above) that occurs for a single experiment with an excitation frequency and amplitude is shown in figure 8. Again, the experimentally realized initial conditions are uncontrollable and therefore again unknown. As it can be seen, the excitation amplitude is not uniformly distributed, due to influences of the vibrating table. The actual occurring base excitation amplitude is determined by the RMS value of the measured base excitation. The same rules to distinguish the type of solution are applied.

In figure 9 equivalent results of numerical simulations are shown. Again, time integration is performed using NDSolve in Mathematica 11 with default settings. For a 1:1 comparison of the results, the same excitation and initial conditions would need to be considered. This is impossible as described above as there are very restricted possibilities to control the initial conditions in the experimental setup. For this reason, again more simulations are done as experiments to cover a broader range of initial conditions. For simulations this is easier to perform as they are not as time consuming and can be done partly parallel.

For each excitation 25 simulations are performed, where the initial conditions are equidistant displacements $x(t=0)$ in the range of $[-3x_1, 3x_1]$ with zero velocity. Only if always the same solution occurred, a filled squared marker of corresponding color is used. If the same solution occurs between 15 and 24 times out of 25, an diamond marker of the lighter color of the solution that occurred the most is used. Further, no marker is used, if no solution appeared more than at least 15 out of 25 times. Note that, for these criteria, chaotic solutions are less likely on the map and never occur 25 out of 25 times for a certain excitation. Consequently no squared grey marker can be found, but grey diamond markers are to be seen on the map in the same regions chaos appeared experimentally.

Again, when comparing both results, similar characteristics can be found. Overall, the model is in general suitable to predict the experimental results, but in detail deviations can be found. In good agreement, for example, are the position of chaotic solutions (grey) and that for small excitation amplitudes (below 2 m/s^2), where mostly intrawell solutions exist. Differences are again shifts of the different regions to higher frequencies in the model results, as can be seen in the large red region. Similar theoretical investigations with maps of this kind can also be found in [Panyam et al. (2014)], which concur with the results of this paper.

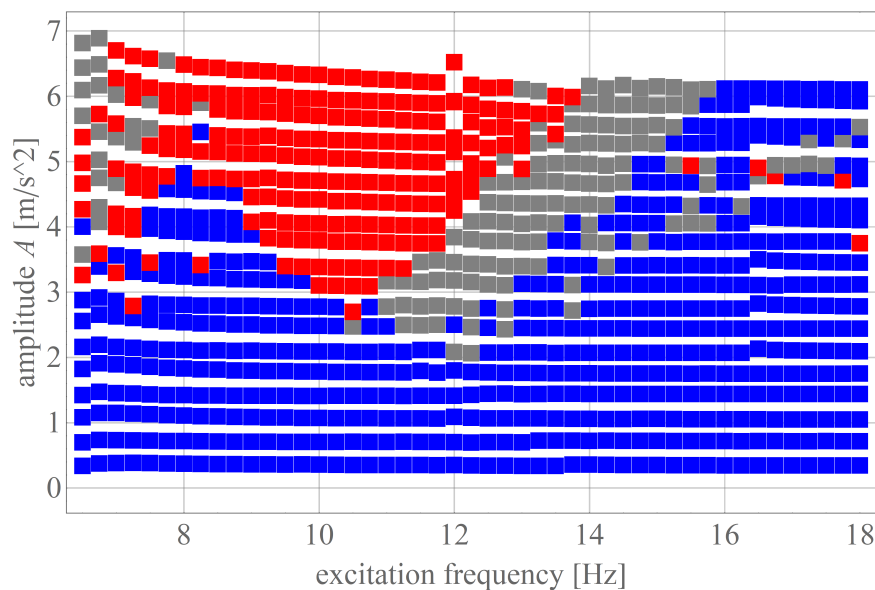


Fig. 8: Map of experimental results of the system response for different excitation frequencies and different amplitudes of harmonic acceleration. Only one experiment for each excitation is performed, wherefore only one solution occurred and uniquely defines the color of the marker. Color code corresponding to figure 5.

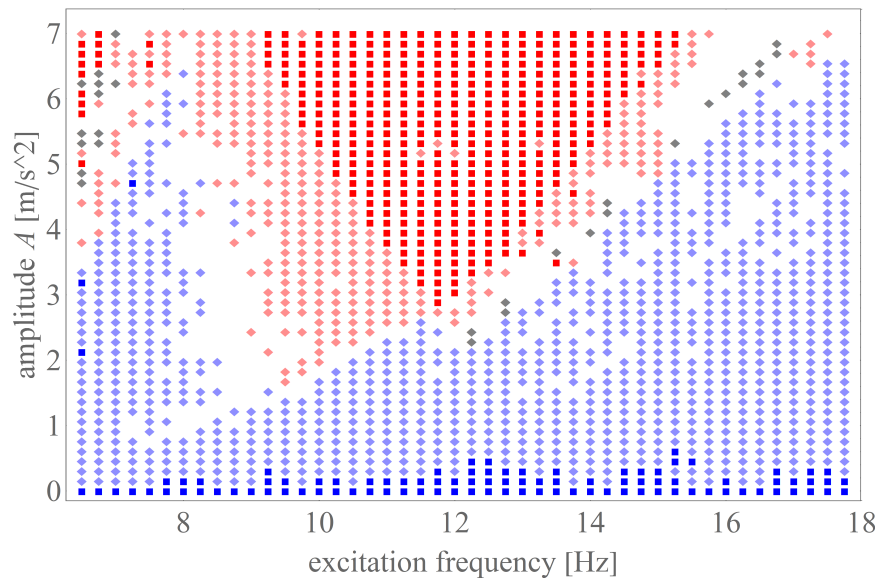


Fig. 9: Map of numerical results of the system responses found by time integration to be compared with figure 8. Color code corresponding to figure 5.

5 Conclusions

Energy harvesting performed by a bistable cantilever beam has attracted much attention in the past years. In most of the corresponding publications, the restoring force of the energy harvesting system is assumed to be of third degree, i.e. cubic. This modeling leads to the bistable Duffing equation. Corresponding model parameters are found heuristically.

In this paper, the assumption, that the restoring force is a cubic polynomial depending solely on the beam tip displacement, is investigated for suitability. Extensive experiments are performed to experimentally determine the system response for varying harmonic base excitations. A comparison to numerical results by time integration of the corresponding Duffing model is presented. The biggest issue is that the initial conditions cannot be controlled on the experimental setup that is used. Hence, the diversity of the solutions is probably not fully represented. To overcome this limitation several experiments and many simulations with varying initial conditions are done to increase the probability of occurrence of the respectively existing different solutions. In any case, the final steady solution of the system is in the focus of interest. Although there is no guarantee that all possible solutions are found, neither experimentally nor numerically, the occurring solutions are in good agreement and the results are broad enough for a comparison of the general characteristics. In fact the results show that in general the model covers most of the characteristics that can be seen in experiments but may have deviations. More specific, there might be a slight shift of the existence of solutions towards larger frequencies in theory. This might lead to false predictions when optimizing an energy harvesting system by tuning it to an existing harmonic excitation of a specific frequency. In general, the cubic restoring characteristics seems to be a good model, if the requirements on the accurateness of the model are not too high. On the other hand, as e.g. described in [Lentz (2018)] or [Noll et al. (2019a)], there may be specific cases where higher order approximations or in general extended modeling may be necessary.

6 Funding

This study was funded by Deutsche Forschungsgemeinschaft (DFG, German Research Foundation) - WA 1427/23-1,2.

References

- S. Adhikari, M. I. Friswell, and D. J. Inman. Piezoelectric energy harvesting from broadband random vibrations. *Smart Materials and Structures*, 18(11), 2009. ISSN 09641726. doi: [10.1088/0964-1726/18/11/115005](https://doi.org/10.1088/0964-1726/18/11/115005).
- Mohammed F. Daqaq, Ravindra Masana, Alper Erturk, and D. Dane Quinn. On the Role of Nonlinearities in Vibratory Energy Harvesting: A Critical Review and Discussion. *Applied Mechanics Reviews*, 66(4):40801, 2014. ISSN 0003-6900. doi: [10.1115/1.4026278](https://doi.org/10.1115/1.4026278). URL <http://appliedmechanicsreviews.asmedigitalcollection.asme.org/article.aspx?doi=10.1115/1.4026278>.
- A. S. De Paula, D. J. Inman, and M. A. Savi. Energy harvesting in a nonlinear piezomagnetoelastic beam subjected to random excitation. *Mechanical Systems and Signal Processing*, 54:405–416, 2015. ISSN 10961216. doi: [10.1016/j.ymssp.2014.08.020](https://doi.org/10.1016/j.ymssp.2014.08.020). URL <http://dx.doi.org/10.1016/j.ymssp.2014.08.020>.
- A. Erturk and D. J. Inman. Broadband piezoelectric power generation on high-energy orbits of the bistable Duffing oscillator with electromechanical coupling. *Journal of Sound and Vibration*, 330(10):2339–2353, 2011a. ISSN 0022460X. doi: [10.1016/j.jsv.2010.11.018](https://doi.org/10.1016/j.jsv.2010.11.018). URL <http://www.sciencedirect.com/science/article/pii/S0022460X10007807>.
- A. Erturk and D. J. Inman. *Piezoelectric Energy Harvesting*. John Wiley & Sons, Ltd, 2011b. doi: [10.1002/9781119991151](https://doi.org/10.1002/9781119991151).

- A. Erturk, J. Hoffmann, and D. J. Inman. A piezomagnetoelastic structure for broadband vibration energy harvesting. *Applied Physics Letters*, 94(25):254102, 2009.
- R. L. Harne and K. W. Wang. A review of the recent research on vibration energy harvesting via bistable systems. *Smart Materials and Structures*, 22(2), 2013. ISSN 09641726. doi: [10.1088/0964-1726/22/2/023001](https://doi.org/10.1088/0964-1726/22/2/023001).
- H. S. Kim, J. H. Kim, and J. Kim. A review of piezoelectric energy harvesting based on vibration. *International Journal of Precision Engineering and Manufacturing*, 12(6):1129–1141, 2011. ISSN 12298557. doi: [10.1007/s12541-011-0151-3](https://doi.org/10.1007/s12541-011-0151-3).
- C. Lan and W. Qin. Enhancing ability of harvesting energy from random vibration by decreasing the potential barrier of bistable harvester. *Mechanical Systems and Signal Processing*, 85:71–81, 2017. ISSN 10961216. doi: [10.1016/j.ymssp.2016.07.047](https://doi.org/10.1016/j.ymssp.2016.07.047). URL <http://dx.doi.org/10.1016/j.ymssp.2016.07.047>.
- L. Lentz. Zur Modellbildung und Analyse von bistabilen Energy-Harvesting Systemen. *Dissertation, TU Berlin*, 2018.
- L. Lentz and U. von Wagner. Multi-mode model of a piezomagnetoelastic energy harvester under random excitation. *Pamm*, 15(1): 259–260, 2015. doi: [10.1002/pamm.201510120](https://doi.org/10.1002/pamm.201510120).
- L. Lentz, H. T. Nguyen, and U. von Wagner. Energy harvesting from bistable systems under random excitation. *Machine Dynamics Research*, 41, 2017.
- G. Litak, M. I. Friswell, and S. Adhikari. Magnetopiezoelastic energy harvesting driven by random excitations. *Applied Physics Letters*, 96(21):12–15, 2010. ISSN 00036951. doi: [10.1063/1.3436553](https://doi.org/10.1063/1.3436553).
- F. C. Moon and P. J. Holmes. A magnetoelastic strange attractor. *Journal of Sound and Vibration*, 65(2):275–296, 1979.
- M.-U. Noll. Energy harvesting system. *figshare*, 2018. doi: <https://doi.org/10.6084/m9.figshare.7492208.v1>.
- M.-U. Noll, L. Lentz, and U. von Wagner. On the Improved Modeling of the Magnetoelastic Force in a Vibrational Energy Harvesting System. *Journal of Vibrational Engineering and Technologies*, (0123456789), 2019a. ISSN 25233939. doi: [10.1007/s42417-019-00159-4](https://doi.org/10.1007/s42417-019-00159-4). URL <https://doi.org/10.1007/s42417-019-00159-4>.
- M.-U. Noll, L. Lentz, and U. von Wagner. on the Discretization of a Bistable Cantilever Beam With Application To Energy Harvesting. *Facta Universitatis, Series: Mechanical Engineering*, 17(2):125, 2019b. ISSN 0354-2025. doi: [10.22190/fume190301031n](https://doi.org/10.22190/fume190301031n).
- M. Panyam, R. Masana, and M. F. Daqaq. On approximating the effective bandwidth of bi-stable energy harvesters. *International Journal of Non-Linear Mechanics*, 67:153–163, 2014. ISSN 00207462. doi: [10.1016/j.ijnonlinmec.2014.09.002](https://doi.org/10.1016/j.ijnonlinmec.2014.09.002). URL <http://dx.doi.org/10.1016/j.ijnonlinmec.2014.09.002>.
- S. P. Pellegrini, N. Tolou, M. Schenk, and J. L. Herder. Bistable vibration energy harvesters: A review. *Journal of Intelligent Material Systems and Structures*, 24(11):1303–1312, 2013. ISSN 1045389X. doi: [10.1177/1045389X12444940](https://doi.org/10.1177/1045389X12444940).
- S. Priya. Advances in energy harvesting using low profile piezoelectric transducers. *Journal of Electroceramics*, 19(1):165–182, 2007. ISSN 13853449. doi: [10.1007/s10832-007-9043-4](https://doi.org/10.1007/s10832-007-9043-4).
- J. I. Tam and P. Holmes. Revisiting a magneto-elastic strange attractor. *Journal of Sound and Vibration*, 333(6):1767–1780, 2014. ISSN 0022460X. doi: [10.1016/j.jsv.2013.11.022](https://doi.org/10.1016/j.jsv.2013.11.022). URL <http://dx.doi.org/10.1016/j.jsv.2013.11.022>.
- C. Wei and X. Jing. A comprehensive review on vibration energy harvesting: Modelling and realization. *Renewable and Sustainable Energy Reviews*, 74(November 2016):1–18, 2017. ISSN 18790690. doi: [10.1016/j.rser.2017.01.073](https://doi.org/10.1016/j.rser.2017.01.073). URL <http://dx.doi.org/10.1016/j.rser.2017.01.073>.
- H. Westermann, M. Neubauer, and J. Wallaschek. Modeling of a nonlinear vibration-based energy harvesting system as a Duffing oscillator. *Solid State Phenomena*, 198:663–668, 2013. ISSN 10120394. doi: [10.4028/www.scientific.net/SSP.198.663](https://doi.org/10.4028/www.scientific.net/SSP.198.663).

On the Analytical Estimation for Isotropic Approximation of Elastic Properties applied to Polycrystalline Cubic Silicon used at Solar Cells

Marcus Aßmus*, Rainer Glüge, Holm Altenbach

Otto von Guericke University, Institute of Mechanics, Universitätsplatz 2, 39108 Magdeburg, Germany

Abstract: The present contribution is concerned with the effective mechanical parameters of polycrystalline silicon used for solar cells. Thereby, an analytical scheme for the prediction of elastic properties of polycrystals is reviewed, applied and verified. Emphasis is on first-order bounds and derived estimates. Based on cubic symmetry of a single crystal the projector representation is exploited for the description of the constitutive equations. The elasticity tensor is developed for several assumptions which stem from rather classical homogenization schemes. This results in a rational representation and determination of linear elastic material parameters of a homogeneous, macroscopically isotropic comparison material. The analytically determined parameters are compared to experimental data. It is found that the present procedure reproduces the experimental results in very close proximity.

Keywords: solar energy materials, solar cells, polycrystals, cubic system, homogenization, mechanical properties

1 Introduction

Silicon is the most commonly used semiconductor material for solar cells in photovoltaic modules. The actual market share is around 90% (Philipps and Warmuth, 2019). Basically a distinction is here made between mono- and polycrystalline silicon. Although higher electrical efficiencies can be achieved with monocrystalline silicon, polycrystalline silicon is used more widely with a market share of approximately 65%. This is not least due to its cheaper production (Philipps and Warmuth, 2019) whereby in principle several fabrication methods are possible (Petersen, 1982). During the service life of photovoltaic modules, the built-in solar cells are exposed to different mechanical loading scenarios. To name two extremes as an example, high snow loads at low temperatures far below freezing point or high wind loads at temperatures above 60 degrees Celsius can occur. The specification of the temperature is important here since the solar cells are embedded in an encapsulant whose material is strongly temperature sensitive. Solar cells should be able to withstand these stresses for periods of at least 20 years. From an engineering point of view, strength analyses are necessary therefore. Such analyses are of immense importance since failures at solar cells are correlated with power loss and decreased energy harvest (Köntges et al., 2014).

In present work we will focus on polycrystalline silicon. Aggregates of silicon consist of monocrystals obeying a cubic symmetry. Due to the complexity of geometrical models for such aggregates, the necessity often arises to work with a comparison medium for the discrete microstructure. It is in particular advantageous to work with effective properties during the design process for structural analysis. According to Petersen (1982), the effective Young's modulus of polycrystalline silicon is around $150 \cdot 10^3$ to $170 \cdot 10^3 \text{ N/mm}^2$, referring to various sources. This is certainly a very broad range ($\Delta_Y = 20 \cdot 10^3 \text{ N/mm}^2$), which means that results of strength analysis will spread over an equally broad area. This is why there are various efforts to substantiate effective values of polycrystalline silicon, cf. (Hopcraft et al., 2010).

In mechanics, computational and analytical methods for such estimations have proven successful, cf. Böhm (2020). The attraction of an analytical method lies in its usually simple handling and the rapid attainment of results, at least in comparison to computational methods. In the context of analytical homogenization methods, first-order (Voigt, 1889; Reuss, 1929) and second-order (Hashin and Shtrikman, 1962a,b) estimates, self-consistent estimates (Christensen and Lo, 1979) and statistical methods (Kröner, 1958) exist. Basic reviews of different methods to determine effective elastic parameters are presented in Kröner (1972) or Lobos Fernández (2018). If the morphology of the microstructure is sufficiently isotropic first-order estimates deliver results with sufficient accuracy. The following assumptions are made in the course of present investigations.

- We consider silicon mono- and polycrystals where physical and geometrical linearity is a reasonable assumption in the elastic range.
- The silicon monocrystal possesses a cubic crystal symmetry.
- The crystal orientation of the bulk features a uniform distribution.
- The interaction of the crystals and the influence of the distribution functions of the crystal interfaces and the crystal edges on the symmetry of the macroscopic elastic behavior are neglected.

The consideration of a uniform distribution of the crystal orientation is equivalent to an isotropic crystal orientation function. Morphological investigations of solar cells showed crystallographic textures with no evidence of preferred orientation Stokkan et al. (2018), at least in the preferential range of moderate cooling rates during production, cf. Yang et al. (2015). The

* E-mail address: marcus.assmus@ovgu.de

above mentioned assumption does therefore not contradict physical reality. In context of a preferably accurate prediction for a polycrystal consisting of cubic monocrystals, a discrete number of crystals is necessary to guarantee statistically isotropy of the bulk. Following [Elvin \(1996\)](#) this is around 230 crystals while [rds \(2003\)](#) provides a specific equation obeying the convergence of the prediction error via the increase of the number of crystals. Compared with [Basore \(1994\)](#), this restriction seems sufficiently fulfilled with polycrystalline silicon solar cells. Nevertheless, these values do not seem to bound the possible crystal numbers. It is important to note that the present analytical approaches are based on an infinite number of crystals ([Hill, 1952](#)). The resulting approximations therefore loose quality with decreasing crystal numbers. However, since the contrast of the elastic properties of the components made of polycrystalline silicon is comparatively small, the first-order estimates incorporating the restrictions named above result in comparatively close approximations.

Notation. Throughout the whole text, a direct tensor notation is preferred. First- and second-order tensors are denoted by lowercase and uppercase bold letters, e.g., \mathbf{a} and \mathbf{A} , respectively. Fourth-order tensors are designated by uppercase blackboard bold letters, e.g. \mathbb{A} . In continuation, some operations between these tensors need to be defined which will be done based on a three-dimensional orthonormal basis. For indices $i, j, k, \dots \in \{1, 2, 3\}$ holds. The Einstein summation convention is applied. Common operations are the dyadic product

$$\mathbf{a} \otimes \mathbf{b} = a_i b_j \mathbf{e}_i \otimes \mathbf{e}_j = \mathbf{C}, \quad (1)$$

the scalar product

$$\mathbf{a} \cdot \mathbf{b} = a_i b_j \mathbf{e}_i \cdot \mathbf{e}_j = a_i b_i = c, \quad (2)$$

the composition of a second- and a first-order tensor

$$\mathbf{A} \cdot \mathbf{a} = A_{lm} a_i \mathbf{e}_l \otimes \mathbf{e}_m \cdot \mathbf{e}_i = A_{li} a_i \mathbf{e}_l = \mathbf{d}, \quad (3)$$

the composition of two second-order tensors

$$\mathbf{A} \cdot \mathbf{B} = A_{lm} B_{no} \mathbf{e}_l \otimes \mathbf{e}_m \cdot \mathbf{e}_n \otimes \mathbf{e}_o = A_{lm} B_{mo} \mathbf{e}_l \otimes \mathbf{e}_o = \mathbf{D}, \quad (4)$$

the double scalar product between two second-order tensors

$$\mathbf{A} : \mathbf{B} = A_{lm} B_{no} \mathbf{e}_l \otimes \mathbf{e}_m : \mathbf{e}_n \otimes \mathbf{e}_o = A_{lm} B_{lm} = d, \quad (5)$$

the double scalar product between a fourth- and a second-order tensor

$$\mathbb{A} : \mathbf{B} = A_{pqrs} B_{no} \mathbf{e}_p \otimes \mathbf{e}_q \otimes \mathbf{e}_r \otimes \mathbf{e}_s : \mathbf{e}_n \otimes \mathbf{e}_o = A_{pqrs} B_{rs} \mathbf{e}_p \otimes \mathbf{e}_q = \mathbf{E}, \quad (6)$$

the double scalar product between two fourth-order tensors

$$\mathbb{A} : \mathbb{B} = A_{pqrs} B_{tuvw} \mathbf{e}_p \otimes \mathbf{e}_q \otimes \mathbf{e}_r \otimes \mathbf{e}_s : \mathbf{e}_t \otimes \mathbf{e}_u \otimes \mathbf{e}_v \otimes \mathbf{e}_w = A_{pqrs} B_{rsuv} \mathbf{e}_p \otimes \mathbf{e}_q \otimes \mathbf{e}_v \otimes \mathbf{e}_w = \mathbb{F}, \quad (7)$$

and the fourfold scalar product between two fourth-order tensors

$$\mathbb{A} :: \mathbb{B} = A_{pqrs} B_{tuvw} \mathbf{e}_p \otimes \mathbf{e}_q \otimes \mathbf{e}_r \otimes \mathbf{e}_s :: \mathbf{e}_t \otimes \mathbf{e}_u \otimes \mathbf{e}_v \otimes \mathbf{e}_w = A_{pqrs} B_{pqrs} = g. \quad (8)$$

The inverse of a tensor is defined by

$$\mathbf{A}^{-1} \cdot \mathbf{A} = \mathbf{A} \cdot \mathbf{A}^{-1} = \mathbf{1} \quad (9)$$

while the transposed of a tensor is given by

$$\mathbf{a} \cdot \mathbf{A}^\top \cdot \mathbf{b} = \mathbf{b} \cdot \mathbf{A} \cdot \mathbf{a}. \quad (10)$$

Herein, $\mathbf{1} = \mathbf{e}_i \otimes \mathbf{e}_i$ is the identity on first order tensors. For an orthogonal tensor, $\mathbf{B}^{-1} = \mathbf{B}^\top$ holds true. We furthermore introduce the Rayleigh product which maps all basis vectors of a tensor simultaneously without changing components. It is defined for a dyad and a tensor of arbitrary order. E.g., when applied to a tetrad, the product is

$$\mathbf{B} \star \mathbb{A} = A_{ijkl} (\mathbf{B} \cdot \mathbf{e}_i) \otimes (\mathbf{B} \cdot \mathbf{e}_j) \otimes (\mathbf{B} \cdot \mathbf{e}_k) \otimes (\mathbf{B} \cdot \mathbf{e}_l) \quad \text{with } A_{ijkl} = \mathbb{A} :: \mathbf{e}_i \otimes \mathbf{e}_j \otimes \mathbf{e}_k \otimes \mathbf{e}_l. \quad (11)$$

The Frobenius norm of fourth-, second, and first-order tensors is defined as follows.

$$\|\mathbb{A}\| = [\mathbb{A} :: \mathbb{A}]^{\frac{1}{2}} \quad \|\mathbf{A}\| = [\mathbf{A} : \mathbf{A}]^{\frac{1}{2}} \quad \|\mathbf{a}\| = [\mathbf{a} \cdot \mathbf{a}]^{\frac{1}{2}} \quad (12)$$

Overlined quantities indicate effective measures.

2 Theoretical Background

Silicon is a brittle material. Its mechanical behaviour is characterised by linear elasticity until fracture. This legitimates the use of Hooke's law. Considering a polycrystalline aggregate, the linear relation between stress \mathbf{T} and strain \mathbf{E} holds true for every single crystal.

$$\mathbf{T} = \mathbb{C} : \mathbf{E} \quad (13)$$

Using the eigenprojector representation, it is possible to represent the stiffness tensor \mathbb{C} as a linear combination of eigenprojectors \mathbb{P}_J and eigenvalues λ_J (Halmos, 1958; Mehrabadi and Cowin, 1990).

$$\mathbb{C} = \sum_{J=1}^Z \lambda_J \mathbb{P}_J \quad (14)$$

In general, the number of distinct eigenvalues λ_J of \mathbb{C} is in the range $2 \leq Z \leq 6$. Any admissible set of projectors fulfil subsequent projector rules (Rychlewski, 1995).

$$\mathbb{P}_J : \mathbb{P}_J = \mathbb{P}_J \quad \mathbb{P}_J : \mathbb{P}_L = \mathbb{0} \quad \forall J \neq L \quad \sum \mathbb{P}_J = \mathbb{I}^{\text{sym}} \quad \mathbb{P}_J :: \mathbb{P}_J = NS \quad (15)$$

Herein, NS is the number of dimensions of the subspace. In the case of cubic symmetry (superscript c), this method results in $Z = 3$ distinct eigenvalues and projectors.

$$\mathbb{C}^c = \lambda_1^c \mathbb{P}_1^c + \lambda_2^c \mathbb{P}_2^c + \lambda_3^c \mathbb{P}_3^c \quad (16)$$

The projectors are expressed as follows (Rychlewski and Zhang, 1989).

$$\mathbb{P}_1^c = \frac{1}{3} \mathbf{1} \otimes \mathbf{1} \quad \mathbb{P}_2^c = \mathbb{D} - \mathbb{P}_1^c \quad \mathbb{P}_3^c = \mathbb{I}^{\text{sym}} - (\mathbb{P}_1^c + \mathbb{P}_2^c) \quad (17)$$

The second and the third cubic projectors contain the anisotropic portion

$$\mathbb{D} = \sum_{i=1}^3 \mathbf{g}_i \otimes \mathbf{g}_i \otimes \mathbf{g}_i \otimes \mathbf{g}_i = \mathbf{Q} \star \sum_{i=1}^3 \mathbf{e}_i \otimes \mathbf{e}_i \otimes \mathbf{e}_i \otimes \mathbf{e}_i \quad (18)$$

where $\mathbf{g}_i \quad \forall i = \{1, 2, 3\}$ denote the orthonormal lattice vectors of the single crystal, which are related to a fixed (sample) reference basis $\mathbf{e}_i \quad \forall i = \{1, 2, 3\}$ by means of an proper orthogonal tensors \mathbf{Q} , e.g. $\mathbf{g}_i = \mathbf{Q} \cdot \mathbf{e}_i$. Furthermore, $2\mathbb{I}^{\text{sym}} = \mathbf{e}_i \otimes \mathbf{e}_j \otimes (\mathbf{e}_i \otimes \mathbf{e}_j + \mathbf{e}_j \otimes \mathbf{e}_i)$ is the identity on symmetric second-order tensors. The eigenvalues are determined by the projection of the constitutive tensor onto the space of the respective symmetry group.

$$\lambda_J = \mathbb{C} :: \frac{\mathbb{P}_J}{\|\mathbb{P}_J\|^2} \quad (19)$$

The three distinct eigenvalues in Eq. (16) are as follows with respect to the lattice vectors \mathbf{g}_i (Sutcliffe, 1992).

$$\lambda_1^c = C_{1111} + 2C_{1122}, \quad \lambda_2^c = C_{1111} - C_{1122}, \quad \lambda_3^c = 2C_{2323} \quad (20)$$

The degree of anisotropy of the cubic single crystals can be described as $\lambda_3^c - \lambda_2^c$, turning to zero in the case of isotropy. By the aid of the projector representation, it is trivial to determine the inverse of the stiffness tensor.

$$(\mathbb{C}^c)^{-1} = \frac{1}{\lambda_1^c} \mathbb{P}_1^c + \frac{1}{\lambda_2^c} \mathbb{P}_2^c + \frac{1}{\lambda_3^c} \mathbb{P}_3^c = \mathbb{S}^c \quad (21)$$

In analogy to Eq. (19), the eigenvalues are determined by taking the scalar product of the projectors and this compliance.

$$\frac{1}{\lambda_J} = \mathbb{S} :: \frac{\mathbb{P}_J}{\|\mathbb{P}_J\|^2} \quad (22)$$

First endeavors to determine the overall elasticity tensor of polycrystals were made by Woldemar Voigt and Andr as (Andre) Reuss. Voigt (1889) assumed a uniform, i.e., isotropic crystal orientation distribution function and a homogeneous strain field in the aggregate. Reuss (1929) suggested an corresponding estimate based on a homogeneous orientation distribution function and a homogeneous stress field. Generally, these volume averages are anisotropic. If and only if the polycrystal contains a sufficiently large number of crystals, macroscopic homogeneity and isotropy results (Hill, 1952), i.e. the texture is vanishing. For such isotropic microstructures, the crystals differ only with respect to their orientation. The approaches by Voigt and Reuss can be written as follows.

$$\mathbb{C}^V = \int_{\mathcal{Q}} f(\mathbf{Q}) \mathbb{C}^c(\mathbf{Q}) d\mathbf{Q} \quad \mathbb{S}^R = \int_{\mathcal{Q}} f(\mathbf{Q}) \mathbb{S}^c(\mathbf{Q}) d\mathbf{Q} \quad (23)$$

Herein $f(\mathbf{Q})$ specifies the volume fraction dV/v of crystals with the orientation \mathbf{Q} (Bunge, 1965) and dQ is the volume element in \mathcal{SO}_3 (special orthogonal group). Obviously, $\mathbb{C}^R \neq \mathbb{C}^V$ holds. These arithmetic and harmonic means of the stiffness tensors correspond to the assumption of homogeneous strain and stress fields, respectively. If only discrete orientations are of interest as in the case of polycrystalline silicon, the average over the orientation space can be formulated as weighted sum of the crystals volume fraction corresponding to the specific orientation and the affiliated elasticity tensor.

$$\mathbb{C}^V = \sum_{\gamma=1}^{\eta} v_{\gamma} \mathbb{C}_{\gamma}^c \quad \mathbb{S}^R = \sum_{\gamma=1}^{\eta} v_{\gamma} \mathbb{S}_{\gamma}^c \quad (24)$$

Herein, η represents the number of crystals under consideration. Both estimates result in macroscopically isotropic elasticity parameters. In context of the elasticity tensor \mathbb{C}^c , the coincidence of the second and third eigenvalue is a necessary and sufficient condition for an isotropic material. Hence, expression (16) reduces as follows whereby $Z = 2$ holds true in view of Eq. (14).

$$\mathbb{C}^{\circ} = \lambda_1^{\circ} \mathbb{P}_1^{\circ} + \lambda_2^{\circ} \mathbb{P}_2^{\circ} \quad (25)$$

We can furthermore introduce the isotropic compliance.

$$(\mathbb{C}^{\circ})^{-1} = \frac{1}{\lambda_1^{\circ}} \mathbb{P}_1^{\circ} + \frac{1}{\lambda_2^{\circ}} \mathbb{P}_2^{\circ} = \mathbb{S}^{\circ} \quad (26)$$

While the first projector coincides with the one of the cubic case ($\mathbb{P}_1^{\circ} = \mathbb{P}_1^c$), the second is determined as follows.

$$\mathbb{P}_2^{\circ} = \mathbb{P}_2^c + \mathbb{P}_3^c = \mathbb{I}^{\text{sym}} - \mathbb{P}_1^{\circ} \quad (27)$$

Due to the isotropic nature of volumetric changes in case of cubic crystal symmetry, $\lambda_1^{\circ} = \lambda_1^c$ holds true (Hill, 1952). In the isotropic case, $\lambda_2^{\circ} = C_{1111} - C_{1122} = 2C_{2323}$ also holds. Considering the second eigenvalue for an isotropic comparison material arising from the average theorems mentioned above, the second and third eigenvalue of the cubic symmetry have to be weighted according to their deviator space dimensions, cf. Walpole (1984) and Rychlewski (1984). This requires an allocation for λ_2° , either to the Voigt (homogeneous strain) or the Reuss (homogeneous stress) assumption ($\lambda_2^V \vee \lambda_2^R$).

$$\lambda_2^V = \frac{2}{5} \lambda_2^c + \frac{3}{5} \lambda_3^c \quad \lambda_2^R = \left[\frac{2}{5} \frac{1}{\lambda_2^c} + \frac{3}{5} \frac{1}{\lambda_3^c} \right]^{-1} \quad (28)$$

Above introduced stiffnesses constitute upper and lower bounds of the strain energy density (Nemat-Nasser and Hori, 1993). To be exact, the Voigt bound is equal to the first-order upper bound, whereas the Reuss bound equals the first-order lower bound. It was found by Hill (1952) that the range for the true effective stiffness $\bar{\mathbb{C}}$ is bounded by the Voigt (arithmetic) and the Reuss (harmonic) estimate. In the sense of positive definiteness ($\mathbf{A} : \mathbb{C} : \mathbf{A} > 0 \forall \mathbf{A} \neq \mathbf{0}$) we can state the following.

$$\mathbb{C}^V \geq \bar{\mathbb{C}} \geq \mathbb{C}^R \quad (29)$$

Hill (1952) suggested an arithmetic (H+) and an geometric mean (H-) of these isotropic bounds as good approximations, whereby these statements are based on pure empiricism.

$$\mathbb{C}^{\text{H}+} = \frac{1}{2} [\mathbb{C}^V + \mathbb{C}^R] \quad \mathbb{C}^{\text{H}-} = \exp \left(\frac{1}{2} [\log \mathbb{C}^V + \log \mathbb{C}^R] \right) \quad (30)$$

The latter is usually ignored in the literature, c.f. Morawiec (2004). Herein, we can introduce $\log \mathbb{C} = \sum \log(\lambda_J) \mathbb{P}_J$ and $\exp \mathbb{C} = \sum \exp(\lambda_J) \mathbb{P}_J$ since $J \in \{1, 2\}$ holds. Using such representation and considering the projector rules introduced in Eqs. (15), Eqs. (30) can be easily transformed into the subsequent form.

$$\mathbb{C}^{\text{H}+} = \lambda_1^{\text{H}+} \mathbb{P}_1^{\circ} + \lambda_2^{\text{H}+} \mathbb{P}_2^{\circ} \quad \mathbb{C}^{\text{H}-} = \lambda_1^{\text{H}-} \mathbb{P}_1^{\circ} + \lambda_2^{\text{H}-} \mathbb{P}_2^{\circ} \quad (31)$$

Herein, $\lambda_1^{\text{H}-} = \lambda_1^{\text{H}+} = \lambda_1^{\circ} = \lambda_1^c$ hold true since $\lambda_1^V = \lambda_1^R$ is valid. For the second eigenvalues $\lambda_2^{\text{H}\pm} \forall \pm \in \{+ \vee -\}$, the arithmetic and the geometric mean holds, respectively.

$$\lambda_2^{\text{H}+} = \frac{1}{2} [\lambda_2^V + \lambda_2^R] \quad \lambda_2^{\text{H}-} = [\lambda_2^V \lambda_2^R]^{\frac{1}{2}} \quad (32)$$

Since the geometric mean is smaller than the arithmetic, but both values lie inbetween the bounds of Voigt and Reuss, following representation holds.

$$\mathbb{C}_{\max} \geq \mathbb{C}^V \geq \mathbb{C}^{\text{H}+} \geq \mathbb{C}^{\text{H}-} \geq \mathbb{C}^R \geq \mathbb{C}_{\min} \quad (33)$$

However, in the literature it is often referred that the choice of the arithmetic mean is reasonable, due to a better agreement with experiments. We will deal with this proposition in a subsequent section. The orientational dependencies of the Young's modulus for a stiffness tensor \mathbb{C} with arbitrary material symmetry can be presented considering the tensile direction \mathbf{d} , where \mathbf{d} is

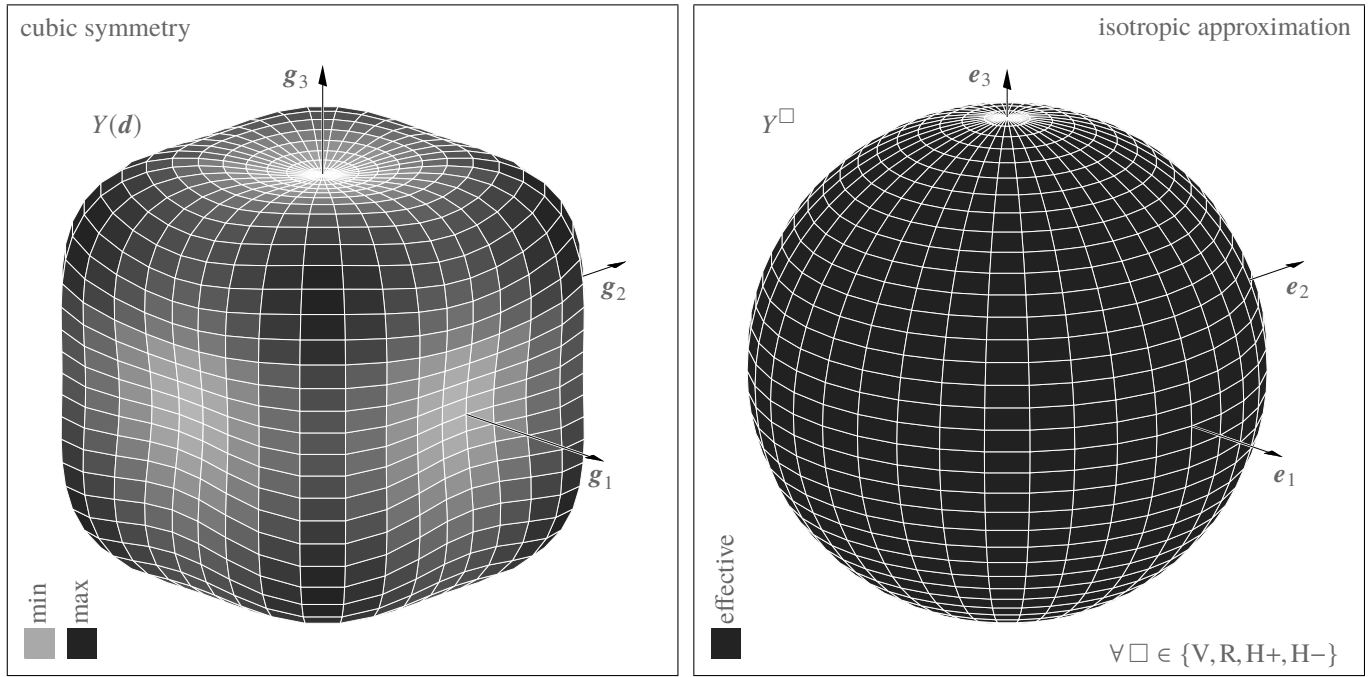


Fig. 1: Spatial plot of Young's modulus $Y(\mathbf{d})$ of a single crystal and isotropic approximation Y^\square of the polycrystalline aggregate

parametrized in spherical coordinates with $\|\mathbf{d}\| = 1$ (Hayes, 1972; Rychlewski, 1995). Since from an experimental standpoint, the Young's modulus, defined as the ratio of stress and strain in \mathbf{d} , is measured in most cases, we confine further spatial comparisons of the different estimates to this measure.

$$Y(\mathbf{d}) = [(\mathbf{d} \otimes \mathbf{d}) : \mathbb{S}^\square : (\mathbf{d} \otimes \mathbf{d})]^{-1} \quad \forall \square \in \{V, R, H+, H-\} \quad (34)$$

However, results of estimations based on Eq. (25) with eigenvalues (28) or (32) are isotropic approximations. Hence, it is possible to determine its orientation-independent engineering parameters.

$$Y^\square = \frac{3\lambda_1^c \lambda_2^\square}{2\lambda_1^c + \lambda_2^\square} \quad \nu^\square = \frac{\lambda_1^c - \lambda_2^\square}{2\lambda_1^c + \lambda_2^\square} \quad \forall \square \in \{V, R, H+, H-\} \quad (35)$$

Herein, Y is Young's modulus and ν is Poisson's ratio. Furthermore, the bulk K and the shear G moduli arise naturally.

$$3K = \lambda_1^c \quad 2G^\square = \lambda_2^\square \quad \forall \square \in \{V, R, H+, H-\} \quad (36)$$

Subsequent relations emerge.

$$Y^\square = \frac{9KG^\square}{3K + G^\square} \quad \nu^\square = \frac{3K - 2G^\square}{2(3K + G^\square)} \quad \forall \square \in \{V, R, H+, H-\} \quad (37)$$

The procedure often quoted as Voigt-Reuss-Hill average merely results in engineering parameters of the arithmetic mean ($Y^\square, \nu^\square, K^\square, G^\square \forall \square \in \{H+\}$).

Note that the whole procedure presented here is based on the second and third eigenvalue of the cubic system solely. As a result, the approximation of the isotropic elasticity and compliance tensor simplifies to the following expression.

$$\mathbb{C}^\circ = \lambda_1 \mathbb{P}_1 + \lambda_2^\square \mathbb{P}_2^\circ \quad \forall \square \in \{V, R, H+, H-\} \quad (38)$$

Within the eigenspaces, all calculations can be traced back to scalars. This method is therewith easy to handle compared to laborious operations by application of the vector-matrix-notation, as often referred to in the literature. This simplicity and elegance is based on the projector representation.

3 Application and Results

When evaluating the results of the estimations described in the previous section, values for the cubic parameters of a single crystal are considered, which originate from Hosford (1993).

$$C_{1111} = 166.2 \cdot 10^3 \frac{\text{N}}{\text{mm}^2} \quad C_{1122} = 64.4 \cdot 10^3 \frac{\text{N}}{\text{mm}^2} \quad C_{2323} = 79.7 \cdot 10^3 \frac{\text{N}}{\text{mm}^2} \quad (39)$$

This results in subsequent eigenvalues.

$$\lambda_1^c = 295 \cdot 10^3 \frac{\text{N}}{\text{mm}^2} \quad \lambda_2^c = 101.8 \cdot 10^3 \frac{\text{N}}{\text{mm}^2} \quad \lambda_3^c = 159.4 \cdot 10^3 \frac{\text{N}}{\text{mm}^2} \quad (40)$$

Tab. 1: Young's modulus Y and Poisson's ratio ν of different estimates, bounds and their spans

Y_{\min}	Y_{\max}	Y^V	Y^R	Y^{H+}	Y^{H-}	$\Delta_Y^{\min \max}$	Δ_Y^{VR}	$\Delta_Y^{H\pm}$
$130.200 \cdot 10^3$	$188.260 \cdot 10^3$	$166.141 \cdot 10^3$	$159.773 \cdot 10^3$	$162.971 \cdot 10^3$	$162.933 \cdot 10^3$	$58.060 \cdot 10^3$	$6.368 \cdot 10^3$	38.133
ν_{\min}	ν_{\max}	ν^V	ν^R	ν^{H+}	ν^{H-}	$\Delta_\nu^{\min \max}$	Δ_ν^{VR}	$\Delta_\nu^{H\pm}$
0.062	0.363	0.218	0.229	0.223	0.223	0.300	0.011	$6.5 \cdot 10^{-5}$

(Y in N/mm², ν is dimensionless)

A common measure to quantify the extent of anisotropy in a cubic system is the Zener ratio $ZR = \lambda_3^2/\lambda_2^2$ (Zener, 1948). If materials are isotropic, $ZR = 1$ holds true. For material parameters of monocrystalline silicon listed in Eq. (40), $ZR \approx 1.57$ results. Compared to other cubic materials (e.g. copper, silver, gold, lead), the degree of anisotropy for monocrystalline silicon is moderate. For further anisotropy measures and physical explanations, cf. Ranganathan and Ostoja-Starzewski (2008).

For the further examinations we mainly refer to Young's modulus as it is more significant in comparison to Poisson's ratio and also has the broadest application in materials technology. The directional dependence of a single silicon crystal according to Eq. (34) shows the following parameters where seven directions are under consideration. Due to the crystallographic equivalence of some directions, only three of them are characteristic.

$$Y(\mathbf{d}) = \begin{cases} 130.2 \cdot 10^3 \frac{\text{N}}{\text{mm}^2} & \text{if } \mathbf{d} = \mathbf{g}_i \\ 169.4 \cdot 10^3 \frac{\text{N}}{\text{mm}^2} & \text{if } \mathbf{d} = \mathbf{n}_i \\ 188.2 \cdot 10^3 \frac{\text{N}}{\text{mm}^2} & \text{if } \mathbf{d} = \mathbf{n}_S \end{cases} \quad (41)$$

Here, the normals

$$\mathbf{n}_1 = \frac{(\mathbf{g}_1 + \mathbf{g}_2)}{\sqrt{2}}, \quad (42a)$$

$$\mathbf{n}_2 = \frac{(\mathbf{g}_1 + \mathbf{g}_3)}{\sqrt{2}}, \quad (42b)$$

$$\mathbf{n}_3 = \frac{(\mathbf{g}_2 + \mathbf{g}_3)}{\sqrt{2}}, \text{ and} \quad (42c)$$

$$\mathbf{n}_S = \frac{(\mathbf{g}_1 + \mathbf{g}_2 + \mathbf{g}_3)}{\sqrt{3}} \quad (42d)$$

have been introduced. Thereby, $\mathbf{n}_i \forall i = \{1, 2, 3\}$ are face diagonals ($\langle 110 \rangle$, $\langle 101 \rangle$, and $\langle 011 \rangle$) while \mathbf{n}_S is a space diagonal ($\langle 111 \rangle$) of the cubic primitive cell. Again, $\mathbf{g}_i \forall i = \{1, 2, 3\}$ are directions of the crystals orthonormal basis ($\langle 100 \rangle$, $\langle 010 \rangle$, and $\langle 001 \rangle$). Angle brackets used here refer to Miller indices (Miller, 1839). The orientation dependent Young's modulus can be plotted according to the procedure discussed in Nordmann et al. (2018)¹, which is based on the work of Rychlewski (1995) and Böhlke and Brüggemann (2001). In doing so, we derive the graphical representation given at the left-hand side of Fig. 1. This plot visualizes the directional dependence of Young's modulus for a single crystal. It becomes obvious for cubic silicon, that

$$Y(\mathbf{n}_S) = Y_{\max} \quad \text{and} \quad Y(\mathbf{g}_i) = Y_{\min} \quad (43)$$

hold true. Both values are elementary bounds of the single crystal elasticity. Material parameters determined according to the procedure given in Sect. 2 are given in Tab. 1. There, additionally, the bandwidths spanned

- by the single crystal minimum and maximum values $\Delta_Y^{\min \max} = Y_{\max} - Y_{\min}$,
- by the Voigt and Reuss bounds $\Delta_Y^{VR} = Y^V - Y^R$, and
- by the arithmetic and geometric means thereof $\Delta_Y^{H\pm} = Y^{H+} - Y^{H-}$

are given. The bandwidths of resulting Poisson's ratios given there are determined in analogous manner. Considering the Young's moduli determined, the right-hand side of Fig. 1 visualizes the directional dependence of all estimates for the polycrystalline aggregate. Clearly, since these estimates are isotropic approximations, the Young's modulus body is spherical.

4 Comparison and Discussion

All further evaluations refer to Young's modulus as it is the substantial parameter, at least in isotropic material engineering. On the other hand, Poisson's ratio of polycrystalline silicon has not been well studied experimentally and hardly any data is available. Firstly, the bandwidths resulting from the bounding values determined here are shown in Fig. 2. Considering first the single

¹See also: <https://tinyurl.com/visualising-elastic-anisotropy>

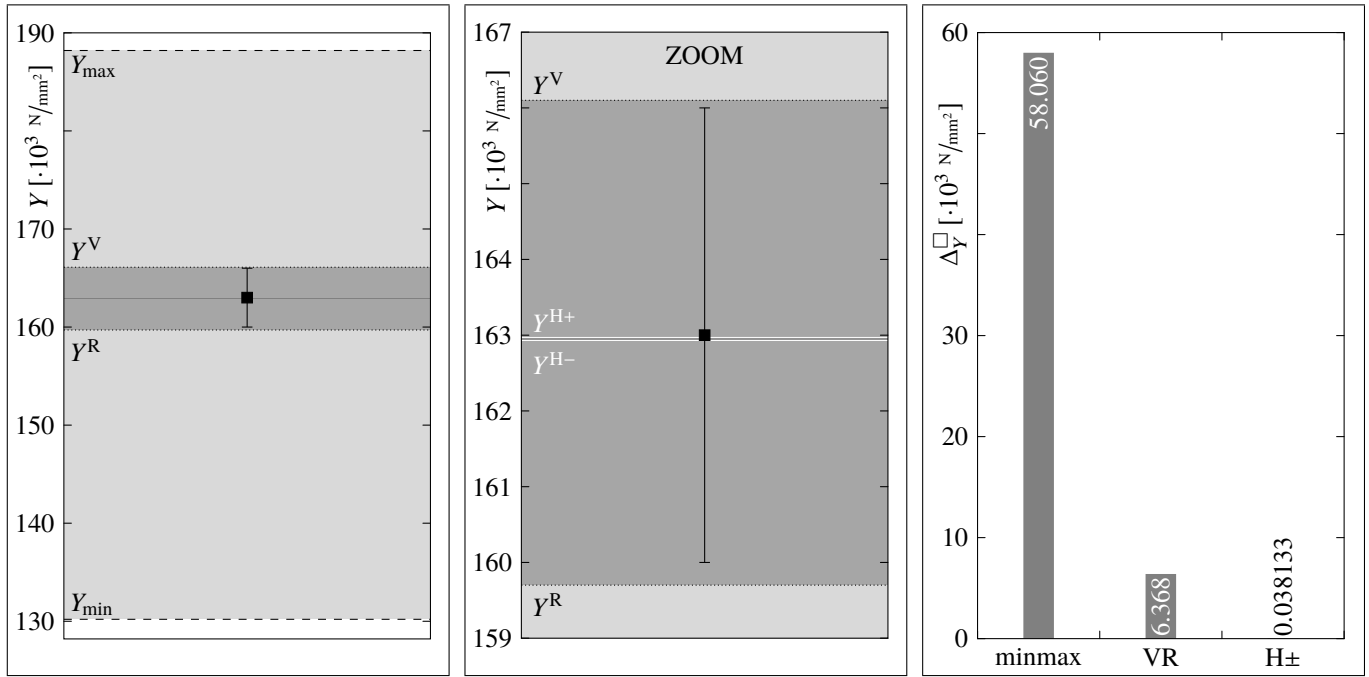


Fig. 2: Spans of extremes and isotropic bounds as well as scattering of experimental results within these ranges (■ - experiments)

crystal extremes we notice a large bandwidth ($\Delta Y^{\min\max} \approx 58.0 \cdot 10^3 \text{ N/mm}^2$) which doubles the statements for Young's modulus scattering of Petersen (1982). The bandwidth of Voigt and Reuss bound is considerably smaller ($\Delta Y^{\min\max} \approx 6.4 \cdot 10^3 \text{ N/mm}^2$, about 11% of $\Delta Y^{\min\max}$). Hill's bounds span a comparatively small band of $\Delta Y^{\text{H}\pm} \approx 38.1 \text{ N/mm}^2$ which is around 0.6% of the Voigt-Reuss bandwidth. For comparison we use experimental data from Michalíček et al. (1995). Unfortunately, in Michalíček et al. (1995), no tolerance for these measurements is given. Following the compilations of Sharpe (2002), there is a minimal measurement scattering of $\pm 3 \cdot 10^3 \text{ N/mm}^2$ depending on the experimental method for determining the Young's modulus. For visualization purposes we therefore use $Y^{\text{exp}} = (163.0 \pm 3) \cdot 10^3 \text{ N/mm}^2$ as experimental reference in context of Fig. 2. Obviously, the effective value of Young's modulus is slightly smaller than the mean of the experimental results, at least in the light of $Y^{\text{H}+}$ and $Y^{\text{H}-}$. Thereby we can recognize that the scattering of these experiments lies in between Voigt and Reuss bound. However, these bandwidths are juxtaposed comparatively in Fig. 2 on the right-hand side. We additionally can state the distances of Young's moduli in form of scalar values, indicating an absolute error.

$$d_Y^{\square} = Y^{\square} - Y^{\text{exp}} \quad \forall \square \in \{\text{max, min, V, R, H+}, \text{H-}\} \quad (44)$$

The results are visualized in Fig. 3, left-hand side. Clearly, the distances to the extremes of the monocrystal are the largest. Distances to Voigt and Reuss bounds are smaller by an order of magnitude. These bounds are almost symmetric around the experimental mean. Hills averages are smaller by two orders of magnitude compared to Voigt-Reuss bounds. Both of Hill's averages are smaller than the experimental mean, i.e. we underestimate the experimental findings by present strategy. Obviously the absolute value of Hill's arithmetic mean $d_Y^{\text{H}+}$ is closest to the experimental mean. Ultimately this underlines the choice of the arithmetic mean according to Hill (1952), at least for present investigations. For further comparison with respect to experimental findings, we analyze the ratio between experimental mean and computed value of Young's modulus.

$$YR^{\square} = \frac{Y^{\square}}{Y^{\text{exp}}} \quad \forall \square \in \{\text{max, min, V, R, H+}, \text{H-}\} \quad (45)$$

Results of this ratio are visualized in Fig. 3, center. Minimum and Maximum values of the single crystal range around to the experimental value with approximately ${}_{-0.20}^{+0.15} Y^{\text{exp}}$. Voigt and Reuss bounds significantly reduce this ratios to around ${}_{-0.02}^{+0.02} Y^{\text{exp}}$. This is being undercut by Hill's averages by two orders of magnitude (${}_{-0.0004}^{-0.0002} Y^{\text{exp}}$). Here we can also identify the closest approximation with $Y^{\text{H}+}$ to the experiments. We furthermore introduce the relative error of present estimates.

$$e_Y^{\square} = \frac{d_Y^{\square}}{Y^{\text{exp}}} \quad \forall \square \in \{\text{V, R, H+}, \text{H-}\} \quad (46)$$

These measures are given in Fig. 3, right-hand side. It turns out that the error caused when working with Voigt and Reuss estimates is below $\pm 2\%$. This error is decreased to approximately -0.04% when working with Hill's geometric mean and finally to around -0.02% when applying Hill's arithmetic mean.

In spite of all the numerical deviations determined here, we have to consider the scattering of the experimental results of around $\pm 3 \cdot 10^3 \text{ N/mm}^2$. In this context we have to register $\Delta Y^{\text{S}\pm} \approx 6 \cdot 10^3 \text{ N/mm}^2$, $d_Y^{\text{S}+} \approx 3 \cdot 10^3 \text{ N/mm}^2$, $d_Y^{\text{S}-} \approx -3 \cdot 10^3 \text{ N/mm}^2$, $YR^{\text{S}+} \approx 1.0184$, $YR^{\text{S}-} \approx 0.9816$, $e_Y^{\text{S}+} \approx 1.8 \cdot 10^{-2}$, and $e_Y^{\text{S}-} \approx -1.8 \cdot 10^{-2}$ while the superscript index $\text{S}\pm$ indicates the bounds resulting from scattering. The error caused by the scattering in the experimental findings causes an error of around 1.8%. As already visualized in Fig. 2 (center), this clarifies that the experimental findings vary in the range of the Voigt-Reuss bounds.

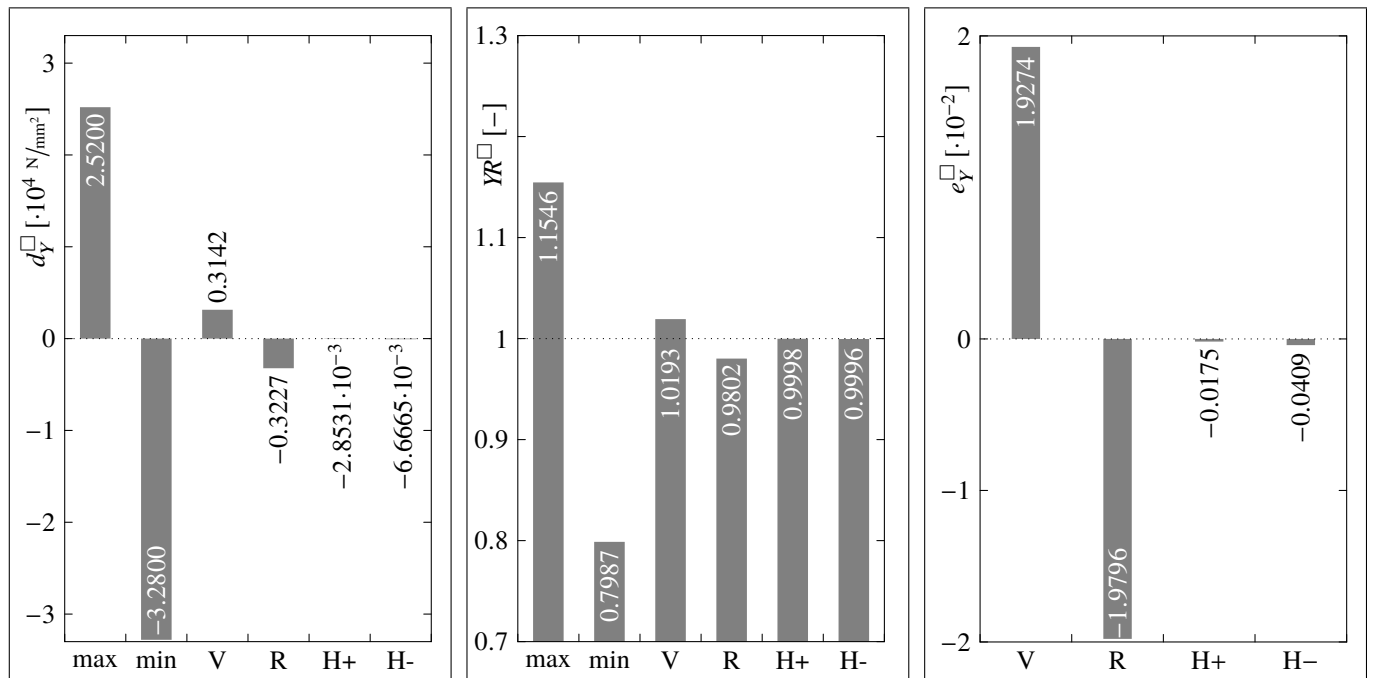


Fig. 3: Distances and ratios of experimental to calculated solutions and associated relative error of Young's modulus estimations

5 Summary and Conclusions

In the foregoing investigations we have predicted the elastic properties of polycrystalline silicon used for solar cells. The predictions were determined by the aid of first-order estimates of analytical homogenization methods. These estimates are based on assumptions for macroscopic homogeneity and isotropy for aggregates of cubic crystals. The whole procedure is based on simplest bounds followed by empirical averages. Present homogenization approach is being applied by the aid of the eigenprojector representation. The advantage of this approach is that we can reduce the tensorial quantities to scalar ones, i.e. this simplifies the computation considerably. This is also an advantage in comparison to computations often done via laborious matrix computations, cf. [den Toonder et al. \(1999\)](#). Based on the invariance of the first eigenvalue of the stiffness (or bulk modulus), the calculus is reduced to the second and third eigenvalue, i.e. the computations reduce to Eqs. (28) and (32).

In context of the results gained therewith when applied to silicon we may conclude that it is sufficient to use Voigt and Reuss bounds and determine the arithmetic mean value proposed by Hill. The latter one predicts the experimental value with sufficient accuracy, i.e. for the given effective material properties, $\mathbb{C}^{\text{H+}}$ is a reasonable approximation for $\bar{\mathbb{C}}$. The quality of this prediction can basically be improved by increasing the order of approximation. This means that the bandwidths of the upper and lower bounds are becoming smaller and smaller. The application of such improvements remains contestable, at least in context of the scattering of the Young's moduli determined at polycrystalline silicon. For polycrystalline silicon, the results imply that the procedure well known as Voigt-Reuss-Hill average provides sufficiently accurate results.

However, the use of silicon for mechanical structures is widespread, so the parameters for this material have been investigated thoroughly. Therefore, the initial values of present calculations, cf. Eq. (39), may scatter to a certain extent ($\pm 500 \text{ N/mm}^2$). In the present treatise we waived the representation of the error propagation caused by the scattering of initial material parameters of the monocrystal. This surely is a problem of experimental mechanics which also concerns the measurements on polycrystalline silicon for solar cells. To counter this problem, sensitive measurements are required at both, the constituents forming the aggregate and the aggregate itself, while one always has to consider the accuracy of the measurement equipment. This is also dependent on the method used, e.g. tension, bending, resonance, indentation, ultrasonic, or bulge test respectively.

The morphology and topology of the material can have an important influence on the effective properties which cannot be considered by the isotropic Voigt and Reuss estimates. For more precise computations, one will have to consider the crystallographic texture, cf. [Morawiec \(2004\)](#). Hereby, the extent of anisotropic effects strongly depends on the degree of crystallographic texture. However, in this case one must consider that both, Voigt and Reuss bounds are anisotropic, i.e. $\|\mathbb{C}^{\text{aniso}}\| = \|\mathbb{C}^{\square} - \mathbb{C}^{\square}\| \neq 0 \forall \square \in \{V, R\}$. On the one hand this needs theoretical considerations for the analysis of textures, which can be found in the literature [Kocks et al. \(1998\)](#). On the other hand, experimental investigations on crystal orientation distribution functions of polycrystalline silicon aggregates used for solar cells are necessary to feed such models. Such studies however, are absent.

Acknowledgement

This work was triggered during a visit stay at Griffith University (Australia) while the first author was fellow of the German Research Foundation (grant number 83477795), whose support he very gratefully acknowledges. He furthermore likes to thank Andreas Öchsner for his kind hospitality during this stay. The topic was stimulated by discussions with Zia Javanbakht, to whom he wishes to express many thanks.

Appendix

A.1 Equivalent vector-matrix based procedure

In engineering, especially in the geometrically linear setting of classical continuum theory, a vector-matrix representation finds broad application. This is possible since present mechanical problem is set in the space of symmetric tensors. To be exact, the stress $\mathbf{T} = T_{ij}\mathbf{e}_i \otimes \mathbf{e}_j$ and strain tensor $\mathbf{E} = E_{kl}\mathbf{e}_k \otimes \mathbf{e}_l$ are symmetric, i.e.

$$\begin{aligned} \mathbf{a} \cdot \mathbf{T} &= \mathbf{T} \cdot \mathbf{a} & \mathbf{T} &= \mathbf{T}^\top & T_{ij} &= T_{ji} \\ \mathbf{a} \cdot \mathbf{E} &= \mathbf{E} \cdot \mathbf{a} & \mathbf{E} &= \mathbf{E}^\top & E_{kl} &= E_{lk} \end{aligned}$$

and the constitutive tensor $\mathbb{C} = C_{ijkl}\mathbf{e}_i \otimes \mathbf{e}_j \otimes \mathbf{e}_k \otimes \mathbf{e}_l$ features left sub-symmetry, right sub-symmetry and major symmetry, i.e.

$$\begin{aligned} \mathbf{A} : \mathbb{C} : \mathbf{B} &= \mathbf{B} : \mathbb{C} : \mathbf{A} & C_{ijkl} &= C_{klij} & \text{major symmetry} \\ \mathbf{A} : \mathbb{C} &= \mathbf{A}^\top : \mathbb{C} & C_{ijkl} &= C_{jikl} & \text{left subsymmetry} \\ \mathbb{C} : \mathbf{A} &= \mathbb{C} : \mathbf{A}^\top & C_{ijkl} &= C_{ijlk} & \text{right subsymmetry} \end{aligned}$$

for arbitrary $\mathbf{a}, \mathbf{A}, \mathbf{B}$. Due to the symmetries given we can uniquely assign vectors and matrices to these tensors. In accordance with the operations in Sect. 2, we can then execute the algebraic operations analogously in a vector-matrix notation. To derive such a representation we first introduce a six-dimensional basis (Brannon, 2018), which we will call Kelvin basis, cf. Thomson (1856).

$$\mathbf{K}_i = \mathbf{e}_i \otimes \mathbf{e}_i \quad \forall i = \{1, 2, 3\} \quad (\text{A.1a})$$

$$\mathbf{K}_{3ND-i-j} = \frac{\sqrt{2}}{2} [\mathbf{e}_i \otimes \mathbf{e}_j + \mathbf{e}_j \otimes \mathbf{e}_i] \quad \forall i, j = \{1, 2, 3\} \text{ while } i < j \quad (\text{A.1b})$$

Herein, ND is the number of dimensions under consideration ($ND = 3$). Obviously our ordering is in accordance with classical Voigt notation (Voigt, 1889), while the normalization with $\sqrt{2}$ differs from the classical representation where only the symmetric part is applied. Since the index of these second-order bases is running from 1 to 6, we introduce greek indices so that $\mathbf{K}_\alpha \forall \alpha = \{1, \dots, 6\}$ holds. The Kelvin basis is orthonormal.

$$\mathbf{K}_\alpha : \mathbf{K}_\beta = \delta_{\alpha\beta} \quad (\text{A.2})$$

A six-dimensional vector representation of stresses and strains is possible while the components are defined as follows.

$$T_\alpha = \mathbf{T} : \mathbf{K}_\alpha \quad \forall \alpha = \{1, \dots, 6\} \quad (\text{A.3a})$$

$$E_\beta = \mathbf{E} : \mathbf{K}_\beta \quad \forall \beta = \{1, \dots, 6\} \quad (\text{A.3b})$$

Both vectors are related by a six-by-six-matrix which is based on the constitutive tensor. We can determine the coefficients of this constitutive matrix by the following calculation rule.

$$C_{\alpha\beta} = \mathbf{K}_\alpha : \mathbb{C} : \mathbf{K}_\beta \quad \forall \alpha, \beta = \{1, \dots, 6\} \quad (\text{A.4})$$

Due to the calculation rules shown, all indices of the vector-matrix notation (α, β) can be assigned to the tensor notation (i, j, k, l), and vice versa. Thus, the tensors $\mathbf{T}, \mathbf{E}, \mathbb{C}$ may also be written as follows.

$$\mathbf{T} = T_\alpha \mathbf{K}_\alpha \quad (\text{A.5a})$$

$$\mathbf{E} = E_\beta \mathbf{K}_\beta \quad (\text{A.5b})$$

$$\mathbb{C} = C_{\alpha\beta} \mathbf{K}_\alpha \otimes \mathbf{K}_\beta \quad (\text{A.5c})$$

We can achieve the vector-matrix representation of the constitutive law by the arrangement of the coefficients.

$$\begin{bmatrix} T_1 \\ T_2 \\ T_3 \\ T_4 \\ T_5 \\ T_6 \end{bmatrix} = \begin{bmatrix} C_{11} & C_{12} & C_{13} & C_{14} & C_{15} & C_{16} \\ & C_{22} & C_{23} & C_{24} & C_{25} & C_{26} \\ & & C_{33} & C_{34} & C_{35} & C_{36} \\ & & & C_{44} & C_{45} & C_{46} \\ & & & & C_{55} & C_{56} \\ \text{sym} & & & & & C_{66} \end{bmatrix} \begin{bmatrix} E_1 \\ E_2 \\ E_3 \\ E_4 \\ E_5 \\ E_6 \end{bmatrix} \quad (\text{A.6})$$

Herein, the matrix $[C_{\alpha\beta}]$ takes the general anisotropic form. For the sake of completeness we provide the assignment of the parameters with indices i, j, k, l and α, β . These are relations of the stresses

$$T_1 = T_{11} \quad T_2 = T_{22} \quad T_3 = T_{33} \quad T_4 = \sqrt{2}T_{23} \quad T_5 = \sqrt{2}T_{13} \quad T_6 = \sqrt{2}T_{12},$$

the strains

$$E_1 = E_{11} \quad E_2 = E_{22} \quad E_3 = E_{33} \quad E_4 = \sqrt{2}E_{23} \quad E_5 = \sqrt{2}E_{13} \quad E_6 = \sqrt{2}E_{12},$$

and the constitutive coefficients for an aelotropic material

$$\begin{aligned} C_{11} &= C_{1111} & C_{12} &= C_{1122} & C_{13} &= C_{1133} & C_{14} &= \sqrt{2}C_{1123} & C_{15} &= \sqrt{2}C_{1113} & C_{16} &= \sqrt{2}C_{1112} \\ & & C_{22} &= C_{2222} & C_{23} &= C_{2233} & C_{24} &= \sqrt{2}C_{2223} & C_{25} &= \sqrt{2}C_{2213} & C_{26} &= \sqrt{2}C_{2212} \\ & & & & C_{33} &= C_{3333} & C_{34} &= \sqrt{2}C_{3323} & C_{35} &= \sqrt{2}C_{3313} & C_{36} &= \sqrt{2}C_{3312} \\ & & & & & & C_{44} &= 2C_{2323} & C_{45} &= 2C_{2313} & C_{46} &= 2C_{2312} \\ & & & & & & & & C_{55} &= 2C_{1313} & C_{56} &= 2C_{1312} \\ & & & & & & & & & & C_{66} &= 2C_{1212}, \end{aligned}$$

while $C_{\alpha\beta} = C_{\beta\alpha}$ holds. This modified representation was already used, e.g., by [Fedorov \(1968\)](#). When introducing sans serif, upright, bold minuscules for vectors and sans serif, upright, bold majuscules for matrices, we can write generalized Hooke's law of Eq. (A.6) in the form $\mathbf{t} = \mathbf{C}\mathbf{e}$. Due to the normalization factor introduced in Eq. (A.1b), the following relations between vector-matrix and tensor notation hold.

$$\mathbf{t}^\top \mathbf{t} = \mathbf{T} : \mathbf{T} \quad \mathbf{e}^\top \mathbf{e} = \mathbf{E} : \mathbf{E} \quad \mathbf{t}^\top \mathbf{e} = \mathbf{T} : \mathbf{E} \quad (\text{A.7})$$

Furthermore, \mathbf{C} features the same invariants, eigenvalues, and eigendirections as \mathbb{C} and obeys the major symmetry ([Nordmann et al., 2018](#)). The normalization also enables to apply operations like trace, determinant, matrix multiplications and so on at components of six-by-six matrices.² In context of cubic symmetry, the occupiedness of \mathbf{C} reduces as follows when lattice basis and (sample) reference basis coincide.

$$\mathbf{C}^c = \begin{bmatrix} C_{11} & C_{12} & C_{12} & 0 & 0 & 0 \\ & C_{11} & C_{12} & 0 & 0 & 0 \\ & & C_{11} & 0 & 0 & 0 \\ & & & C_{44} & 0 & 0 \\ & & & & C_{44} & 0 \\ \text{[sym]} & & & & & C_{44} \end{bmatrix} \quad \text{with} \quad \begin{aligned} C_{11} &= C_{1111} \\ C_{12} &= C_{1122} \\ C_{44} &= 2C_{2323} \end{aligned} \quad (\text{A.8})$$

Obviously we can identify $C_{11} = 1/3(\lambda_1^c + 2\lambda_2^c)$, $C_{12} = 1/3(\lambda_1^c - \lambda_2^c)$, and $C_{44} = 1/2\lambda_3^c$ and find a projector representation for the elasticity matrix in analogy to Eq. (16) ([Halmos, 1958](#)). As was introduced at the elasticity matrix in Eq. (A.4), we determine matrix coefficients of the projectors also.

$$(P_{\alpha\beta})_J^c = \mathbf{K}_\alpha : \mathbb{P}_J^c : \mathbf{K}_\beta \quad \forall \alpha = \{1, \dots, 6\} \wedge J = \{1, \dots, 3\} \quad (\text{A.9})$$

Ordering all coefficients, the cubic projectors are represented by six-by-six matrices as follows.

$$\mathbf{P}_1^c = \begin{bmatrix} \frac{1}{3} & & & & & \\ & \frac{1}{3} & & & & \\ & & \frac{1}{3} & & & \\ & & & 0 & 0 & 0 \\ & & & 0 & 0 & 0 \\ & & & 0 & 0 & 0 \\ & & & 0 & 0 & 0 \\ & & & 0 & 0 & 0 \\ \text{[sym]} & & & & & 0 \end{bmatrix} \quad \mathbf{P}_2^c = \begin{bmatrix} \frac{2}{3} & -\frac{1}{3} & -\frac{1}{3} & 0 & 0 & 0 \\ & -\frac{1}{3} & -\frac{1}{3} & 0 & 0 & 0 \\ & & -\frac{1}{3} & 0 & 0 & 0 \\ & & & \frac{2}{3} & 0 & 0 \\ & & & & 0 & 0 \\ & & & & 0 & 0 \\ & & & & 0 & 0 \\ \text{[sym]} & & & & & 0 \end{bmatrix} \quad \mathbf{P}_3^c = \begin{bmatrix} 0 & 0 & 0 & 0 & 0 & 0 \\ & 0 & 0 & 0 & 0 & 0 \\ & & 0 & 0 & 0 & 0 \\ & & & 0 & 0 & 0 \\ & & & & 1 & 0 \\ & & & & & 1 \\ \text{[sym]} & & & & & & 1 \end{bmatrix} \quad (\text{A.10})$$

This representation holds only when the reference vectors of the orthonormal system are lattice vectors. In this context we can write the constitutive matrix as sum of eigenvalues and corresponding projection matrices.

$$\mathbf{C}^c = \lambda_1^c \mathbf{P}_1^c + \lambda_2^c \mathbf{P}_2^c + \lambda_3^c \mathbf{P}_3^c \quad (\text{A.11})$$

The compliance $\mathbf{S} = \mathbf{C}^{-1}$ is determined through $\mathbf{S}\mathbf{C}^{-1} = \mathbf{1}$ while $\mathbf{1}$ is the identity matrix.

$$\mathbf{S}^c = \frac{1}{\lambda_1^c} \mathbf{P}_1^c + \frac{1}{\lambda_2^c} \mathbf{P}_2^c + \frac{1}{\lambda_3^c} \mathbf{P}_3^c \quad (\text{A.12})$$

²For instance, the present strategy to reduce to a vector-matrix notation keeps us from an incorrect determination of the eigenvalues of the stiffness matrix as done through various softwares circulating out there. However, when original Voigt notation is used, $\lambda_J(\mathbf{C}) = \lambda_J(\mathbb{C})$ has no general validity since the physical parameters C_{ijkl} in \mathbf{C} are not normalized with the metric.

For the sake of completeness we give the cubic compliance in terms of the coefficients $C_{\alpha\beta}$.

$$\mathbf{S}^c = \begin{bmatrix} S_{11} & S_{12} & S_{12} & 0 & 0 & 0 \\ & S_{11} & S_{12} & 0 & 0 & 0 \\ & & S_{11} & 0 & 0 & 0 \\ & & & S_{44} & 0 & 0 \\ \text{sym} & & & & S_{44} & 0 \\ & & & & & S_{44} \end{bmatrix} \quad \text{with} \quad \begin{aligned} S_{11} &= \frac{C_{11} + C_{12}}{(C_{11} - C_{12})(C_{11} + 2C_{12})} \\ S_{12} &= \frac{-C_{12}}{(C_{11} - C_{12})(C_{11} + 2C_{12})} \\ S_{44} &= \frac{1}{C_{44}} \end{aligned}$$

Herein, $S_{11} = (2\lambda_1^c + \lambda_2^c)/(3\lambda_1^c\lambda_2^c)$, $S_{12} = (\lambda_2^c - \lambda_1^c)/(3\lambda_1^c\lambda_2^c)$, and $S_{44} = 2/\lambda_3^c$ hold. In analogy to the tensorial description we can give representations of Voigt and Reuss homogenization schemes in matrix notation, cf. Eq. (24).

$$\mathbf{C}^V = \sum_{\gamma=1}^n v_\gamma \mathbf{C}_\gamma^c \quad \mathbf{S}^R = \sum_{\gamma=1}^n v_\gamma \mathbf{S}_\gamma^c \quad \forall \eta \in \mathcal{N}^+ \quad (\text{A.14})$$

The isotropic constitutive law can be written as follows.

$$\mathbf{C}^\circ = \lambda_1^\circ \mathbf{P}_1^\circ + \lambda_2^\circ \mathbf{P}_2^\circ \quad (\text{A.15})$$

Applying the isotropic projectors of Eq. (27) in Eq. (A.9) yields the components $(P_{\alpha\beta})_J^\circ \forall J = \{1, 2\}$. The equivalent matrix representation for isotropic projectors is then given as follows.

$$\mathbf{P}_1^\circ = \begin{bmatrix} \frac{1}{3} & & & & & \\ & \frac{1}{3} & & & & \\ & & \frac{1}{3} & & & \\ & & & 0 & 0 & 0 \\ & & & 0 & 0 & 0 \\ & & & 0 & 0 & 0 \\ \text{sym} & & & & 0 & 0 \\ & & & & & 0 \end{bmatrix} \quad \mathbf{P}_2^\circ = \begin{bmatrix} \frac{2}{3} & & & & & \\ & -\frac{1}{3} & & & & \\ & & -\frac{1}{3} & & & \\ & & & 0 & 0 & 0 \\ & & & -\frac{1}{3} & & \\ & & & & \frac{2}{3} & \\ & & & & & 1 & 0 & 0 \\ \text{sym} & & & & & & 1 & 0 \\ & & & & & & & 1 \end{bmatrix} \quad (\text{A.16})$$

Here again $\mathbf{P}_1^\circ = \mathbf{P}_1^c = \mathbf{P}_1$ holds. The isotropic elasticity matrix can be presented as $[C_{\alpha\beta}]^\circ = \mathbf{C}^\circ$.

$$\mathbf{C}^\circ = \begin{bmatrix} C_{11} & C_{12} & C_{12} & 0 & 0 & 0 \\ & C_{11} & C_{12} & 0 & 0 & 0 \\ & & C_{11} & 0 & 0 & 0 \\ & & & C_{44} & 0 & 0 \\ \text{sym} & & & & C_{44} & 0 \\ & & & & & C_{44} \end{bmatrix} \quad \text{with} \quad \begin{aligned} C_{11} &= \frac{Y^\circ(1-\nu^\circ)}{(1-2\nu^\circ)(1+\nu^\circ)} \\ C_{12} &= \frac{Y^\circ\nu^\circ}{(1-2\nu^\circ)(1+\nu^\circ)} \\ C_{44} &= \frac{Y^\circ}{2(1+\nu^\circ)} \end{aligned} \quad (\text{A.17})$$

Herein, the material parameters Y° and ν° hold for all isotropic approximations $\circ \in \{V, R, H+, H-\}$. Alternatively we can state the three isotropic coefficients $C_{\alpha\beta}$ in terms of K° and G° ,

$$C_{11} = K^\circ + \frac{4}{3}G^\circ \quad C_{12} = K^\circ - \frac{2}{3}G^\circ \quad C_{44} = G^\circ, \quad (\text{A.18})$$

or in terms of λ_1° and λ_2° .

$$C_{11} = \frac{1}{3}(\lambda_1^\circ + 2\lambda_2^\circ) \quad C_{12} = \frac{1}{3}(\lambda_1^\circ - \lambda_2^\circ) \quad C_{44} = \lambda_2^\circ, \quad (\text{A.19})$$

The homogenization is here also based on the eigenvalues $\lambda_J^c \forall J \in \{2, 3\}$ while applying Eqs. (28) and (32). Again, $\lambda_1^c = \lambda_1^\circ = \lambda_1^\square \forall \square \in \{V, R, H+, H-\}$ holds. Finally we can present the results in form of constitutive matrices of the different estimates by the aid of projectors.

$$\mathbf{C}^\square = \lambda_1^\square \mathbf{P}_1^\square + \lambda_2^\square \mathbf{P}_2^\square \quad \forall \square \in \{V, R, H+, H-\} \quad (\text{A.20})$$

The present procedure naturally yields identical results as given in Tab. 1.

A.2 Equivalence of different representations of Hooke's laws

Engineers are usually confused about the projector representation of constitutive laws. We here want to verify the equivalence of different representations of Hooke's law, at least in the case of isotropy. We start with the projector representation of the constitutive tensor

$$\mathbf{C}^\circ = \lambda_1^\circ \mathbb{P}_1^\circ + \lambda_2^\circ \mathbb{P}_2^\circ \quad (\text{A.21})$$

while we want to point out that the isotropic projectors \mathbb{P}_1° and \mathbb{P}_2° map the strain tensor \mathbf{E} into its dilatoric and deviatoric part, respectively.

$$\mathbb{P}_1^\circ : \mathbf{E} = \mathbf{E}^{\text{dil}} \quad \mathbb{P}_2^\circ : \mathbf{E} = \mathbf{E}^{\text{dev}} \quad (\text{A.22})$$

This dil-dev split is additive.

$$\mathbf{E} = \mathbf{E}^{\text{dil}} + \mathbf{E}^{\text{dev}} \quad (\text{A.23})$$

We can thus write our constitutive law $\mathbf{T} = \mathbb{C}^\circ : \mathbf{E}$ as follows.

$$\mathbf{T} = \lambda_1^\circ \mathbf{E}^{\text{dil}} + \lambda_2^\circ \mathbf{E}^{\text{dev}} \quad (\text{A.24})$$

Using the relations of Eq. (36) yields a well-known form of Hooke's law.

$$\mathbf{T} = 3K\mathbf{E}^{\text{dil}} + 2G\mathbf{E}^{\text{dev}} \quad (\text{A.25})$$

In the light of (A.23) we can reformulate this representation.

$$\mathbf{T} = 3K\mathbf{E}^{\text{dil}} + 2G(\mathbf{E} - \mathbf{E}^{\text{dil}}) \quad (\text{A.26a})$$

$$= 3K\mathbf{E}^{\text{dil}} + 2G\mathbf{E} - 2G\mathbf{E}^{\text{dil}} \quad (\text{A.26b})$$

$$= (3K - 2G)\mathbf{E}^{\text{dil}} + 2G\mathbf{E} \quad (\text{A.26c})$$

We already know that $\mathbf{E}^{\text{dil}} = \frac{1}{3}[\mathbf{E} : \mathbf{1}]\mathbf{1}$ holds and obtain the following representation.

$$\mathbf{T} = \left(K - \frac{2}{3}G \right) [\mathbf{E} : \mathbf{1}]\mathbf{1} + 2G\mathbf{E} \quad (\text{A.27})$$

We furthermore introduce the first ($\lambda = K - 2/3G$, please note that this λ is without any index) and the second Lamé parameter ($\mu = G$), cf. Lamé (1852).

$$\mathbf{T} = \lambda[\mathbf{E} : \mathbf{1}]\mathbf{1} + 2\mu\mathbf{E} \quad (\text{A.28})$$

We are aware that $\mathbf{E} : \mathbf{1} = \text{tr}\mathbf{E}$. However, Eq. (A.28) is known as Lamé representation, established in civil engineering. As the relations

$$\lambda = \frac{\nu Y}{(1 - 2\nu)(1 + \nu)} \quad \text{and} \quad \mu = \frac{1}{2} \frac{Y}{(1 + \nu)} \quad (\text{A.29})$$

hold in the case of isotropy, we can also write the constitutive law in the form

$$\mathbf{T} = \frac{\nu Y}{(1 - 2\nu)(1 + \nu)} [\mathbf{E} : \mathbf{1}]\mathbf{1} + \frac{Y}{(1 + \nu)} \mathbf{E} \quad (\text{A.30})$$

which seems to be more familiar to mechanical engineers.

References

- P. A. Basore. Defining terms for crystalline silicon solar cells. *Progress in Photovoltaics: Research and Applications*, 2(2): 177–179, 1994. doi: [10.1002/pip.4670020213](https://doi.org/10.1002/pip.4670020213).
- T. Böhlke and C. Brüggemann. Graphical representation of the generalized Hooke's law. *Technische Mechanik*, 21(2):145–158, 2001. URL http://www.uni-magdeburg.de/ifme/zeitschrift_tm/2001_Heft2/Boehlke_Brueggeman.pdf.
- H. J. Böhm. A Short Introduction to Continuum Micromechanics. ILSB Report 207, Institute of Lightweight Design and Structural Biomechanics (ILSB), Vienna University of Technology, Vienna, Austria, 2020. URL <https://www.ilsb.tuwien.ac.at/links/downloads/ilsbrep206.pdf>.
- R. M. Brannon. *Rotation, Reflection, and Frame Changes: Orthogonal tensors in computational engineering mechanics*. IOP Publishing, Bristol, 2018. doi: [10.1088/978-0-7503-1454-1](https://doi.org/10.1088/978-0-7503-1454-1).
- H. J. Bunge. Zur Darstellung allgemeiner Texturen. *Zeitschrift für Metallkunde*, 56(-):872–874, 1965.
- R. M. Christensen and K. H. Lo. Solutions for effective shear properties in three phase sphere and cylinder models. *Journal of the Mechanics and Physics of Solids*, 27(4):315–330, 1979. doi: [10.1016/0022-5096\(79\)90032-2](https://doi.org/10.1016/0022-5096(79)90032-2).
- J. M. J. den Toonder, J. A. W. van Dommelen, and F. P. T. Baaijens. The relation between single crystal elasticity and the effective elastic behaviour of polycrystalline materials: theory, measurement and computation. *Modelling and Simulation in Materials Science and Engineering*, 7(6):909–928, 1999. doi: [10.1088/0965-0393/7/6/301](https://doi.org/10.1088/0965-0393/7/6/301).

- A. A. Elvin. Number of grains required to homogenize elastic properties of polycrystalline ice. *Mechanics of Materials*, 22(1): 51–64, 1996. doi: [10.1016/0167-6636\(95\)00024-0](https://doi.org/10.1016/0167-6636(95)00024-0).
- F. I. Fedorov. *Theory of Elastic Waves in Crystals*. Plenum Press, New York, 1968. doi: [10.1007/978-1-4757-1275-9](https://doi.org/10.1007/978-1-4757-1275-9).
- P. R. Halmos. *Finite-Dimensional Vector Spaces*. Springer, New York, 1958. doi: [10.1007/978-1-4612-6387-6](https://doi.org/10.1007/978-1-4612-6387-6).
- Z. Hashin and S. Shtrikman. On some variational principles in anisotropic and nonhomogeneous elasticity. *Journal of the Mechanics and Physics of Solids*, 10(4):335–342, 1962a. doi: [10.1016/0022-5096\(62\)90004-2](https://doi.org/10.1016/0022-5096(62)90004-2).
- Z. Hashin and S. Shtrikman. A variational approach to the theory of the elastic behaviour of polycrystals. *Journal of the Mechanics and Physics of Solids*, 10(4):343–352, 1962b. doi: [10.1016/0022-5096\(62\)90005-4](https://doi.org/10.1016/0022-5096(62)90005-4).
- M. Hayes. Connexions between the moduli for anisotropic elastic materials. *Journal of Elasticity*, 2(2):135–141, 1972. doi: [10.1007/BF00046063](https://doi.org/10.1007/BF00046063).
- R. Hill. The elastic behaviour of a crystalline aggregate. *Proceedings of the Physical Society. Section A*, 65(5):349–354, 1952. doi: [10.1088/0370-1298/65/5/307](https://doi.org/10.1088/0370-1298/65/5/307).
- M. A. Hopcraft, W. D. Nix, and T. W. Kenny. What is the young’s modulus of silicon? *Journal of Microelectromechanical Systems*, 19(2):229–330, 2010. doi: [10.1109/JMEMS.2009.2039697](https://doi.org/10.1109/JMEMS.2009.2039697).
- W. F. Hosford. *The Mechanics of Crystals and Textured Polycrystals*. Oxford University Press, 1993.
- U. F. Kocks, C. N. Tomé, H. R. Wenk, A. J. Beaudoin, and H. Mecking. *Texture and Anisotropy: Preferred Orientations in Polycrystals and Their Effect on Materials Properties*. Cambridge University Press, 1998.
- M. Köntges, S. Kurtz, C. Packard, U. Jahn, K. A. Berger, K. Kato, T. Friesen, H. Liu, and M. Van Iseghem. Review of failures of pv modules, 2014. URL http://iea-pvps.org/fileadmin/dam/intranet/ExCo/IEA-PVPS_T13-01_2014_Review_of_Failures_of_Photovoltaic_Modules_Final.pdf.
- E. Kröner. Berechnung der elastischen Konstanten des Vielkristalls aus den Konstanten des Einkristalls. *Zeitschrift für Physik*, 151(4):504–518, 1958. doi: [10.1007/BF01337948](https://doi.org/10.1007/BF01337948).
- E. Kröner. *Statistical continuum mechanics*. Number 92 in CISM International Centre for Mechanical Sciences. Springer, 1972. doi: [10.1007/978-3-7091-2862-6](https://doi.org/10.1007/978-3-7091-2862-6).
- G. Lamé. *Leçons sur la théorie mathématique de l’élasticité des corps solides*. Bachelier, 1852. URL <https://gallica.bnf.fr/ark:/12148/bpt6k5747708p>.
- M. Lobos Fernández. *Homogenization and materials design of mechanical properties of textured materials based on zeroth-, first- and second-order bounds of linear behavior*. PhD thesis, Karlsruher Institut für Technologie (KIT), 2018.
- M. M. Mehrabadi and S. C. Cowin. Eigentensors of linear anisotropic elastic materials. *The Quarterly Journal of Mechanics and Applied Mathematics*, 43(1):15–41, 1990. doi: [10.1093/qjmam/43.1.15](https://doi.org/10.1093/qjmam/43.1.15).
- M. A. Michalicek, D. E. Séné, and V. M. Bright. Advanced modeling of micromirror devices. In *Proceedings of the International Conference on Integrated Micro/Nanotechnology for Space Applications*, pages 224–239, Houston, 1995.
- W. H. Miller. *A Treatise on Crystallography*. Deighton, Cambridge, 1839. URL <https://archive.org/details/treatiseoncrysta00millrich>.
- A. Morawiec. *Orientations and Rotations: Computations in Crystallographic Textures*. Springer, Berlin Heidelberg, 2004. doi: [10.1007/978-3-662-09156-2](https://doi.org/10.1007/978-3-662-09156-2).
- S. Nemat-Nasser and M. Hori. *Micromechanics: Overall Properties of Heterogeneous Solids*. Elsevier, New York, 1993.
- J. Nordmann, M. Aßmus, and H. Altenbach. Visualising elastic anisotropy: Theoretical background and computational implementation. *Continuum Mechanics and Thermodynamics*, 30(4):689–708, 2018. doi: [10.1007/s00161-018-0635-9](https://doi.org/10.1007/s00161-018-0635-9).
- K. E. Petersen. Silicon as a mechanical material. *Proceedings of the IEEE*, 70(5):420–457, 1982. doi: [10.1109/PROC.1982.12331](https://doi.org/10.1109/PROC.1982.12331).
- S. Philipps and W. Warmuth. Photovoltaics report. Technical report, Fraunhofer Institute for Solar Energy Systems, Freiburg i.Br., Germany, November 2019.
- S. I. Ranganathan and M. Ostoja-Starzewski. Universal elastic anisotropy index. *Phys. Rev. Lett.*, 101:055504–1–4, 2008. doi: [10.1103/PhysRevLett.101.055504](https://doi.org/10.1103/PhysRevLett.101.055504).
- M. Nygård. Number of grains necessary to homogenize elastic materials with cubic symmetry. *Mechanics of Materials*, 35(11): 1049–1057, 2003. doi: [10.1016/S0167-6636\(02\)00325-3](https://doi.org/10.1016/S0167-6636(02)00325-3).
- A. Reuss. Berechnung der Fließgrenze von Mischkristallen auf Grund der Plastizitätsbedingung für Einkristalle. *Zeitschrift für Angewandte Mathematik und Mechanik*, 9(1):49–58, 1929. doi: [10.1002/zamm.19290090104](https://doi.org/10.1002/zamm.19290090104).
- J. Rychlewski. On Hooke’s law. *Journal of Applied Mathematics and Mechanics*, 48(3):303–314, 1984. doi: [10.1016/0021-8928\(84\)90137-0](https://doi.org/10.1016/0021-8928(84)90137-0).
- J. Rychlewski. Unconventional approach to linear elasticity. *Archives of Mechanics*, 47(5):149–171, 1995.
- J. Rychlewski and J. M. Zhang. Anisotropic Degree of Elastic Materials. *Archives of Mechanics*, 41(5):697–715, 1989.
- W. N. Sharpe. chapter Mechanical properties of MEMS materials. CRC Press, Boca Raton, 2002.
- G. Stokkan, A. Song, and B. Rynningen. Investigation of the grain boundary character and dislocation density of different types of high performance multicrystalline silicon. *Crystals*, 8(9), 2018. doi: [10.3390/cryst8090341](https://doi.org/10.3390/cryst8090341).
- S. Sutcliffe. Spectral Decomposition of the Elasticity Tensor. *Journal of Applied Mechanics*, 59(4):762–773, 1992. doi: [10.1115/1.2894040](https://doi.org/10.1115/1.2894040).

- W. Thomson. Elements of a mathematical theory of elasticity. *Philosophical Transactions of the Royal Society of London*, 146: 481–498, 1856. URL <http://www.jstor.org/stable/108596>.
- W. Voigt. Über die Beziehung zwischen den beiden Elasticitätskonstanten isotroper Körper. *Wiedemann'sche Annalen*, 38: 573–587, 1889. doi: [10.1002/andp.18892741206](https://doi.org/10.1002/andp.18892741206).
- L. J. Walpole. Fourth-rank tensors of the thirty-two crystal classes: Multiplication tables. *Proceedings of the Royal Society of London. Series A, Mathematical and Physical Sciences*, 391(1800):149–179, 1984. URL <http://www.jstor.org/stable/2397534>.
- Y. M. Yang, A. Yu, B. Hsu, W. C. Hsu, A. Yang, and C. W. Lan. Development of high-performance multicrystalline silicon for photovoltaic industry. *Progress in Photovoltaics: Research and Applications*, 23(3):340–351, 2015. doi: [10.1002/pip.2437](https://doi.org/10.1002/pip.2437).
- C. M. Zener. *Elasticity and Anelasticity of Metals*. University of Chicago press, Chicago, 1948.

A study on harmonic excitation based experimental characterization of damping materials for acoustic simulations

Lars Spannan^{1*}, Fabian Duvigneau¹, Maria Gavila Lloret², Christian Daniel¹, Daniel Juhre¹, and Elmar Woschke¹

¹ Otto-von-Guericke University, Institute of Mechanics, Universitätsplatz 2, 39106 Magdeburg, Germany

² BMW AG, Knorrstraße 147, 80788 München, Germany

Abstract: The presented study deals with the experimental characterization of damping materials for acoustic simulations with respect to the stiffness and damping in dependence of the excitation frequency, i.e. frequency-dependent elasticity modulus. The test rigs under consideration utilize a shaker, acceleration sensors and a laser Doppler vibrometer (LDV) to measure oscillating behaviour at frequencies ranging from 20 to 2000 Hz. Suitable mounting properties of the test rigs are examined experimentally and by finite element analysis. The applicability of the gained results for acoustic simulations is investigated with results from a window test setup.

Keywords: foam, damping, stiffness, characterization, acoustics

1 Introduction

During the last years, the reduction of sound transmission towards the passengers cabin in automobiles gained importance in order to improve the driving experience and customer satisfaction. Beside the reduction of noise sources, passive elements such as damping layers are widely used to lower the level of noise transmitted to the passengers. In order to assess the choice of material, structure and geometry for such elements in the early development stages, simulative approaches are striven for. Such simulation approaches were already developed, for example, for a holistic consideration of engines by [Duvigneau et al. \(2016\)](#). The main difficulty of all numerical analyses in acoustics is an accurate modelling of the vibroacoustic properties of the damping materials, which are used in almost every real world application that presents acoustic issues. A proper modelling of damping materials is also of utmost importance if innovative materials, such as acoustic metamaterials ([Duvigneau and Duczek \(2017\)](#)), are under investigation to find an optimal design for the given task.

Experimental methods are used to determine the material properties required for the models used in the acoustic simulations. The main assumption for a macroscopic description of the dynamic behaviour assumes homogenized material properties, often in combination with isotropic and linear media.

The skeleton of polymeric poroelastic materials, such as polyurethane foams frequently used in the automotive industry for acoustic treatment, have a viscoelastic behaviour. This means that under deformation the material exhibits viscous as well as elastic characteristics ([Lakes \(1998\)](#)). For the typical deformation amplitudes that noise control treatments undergo, the behaviour remains in the linear viscoelastic regime. Additionally, in the present study we assume isotropic material behaviour. Unlike elastic materials, the loading and unloading paths for a viscoelastic material are not the same. The dissipated energy per cycle inside the material due to viscoelastic losses is known as hysteresis loss.

The methods for the characterization of the elastic parameters can be classified in three groups ([Renault \(2008\)](#)). First, there are approaches based on the velocity at which waves propagate inside the poroelastic material. For instance, the velocity of the Rayleigh waves can be related to the shear modulus G and the Poisson ratio ν of the material ([Allard et al. \(2002\)](#); [Boeckx et al. \(2005\)](#)). In order to identify these, a layer of poroelastic material is fixed to a rigid plate on one of its ends. On the other end, the layer is excited with a harmonic signal through a shaker. A laser vibrometer is employed to measure the displacement on the surface. The fitting of the theoretical and the measured phase velocities delivers frequency-dependent values for G and ν . In order to calculate the theoretical solution, the poromechanical parameters need to be determined beforehand, which is a cumbersome and expensive process. The method utilized in this paper does not need the identification of the poromechanical parameters in advance. In the second kind of characterization methods, the shear modulus and the Poisson ratio are calculated with the help of acoustic methods. A material sample with rigid backing is excited by a monopole source. A microphone located near the sample measures the pressure resulting from the direct and the reflected fields. After that, the poroelastic material is replaced by a rigid, impervious surface and the procedure is repeated. The ratio between the two pressures is then calculated. Again, from the contrast between the obtained values and the theoretical solution, provided that the poromechanical parameters are known, the elastic parameters G and ν can be derived, see [Allard et al. \(2005\)](#).

The third group is formed by the vibrational methods, which are based on the response of the material subjected to mechanical excitation. The vibrational approaches are further broken down into two categories: The quasi-static methods, in which the inertial effects are neglected, and the dynamic techniques, which include them. In the quasi-static compression approach proposed by [Langlois et al. \(2001\)](#) two material samples of different shape factor are measured. The shape factor is defined as the ratio

of half the radius to the thickness of a cylindrical sample. After that, several finite element simulations on elastic solids under compression are run to obtain polynomial relations that link the measured compression stiffness to the elasticity modulus, the Poisson's ratio and the shape factor. In order to account for the inertial effects, this setup can be modified to conduct a dynamic uni-axial compression, like the configuration presented by [Pritz \(1986, 1994\)](#).

A review of other quasi-static and dynamic experimental methods, including torsion and shear loading can be found in [Renault \(2008\)](#) and [Jaouen et al. \(2008\)](#). In the scope of [Gavila Lloret \(2018\)](#) six different poroelastic foams were analysed following these methods. It can be noted that the values of the elasticity modulus obtained with the quasi-static compression method ([Langlois et al. \(2001\)](#)) are systematically lower than the ones provided by the dynamic method ([Pritz \(1986\)](#)) since the former neglects the inertial effects. As the frequency increases, the inertial force increases and gets significant in comparison to the elastic force in the system, see [Koblar and Boltežar \(2016\)](#). Therefore the utilization of dynamic characterization techniques becomes necessary.

As already mentioned, the dynamic behaviour of the solid skeleton is viscoelastic and frequency-dependent. [Rigobert et al. \(2004\)](#) and [Van der Kelen et al. \(2014\)](#) give two examples on the modelling of a poroelastic layer that covers a structurally excited plate. In both cases the foam layer was described using the full poroelastic formulation. It was first found that the application of the quasi-static elastic parameters resulted in a poor comparability with the experimental data. In a second step, a frequency-dependent profile for the elastic properties was defined by fitting the calculated predictions to the reference data sets. Even if this derivation leads to a good prediction of the vibroacoustic behaviour, it presents the great disadvantage that a measurement of the complete setup is first needed in order to obtain the frequency-dependent parameters. At this point, we address presentable measurement methods that follow a simple and robust approach, while the number of material parameters remains low and parameters without physical interpretation are renounced. In addition, the measurement of the complete experimental setup for model-updating purposes is undesired. In such cases the advantages of numerical simulations would be lost.

The theory of poroelasticity by [Biot \(1956a,b\)](#); [Allard and Daigle \(1994\)](#) is the state of the art in numerical modelling of poroelastic media. Its main underlying assumption is the homogenization. This means that, provided that the lengths of the waves propagating inside the material are much larger than the pore size, the biphasic aggregate can be considered as a homogeneous medium in which the two phases are simultaneously present. Consequently, the resolution of the pores on the micro scale is avoided. The two governing equations have the form of a fluid-structure interaction problem with the particularity that the mechanical coupling between the elastic frame deformation and the fluid behaviour is not limited to the fluid structure interfaces, but is of a volume nature. The coefficients of the equation can be grouped into three classes - fluid properties, elastic and poromechanical parameters. The first set includes the material properties of the filling fluid, namely its density, its viscosity and the speed of sound. The elastic parameters characterize the response of the frame in vacuum and are typically the Young's modulus, the Poisson ratio, the structural damping coefficient and the density of the drained material. The poromechanical parameters help to link the microscopic thermal and viscous effects at a local level with the changes in the macroscopic effective bulk modulus and effective dynamic density. This requires a constitutive model as, for example, the one proposed by [Johnson et al. \(1987\)](#), [Champoux and Allard \(1991\)](#) (JCA), which is employed as reference for the conducted numerical simulation in section 4.1. Some procedures to determine the values of these mentioned material parameters can be found in [Jaouen et al. \(2008\)](#); [Salissou and Panneton \(2007\)](#); [Atalla and Panneton \(2005\)](#).

An alternative to the complex poroelastic modelling is the simplification of the material as an elastic solid. This approach has the major advantage of avoiding the characterization of the poromechanical parameters, which is a laborious task and requires specific test equipment. However, since the presence of the fluid phase is neglected, some dissipation mechanisms inside the poroelastic medium may not be correctly represented, especially at high frequencies. In particular, if constant elastic material parameters are used, large differences at higher frequencies occur as presented by [Van der Kelen et al. \(2014\)](#).

An option to include the missing mechanisms is to condense the additional effects by means of frequency-dependent elastic parameters, which is pursued in the paper at hand. The frequency-dependent characterization of poroelastic materials, which is carried out analogously to classical viscoelastic media, was also utilized by [Cuenca et al. \(2014\)](#) and [Finnveden et al. \(2014\)](#). An experimental setup to determine frequency-dependent elasticity modulus and Poisson ratio based on sine burst excitation is proposed by [Bonfiglio and Pompoli \(2015\)](#). One general trend that can be identified is an increasing elasticity modulus with frequency. This is a common progression for polymers and other viscoelastic materials, which do not have a crystalline structure ([Sfaoui \(1995\)](#); [Ferry \(1980\)](#)). Since the frame of the investigated polyurethane foams is also a viscoelastic material, such a frequency behaviour is to be expected. In comparison to poroelastic models it needs less (exclusively physical) parameters, which are easier to interpret and can be identified in parallel with the same experimental setup. Moreover, poroelastic models do not work properly for foams with closed cells as closed pores are neglected in the sense that they are counted as part of the solid structure ([Pride and Berryman \(1998\)](#)). Finally, the material modelling within the numerical simulation is also straightforward beside causing fewer degrees of freedom.

In the following section two experimental methods are described and frequency-dependent complex elasticity moduli are derived. The limits of the methods and influences arising from the boundary conditions are discussed. Regarding the latter, the choice of lightweight but sufficiently stiff bearings, which load the foam samples, is investigated experimentally and by finite element analysis. Different designs and arrangements of the test set-up are presented and their advantages and disadvantages are evaluated in order to determine a preferred variant for engineering practice. Section 3 sums up the measurement results of the frequency-dependent elasticity moduli of two structurally different foams gained from the final measurement setup. The determination of the material properties gets more challenging with higher excitation frequencies due to the required energy, therefore the testing frequency ranges from 20 to 2000 Hz. Section 4 presents a window test rig and the associated acoustic simulation model in which the applicability of the presented characterization method is examined. In section 5 a conclusion and an outlook are given.

Tab. 1: Specimen overview of two foams of bright (B) and dark (D) colour with edge lengths of 30 mm and 50 mm or diameters of 30 mm, respectively. Specimen duplicates are enumerated by x.

Label	Color	Width W [mm]	Length L [mm]	Height H [mm]
B□50.x	bright	50	50	15.8
B□30.x	bright	30	30	15.8
D□50.x	dark	50	50	10.25
D□30.x	dark	30	30	10.25

Label	Color	Diameter D [mm]	Height H [mm]
B○30.x	bright	30	15.8
D○30.x	dark	30	10.25



Fig. 1: Viscoelastic representation of the material behaviour (left) and foam samples B□50.x (center) and D○30.x (right).

2 Experimental methods

Different experimental methods have been presented in the literature in order to characterize frequency-dependent stiffness and damping behaviour of poroelastic media. A comprehensive study with a focus on reproducibility of the approaches was conducted by several researchers and is published by [Bonfiglio et al. \(2018\)](#), also depicting the challenges. Referring to the literature review given in the introduction we focus on the third group of characterization methods, namely the vibrational methods. Especially, we exclusively consider dynamical methods, as from our point of view the frequency dependency of the material properties is of utmost importance. Consequently, quasi-static methods are not sufficient for this purpose.

In the study at hand, two methods are investigated out of which the material properties are derived. The applied material model is viscoelastic with a frequency-dependent stiffness parameter $c(f)$ and damping parameter $d(f)$, Fig. 1. This characteristic can be represented independently of the specimen geometry by using the apparent complex elasticity modulus E :

$$E(f) = E'(f) + i\bar{E}(f) = c(f)\frac{H}{A} + i2\pi f d(f)\frac{H}{A}. \quad (1)$$

With f , H , A being the frequency under consideration, the foam sample height and the foam surface area under load, respectively. Due to the assumption of constant Poisson ratio in the presented procedures, the given elasticity modulus is an apparent value. A comparison of the results obtained from the measuring methods will be given in section 3, including a discussion on sources of deviations and the influence parameters, as for example the boundary conditions.

Two open cell polyurethane molded foam products with different mechanical properties are considered. For the ease of distinctiveness their colour is used for labelling within this article. One foam is of bright colour and one is of dark colour, identified in the following sections by the characters "B" and "D", respectively. Geometric specifications of the used specimens are summarized in Tab. 1. To verify the reproducibility, multiple specimens of the foam samples were analysed. In general, we used three specimens per specification.

2.1 Resonance Method

The first method utilized represents a suspended mass with support node excitation in vertical direction. Located between two steel plates, the specimen is modelled with a linear spring and a linear damper element connected in parallel, see Fig. 2. The lower mass m_a represents the masses of the movable parts of the shaker, the base plate and the acceleration sensor 1. The mass m_s includes the suspended masses of the top mass and the acceleration sensor 2. The mass of the specimen is equally distributed to the two entities, m_a and m_s . With the assumption of sole vertical movement, the set-up represents a damped oscillator with one degree of freedom with the eigenfrequency of

$$f_0 = \frac{1}{2\pi} \sqrt{\frac{c(f_0)}{m_s}} \quad (2)$$

and the damping factor

$$D = \frac{d(f_0)}{c(f_0)} \pi f_0. \quad (3)$$

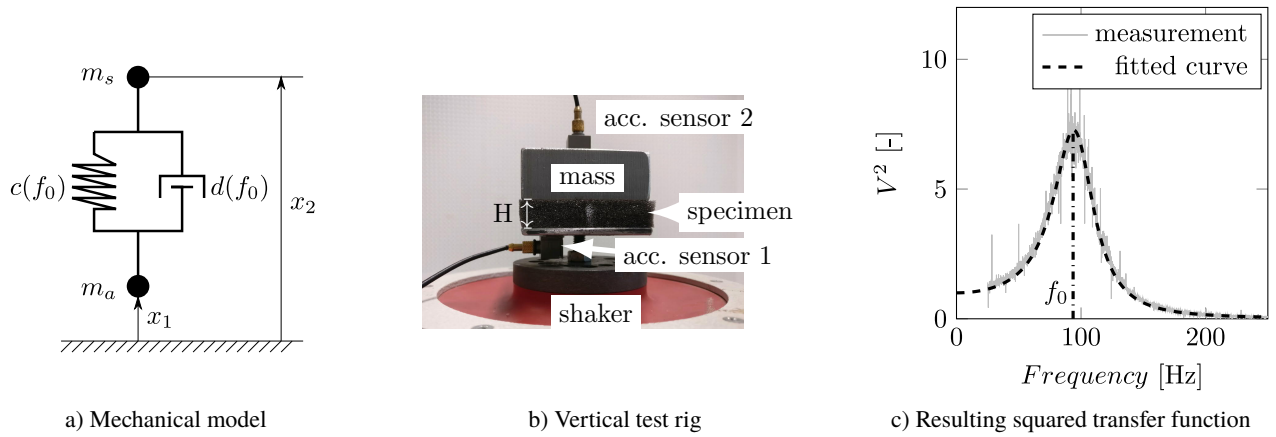


Fig. 2: Resonance measurement arrangement.

The shaker excites with a white Gaussian noise signal that results in a broadband excitation. The acceleration of the base plate \ddot{x}_1 and the response of the top mass \ddot{x}_2 are simultaneously measured. Subsequently, the resulting transfer function V of the Fourier transformations $\mathcal{F}(\ddot{x}_1)$ and $\mathcal{F}(\ddot{x}_2)$ can be fitted to the analytical solution of the one dimensional oscillator model (Nashif et al. (1985))

$$V(\eta, D) = \frac{\mathcal{F}(\ddot{x}_2)}{\mathcal{F}(\ddot{x}_1)} = \frac{\sqrt{1 + 4D^2\eta^2}}{\sqrt{(1 - \eta^2)^2 + 4D^2\eta^2}} \quad (4)$$

or the squared form

$$V^2(\eta, D) = \frac{1 + 4D^2\eta^2}{(1 - \eta^2)^2 + 4D^2\eta^2}, \quad (5)$$

respectively, with $\eta = f/f_0$ being the tuning ratio. Eq. 5 is fitted to the measured data in a least-square sense in order to obtain the resonance frequency f_0 and the dimensionless damping factor D as presented in Fig. 2 c). Taking into account the specimen height H and the orthogonal face area A , the viscoelastic behaviour can also be reformulated as the real part E' and imaginary part \bar{E} of the complex elasticity modulus, according to Eqs. (1), (2) and (3)

$$E'(f_0) = 4\pi^2 f_0^2 m_s \frac{H}{A}, \quad (6)$$

$$\bar{E}(f_0, D) = 2 D E'. \quad (7)$$

In order to obtain a frequency-dependent description of the material behaviour, the procedure has to be carried out with different top masses m_s to realize different resonance frequencies. With a view on acoustics applications, this method is limited regarding high frequencies requiring lightweight top masses, which are prone to detach from the specimen.

2.1.1 Measurement Results

As noted above, the major drawback of the method presented in Sec. 2.1 is the relatively low maximum testing frequency because of the limitation in the weight of the top masses. The presented foams with edge lengths of 50 mm were tested with weights ranging from 67 g to 418 g, resulting in a resonance frequency range from 33 Hz to 181 Hz, which is hardly relevant for acoustical problems. The calculated real and imaginary parts of the elasticity modulus according to Eq. (6) and Eq. (7) are summarized in Tab. 2 and depicted in Fig. 3. The results show good repeatability and an increase in stiffness with frequency. This is particularly evident for the bright foam. The specified standard deviation results from eight measurements with one for each possible orientation of the foam. One cause of deviation may arise due to the imperfections in the foam structure, as can be seen in Fig. 1.

In an attempt to expand the frequency range by utilizing adhesive tape and strong fast-acting adhesives in order to prevent detachment, a significant influence on the stiffness and damping results was identified, see Tab. 2 variations a) and b). With the help of the adhesives the detachment of the 71 g mass could be prevented, but the two adhesive modifications led to significantly different results. Additionally, with higher excitation amplitudes, referenced as condition c), the top mass can separate, which causes deviations of the resulting stiffness. The positioning of the acceleration sensors, condition d), also gives rise to variations in the results due to non strict one dimensional movement. Therefore, a centred positioning of the sensors is advised in order to minimize the influence due to tilting motion of the masses. Furthermore, it cannot be ruled out that the resulting viscoelastic properties may be influenced by the pre-compression or the compression rate of the foam during the experiment due to the variation of the top load. Due to the limited frequency range, investigations with the resonance method were discontinued and further investigations regarding the influences mentioned above were not conducted.

Tab. 2: Tests with the resonance procedure and modifications of the boundary conditions. -) Standard configuration. a) Using adhesive tape. b) Using strong fast-acting adhesive. c) High excitation amplitude. d) Sensors not centered. The specified bounds represent standard deviations resulting from eight repetitions, one for each different orientation.

Spec.	cond.	m_s [g]	f_0 [Hz]	E' [kN/m ²]	\bar{E} [kN/m ²]
D□50.1	-	418	74.49 ± 0.71	375.52 ± 7.21	46.26 ± 4.63
D□50.2	-	357	78.41 ± 0.83	355.79 ± 7.48	43.24 ± 1.37
D□50.3	-	357	80.57 ± 1.07	375.61 ± 10.09	46.85 ± 6.46
D□50.1	-	211	103.36 ± 1.06	342.55 ± 61.49	40.75 ± 7.23
D□50.1	a)	71	181.02 ± 7.96	375.21 ± 32.54	75.01 ± 1.27
D□50.1	b)	71	159.96 ± 2.53	292.65 ± 9.23	49.90 ± 1.18
D□50.1	b), d)	71	144.19 ± 0.24	237.74 ± 0.80	44.83 ± 0.50
B□50.2	-	357	33.20 ± 4.27	99.38 ± 25.49	34.94 ± 8.66
B□50.1	-	110	77.12 ± 0.80	162.89 ± 3.35	68.92 ± 1.20
B□50.1	-	89	96.81 ± 2.23	207.88 ± 9.58	81.07 ± 9.94
B□50.1	-	71	100.32 ± 5.55	177.91 ± 20.29	86.66 ± 17.08
B□50.1	c)	71	69.04 ± 3.27	84.16 ± 8.00	56.78 ± 5.52
B□50.2	c)	71	96.05 ± 1.76	162.66 ± 5.95	97.53 ± 3.82
B□50.2	-	67	102.51 ± 1.31	174.79 ± 4.46	72.99 ± 1.44
B□50.3	-	67	97.60 ± 1.05	158.44 ± 3.41	68.04 ± 1.73

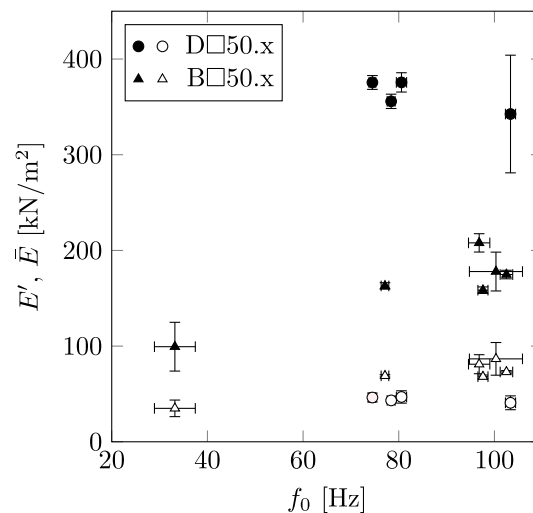


Fig. 3: Real (E' , black marker) and imaginary (\bar{E} , white marker) parts of the elasticity moduli measured for the dark (D, round marker) and bright (B, triangular marker) foam samples in standard configuration without adhesives. The error bars represent the bounds specified in Tab. 2.

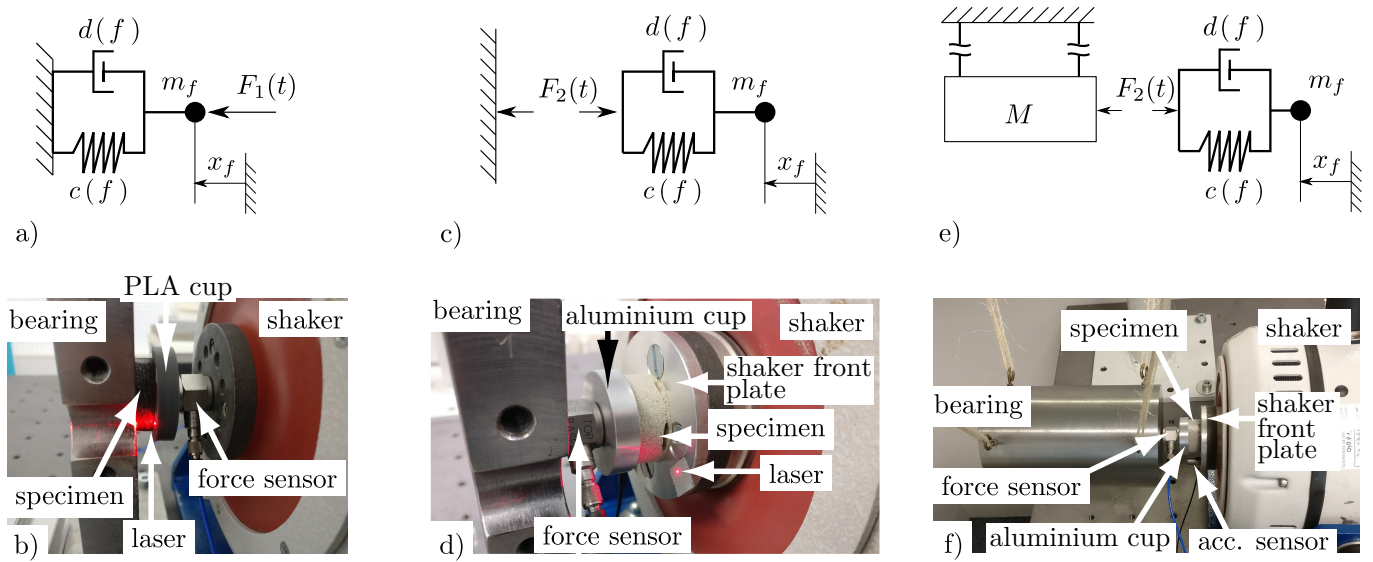


Fig. 4: Horizontal measurement arrangements. Shaker facing force sensor position: a) Mechanical model. b) Test rig. Bearing facing force sensor position: c) Mechanical model. d) Test rig. Seismic mass bearing: e) Mechanical model. f) Test rig.

2.2 Harmonic loading method

For the second characterization method, the specimen is horizontally aligned between the shaker and a bearing, which is assumed to be rigid. Different arrangements for the bearing have been investigated, as displayed in Fig. 4. The configurations in Fig. 4 a)-d) include a fixed bearing, but with different order of the specimen and the force sensor in the load path. In the setup in Fig. 4 e)-f) a seismic mass bearing hangs in a free-free boundary condition. The shaker provides a harmonic force F that loads the specimen at a frequency f .

A laser Doppler vibrometer (LDV) is utilized to measure the deflection x_f . After a few oscillations, the steady state is reached and the periodic solution

$$x_f(t) = \check{x}_f \sin(2\pi ft + \psi) \quad (8)$$

with amplitude \check{x}_f and phase ψ remains. For the setup in Fig. 4 e)-f) using the seismic mass bearing, the acceleration

$$\check{\check{x}}_f(t) = \check{\check{x}}_f \sin(2\pi ft + \psi) = -4\pi^2 f^2 \check{x}_f \sin(2\pi ft + \psi) \quad (9)$$

is measured with an appropriate acceleration sensor due to the lack of optical access for the LDV. The deflection amplitude is calculated by

$$\check{\check{x}}_f = \check{x}_f (-4\pi^2 f^2)^{-1}. \quad (10)$$

The approach with an acceleration sensor turned out to be just as feasible as the displacement measurement with the LDV. Again, the porous medium is modelled with a linear spring-damper combination with one single degree of freedom. This leads to the following balance of forces

$$F_1(t) = c x_f + d \dot{x}_f + m_f \ddot{x}_f \quad (11)$$

in the case where the force sensor is positioned between the shaker and the specimen, see Fig. 4 a). The mass m_f combines the weight of the adapter plate and partial contributions by the force sensor and the specimen. The determination of the latter two is prone to errors. Combining Eq. (8) and Eq. (11), the inertial force can be obtained as second derivative of the deflection signal with respect to time. The calculated inertial force is subtracted from the force signal to obtain the loading force \bar{F} acting on the foam

$$\bar{F} = F_1(t) - m_f \ddot{x}_f(t) = c x_f(t) + d \dot{x}_f(t). \quad (12)$$

Due to the error-prone determination of the inertial component, this approach has a lower accuracy than the setup, where the force sensor is mounted between the specimen and the bearing. In the latter cases, Fig. 4 c)-f), inertial forces are not recorded by the force sensor and the compliance of the foam is assumed to be dominant, leading to

$$\bar{F} = F_2(t) = c x_f(t) + d \dot{x}_f(t). \quad (13)$$

The theoretical force-deflection diagram according to Eq. (13) yields an elliptical hysteresis curve which is met by the experimental data quite well, Fig. 5. The hysteresis loss W_D can be calculated with the integral of the foam loading force with respect to the load path

$$W_D = \oint \bar{F} dx_f. \quad (14)$$

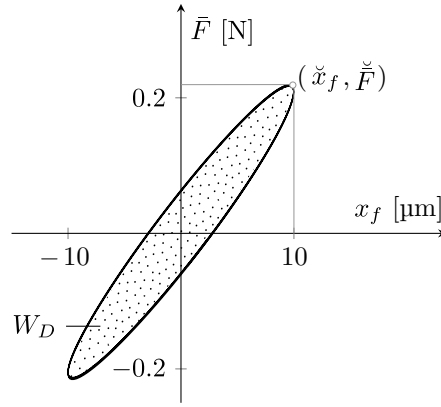


Fig. 5: Hysteresis loss of an example measurement of B○30.3 at 1100 Hz.

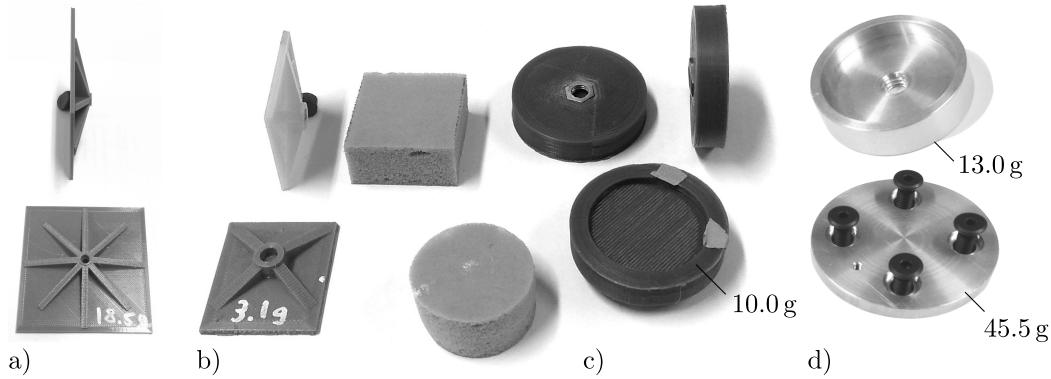


Fig. 6: Test setup iterations. a) PLA die with 70 mm edge length, 2 mm ground plate height and 18.5 g mass b) PLA die with 30 mm edge length, 2 mm ground plate height and 3.1 g mass c) PLA die with 10.0 g mass for cylindrical probes of 30 mm diameter d) final design with aluminium cup (top) for 30 mm diameter probes and shaker front plate (bottom).

According to Eqs. (8) and (13), the stiffness and damping coefficients for the particular loading frequency f is gained by

$$c(f) = \frac{\ddot{\bar{F}}}{\ddot{x}_f}, \quad (15)$$

$$d(f) = \frac{W_D}{\ddot{x}_f^2 2\pi^2 f}. \quad (16)$$

Recalling Eq. (1), the real and imaginary part of the elasticity modulus are

$$E'(f) = c(f) \frac{H}{A} \quad (17)$$

$$\bar{E}(f) = \frac{W_D(f)}{\ddot{x}_f^2 \pi} \frac{H}{A}. \quad (18)$$

2.2.1 Test set-up optimization

The frequency range of the method described in Sec. 2.2 is limited by the power of the shaker, the mass to be moved and the specified displacement amplitude. Therefore, several mass reducing iterations of the set-up were investigated in order to maximize the frequency range without violating the assumption of a rigid set-up and dominant compliance due to the foam.

The first design with a square steel sheet with an edge length of 70 mm and a thickness of 0.75 mm showed evident flexibility during operation. In the first step, the steel sheet was replaced by a rapid prototyped die with an edge length of 70 mm and a ground plate height of 2 mm made of PLA (polylactide), depicted in Fig. 6 a). In order to test the assumption of rigidity, a smaller die with an edge length of 30 mm and a ground plate height of 2 mm was used to test the square foam specimens with 30 mm edge length, Fig. 6 b). Despite the benefit of higher frequency ranges, a comparison of the determined frequency-dependent elasticity moduli with the two PLA dies showed a significant discrepancy. For that reason, finite element analyses were carried out in order to evaluate the rigidity assumption of the PLA die from Fig. 6 b), which is less compliant because of the geometry.

Finite element analysis (FEA) evaluation

A finite element representation of the experimental setup was modelled to identify measurement deviations due to compliant components. The geometrical parameters and material properties used for the foam domain are specified in Tab. 3. Due to the

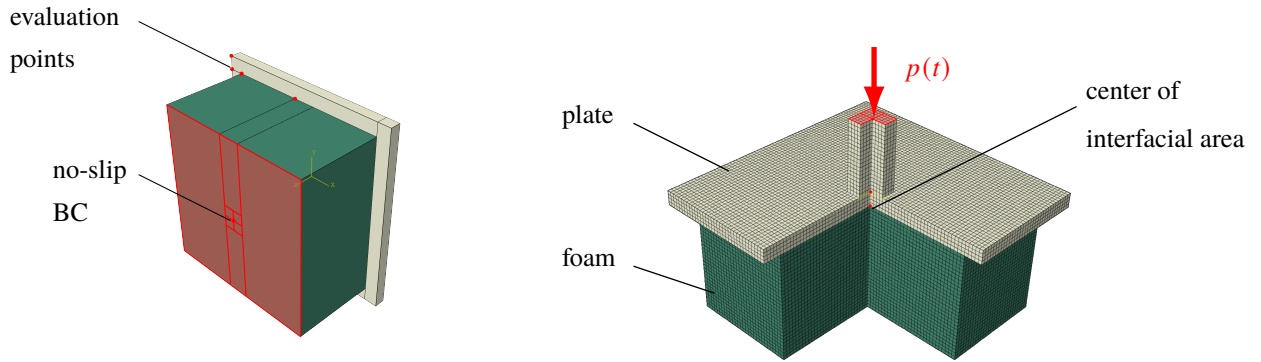


Fig. 7: Utilized grid in the finite element analysis.

Tab. 3: Isotropic elastic parameters and geometry of the foam domain in the FEA.

E'_{foam} [kN/m ²]	ρ_{foam} [kg/m ³]	ν_{foam} [-]	L_{foam} [mm]	B_{foam} [mm]	H_{foam} [mm]
5000	25.4	0.3	30	30	15.75

assumption of increased stiffness of the foam at higher frequencies the finite element analysis was carried out for a maximum anticipated elasticity modulus of $E'_{\text{foam}} = 5000 \text{ kN/m}^2$. The simulation parameters are summarized in Tab. 4. Fig. 7 shows the domain discretization as well as the load-controlled boundary conditions. According to Lerch *et al.* (2009) and the material data in Tab. 3, resonances may occur above the border frequencies

$$\frac{\sqrt{E'_{\text{foam}}(1-\nu)}}{\sqrt{\rho(1-\nu-2\nu^2)} \cdot 2 \cdot \max(L, B, H)} \approx 8580 \text{ Hz}$$

for longitudinal wave propagation and

$$\frac{\sqrt{E'_{\text{foam}}}}{\sqrt{2\rho(1+\nu)} \cdot 2 \cdot \max(L, B, H)} \approx 4586 \text{ Hz}$$

for transversal wave propagation, respectively. With a testing frequency of 500 Hz a sufficient gap to the critical values is kept. In a first analysis, the die was modelled rigidly in order to compare the elasticity modulus derived from the force and deflection data to the input values, Tab. 3. With this analysis the suitability of the chosen boundary conditions, the time integration method, the excitation amplitude, the number of load cycles, the mesh discretization and the element type, see Tab. 4, was verified. A harmonic pressure load is applied at the square tip of a pin in the centre of the die, see Fig. 7, while the mesh is continuous at the boundary between the die domain and the foam domain. The deflection of all nodes on the opposite area of the foam domain is constrained in the load direction, whilst all three translational degrees of freedom of the central node of this face are constrained, too. As a consequence, contact formulations and possible gaps due to the axial movement are avoided in the interface area.

The analysis shows that the variation of the excitation amplitude, the number of load cycles, the load frequency and the foam elasticity modulus do not affect the results significantly. The derived elasticity modulus shows a deviation of approximately five percent with respect to the input value, which is considered sufficient. Inadequate discretization in time or mesh size can be identified not only by an increased deviation from the input value but also by hysteresis development in the force-deflection correlation, whilst material damping is not considered in the FE-model and a hysteresis is not to be expected.

The results of the FEA with a compliantly modelled die show a significant discrepancy to the rigid reference model, see Tab. 5, which is also evident when comparing the contour plots of the deflections in the loading direction in Fig. 8. The thickness of 2 mm for a plate shaped die of PLA material is not sufficient to fulfil the assumption of rigidity and the foam is loaded non-uniformly. The method can therefore be improved by choosing a die material with higher elasticity modulus or a stiffer geometry. Results of subsequent FE-models presented in Tab. 5 show that the compliance of the die in comparison to the foam gets negligible if the Young's modulus reaches values of the order of magnitude of steel or the thickness is increased to 6 mm. Aiming for a lightweight

Tab. 4: FEA simulation parameters.

Time integration	explicit, central diff.
Maximum time step size	$8 \times 10^{-5} \text{ s}$
Excitation amplitude	1 N/mm^2
Deflection amplitude	$\approx 80 \mu\text{m}$
Number of load cycles	10
Mesh factor (MF)	0.5 . . . 10
Maximum element size	$H_{\text{foam}}/(10 \cdot \text{MF})$
Element type	linear hexahedrons

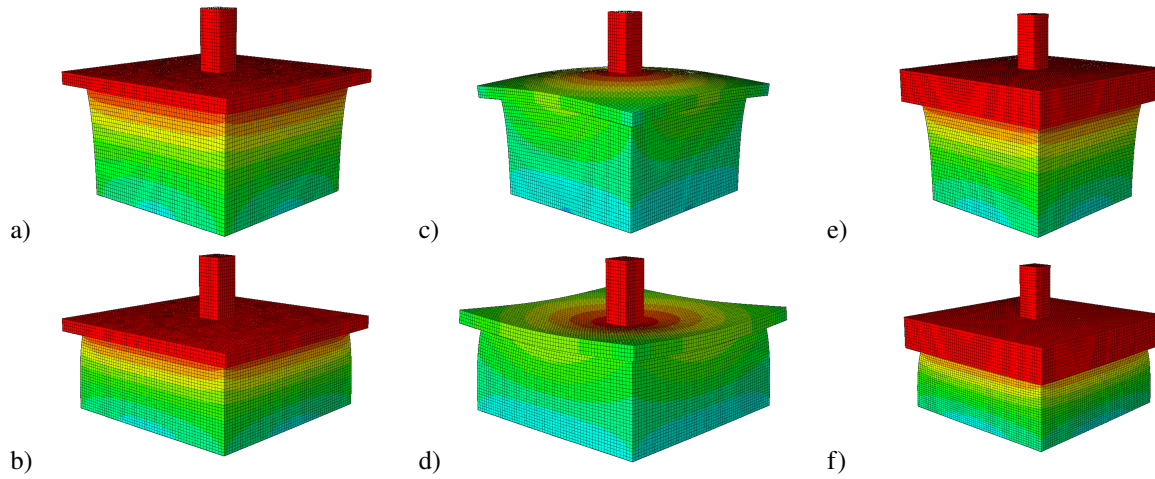


Fig. 8: FEA model deflections for different die properties. a),b) rigid die c),d) 2 mm thick die e),f) 6 mm thick die. Deflections are displayed with a scaling factor of 50.

Tab. 5: FEA results for an exemplary loading frequency of 500 Hz. Foam sample edge lengths are 30 mm. The center of the interfacial area is used for the evaluation.

E_{plate} [kN/m ²]	H_{plate} [mm]	H_{foam} [mm]	diff. to rigid [%]
5×10^6	2	15.75	29.43
50×10^6	2	15.75	7.81
210×10^6	2	15.75	4.79
5×10^6	6	15.75	5.08
5×10^6	2	20.0	25.61
5×10^6	2	30.0	19.31

structure, the increase of the PLA die height is favourable. Increasing the foam height also reduces the deviation, but undesirable lateral slip movements in the test bench are to be expected. In a following iteration, a hollow die with inner supporting structures, Fig. 6 c) is used to test round samples of foams with diameters of 30 mm. It was found that the used threaded connection to the shaker influenced the measurements detrimentally and despite the lower density of the PLA material, the use of aluminium parts result in a better stiffness to weight ratio. The final design consists of an aluminium plate shielding the shaker face and the force sensor mounted between the bearing and an aluminium cup, Fig. 4 d) and Fig. 6 d). The tested seismic mass bearing was not pursued further due to the cumbersome overall setup and adjustment of the initial compression of the foam at rest due to slow decay of the seismic mass swing motions. Under the assumption of a sufficiently stiff setup, the frequency-dependent properties were determined and the influence factors in the experimental process were investigated. The results are presented in the following section.

3 Measurement results

After discarding unsuitable setups and configurations, the preferred procedures were repeated with eight orientations of three foam samples for each foam material. Each facial area of the cylindrical samples is loaded four times while being unmounted and remounted with a 90° rotation along the loading axis between each measurement. This results in a total of 24 measurements for each material from which the standard deviation is calculated. All samples are cylindrical and the loading direction is always coinciding with the cylinder axis which matches the rising direction during manufacturing. The orientation also corresponds to the application direction of the acoustic treatment. The loading amplitude was specified with $\ddot{x} = 10 \mu\text{m}$, which achieves a sufficient signal-to-noise ratio. The results shown below compare the derived parameters with those from the resonance method. An increase in the standard deviation of the gained results is evident for frequencies above 1200 Hz, especially for the bright foam. This may be a consequence of its inhomogeneous structure, which is visible in Fig. 1. Comparing both measurement methods presented, a good agreement at low frequencies near 100 Hz can be found for the imaginary part of the elasticity modulus for both foams, see Fig. 10, and for the real part of the elasticity modulus for the bright foam. In addition, Fig. 10 shows the associated damping loss factor underlining the good agreement of the mean value of both methods for the bright foam. Only the real part of the elasticity modulus of the dark foam shows considerable deviations between both measurement methods, see Fig. 9. This deviation may be caused by a significant dependence of the foam properties on the pre-load and compression rate due to the different top masses used in the resonance method leading to a higher elasticity modulus. This dependency seems to be less distinct for the bright foam. The undesired influence of the pre-load is inherent to the measuring principle of the resonance method whereas pre-compression and compression rate can be adjusted in the harmonic loading method.

Considering both parts of the elasticity modulus, a distinct frequency dependence in the stiffness and damping behaviour is evident from the gained results and needs to be considered in material models for the following numerical simulations. With respect to the gained results at 100 Hz, the real part of the elasticity modulus at 2000 Hz shows an increase by 275% for the bright foam and 62%

for the dark foam, respectively. The imaginary part of the elasticity modulus of the dark foam increases by 380% in the frequency domain ranging from 100 Hz to 2000 Hz. The imaginary part of the elasticity modulus of the bright foam varies between 66 kN/m^2 and 400 kN/m^2 . The outlier for both foams at 700 Hz is linked to a resonance frequency in the test setup which should be resolved in future measurements as proposed in the outlook.

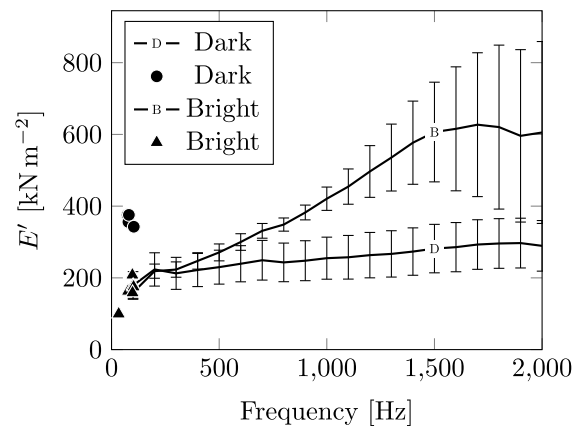


Fig. 9: Measurement results of the real part E' of the elasticity modulus of the bright (B) and dark (D) foam. Markers ● and ▲ represent results of the resonance method.

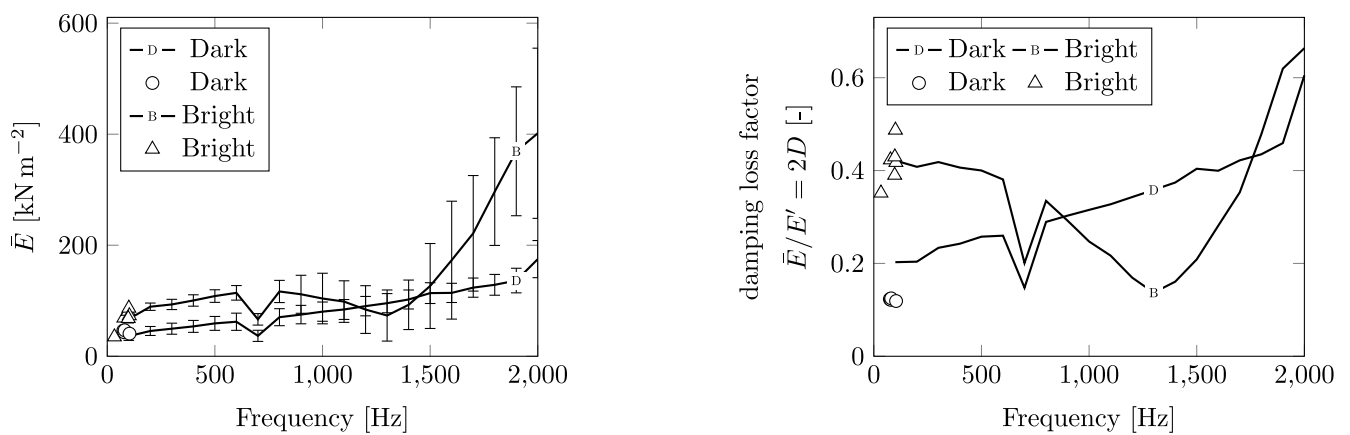


Fig. 10: Measurement results of the imaginary part \bar{E} of the elasticity modulus (left) and the associated damping loss factor (right) of the bright (B) and dark (D) foam. Markers ○ and △ represent results of the resonance method.

3.1 Influence factors on the measurement results

Due to the manual arrangement of the shaker position, slight variations in the alignment of the foam sample in the test setup may occur. For this reason, a study on the influence of misalignments and the loading amplitude was conducted. Starting with the angular misalignment with respect to the loading plane, Fig. 11 a) and b), two additional measurements with noticeable misalignments were carried out. Again, the outlier at 700 Hz is attributable to a resonance frequency in the experimental setup. The data show that the deviation from the mean results is close to the standard deviation, although the misalignment is exaggerated and visible to the eye. A tendency of decreasing values for the real and imaginary part of the elasticity modulus is noticeable. Misalignments during a characterization procedure, which is executed with the necessary diligence, are much smaller than the extreme examples presented here and therefore considered tolerable. Consequently, the robustness of the presented method with regard to angular misalignment is shown.

Additionally, the manual positioning of the shaker relative to the bearing can result in longitudinal variances in the loading direction which can induce an initial compression of the foam. The initial loading must at least be larger than the loading amplitude in order to prevent a lift-off from the bearing or the shaker face-plate. If this requirement is fulfilled, the use of adhesives is unnecessary. Measurements with increasing initial compression of the foam sample were carried out and are presented in Fig. 12. It is evident that the real part as well as the imaginary part of the elasticity modulus decreases in the examined frequency range for both foams when the initial loading is increased. The maximum height reductions considered are 3 mm for the dark and 4.8 mm for the bright foam specimen, respectively. Considering that the initial loading paths are in the range of millimetres and that relative deviations of up to -35% may occur, this error must be reduced to a minimum. In order to achieve this, the shaker is carefully positioned and the initial foam thickness in the test bench is previously measured. It is assumed that only compressions of less than one millimetre occur during the regular measurements. As a result, a deviation of less than 10% is to be expected under the aspired avoidance of this influence. Conversely, the frequency dependence of the elasticity modulus is distinct and the results keep an advantage in comparison to the resonance characterization method, which only uses a few data points in the lower frequency domain.

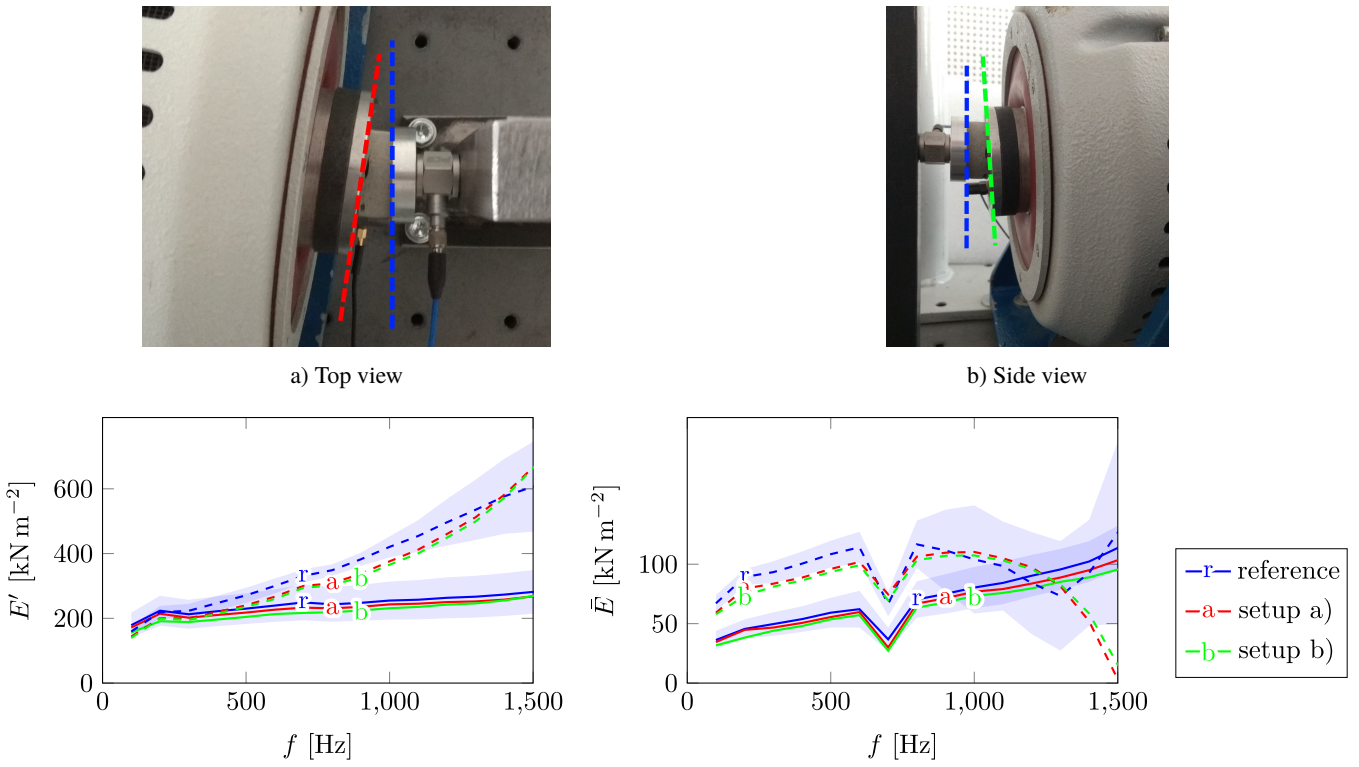


Fig. 11: Measurement with exaggerated misalignment of the foam loading. Solid lines: Dark foam. Dashed lines: Bright foam. The filled area represents the standard deviation from Fig. 9 and Fig. 10.

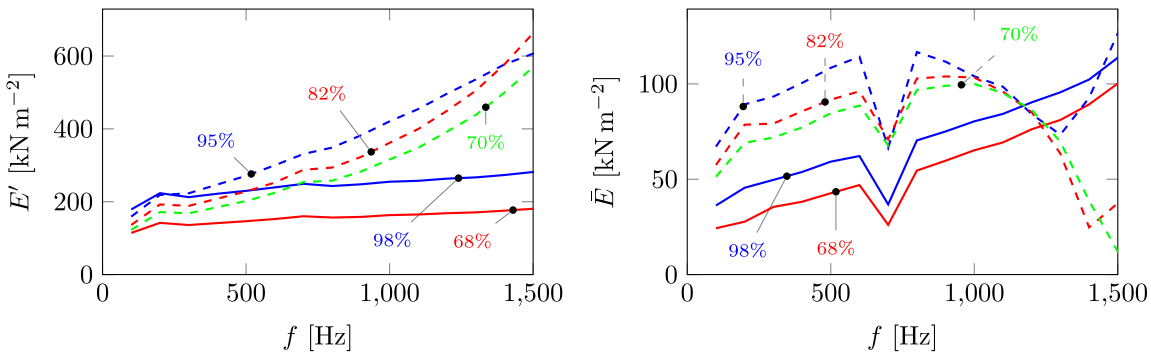


Fig. 12: Measurement with initial compression of the foam. Indicators represent the relative height with respect to the initial height of the foam samples. Solid lines: Dark foam. Dashed lines: Bright foam.

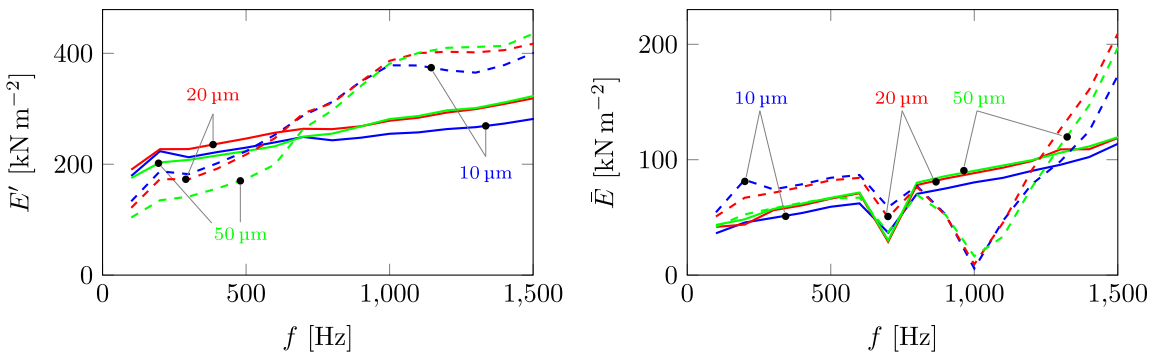


Fig. 13: Measurements with different loading amplitudes. Solid lines: Dark foam. Dashed lines: Bright foam.

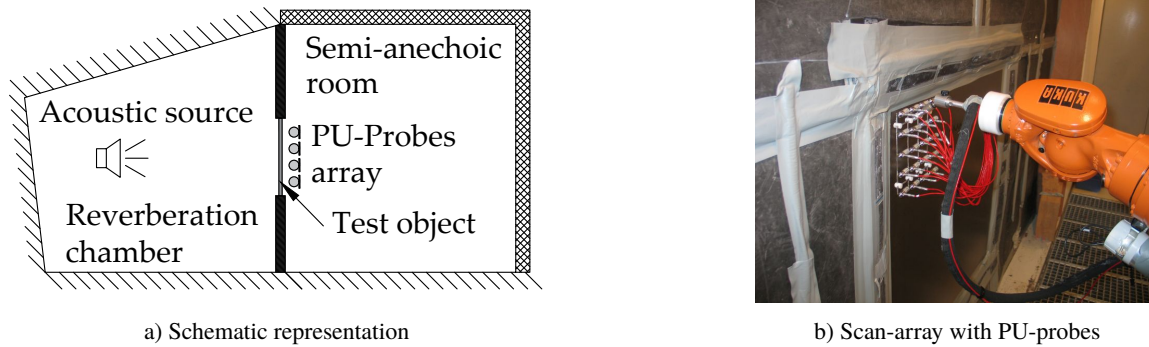


Fig. 14: Window test bench for transmission loss experiments.

As can be seen in Fig. 13, the increase of the loading amplitude from $10\ \mu\text{m}$ to $20\ \mu\text{m}$ and $50\ \mu\text{m}$ has little influence on the resulting elasticity modulus. Amplitudes below $10\ \mu\text{m}$ were found to be not appropriate due to the decreasing signal-to-noise ratio. Because of the limitation in the power output of the shaker, the minimal feasible loading amplitude of $10\ \mu\text{m}$ is chosen in order to maximize the testable frequency range. In order to model the targeted insertion loss characteristics of the foams, the results at different initial compressions and different loading amplitudes may be extrapolated to a compression free state.

4 Application example

4.1 Window test bench as evaluation reference

In order to evaluate the accuracy of the measured frequency-dependent elasticity moduli to describe the material behaviour, several spring-mass systems were measured in a window test bench, see Fig. 14. A spring-mass system is a commonly employed noise control treatment that is formed by a poroelastic layer and a heavy layer. The system is attached to a thin steel plate, Fig. 15. This test bench is formed by two separated rooms, a reverberation chamber and a semi-anechoic room. An opening, also called window, connects the two rooms. Inside the reverberation chamber the combination of an acoustic source with the reflecting walls produces a diffuse pressure field that acts as the excitation. Hence, airborne noise transmission is investigated. In a complementary study on the acoustic behaviour of excited structures by Schrader et al. (2018), structure-borne noise was investigated. It has been determined that a frequency-dependent modelling approach achieved better results compared to constant material parameters but in a summary, no model delivered satisfactory results. This leads to the question whether alternative modelling approaches have to be pursued in order to reproduce structure-borne noise propagation.

In the connecting window the test object is placed. The basis geometry is a 1 m by 1 m steel plate of 0.75 mm thickness on which the different spring-mass systems are attached. The acoustic energy is transmitted through the object into the semi-anechoic room. The absorbing walls in this room allow an acoustic investigation under free field conditions without reflections.

The performance of the different spring-mass systems is determined by the insertion loss (IL). This quantity, commonly used in the evaluation of acoustic treatments, is defined as the difference of the sound power radiated by a bare plate Π_{rad}^{plate} and by the plate with the acoustic treatment Π_{rad}^{NCT} attached, Eq. (19).

$$IL[\text{dB}] = \Pi_{rad}^{plate} [\text{dB}] - \Pi_{rad}^{NCT} [\text{dB}] \quad (19)$$

The measurement of the radiated power was conducted with an array of PU-probes. These probes can simultaneously measure the sound pressure and sound velocity in the near field of the test object. The product of the two quantities is the sound intensity, whose integration over the complete surface results in the sound power. To facilitate the scanning process the array was installed on a robotic arm, as shown in Fig. 14 b).

4.2 Simulation model for material property evaluation

The same configuration found in the window test bench was reproduced in a numerical model, which is displayed in Fig. 15. On the basis steel plate, a diffuse pressure field is applied. This field results as the superposition of plane waves with different incident angles that are randomly determined. The total number of waves required to ensure the diffusivity of the field was previously investigated in detail by Gavila Lloret (2018). In real applications, especially on the edges of the finite plate, there is not a perfectly diffuse field. This behavior is numerically implemented by limiting the maximum incident angle of the waves to 78° (Zeller (2012)). The remaining face of the plate is connected to the poroelastic foam layer and to the heavy layer that assemble the spring-mass system. The system radiates into the receiving fluid. In order to simulate the free radiation conditions this fluid is composed of a finite fluid volume with infinite elements on its outer layer, which is a numerical procedure to extend the domain and avoid unwanted reflections (Gavila Lloret et al. (2020)). Over this surface the total radiated power can be retrieved. The insertion loss is the quantity selected for the evaluation of the results, analogously to the measurement setup.

For the resolution with the finite element method and due to their small thickness, the steel plate and the heavy layer are discretized with solid shell elements of second order. Quadratic hexahedral elements have been employed for the discretization of the foam layer, and linear hexahedral and tetrahedral elements are chosen for the fluid domain.

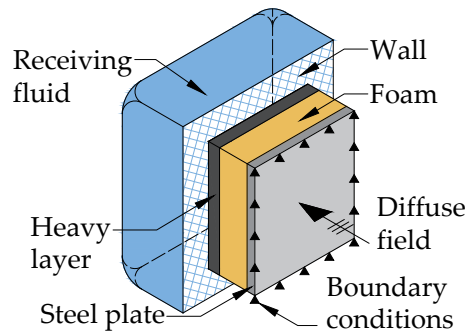


Fig. 15: Sketch of the simulation model.

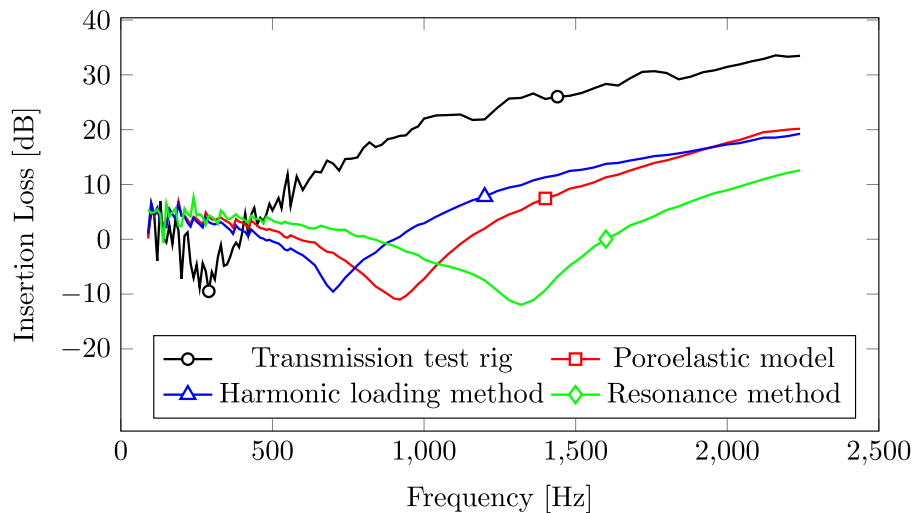


Fig. 16: Comparison of the measured and simulated insertion loss for the dark foam.

Standard values for the material properties have been applied to all components with exception to the foam, for which the properties obtained with the different characterization procedures, namely, the resonance method and the harmonic loading method, are used. It was found that the influence of the imaginary part of the elasticity modulus on the insertion loss is small and the stiffness property provided by the real part of the elasticity modulus is dominant. Regarding the resonance method, constant elasticity moduli of $E = 355.8 \text{ kN/m}^2 + i \cdot 43.25 \text{ kN/m}^2$ for the dark foam and $E = 158.5 \text{ kN/m}^2 + i \cdot 68 \text{ kN/m}^2$ for the bright foam were considered, based on the previous results at the highest attainable frequencies. The frequency-dependent data obtained from the harmonic loading method are indicated in Fig. 9 and Fig. 10.

In addition, the poroelastic model developed by Johnson et al. (1987); Champoux and Allard (1991) is also evaluated as reference. The required input parameters for the poroelastic model were provided by a commercial third party company. In comparison, the presented harmonic loading method for material parameter identification is easier to conduct, which is reflected in less effort in the measurement setup and implementation of the material model.

Regarding the results for the dark foam, Fig. 16, the stiffer material characterization from the resonance measuring method becomes apparent and shows that the results from the harmonic loading method are closer to the measurement results. Overall, none of the issued models meet the minimum insertion loss, which is located near 250 Hz in the experimental data. Regarding the location of the minimum, the results from the harmonic loading method show the smallest deviation. Comparing the slope of the insertion loss after the minimum qualitatively, the harmonic loading method results show the best agreement.

As can be seen from the results for the bright foam, Fig. 17, the resonance method and the harmonic loading method show a minimum in the insertion loss with approximately -2.8 dB at 420 Hz while the experimental results indicate a minimum with -1.4 dB at 240 Hz and the poroelastic model shows -4.7 dB at 480 Hz, respectively. Regarding the slope of the insertion loss, the data from the harmonic loading method shows the best agreement in the frequency range up to 1 kHz. In the frequency range above 1 kHz the slope of the poroelastic model agrees best with the experimental data.

5 Conclusion

In the present study the identification of frequency-dependent viscoelastic material parameters for two foam types was conducted. Two characterization methods with shaker test rigs were presented and their properties have been discussed. The resonance characterization method is limited regarding the evaluable frequency range, whereas the harmonic loading procedure is an economical method that delivers satisfying results for frequencies up to 2 kHz with the presented setup.

It is noted that during measurements the force sensor should be mounted on the bearing side and not on the shaker side. That way it is possible to avoid compensation calculations due to inertial forces. Furthermore, the initial loading of the foam has an influence on the resulting elasticity modulus for the foams under consideration. Therefore, an initial loading should be established in the

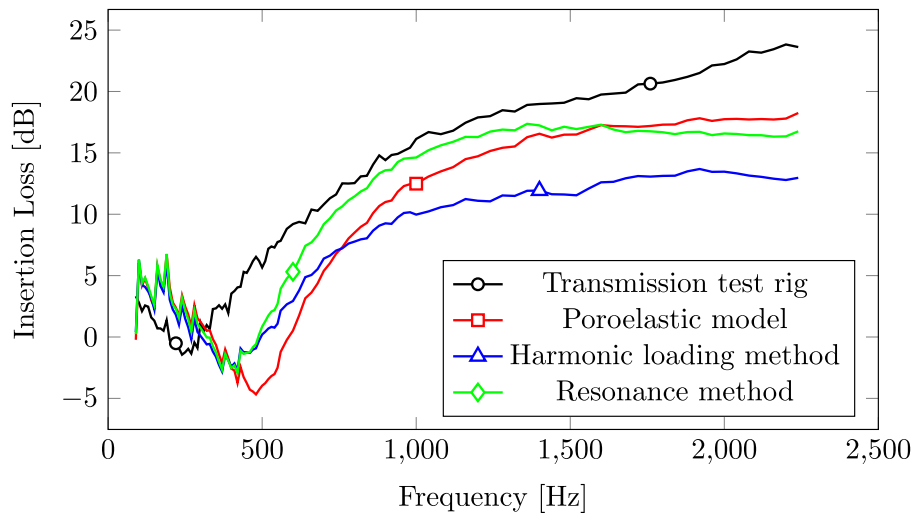


Fig. 17: Comparison of the measured and simulated insertion loss for the bright foam.

measurements which represents the final installation of the damping material.

The gained data was used in order to simulate the insertion loss achieved with the usage of the foams in spring-mass systems for noise control. The air-borne noise transmission was evaluated. From the results, the presented method in its current form is not considered sufficient for detailed insertion loss estimations but the obtained data lies in the range of the reference data, which was derived from a poroelastic simulation model and the associated parameter identification tests. In further studies it is to be considered to extend the method by samples of different shape factors in order to map possible frequency dependency of the Poisson ratio, similar to [Langlois et al. \(2001\)](#). As already mentioned, the method is characterized by less effort and simple implementation. The presented measurement deviations are in line with the statements made by [Bonfiglio et al. \(2018\)](#) regarding limited reproducibility. In order to shift resonance frequencies of the set-up out of the measuring range, the bearing mass is to be increased. Additionally, the implementation of a movable carriage to position the shaker more precisely should be considered.

Acknowledgement

The second author is a member of the joint project “Kompetenzzentrum eMobility - KeM”, which is financially supported by the European Union and the German State of Saxony-Anhalt. This support is gratefully acknowledged.

References

- J. F. Allard and G. Daigle. Propagation of sound in porous media: Modeling sound absorbing materials. *J. Acoust. Soc. Am.*, 95: 2785–2785, 1994. ISSN 0001-4966. doi: [10/cs5gbg](#).
- J. F. Allard, G. Jansens, G. Vermeir, and W. Lauriks. Frame-borne surface waves in air-saturated porous media. *J. Acoust. Soc. Am.*, 111(2):690–696, 2002. doi: [10/bjkdbf](#).
- J. F. Allard, M. Henry, L. Boeckx, P. Leclaire, and W. Lauriks. Acoustical measurement of the shear modulus for thin porous layers. *J. Acoust. Soc. Am.*, 117(4):1737–1743, 2005. doi: [10/b8cpds](#).
- Y. Atalla and R. Panneton. Inverse acoustical characterization of open cell porous media using impedance tube measurements. *Canadian Acoustics*, 33(1):11–24, 2005. ISSN 2291-1391.
- M. A. Biot. Theory of propagation of elastic waves in a fluid-saturated porous solid. i. low-frequency range. *J. Acoust. Soc. Am.*, 28(2):168–178, 1956a. doi: [10/dw58r8](#).
- M. A. Biot. Theory of propagation of elastic waves in a fluid-saturated porous solid. ii. higher frequency range. *J. Acoust. Soc. Am.*, 28(2):179–191, 1956b. doi: [10/dv5c7p](#).
- L. Boeckx, P. Leclaire, P. Khurana, C. Glorieux, W. Lauriks, and J. F. Allard. Investigation of the phase velocities of guided acoustic waves in soft porous layers. *J. Acoust. Soc. Am.*, 117(2):545–554, 2005. doi: [10/dq2ghs](#).
- P. Bonfiglio and F. Pompili. Determination of the dynamic complex modulus of viscoelastic materials using a time domain approach. *Polymer Testing*, 48:89–96, 2015. doi: [10/f744cp](#).
- P. Bonfiglio et al. How reproducible are methods to measure the dynamic viscoelastic properties of poroelastic media? *J. Sound Vib.*, 428:26–43, 2018. doi: [10/c53q](#).
- Y. Champoux and J. F. Allard. Dynamic tortuosity and bulk modulus in air-saturated porous media. *J. Appl. Phys.*, 70:1975–1979, 1991. ISSN 0021-8979. doi: [10/d2fgwv](#).
- J. Cuenca, C. Van der Kelen, and P. Göransson. A general methodology for inverse estimation of the elastic and anelastic properties of anisotropic open-cell porous materials – with application to a melamine foam. *J. Appl. Phys.*, 115(8):084904, 2014. doi: [10/f23f73](#).

- F. Duvigneau and S. Duczek. A numerical study on the potential of acoustic metamaterials. In H. Altenbach, E. Carrera, and G. Kulikov, editors, *Analysis and Modelling of Advanced Structures and Smart Systems*, Advanced Structured Materials, pages 11–34. Springer, 2017. doi: [10/c2tc](#).
- F. Duvigneau, S. Nitzschke, E. Woschke, and U. Gabbert. A holistic approach for the vibration and acoustic analysis of combustion engines including hydrodynamic interactions. *Arch. Appl. Mech.*, 86:1887–1900, 2016. doi: [10/f89p87](#).
- J. D. Ferry. *Viscoelastic Properties of Polymers*. Wiley-Blackwell, 1980. ISBN 0471048941.
- S. Finnveden, N. E. Hörlin, and M. Barbagallo. Dynamic characterization of viscoelastic porous foams used in vehicles based on an inverse finite element method. *J. Acoust. Soc. Am.*, 135(4):1834–1843, 2014. doi: [10/f22t2d](#).
- M. Gavila Lloret. *Prediction of the airborne sound transmission through a car front end model including poroelastic acoustic treatments*. PhD thesis, Otto von Guericke University Magdeburg, 2018.
- Maria Gavila Lloret, Gregor Müller, Fabian Duvigneau, and Ulrich Gabbert. On the numerical modeling of poroelastic layers in spring-mass systems. *Applied Acoustics*, 157:106996, 2020. doi: [10/ggj3zj](#).
- L. Jaouen, A. Renault, and M. Deverge. Elastic and damping characterizations of acoustical porous materials: Available experimental methods and applications to a melamine foam. *Appl. Acoust.*, 69(12):1129–1140, 2008. doi: [10/c57kev](#).
- D. L. Johnson, J. Koplik, and R. Dashen. Theory of dynamic permeability and tortuosity in fluid-saturated porous media. *J. Fluid Mech.*, 176:379, 1987. ISSN 0022-1120. doi: [10/bm7st4](#).
- D. Koblar and M. Boltežar. Evaluation of the frequency-dependent Young’s modulus and damping factor of rubber from experiment and their implementation in a finite-element analysis. *Exp. Tech.*, 40(1):235–244, 2016. doi: [10/f86svc](#).
- R. S. Lakes. *Viscoelastic solids*. CRC press, 1998. ISBN 9780849396588.
- C. Langlois, R. Panneton, and N. Atalla. Polynomial relations for quasi-static mechanical characterization of isotropic poroelastic materials. *J. Acoust. Soc. Am.*, 110(6):3032–3040, 2001. doi: [10/b2wqck](#).
- R. Lerch, G. Sessler, and D. Wolf. *Technische Akustik*. Springer-Verlag Berlin Heidelberg, 2009.
- A. D. Nashif, D. I. Jones, and J. P. Henderson. *Vibration Damping*. John Wiley & Sons, Inc., 1985. ISBN 9780471867722.
- S. R. Pride and J. G. Berryman. Connecting theory to experiment in poroelasticity. *J. Mech. Phys. Solids*, 46(4):719–747, 1998. doi: [10/dqfj2p](#).
- T. Pritz. Frequency dependence of frame dynamic characteristics of mineral and glass wool materials. *J. Sound Vib.*, 106(1): 161–169, 1986. doi: [10/ct5rfr](#).
- T. Pritz. Dynamic Young’s modulus and loss factor of plastic foams for impact sound isolation. *J. Sound Vib.*, 178(3):315–322, 1994. doi: [10/dfbs9n](#).
- A. Renault. *Caractérisation mécanique dynamique de matériaux poro-viscoélastiques (Dynamic mechanical characterization of poro-visco-elastic materials)*. PhD thesis, Université de Sherbrooke, 2008.
- S. Rigobert, F. C. Sgard, and N. Atalla. A two-field hybrid formulation for multilayers involving poroelastic, acoustic, and elastic materials. *J. Acoust. Soc. Am.*, 115(6):2786–2797, 2004. doi: [10/cpgtqz](#).
- Y. Salissou and R. Panneton. Pressure/mass method to measure open porosity of porous solids. *J. Appl. Phys.*, 101:124913, 2007. ISSN 0021-8979. doi: [10/frm5hg](#).
- P. Schrader, F. Duvigneau, M. Gavila Lloret, H. Rottengruber, and U. Gabbert. Finite element analysis of the acoustic behavior of poroelastic materials based on experimentally determined frequency-dependent material properties. In *28th edition of the Biennial ISMA conference on Noise and Vibration Engineering*, Leuven, 2018.
- A. Sfaoui. On the viscoelasticity of the polyurethane foam. *J. Acoust. Soc. Am.*, 97(2):1046–1052, 1995. doi: [10/bspvtm](#).
- C. Van der Kelen, P. Göransson, B. Pluymers, and W. Desmet. On the influence of frequency-dependent elastic properties in vibro-acoustic modelling of porous materials under structural excitation. *J. Sound Vib.*, 333(24):6560–6571, 2014. doi: [10/f22tf6](#).
- P. Zeller. *Handbuch Fahrzeugakustik*, volume 2. Vieweg+Teubner Verlag, Wiesbaden, Springer, 2012.

Longitudinal Fracture Analysis of an Inhomogeneous Stepped Rod with Two Concentric Cracks in Torsion

Victor Rizov^{1*}, and Holm Altenbach²

¹ Department of Technical Mechanics, University of Architecture, Civil Engineering and Geodesy, 1 Chr. Smirnensky blvd., 1046 – Sofia, Bulgaria

² Lehrstuhl für Technische Mechanik, Fakultät für Maschinenbau, Otto-von-Guericke-Universität Magdeburg, Universitätsplatz 2, 39106 Magdeburg, Deutschland

Abstract: Analysis of the longitudinal fracture behaviour of an inhomogeneous stepped rod with two concentric longitudinal cracks is developed. The stepped rod has circular cross-section and exhibits continuous material inhomogeneity in radial direction. The material has non-linear elastic mechanical behaviour. The rod is subjected to torsion. The two cracks present concentric circular cylindrical surfaces. Thus, the fronts of the cracks are circles. The fracture is studied in terms of the strain energy release rate by considering the complementary strain energy stored in the rod. Solutions to the strain energy release rate are derived at different lengths of the two cracks. The balance of the energy is analyzed in order to verify the solutions. It is shown that the solutions can be applied also when the stepped rod is inhomogeneous in both radial and length directions. The solutions are used in order to evaluate the influences of the locations of the two concentric cracks in radial direction and the material inhomogeneity in radial and length directions on the longitudinal fracture behaviour of the stepped rod.

Keywords: longitudinal fracture behaviour, inhomogeneous stepped rod, two concentric longitudinal cracks

1 Introduction

One of the most important features of the load-bearing structural members and components exhibiting continuous (smooth) material inhomogeneity is the fact that the material properties are continuous functions of the coordinates (Tokovyy and Ma, 2008; Tokova et al., 2017; Tokovyy and Ma, 2013, 2016). The inhomogeneous structural materials present a great deal of interest for researchers mainly because certain kinds of inhomogeneous materials such as functionally graded materials have been increasingly used in various branches of practical engineering in the last three decades. Functionally graded materials are inhomogeneous composites manufactured by mixing of two or more constituent materials. Smooth spatial variation of material properties along one or more directions in the solid is obtained by continuously changing the microstructure of functionally graded materials during manufacturing. The fact that the material properties of functionally graded materials can be formed technologically in order to meet different performance requirements in different parts of a structural member is the basic advantage of functionally graded materials over the homogeneous structural materials (Altunsaray and Bayer, 2014; Jha et al., 2013; Knoppers et al., 2003; Mahamood and Akinlabi, 2017; Miyamoto et al., 1999; Nemat-Allal et al., 2011; Uysal and Kremzer, 2017; Uysal, 2016; Uysal and Güven, 2016). Therefore, functionally graded materials are frequently used in aeronautics, nuclear reactors, electronics and biomedicine.

Analysis of fracture behaviour plays a very important role in the design of inhomogeneous (functionally graded) structural members and components (Carpinteri and Pugno, 2006; Erdogan, 1995; Paulino, 2002; Tilbrook et al., 2005; Uysal and Güven, 2016).

Various works on fracture behaviour of linear-elastic composite materials with continuously inhomogeneous (functionally graded) composition have been reviewed in Tilbrook et al. (2005). Analyses of cracks oriented parallel or perpendicular to the direction of the material gradient have been considered. Investigations of failure resistance have also been discussed. Studies of fatigue fracture behaviour of functionally graded composites under cyclic crack loading conditions have been presented too. Different solutions for rectilinear cracks and also for arc cracks and slightly curved cracks in graded materials by applying methods of linear-elastic fracture mechanics have been summarized.

A method for evaluation of the strength of load-bearing functionally graded structures by using linear-elastic fracture mechanics has been developed in Carpinteri and Pugno (2006). Cracks and re-entrant corners have been analyzed. The influences of the varying corner angle and depth on the fracture have been analyzed assuming linear-elastic behaviour of the functionally graded material. It has been shown that the method is useful in engineering applications for predicting the strength of the structural members and components composed by functionally graded materials.

Fundamental problems of linear-elastic fracture mechanics of continuously inhomogeneous (functionally graded) materials and structures have been summarized and discussed in Erdogan (1995). The debonding of functionally graded coatings has been studied. Different aspects of surface fracture behaviour of functionally graded materials have been investigated and discussed in details.

It should be mentioned that certain kinds of inhomogeneous materials such as functionally graded materials can be built-up layer by layer (Mahamood and Akinlabi, 2017) which is a premise for appearance of longitudinal cracks between layers. Thus, longitudinal

* E-mail address: V_RIZOV_FHE@UACG.BG

fracture of inhomogeneous beam structures has been analyzed in a series of publications recently (Rizov, 2017; Rizov, 2018; Rizov, 2018).

In contrast to Rizov (2018) where an inhomogeneous circular shaft of a constant cross-section with one longitudinal crack under torsion is analyzed, the present paper deals with analysis of an inhomogeneous stepped rod of a circular cross-section with two concentric longitudinal cracks loaded in torsion. The stepped rod has non-linear elastic behaviour. It should be noted that the paper is motivated also by the fact that stepped rods loaded in torsion are widely used as components of various structures and mechanisms. Therefore, fracture analysis of stepped rods is an important research topic. In the present paper, the fracture is analyzed in terms of the strain energy release rate. Solutions to the strain energy release rate are derived by considering the complementary strain energy. The solutions are verified by analyzing the balance of the energy. The solutions are applied to evaluate the influence of the locations of the two cracks in radial direction and the material inhomogeneity on the longitudinal fracture behaviour of the stepped rod.

2 Calculation of the strain energy release rate

2.1 Calculation of the strain energy release rate by using the complementary strain energy

An inhomogeneous stepped rod with two longitudinal concentric cracks is shown in Fig. 1. In portions, PQ , QA and AD , the rod has circular cross-sections of radiuses R_1 , R_2 and R_3 , respectively. The lengths of rod portions PQ , QA and AD , are l_1 , l_2 and $l - (l_1 + l_2)$, respectively. The rod is clamped in section, D . The internal and external cracks are circular cylindrical surfaces of radiuses R_1 and R_2 , respectively (Fig. 1). Thus, the fronts of the internal and external cracks are circles of radiuses R_1 and R_2 , respectively. The lengths of the internal and external cracks are a_1 and a_2 , respectively. In portion, QA , the rod is divided by the internal crack in internal and external part. The internal part is treated in the analysis as a rod of circular cross-section of radius R_1 . The external part is treated as a ring-shaped rod of internal and external radiuses R_1 and R_2 . In portion AB the rod is divided by the two cracks in three parts: internal, interstitial and external part. The internal part is treated in the analysis as a rod of circular cross-section of radius R_1 . The interstitial part is treated as a ring-shaped rod of internal and external radiuses R_1 and R_2 , respectively. The external part is treated as ring-shaped rod of internal and external radiuses R_2 and R_3 , in portion AC . In the portion BC the rod is divided by the external crack in two parts: internal and external part. The internal part is treated as a rod of circular cross-section of radius R_2 and length $a_2 - a_1$. The rod is loaded in torsion by three torsion moments T_1 , T_2 and T_3 applied, respectively, in cross-sections P , Q and A , as shown in Fig. 1. The rod exhibits continuous (smooth) material inhomogeneity in radial direction. The material has non-linear elastic behaviour.

The longitudinal fracture is analyzed in terms of the strain energy release rate. For this purpose, first, an elementary increase da_1 of the length of the internal crack is assumed and the strain energy release rate G_{a_1} is expressed as (Rizov, 2018)

$$G_{a_1} = \frac{dU^*}{l_{cf1} da_1} \tag{1}$$

where U^* is the complementary strain energy stored in the beam and l_{cf1} is the length of the front of the internal crack. Since

$$l_{cf1} = 2\pi R_1, \tag{2}$$

Eq. (1) is re-written as

$$G_{a_1} = \frac{dU^*}{2\pi R_1 da_1}. \tag{3}$$

The complementary strain energy is obtained as

$$U^* = U_{IN1}^* + U_{IS1}^* + U_{EX}^* + U_{IN2}^* + U_{CD}^*, \tag{4}$$

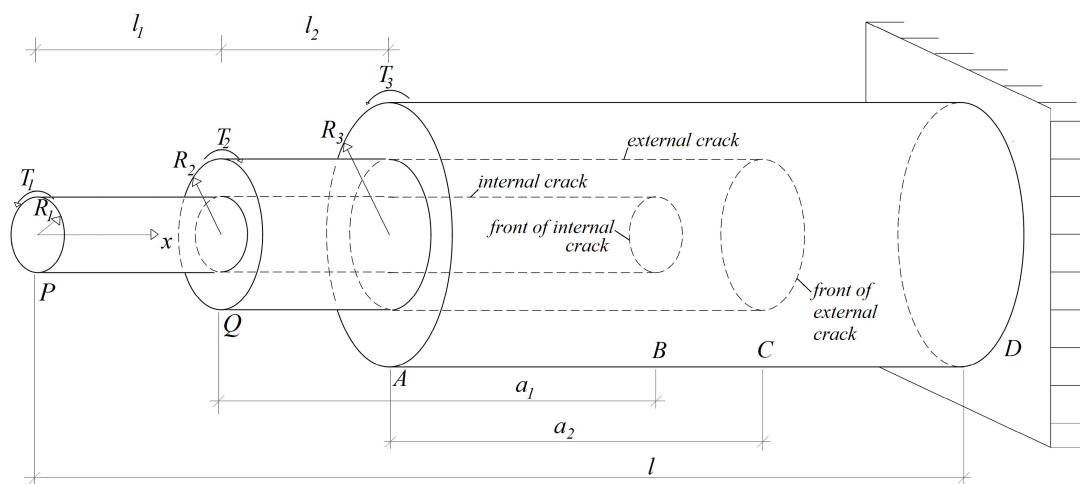


Fig. 1: Geometry and loading of an inhomogeneous stepped rod with two concentric longitudinal cracks

where U_{IN1}^* the complementary strain energy in the rod portion PQ and in the internal parts of portions QA and AB of the rod, U_{IS1}^* is the complementary strain energy in the external part of the rod portion QA and in the interstitial part of the portion AB of the rod, U_{EX}^* is the complementary strain energy in the external part of portion AC of the rod, U_{IN2}^* is the complementary strain energy in the internal part of portion BC of the rod, U_{CD}^* is the complementary strain energy in the un-cracked portion CD of the rod. The complementary strain energy in the rod portion PQ and in the internal parts of portions QA and AB of the rod is expressed as

$$U_{IN1}^* = \int_0^{l_1+a_1} \int_0^{R_1} \int_0^{2\pi} u_{0IN1}^* R dx dR d\varphi, \tag{5}$$

where u_{0IN1}^* is the complementary strain energy density, R and φ are the polar coordinates, x is the longitudinal centroidal axis of the rod. The complementary strain energy density is calculated by using the following formula (Rizov, 2018):

$$u_{0IN1}^* = \tau\gamma - u_{0IN1}, \tag{6}$$

where τ is the shear stress, γ is the shear strain, u_{0IN1} is the strain energy density. In principle, the strain energy density is equal to the area enclosed by the stress-strain diagram. Thus, u_{0IN1} is expressed as

$$u_{0IN1} = \int_0^\gamma \gamma\tau(\gamma) d\gamma. \tag{7}$$

In the present paper, the mechanical behaviour of the material is treated by applying the following non-linear stress-strain relation (Lukash, 1998):

$$\tau = \frac{G\gamma}{\sqrt{1+\gamma^2}}, \tag{8}$$

where G is the shear modulus. By substituting of (8) in (7), one obtains

$$u_{0IN1} = G \left(\sqrt{1+\gamma^2} - 1 \right). \tag{9}$$

The complementary strain energy density is found by substituting of (8) and (9) in (6)

$$u_{0IN1}^* = G \left(1 - \frac{1}{\sqrt{1+\gamma^2}} \right). \tag{10}$$

The rod exhibits continuous material inhomogeneity in radial direction. Thus, the distribution of G in radial direction is treated by using an exponential law

$$G = G_0 e^{p \frac{R}{R_3}}, \tag{11}$$

where

$$0 \leq R \leq R_3. \tag{12}$$

In (11) G_0 is the value of G in the centre of the cross-section of the rod, p is a material property that controls the material inhomogeneity in radial direction.

The distribution of the shear strain in radial direction is treated by applying the Bernoulli's hypothesis for plane sections since rods of a high length to diameter ratio are under consideration in the present paper. Thus, the distribution of γ in the cross-section of the rod portion PQ and in the internal parts of portions QA and AB of the rod is written as

$$\gamma = \gamma_m \frac{R}{R_1}, \tag{13}$$

where

$$0 \leq R \leq R_1. \tag{14}$$

In (13) γ_m is the shear strain at the periphery of the rod portion PQ and at the periphery of the internal parts of portions QA and AB of the rod. The following equation for equilibrium of the elementary forces in the cross-section is used to determine γ_m :

$$T_1 = \int_0^{R_1} \int_0^{2\pi} \tau R^2 dR d\varphi \tag{15}$$

After substituting of (8), (11) and (13) in (15), the equation for equilibrium is solved with respect to γ_m by using the MatLab computer program.

The complementary strain energy in the external part of the rod portion QA and in the interstitial part of portion AB of the rod (Fig. 1)

$$U_{IS1}^* = \int_0^{l_1+a_1} \int_0^{R_1} \int_0^{2\pi} u_{0IS1}^* R dx dR d\varphi, \quad (16)$$

where u_{0IS1}^* is the complementary strain energy density. Equation (10) is applied to derive u_{0IS1}^* . For this purpose, γ is replaced with γ_{IN1} . The distribution of shear strain γ_{IN1} is expressed as

$$\gamma_{IN1} = \gamma_{mIN1} \frac{R}{R_2}, \quad (17)$$

where

$$R_1 \leq R \leq R_2. \quad (18)$$

In (10) γ_{mIN1} is the shear strain at the periphery of the rod portion QA and at the periphery of the interstitial part of portion AB of the rod. The following equation for equilibrium is used to derive γ_{mIN1} (Fig. 1):

$$T_2 = \int_{R_1}^{R_2} \int_0^{2\pi} \tau_{IN1} R^2 dR d\varphi, \quad (19)$$

where the distribution of the shear strain τ_{IN1} is found by replacing of γ with γ_{IN1} in Eq. (8). After substituting of τ_{IN1} in (19), the equation for equilibrium is solved with respect to τ_{mIN1} by the MatLab computer program.

The complementary strain energy U_{EX}^* in the external part of portion AC of the rod is expressed as (Fig. 1)

$$U_{EX}^* = \int_{l_1+l_2}^{l_1+l_2+a_2} \int_{R_2}^{R_3} \int_0^{2\pi} u_{0EX}^* R dx dR d\varphi, \quad (20)$$

(20) where the complementary strain energy density u_{0EX}^* is determined by replacing of γ with γ_{EX} in Eq. (10). The distribution of the shear strain γ_{EX} in the cross-section of the external part of the rod in portion AC is written as

$$\gamma_{EX} = \gamma_{mEX} \frac{R}{R_3}, \quad (21)$$

where

$$R_2 \leq R \leq R_3. \quad (22)$$

The shear strain γ_{mEX} at the periphery of the rod is found by using the following equation for equilibrium (Fig. 1):

$$T_3 = \int_{R_2}^{R_3} \int_0^{2\pi} \tau_{EX} R^2 dR d\varphi, \quad (23)$$

where the distribution of the shear stresses τ_{EX} is obtained by replacing of γ with γ_{EX} in (8). After substituting τ_{EX} in (23), the equation for equilibrium is solved with respect to γ_{EX} by using the MatLab computer program.

The complementary strain energy U_{IN2}^* in the internal part of portion BC of the rod is expressed as (Fig. 1)

$$U_{IN2}^* = \int_{l_1+a_1}^{l_1+l_2+a_2} \int_0^{R_2} \int_0^{2\pi} u_{0IN2}^* R dx dR d\varphi, \quad (24)$$

where the complementary strain energy density u_{0IN2}^* is determined by Eq. (10). For this purpose, γ is replaced with γ_{IN2} . The distribution of the shear strain γ_{IN2} is written as

$$\gamma_{IN2} = \gamma_{mIN2} \frac{R}{R_2}, \quad (25)$$

where

$$0 \leq R \leq R_2. \quad (26)$$

The equation for equilibrium that is used to determine the shear strain γ_{mIN2} at the periphery of the internal part of the rod in portion BC is expressed as

$$T_{IN2} = \int_0^{R_2} \int_0^{2\pi} \tau_{IN2} R^2 dR d\varphi, \tag{27}$$

where T_{IN2} and τ_{IN2} are, respectively, the torsion moment and the shear stresses in the internal portion of the rod. By using Fig. 1, the torsion moment is found as

$$T_{IN2} = T_2 - T_1. \tag{28}$$

The shear stresses τ_{IN2} are found by replacing of γ with γ_{IN2} in Eq. (8). After substituting of τ_{IN2} and (28) in (27)), the equation for equilibrium is solved with respect to γ_{mIN2} by using the MatLab computer program.

The complementary strain energy U_{CD}^* in the un-cracked portion CD of the rod is expressed as (Fig. 1)

$$U_{CD}^* = \int_{l_1+l_2+a_2}^l \int_0^{R_3} \int_0^{2\pi} u_{0CD}^* R dx dR d\varphi, \tag{29}$$

where the complementary strain energy density u_{0CD}^* is determined by applying Eq. (10). For this purpose γ is replaced with γ_{CD} . The distribution of the shear strains γ_{CD} is obtained as

$$\gamma_{CD} = \gamma_{mCD} \frac{R}{R_3}, \tag{30}$$

where

$$0 \leq R \leq R_3. \tag{31}$$

In (30) γ_{mCD} is the shear strain at the periphery of the rod in portion CD . The following equation for equilibrium is used to determine γ_{mCD} :

$$T_{CD} = \int_0^{R_3} \int_0^{2\pi} \tau_{CD} R^2 dR d\varphi, \tag{32}$$

where T_{CD} and τ_{CD} are, respectively, the torsion moment and the shear stresses in the un-cracked portion of the rod. The torsion moment is obtained as (Fig. 1)

$$T_{CD} = T_1 + T_3 - T_2. \tag{33}$$

The shear stresses τ_{CD} are obtained by replacing of γ with γ_{CD} in (7). After substituting of τ_{CD} and (33) in (32), the equation for equilibrium is solved with respect to γ_{mCD} by using the MatLab computer program.

The following expression for the strain energy release rate is obtained by substituting of (4), (5), (16), (20), (24), (29) in (3):

$$G_{a_1} = \frac{1}{2\pi R_1} \left(\int_0^{R_1} \int_0^{2\pi} u_{0IN1}^* R dR d\varphi + \int_{R_1}^{R_2} \int_0^{2\pi} u_{0IS1}^* R dR d\varphi - \int_0^{R_2} \int_0^{2\pi} u_{0IN2}^* R dR d\varphi \right). \tag{34}$$

The integration in (34) is carried-out by the MatLab computer program.

The strain energy release rate is derived also assuming an elementary increase da_2 of the length of the external crack (Fig. 1). For this purpose, Eq. (3) is re-written as

$$G_{a_2} = \frac{dU^*}{2\pi R_2 da_2}. \tag{35}$$

In (35) it is taken into account that the length of the front of the external crack is $2\pi R_2$ (Fig. 1). By substituting of (4), (5), (16), (20), (24), (29) in (35), one derives

$$G_{a_2} = \frac{1}{2\pi R_2} \left(\int_{R_2}^{R_3} \int_0^{2\pi} u_{0EX}^* R dR d\varphi + \int_0^{R_2} \int_0^{2\pi} u_{0IN2}^* R dR d\varphi - \int_0^{R_3} \int_0^{2\pi} u_{0CD}^* R dR d\varphi \right). \tag{36}$$

The integration in (36) is performed by the MatLab computer program.

The longitudinal fracture behaviour of the inhomogeneous stepped rod is analyzed also for the case when the external crack is shorter than the internal one (Fig. 2). In portion AB the rod is divided by the two cracks in internal, interstitial and external parts.

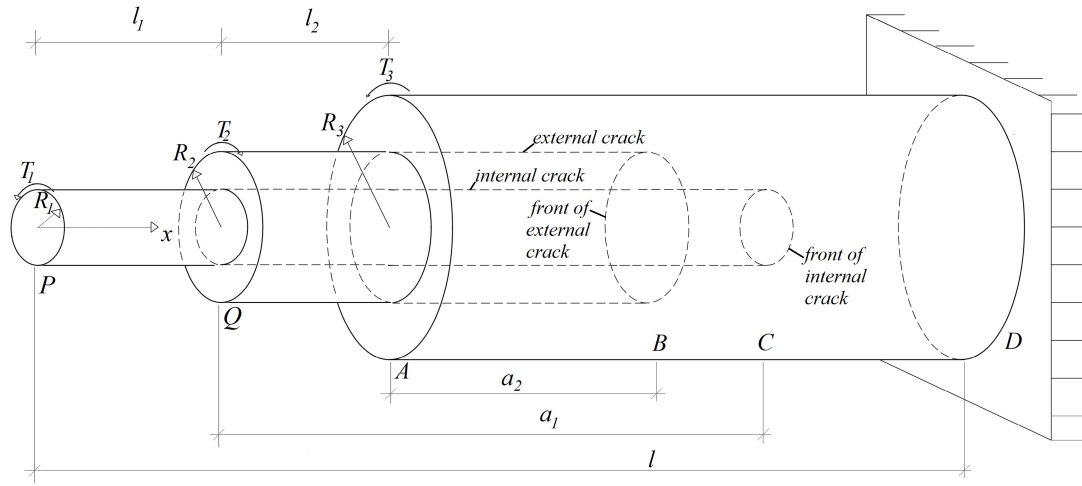


Fig. 2: Inhomogeneous stepped rod configuration in which the external crack is shorter than the internal one

The internal crack divides the portion BC of the rod in internal and external parts. Thus, the complementary strain energy in the rod is expressed as

$$U^* = U_{IN1}^* + U_{IS1}^* + U_{EX1}^* + U_{EX2}^* + U_{CD}^* \tag{37}$$

where U_{IN1}^* is the complementary strain energy in the rod portion PQ and in the internal parts of portions QA and AC of the rod, U_{IS1}^* is the complementary strain energy in the external part of the rod portion QA and in the interstitial part of the portion AB of the rod, U_{EX1}^* is the complementary strain energy in the external part of portion AB of the rod, U_{EX2}^* is the complementary strain energy in the external part of portion BC of the rod, U_{CD}^* is the complementary strain energy in the un-cracked portion CD of the rod.

The complementary strain energy U_{IN1}^* is found by Eq. (5). The complementary strain energy U_{IS1}^* is expressed by Eq. (5). For this purpose a_1 is replaced with a_2 . The complementary strain energy U_{EX1}^* is obtained by Eq. (20).

The complementary strain energy U_{EX2}^* in the external part of portion BC of the rod is written as

$$U_{EX2}^* = \int_{l_1+l_2+a_2}^{l_1+a_1} \int_{R_1}^{R_3} \int_0^{2\pi} u_{0EX2f}^* R d\varphi R dx \tag{38}$$

Equation (10) is applied to obtain the complementary strain energy density u_{0EX2f}^* . For this purpose γ is replaced with γ_{EX2f} . The distribution of the shear strains γ_{EX2f} is written as

$$\gamma_{EX2f} = \gamma_{mEX2f} \frac{R}{R_3} \tag{39}$$

where

$$R_1 \leq R \leq R_3 \tag{40}$$

The shear strain γ_{mEX2f} at the periphery of the rod in portion BC is found from the following equation for equilibrium:

$$T_{EX2f} = \int_{R_1}^{R_3} \int_0^{2\pi} \tau_{EX2f} R^2 dR d\varphi \tag{41}$$

where the torsion moment T_{EX2f} is written as (Fig. 2)

$$T_{EX2f} = T_3 - T_2 \tag{42}$$

The shear stresses τ_{EX2f} are obtained by replacing of γ with γ_{EX2f} in (8). After substituting of τ_{EX2f} and (42) in (41), the equation for equilibrium is solved with respect to γ_{mEX2f} by the MatLab computer program.

Equation (29) is used to derive the complementary strain energy U_{CD}^* in the un-cracked portion CD of the rod. For this purpose a_2 is replaced with a_1 .

By substituting of U_{IN1}^* , U_{IS1}^* , U_{EX1}^* , U_{CD}^* , (37) and (38) in (3), one obtains

$$G_{a_1} = \frac{1}{2\pi R_1} \left(\int_0^{R_1} \int_0^{2\pi} u_{0IN1}^* R dR d\varphi + \int_{R_1}^{R_3} \int_0^{2\pi} u_{0EX2f}^* R dR d\varphi - \int_{R_1}^{R_3} \int_0^{2\pi} u_{0EX2f}^* R dR d\varphi \right) \tag{43}$$

The integration in (34) is carried-out by using the MatLab computer program.

The strain energy release rate is obtained also assuming an elementary increase da_2 of the external crack in the rod shown in Fig. 2.

By substituting of $U_{IN1}^*, U_{IS1}^*, U_{EX1}^*, U_{CD}^*$, (37) and (38) in (35), one derives

$$G_{a_2} = \frac{1}{2\pi R_2} \left(\int_{R_1}^{R_2} \int_0^{2\pi} u_{0IS1}^* R dR d\varphi + \int_{R_2}^{R_3} \int_0^{2\pi} u_{0EX}^* R dR d\varphi - \int_{R_1}^{R_3} \int_0^{2\pi} u_{0EX2f}^* R dR d\varphi \right). \tag{44}$$

The MatLab computer program is used to perform the integration in (4).

2.2 Calculation of the strain energy release rate by considering the energy balance

For verification, the strain energy release rates are derived also by considering the balance of the energy. First, the stepped rod shown in Fig. 1 is analyzed. By assuming a small increase δa_1 of the length of the internal crack, the balance of the energy is written as

$$T_1 \delta\psi_1 + T_2 \delta\psi_2 + T_3 \delta\psi_3 = \frac{\partial U}{\partial a_1} \delta a_1 + G_{a_1} l_{cf1} \delta a_1, \tag{45}$$

where ψ_1, ψ_2 and ψ_3 are, respectively, the angles of twist of the cross-sections P, Q and A of the rod, U is the strain energy stored in the rod. By combining of (2) and (45), one derives

$$G_{a_1} = \frac{T_1}{2\pi R_1} \frac{\partial\psi_1}{\partial a_1} + \frac{T_2}{2\pi R_1} \frac{\partial\psi_2}{\partial a_1} + \frac{T_3}{2\pi R_1} \frac{\partial\psi_3}{\partial a_1} - \frac{1}{2\pi R_1} \frac{\partial U}{\partial a_1}. \tag{46}$$

The angles of twist ψ_1, ψ_2 and ψ_3 are obtained by the integrals of Maxwell-Mohr. The result is

$$\begin{aligned} \psi_1 &= \frac{\gamma_m}{R_1} (l_1 + a_1) + \frac{\gamma_{mIN2}}{R_2} (a_2 - a_1 + l_2) + \frac{\gamma_{mCD}}{R_3} (l - a_2 - l_1 - l_2), \\ \psi_2 &= \frac{\gamma_{mIN1}}{R_2} a_1 + \frac{\gamma_{mIN2}}{R_2} (a_2 - a_1 + l_2) + \frac{\gamma_{mCD}}{R_3} (l - a_2 - l_1 - l_2), \\ \psi_3 &= \frac{\gamma_{mEX}}{R_3} a_2 + \frac{\gamma_{mCD}}{R_3} (l - a_2 - l_1 - l_2). \end{aligned} \tag{47}$$

The strain energy in the rod is written as

$$U = U_{IN1} + U_{IS1} + U_{EX} + U_{IN2} + U_{CD}, \tag{48}$$

where U_{IN1} the complementary strain energy in the rod portion PQ and in the internal parts of portions QA and AB of the rod, U_{IS1} is the complementary strain energy in the external part of the rod portion QA and in the interstitial part of the portion AB of the rod, U_{EX} is the complementary strain energy in the external part of portion AC of the rod, U_{IN2} is the complementary strain energy in the internal part of portion BC of the rod, U_{CD} is the complementary strain energy in the un-cracked portion CD of the rod.

Equation (5) is used to determine U_{IN1} . For this purpose u_{0IN1}^* is replaced with u_{0IN1} . The strain energy U_{IS1} is obtained by replacing of u_{0IS1}^* with u_{0IS1} in Eq. (16). The strain energy density is found by (9). For this purpose γ is replaced with γ_{IN1} . Equation (20) is applied to obtain U_{EX} . For this purpose u_{0EX}^* is replaced with u_{0EX} , where u_{0EX} is found by replacing of γ with γ_{EX} in (9). The strain energy U_{IN2} is found by replacing of u_{0IN2}^* with u_{0IN2} in (24). The strain energy density u_{0IN2} is obtained by replacing of γ with γ_{IN2} in (9). Equation (29) is used to determine U_{CD} by replacing of u_{0CD}^* with u_{0CD} . Equation (9) is applied to obtain the strain energy density u_{0CD} . For this purpose γ is replaced with γ_{CD} .

By substituting of $U_{IN1}, U_{IS1}, U_{EX}, U_{IN2}, U_{CD}$, (47) and (48) in (46), one derives

$$\begin{aligned} G_{a_1} &= \frac{T_1}{2\pi R_1} \left(\frac{\gamma_m}{R_1} - \frac{\gamma_{mIN2}}{R_2} \right) + \frac{T_2}{2\pi R_1} \left(\frac{\gamma_{mIN1}}{R_2} - \frac{\gamma_{mIN2}}{R_2} \right) \\ &- \frac{1}{2\pi R_1} \left(\int_0^{R_1} \int_0^{2\pi} u_{0IN1} R dR d\varphi + \int_{R_1}^{R_2} \int_0^{2\pi} u_{0IS1} R dR d\varphi - \int_0^{R_2} \int_0^{2\pi} u_{0IN2} R dR d\varphi \right) \end{aligned} \tag{49}$$

The integration in (49) is carried-out by the MatLab computer program. The fact that the strain energy release rate obtained by (49) matches exactly that found by (34) is a verification of analysis carried-out assuming increase of the internal crack in the rod shown in Fig. 1.

The strain energy release rate is obtained also assuming a small increase δa_2 of the length of the external crack in the rod shown in Fig. 1. For this purpose, (46) is re-written as

$$G_{a_2} = \frac{T_1}{2\pi R_2} \frac{\partial\psi_1}{\partial a_2} + \frac{T_2}{2\pi R_2} \frac{\partial\psi_2}{\partial a_2} + \frac{T_3}{2\pi R_2} \frac{\partial\psi_3}{\partial a_2} - \frac{1}{2\pi R_2} \frac{\partial U}{\partial a_2}. \tag{50}$$

By substituting of $U_{IN1}, U_{IS1}, U_{EX}, U_{IN2}, U_{CD}$, (47) and (48) in (50), one obtains

$$G_{a_2} = \frac{T_1}{2\pi R_2} \left(\frac{\gamma_{mIN}}{R_1} - \frac{\gamma_{mCD}}{R_3} \right) + \frac{T_2}{2\pi R_2} \left(\frac{\gamma_{mIN2}}{R_2} - \frac{\gamma_{mCD}}{R_3} \right) - \frac{1}{2\pi R_2} \left(\int_{R_2}^{R_3} \int_0^{2\pi} u_{0EX} R dR d\varphi + \int_0^{R_2} \int_0^{2\pi} u_{0IN2} R dR d\varphi - \int_0^{R_3} \int_0^{2\pi} u_{0CD} R dR d\varphi \right) \quad (51)$$

The MatLab computer program is used to carry-out the integration in (51). The strain energy release rate obtained by (51) is exact of that found by (36). This fact is a verification of analysis carried-out assuming increase of the external crack in the rod shown in Fig. 1.

The solutions to the strain energy release rate for the case when the external crack is shorter than the internal one are also verified. For this purpose, the strain energy in the rod shown in Fig. 2 is written as

$$U = U_{IN1} + U_{IS1} + U_{EX1} + U_{EX2} + U_{CD}, \quad (52)$$

where U_{IN1} is the complementary strain energy in the rod portion PQ and in the internal parts of portions QA and AC of the rod, U_{IS1} is the complementary strain energy in the external part of the rod portion QA and in the interstitial part of the portion AB of the rod, U_{EX1} is the complementary strain energy in the external part of portion AB of the rod, U_{EX2} is the complementary strain energy in the external part of portion BC of the rod, U_{CD} is the complementary strain energy in the un-cracked portion CD of the rod.

The strain energy U_{IN1} is obtained by replacing of u_{0IN1}^* with u_{0IN1} in (5). The strain energy U_{IS1} is found by replacing of a_1 and u_{0IS1}^* with a_2 and u_{0IS1} in Eq. (16). The strain energy U_{EX1} is obtained by replacing of u_{0EX}^* with u_{0EX} in Eq. (20). The strain energy U_{EX2} in the external part of portion BC of the rod is found by replacing of u_{0EX2f}^* with u_{0EX2f} in (38). The strain energy density u_{0EX2f} is obtained by replacing of γ with γ_{EX2f} in (9). Equation (29) is applied to derive the strain energy U_{CD} in the un-cracked portion CD of the rod. For this purpose a_2 and u_{0CD}^* are replaced with a_1 and u_{0CD} , respectively.

By using the integrals of Maxwell-Mohr, the angles of twist of the free ends of the internal, interstitial and external parts of the rod are written as (Fig. 2)

$$\begin{aligned} \psi_1 &= \frac{\gamma_m}{R_1} (l_1 + a_1) + \frac{\gamma_{mCD}}{R_3} (l - a_1 - l_1), \\ \psi_2 &= \frac{\gamma_{mIN1}}{R_2} (l_2 + a_2) + \frac{\gamma_{mEX2f}}{R_3} (a_1 - a_2 - l_2) + \frac{\gamma_{mCD}}{R_3} (l - a_1 - l_1), \\ \psi_3 &= \frac{\gamma_{mEX}}{R_3} a_2 + \frac{\gamma_{mEX2f}}{R_3} (a_1 - a_2 - l_2) + \frac{\gamma_{mCD}}{R_3} (l - a_1 - l_1). \end{aligned} \quad (53)$$

First, a small increase δa_1 of the length of the internal crack is assumed (Fig. 2). Thus, by substituting of $U_{IN1}, U_{IS1}, U_{EX1}, U_{EX2}, U_{CD}$, (52), (53) in (46), one arrives at

$$G_{a_1} = \frac{T_1}{2\pi R_1} \left(\frac{\gamma_m}{R_1} - \frac{\gamma_{mCD}}{R_3} \right) + \frac{T_2}{2\pi R_1} \left(\frac{\gamma_{mEX2f}}{R_3} - \frac{\gamma_{mCD}}{R_3} \right) - \frac{1}{2\pi R_1} \left(\int_0^{R_1} \int_0^{2\pi} u_{0IN1} R dR d\varphi + \int_{R_1}^{R_3} \int_0^{2\pi} u_{0EX2} R dR d\varphi - \int_0^{R_1} \int_0^{2\pi} u_{0CD} R dR d\varphi \right) \quad (54)$$

The integration in (54) is carried-out by the MatLab computer program. It should be noted that the strain energy release rate obtained by (54) is exact match of that found by (43).

The strain energy release rate for the rod shown in Fig. 2 is derived also assuming a small increase δa_2 of the length of the external crack. By substituting of $U_{IN1}, U_{IS1}, U_{EX1}, U_{EX2}, U_{CD}$, (52) and (53) in (50), one obtains

$$G_{a_2} = \frac{T_2}{2\pi R_2} \left(\frac{\gamma_{mIN1}}{R_2} - \frac{\gamma_{mEX2f}}{R_3} \right) + \frac{T_3}{2\pi R_2} \left(\frac{\gamma_{mEX}}{R_3} - \frac{\gamma_{mEX2f}}{R_3} \right) - \frac{1}{2\pi R_2} \left(\int_{R_1}^{R_2} \int_0^{2\pi} u_{0IS1} R dR d\varphi + \int_{R_2}^{R_3} \int_0^{2\pi} u_{0EX} R dR d\varphi - \int_{R_1}^{R_3} \int_0^{2\pi} u_{0EX2} R dR d\varphi \right) \quad (55)$$

The MatLab computer program is used to perform the integration in (55). The fact that the strain energy release rate found by (55) is exact match of that obtained by (44) is a verification of the fracture analysis carried-out assuming increase of the external crack in the stepped rod in Fig. 2.

3 Results and discussion

In this section, the solutions to the strain energy release rate derived in the previous section of the paper are used to investigate the influence of various geometrical parameters and material inhomogeneity on the longitudinal fracture behaviour of the stepped rod

with two concentric longitudinal cracks. The strain energy release rate is presented in non-dimensional form by using the formula $G_N = G_{a_1}/(G_0R_3)$. It is assumed that $T_1 = 5 \text{ Nm}$, $T_2 = 8 \text{ Nm}$, $T_3 = 7 \text{ Nm}$, $R_3 = 0.010 \text{ m}$ and $l = 0.500 \text{ m}$.

The influence of the location of the internal crack in radial direction on the fracture behaviour is analyzed. The rod shown in Fig. 1 is considered. The location of the internal crack is characterized by R_1/R_3 ratio. The influence of the location of the internal crack on the fracture is illustrated in Fig. 3, where the strain energy release rate in non-dimensional form is presented as a function of R_1/R_3 ratio at $R_2/R_3 = 0.8$. The curves shown in Fig. 3 indicate that the strain energy release rate increases with increasing of R_1/R_3 ratio. One can observe also in Fig. 3 that the strain energy release rate derived assuming increase of external crack is higher than that obtained assuming increase of the internal crack.

The influence of the material property p on the fracture behaviour is analyzed too. The rod in which the external crack is shorter than the internal one is under consideration (Fig. 1). The solution to the strain energy release rate derived assuming increase of the external crack is applied. One can get an idea about the influence of p on the fracture in Fig. 4 where the strain energy release rate in non-dimensional form is presented as a function of at three R_2/R_3 ratios for $R_1/R_3 = 0.2$ (the ratio R_2/R_3 characterizes the location of the external crack in radial direction).

It can be observed in Fig. 4 that the strain energy release rate decreases with increasing of p . This finding is attributed to the fact that the stiffness of the rod increases with increasing of p . The curves in Fig. 4 indicate that the strain energy release rate increases with increasing of R_2/R_3 ratio.

The longitudinal fracture behaviour is analyzed also for the case when the rod exhibits continuous (smooth) material inhomogeneity in both radial and length directions. The distribution of G_0 along the length of the rod is written as

$$G_0 = G_{0b}e^{q\frac{x}{l}}, \tag{56}$$

where

$$0 \leq x \leq l. \tag{57}$$

In (56) G_{0b} is the value of G_0 at the free end of the rod, q is a material property that controls the material inhomogeneity in the length direction. When the rod is inhomogeneous in radial and length directions, the strain energy release rate can be obtained by applying the solutions derived in the previous section of the paper. For this purpose, the material property G_0 has to be calculated by (56) for the corresponding crack length. The effect of q on the fracture behaviour is illustrated in Fig. 5 where the strain energy release rate in non-dimensional form is presented as a function of q at $a_2/(l - l_1 - l_2) = 0.4$ (the solutions to the strain energy release rate obtained at increase of the external crack in the rods shown in Figs. 1 and 2 are applied). It is evident from Fig. 5 that the strain energy release rate decreases with increasing of q (this behaviour is due to the increase of the stiffness of the rod). The curves in Fig. 5 show also that the strain energy release rate is higher in the stepped rod configuration in which the external crack is shorter (Fig. 2). This finding can be explained by the fact that when the external crack is shorter, the crack front is located in cross-section of the rod in which the stiffness is lower since the stiffness increases from the free end of the rod towards the clamping according to (56).

4 Conclusions

The longitudinal fracture behavior of an inhomogeneous stepped rod with two longitudinal concentric cracks is analyzed in terms of the strain energy release rate. The rod has a circular cross-section. The two concentric longitudinal cracks present circular cylindrical surfaces. The rod under consideration exhibits continuous (smooth) material inhomogeneity in radial direction. Besides, the material has non-linear elastic behaviour. The rod is loaded in torsion. Solutions to the strain energy release rate are derived at different lengths of the two cracks by considering the complementary strain energy stored in the rod. The solutions are verified by analyzing the balance of the energy. It is shown that the solutions can be applied also for stepped rods which exhibit continuous

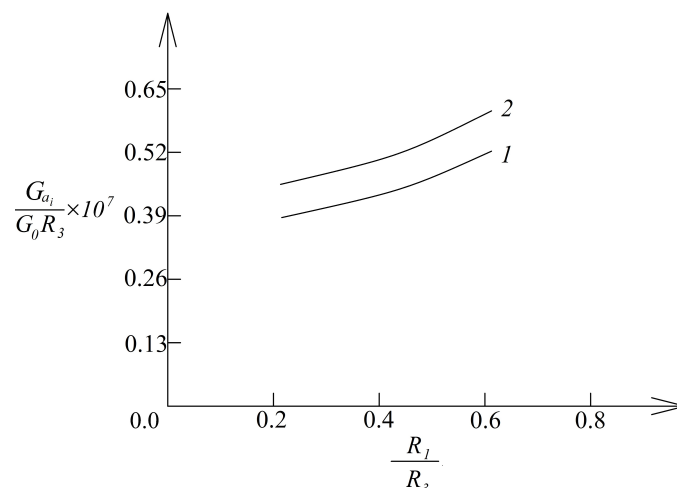


Fig. 3: The strain energy release rate in non-dimensional form presented as a function of R_1/R_3 ratio (curve 1 – at increase of the internal crack and curve 2 – at increase of the external crack)

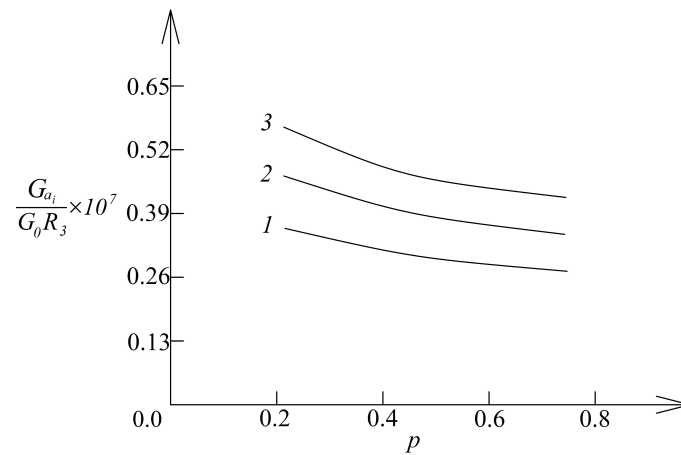


Fig. 4: The strain energy release rate in non-dimensional form presented as a function of p (curve 1 – at $R_2/R_3 = 0.3$, curve 2 – at $R_2/R_3 = 0.5$ and curve 3 – at $R_2/R_3 = 0.7$)

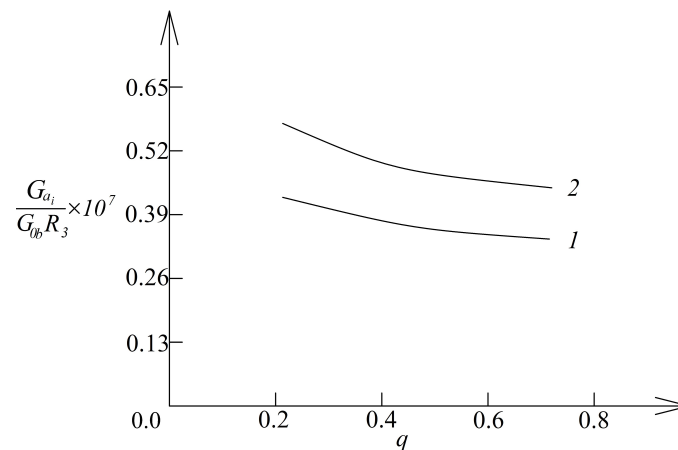


Fig. 5: The strain energy release rate in non-dimensional form presented as a function of q (curve 1 – for the stepped rod shown in Fig. 1 and curve 2 – for the stepped rod in which the external crack is shorter (Fig.2))

material inhomogeneity in both radial and length directions. The influence of the locations of the two cracks in radial direction on the fracture behaviour is investigated. It is found that the strain energy release rate increases with increasing of R_1/R_3 ratio. The increase of R_2/R_3 ratio leads also to increase of the strain energy release rate. The analysis reveals that the strain energy release rate decreases with increasing of material property p . It is found also that the strain energy release rate obtained at increase of external crack is higher than that obtained at increase of the internal crack. Concerning the effect of material inhomogeneity along the length of the rod, it is found that the strain energy release rate decreases with increasing of material property q . The analysis indicates also that the strain energy release rate is higher in the stepped rod in which the external crack is shorter.

Acknowledgement

The first author (V.R.) gratefully acknowledges the financial support by the German Academic Exchange Service (DAAD) for his research stay at the Chair of Engineering Mechanics, Institute of Mechanics, Otto-von-Guericke-Universität Magdeburg, Germany.

References

- Erkin Altunsaray and Ismail Bayer. Buckling of symmetrically laminated quasi-isotropic thin rectangular plates. *Steel and Composite Structures*, 17(3):305–320, 2014.
- Alberto Carpinteri and Nicola Pugno. Cracks and re-entrant corners in functionally graded materials. *Engineering Fracture Mechanics*, 73(10):1279 – 1291, 2006.
- F. Erdogan. Fracture mechanics of functionally graded materials. *Composites Engineering*, 5(7):753 – 770, 1995.
- D.K. Jha, Tarun Kant, and R.K. Singh. A critical review of recent research on functionally graded plates. *Composite Structures*, 96:833 – 849, 2013.
- G.E. Knoppers, J.W. Gunnink, J. van den Hout, and W.P. van Vliet. The reality of functionally graded material products. *TNO Science and Industry*, pages 38 – 43, 2003.
- P. A. Lukash. *Fundamentals of non-linear structural mechanics*. Stroizdat, Moscow, 1998.
- R.M. Mahamood and E.T. Akinlabi. *Functionally Graded Materials*. Springer, 2017.

- Y. Miyamoto, W.A. Kaysser, B.H. Rabin, A. Kawasaki, and R.G. Ford. *Functionally Graded Materials: Design, Processing and Applications*. Kluwer Academic Publishers, Dordrecht/London/Boston, 1999.
- M.M. Nemat-Allal, M.H. Ata, M.R. Bayoumi, and W. Khair-Eldeen. Powder metallurgical fabrication and microstructural investigations of aluminum/steel functionally graded material. *Materials Sciences and Applications*, 2(12):1708–1718, 2011.
- G.H. Paulino. Fracture of functionally graded materials. *Engineering Fracture Mechanics*, 69(14–16):1519–1530, 2002.
- V. Rizov. Multilayered functionally graded non-linear elastic beams with logarithmic material gradient: A delamination analysis. *Technische Mechanik*, 38(2):203–219, 2018.
- Matthew T. Tilbrook, Robert J. Moon, and Mark Hoffman. Crack propagation in graded composites. *Composites Science and Technology*, 65(2):201–220, 2005.
- L. Tokova, A. Yasinsky, and C.-C. Ma. Effect of the layer inhomogeneity on the distribution of stresses and displacements in an elastic multilayer cylinder. *Acta Mechanica*, 228(8):2865–2877, 2017.
- Y. Tokovyy and C.-C. Ma. Analysis of 2D non-axisymmetric elasticity and thermoelasticity problems for radially inhomogeneous hollow cylinders. *Journal Engineering Mathematics*, 61(2–4):171–184, 2008.
- Y. Tokovyy and C.-C. Ma. Three-dimensional temperature and thermal stress analysis of an inhomogeneous layer. *Journal of Thermal Stresses*, 36(8):790–808, 2013.
- Y. Tokovyy and C.-C. Ma. Axisymmetric stresses in an elastic radially inhomogeneous cylinder under length-varying loadings. *ASME Journal of Applied Mechanics*, 83(11):111007 (7 pages), 2016.
- M.U. Uysal. Buckling behaviours of functionally graded polymeric thin-walled hemispherical shells. *Steel and Composite Structures*, 21(4):849–862, 2016.
- M.U. Uysal and U. Güven. A bonded plate having orthotropic inclusion in the adhesive layer under in-plane shear loading. *The Journal of Adhesion*, 92(3):214–235, 2016.
- M.U. Uysal and M. Kremzer. Buckling behaviour of short cylindrical functionally gradient polymeric materials. *Acta Physica Polonica A*, 127(4):1355–1357, 2017.

On the Derivation of HOOKE'S Law for Plane State Conditions

Joachim Nordmann, Marcus Abmus*, Rainer Glüge and Holm Altenbach

Otto von Guericke University, Institute of Mechanics, Universitätsplatz 2, 39106 Magdeburg, Germany

Abstract: We discuss the derivation of HOOKE'S law for plane stress and plane strain states from its general three-dimensional representation. This means that we consider the anisotropic case to ensure a certain generality of our representation. Thereby, two approaches are examined, namely the tensorial representation involving fourth-order tensors over a three-dimensional vector space, and the VOIGT-MANDEL-Notation involving second-order tensors over a six-dimensional vector space. The latter reduces to a vector-matrix notation common in engineering applications. It turns out that both approaches have their merits: The tensorial approach is easier to handle symbolically, the matrix approach is easier to handle numerically. Both procedures are applicable for arbitrary material symmetries. Finally, we answer the question why a material under the assumptions of a plane stress state behaves softer and why it behaves stiffer under a plane strain state compared to the three-dimensional state.

Keywords: Plane stress, Plane strain, Elasticity, HOOKE'S law, Anisotropy

1 Introduction

1.1 Motivation

Commonly, the aim of continuum mechanics is to describe the motion and deformation of an arbitrary body \mathcal{B} in the three-dimensional EUCLIDIAN space \mathcal{E}^3 under given loading. However, in general it is not possible to solve the arising system of Partial Differential Equations (PDEs) without the help of numerical solution schemes like the Finite Element Method (FEM). But more important is that it is not always necessary to solve the full system of PDEs. Often, it is possible to reduce the problem size because in one or two directions no gradients occur, for example due to the specific boundary conditions or when the extension in this direction is small compared to the other two directions. This reduction is quite remarkable: In simulations, the number of degrees of freedom at similar discretisations d is by a factor of $3d^3/(2d^2) = 1.5d$ lower.

Here we discuss the plane stress state (PT) and the plane strain state (PE). In the first state it is assumed that in the normal direction (e_3) to the plane no stress but a deformation occurs, namely a free lateral contraction. In the PE it is assumed that in the normal direction (e_3) to the plane no strains occur, hence there are out-of-plane reaction stresses to this constraint. Historically, these assumptions can be addressed to the works of [Airy \(1863\)](#), [Maxwell \(1870\)](#), [Levy \(1899\)](#), [Flamant \(1892\)](#) and [Golovin \(1881\)](#) among others (e.g. [Michell \(1899\)](#), [Carothers \(1914\)](#), [Love \(1944\)](#)). We mention these scientists to honour their work because commonly these assumptions are used without any reference. For a deeper insight in the history of the PT and PE we refer the interested reader to the review by [Teodorescu \(1964\)](#). The plane states described under the designations generalized plane stress or generalized plane strain remain out of the scope of present treatise.

A famous example for these two states is a gear wheel with a straight-cut and thick teeth which is presented in [Fig. 1](#) (This is the arbitrary body \mathcal{B} , now.). In general, the stress state which arises in a tooth is very complex and to analyse this stress state a three-dimensional analysis is required. However, a faster and more efficient analysis is possible. For a thick teeth under loading the stress state is approximately equal to a PT at the end of the teeth (cf. [Fig. 1](#) left-hand side) and the stress state in the middle of the teeth converges to a PE (cf. [Fig. 1](#) right-hand side). The assumption of a PT at the end of the teeth is possible because at this position no stress in e_3 direction can occur. In the middle, the deformation is symmetric, hence no shear strains E_{13} and E_{23} and normal strain E_{33} occur. Since the teeth can hardly contract along the e_3 -direction due to the attachment to the wheel, a plane strain state is a reasonable and conservative approximation in the middle plane.

The saved time could be used e.g. to consider further influences in the simulation or to perform parametric studies of the teeth geometry, etc. Another famous example for the use of plane states is the field of fracture mechanics (e.g. Phase-Field-Method ([Miehe et al., 2010](#); [Kuhn et al., 2015](#)), Cohesive-Zone-Model ([Barenblatt, 1959](#); [Dugdale, 1960](#))).

By using the PT or PE assumptions and going from the 3D- to the 2D-case one needs to condense the three-dimensional elasticity law from 3D to 2D as well. Although this is not complicated, there appears to be no systematic derivation of this. While the two-dimensional PT and PE stiffnesses are well known and found in textbooks for isotropic materials (e.g. [Altenbach et al. \(2018\)](#); [Chaboche and Lemaitre \(1990\)](#)), an examination of the general anisotropic case is unknown to the authors.

1.2 Organization

The paper is organized as follows. We firstly consider the general tensorial representation that involves fourth-order tensors for both PT and PE states. We proceed by expressing the PT and PE stiffnesses and compliances in a VOIGT-MANDEL type

* E-mail address: marcus.assmus@ovgu.de

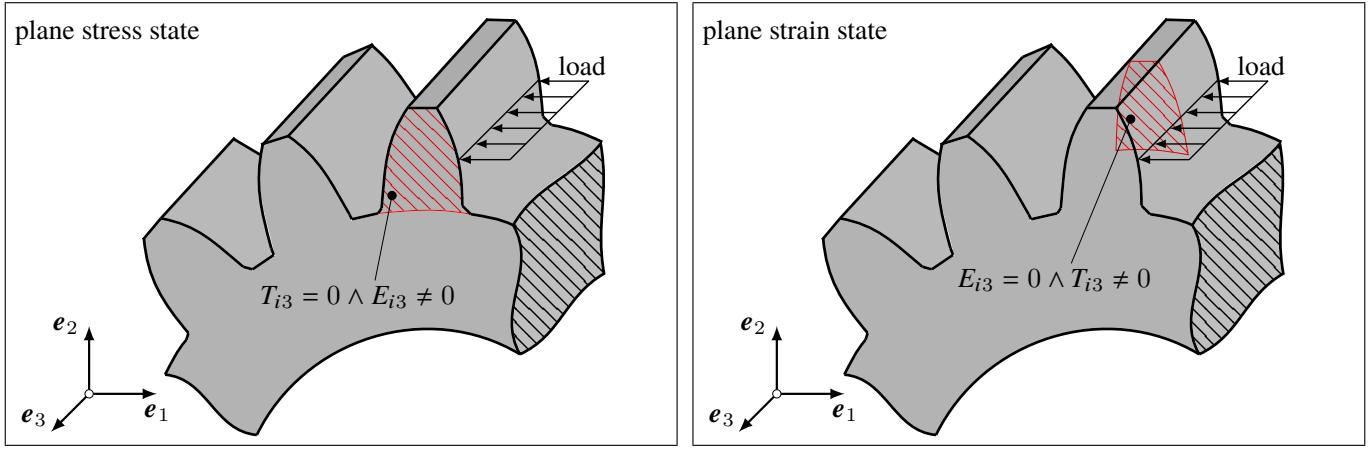


Fig. 1: Gear wheel with a straight-cut under loading based on Wittel et al. (2017) with assumed PT to analyse the stresses at the end of a tooth (left-hand side) and with assumed PE to analyse the stresses in the middle of a tooth (right-hand side) for $i \in \{1, 2, 3\}$

vector-matrix-notation where the indexing is adopted to the plane state conditions. We further on examine simplifications following from different material symmetries. Finally, problems arising of the assumptions of plane states are addressed.

1.3 Notation

We employ a direct tensor notation. Vectors are denoted as $\mathbf{a} = a_i \mathbf{e}_i$, where i is an implicit summation index and $\{\mathbf{e}_1, \mathbf{e}_2, \mathbf{e}_3\}$ is a set of orthonormal base vectors of a Cartesian coordinate system. The scalar product is denoted by $\mathbf{a} \cdot \mathbf{b}$. For example, for the base vectors we have $\mathbf{e}_i \cdot \mathbf{e}_j = \delta_{ij}$, with the KRONECKER symbol δ_{ij} being 1 for $i = j$ and zero for $i \neq j$. Higher order tensors are obtained by the dyadic product and denoted by capital letters, where $\mathbf{A} = \mathbf{a} \otimes \mathbf{b} = A_{ij} \mathbf{e}_i \otimes \mathbf{e}_j$ is an example for a second-order tensor, $\mathbb{C} = \mathbf{A} \otimes \mathbf{B} = C_{ijkl} \mathbf{e}_i \otimes \mathbf{e}_j \otimes \mathbf{e}_k \otimes \mathbf{e}_l$ is an example for a fourth-order tensor, and $\mathbb{E} = \mathbf{A} \otimes \mathbf{B} \otimes \mathbf{C} \otimes \mathbf{D} = E_{ijklmnop} \mathbf{e}_i \otimes \mathbf{e}_j \otimes \mathbf{e}_k \otimes \mathbf{e}_l \otimes \mathbf{e}_m \otimes \mathbf{e}_n \otimes \mathbf{e}_o \otimes \mathbf{e}_p$ is an example for an eighth-order tensor. A tensor-vector product is denoted as $\mathbf{A} \cdot \mathbf{a} = A_{ij} \mathbf{e}_i \otimes \mathbf{e}_j \cdot a_l \mathbf{e}_l = A_{ij} a_l \mathbf{e}_i (\mathbf{e}_j \cdot \mathbf{e}_l) = A_{ij} a_l \delta_{jl} \mathbf{e}_i = A_{ij} a_j \mathbf{e}_i$. The scalar contractions are extended to higher order tensors such that the positivity of the scalar product is maintained, e.g. $\mathbf{A} : \mathbf{A} = A_{ij} \mathbf{e}_i \otimes \mathbf{e}_j : A_{kl} \mathbf{e}_k \otimes \mathbf{e}_l = A_{ij} A_{kl} \delta_{ik} \delta_{jl} = A_{ij} A_{ij}$. We additionally introduce the Rayleigh product which maps all basis vectors of a tensor simultaneously without changing components. When applied between dyad and a tetrad, the product is $\mathbf{B} \star \mathbb{A} = A_{ijkl} (\mathbf{B} \cdot \mathbf{e}_i) \otimes (\mathbf{B} \cdot \mathbf{e}_j) \otimes (\mathbf{B} \cdot \mathbf{e}_k) \otimes (\mathbf{B} \cdot \mathbf{e}_l)$ with components $A_{ijkl} = \mathbb{A} :: \mathbf{e}_i \otimes \mathbf{e}_j \otimes \mathbf{e}_k \otimes \mathbf{e}_l$. A tensor is said to be symmetric when $\mathbf{a} \cdot \mathbf{A} \cdot \mathbf{b} = \mathbf{b} \cdot \mathbf{A} \cdot \mathbf{a}$ holds. With respect to orthonormal bases, this reduces to the index symmetry $A_{ij} = A_{ji}$. The tensor components may be arranged in a matrix, where the index symmetry becomes a transposition across the main diagonal. Hence, for second-order tensors we denote the symmetry by $\mathbf{A} = \mathbf{A}^T$, i.e. $\mathbf{A} \in \text{Sym}$. For detailed explanations of these operations we refer to e.g. Bertram and Glüge (2015). Also, we make use of numerical vectors and matrices which are both indicated by the superscript index M.

$$\mathbf{E}^M = \begin{bmatrix} E_1^M \\ E_2^M \\ E_3^M \end{bmatrix} \quad \mathbb{C}^M = \begin{bmatrix} C_{11}^M & C_{12}^M & C_{13}^M \\ C_{21}^M & C_{22}^M & C_{23}^M \\ C_{31}^M & C_{32}^M & C_{33}^M \end{bmatrix}$$

With regard to vector-matrix calculations we refer to Brannon (2018). This representation is used to analyse some properties of the 2D stiffness and compliance matrix, later on.

2 Continuum Mechanical Propaedeutics

The formulation of the common quasi-static boundary value problem under small deformations for a linear-elastic body is given as follows.

$$\nabla \cdot \mathbf{T} = \mathbf{0} \quad \text{bal. of linear momentum} \quad (1)$$

$$\mathbf{T} = \mathbb{C} : \mathbf{E} \quad \text{constitutive law} \quad (2)$$

$$\mathbf{E} = \frac{1}{2} \left[\nabla \otimes \mathbf{u} + (\nabla \otimes \mathbf{u})^T \right] \quad \text{strain-displacement-relation} \quad (3)$$

Herein, $\mathbf{T} = T_{ij} \mathbf{e}_i \otimes \mathbf{e}_j$ is the stress tensor, $\mathbb{C} = C_{ijkl} \mathbf{e}_i \otimes \mathbf{e}_j \otimes \mathbf{e}_k \otimes \mathbf{e}_l$ is the constitutive tensor, $\mathbf{E} = E_{kl} \mathbf{e}_k \otimes \mathbf{e}_l$ is the linearized strain tensor and $\nabla = \partial/\partial x_i$ represents the nabla operator with respect to the reference configuration. The first index of the stress and strain tensor refers to the force, respectively, displacement direction and the second index refers to the surface normal.

2.1 Three-Dimensional Hooke's Law

We focus on Hooke's law (2), which contains the stiffness tetrad.

$$\mathbb{C} = C_{ijkl} \mathbf{e}_i \otimes \mathbf{e}_j \otimes \mathbf{e}_k \otimes \mathbf{e}_l \quad (4)$$

Further on, $\mathbf{T} \in \text{Sym}$ and $\mathbf{E} \in \text{Sym}$ hold true, along with the following symmetry properties for the constitutive tensor.

$$\begin{aligned} \mathbf{A} : \mathbb{C} : \mathbf{B} = \mathbf{B} : \mathbb{C} : \mathbf{A} & \quad C_{ijkl} = C_{klij} & \text{major symmetry} \\ \mathbf{A} : \mathbb{C} = \mathbf{A}^\top : \mathbb{C} & \quad C_{ijkl} = C_{jikl} & \text{left subsymmetry} \\ \mathbb{C} : \mathbf{A} = \mathbb{C} : \mathbf{A}^\top & \quad C_{ijkl} = C_{ijlk} & \text{right subsymmetry} \end{aligned}$$

Therein, \mathbf{A} and \mathbf{B} are chosen arbitrary. The subsymmetries basically denote the restriction to the subspace of symmetric second-order tensors. The major symmetry is the integrability condition to guarantee that the energy density yields following form.

$$w = \frac{1}{2} \mathbf{E} : \mathbb{C} : \mathbf{E} \quad (5)$$

For the potential relation subsequent expression holds.

$$\mathbf{T} = \frac{\partial w}{\partial \mathbf{E}} \quad (6)$$

Carrying out the inversion of \mathbb{C} on the subspace of symmetric tensors due to the positive definiteness of the stiffness tetrad w.r.t. this space, we obtain the inverse form of Hooke's law.

$$\mathbf{E} = \mathbb{S} : \mathbf{T} \quad (7)$$

Herein, the fourth-order compliance tetrad is used.

$$\mathbb{S} = \mathbb{C}^{-1} = S_{ijkl} \mathbf{e}_i \otimes \mathbf{e}_j \otimes \mathbf{e}_k \otimes \mathbf{e}_l, \quad (8)$$

For \mathbb{S} , the same symmetries hold as for \mathbb{C} . The complementary energy density is defined as follows.

$$w^* = \frac{1}{2} \mathbf{T} : \mathbb{S} : \mathbf{T}, \quad (9)$$

The potential relation then yields following expression.

$$\mathbf{E} = \frac{\partial w^*}{\partial \mathbf{T}}. \quad (10)$$

In linear elasticity we have $w = w^*$. In nonlinear elasticity this does not hold, and it is often not possible to obtain the explicit expression of the corresponding dual energy, formally related to each other by the Legendre transform.

In absence of material symmetries, \mathbb{C} has 21 independent components. If a material symmetry is present, it is usually formalized as a subgroup of the special orthogonal group (Weyl, 1939; Zheng and Boehler, 1994). Then, the symmetry condition $\mathbb{C} = \mathbf{Q}_i * \mathbb{C}$ is used to derive constraints on \mathbb{C} for a set of generators \mathbf{Q}_i of the symmetry group, where the product $*$ is the rotation of the stiffness with the material. Other approaches are possible, for example by using mirror planes. It is known that eight elastic symmetries can be distinguished (Voigt, 1910; Nye, 1985; Cowin and Mehrabadi, 1987; Forte and Vianello, 1996)¹. These can be found, for example, in Weber et al. (2018) in terms of the tensorial notation and in Ting (1996, 2003) in the VOIGT notation.

2.2 Two-Dimensional Hooke's Law

As it is mentioned in Sect. 1 many problems allow the reduction of the system of PDEs (Eqs. (1)-(3)) by assuming a PT or PE. However, these assumptions lead to changes of the components of the constitutive tensor \mathbb{C} because under the PT a deformation in the third direction is possible but it results no stress, vice versa, under the PE no deformation in the third direction results but it remains a stress. However, the form of Eqs. (1)-(3) does not change under a PT or a PE, but we have one less independent equation. Hence, we can write the plane system of PDEs.

$$\nabla^{2D} \cdot \mathbf{T}^{2D} = \mathbf{0} \quad \text{bal. of linear momentum} \quad (11)$$

$$\mathbf{T}^{2D} = \mathbb{C}^{2D} : \mathbf{E}^{2D} \quad \text{constitutive law} \quad (12)$$

$$\mathbf{E}^{2D} = \frac{1}{2} \left[\nabla^{2D} \otimes \mathbf{u}^{2D} + (\nabla^{2D} \otimes \mathbf{u}^{2D})^\top \right] \quad \text{strain-displacement-relation} \quad (13)$$

The inverse form of Hooke's law is then given as follows.

$$\mathbf{E}^{2D} = \mathbb{S}^{2D} : \mathbf{T}^{2D} \quad (14)$$

The quantities with the superscript 2D are reduced by negligence of the third direction (we project in the \mathbf{e}_1 - \mathbf{e}_2 plane with normal vector $\mathbf{n} = \mathbf{e}_3$), hence, the indices i, j, k, l are substituted by $\alpha, \beta, \gamma, \delta$ and run through the values 1, 2 instead of 1, 2, 3. Here, we present a general representation of the stiffness tetrad \mathbb{C}^{2D} which is fully derived from the common anisotropic stiffness tetrad \mathbb{C} , thus, it is possible to use Eqs. (11)-(13).

¹Note that Gurtin (1972) gives 10 different symmetries, namely isotropy and 9 different anisotropic matrices on pages 87 to 89.

3 Generalized Representation of Plane State Conditions

3.1 Plane Stress State

The first step is to rewrite Eq. (1) as follows.

$$T_{\alpha\beta} = 2C_{\alpha\beta 13}E_{13} + 2C_{\alpha\beta 23}E_{23} + C_{\alpha\beta 33}E_{33} + C_{\alpha\beta\gamma\delta}E_{\gamma\delta} \quad (15)$$

$$T_{13} = 2C_{1313}E_{13} + 2C_{1323}E_{23} + C_{1333}E_{33} + C_{13\alpha\beta}E_{\alpha\beta} \quad (16)$$

$$T_{23} = 2C_{2313}E_{13} + 2C_{2323}E_{23} + C_{2333}E_{33} + C_{23\alpha\beta}E_{\alpha\beta} \quad (17)$$

$$T_{33} = 2C_{3313}E_{13} + 2C_{3323}E_{23} + C_{3333}E_{33} + C_{33\alpha\beta}E_{\alpha\beta} \quad (18)$$

Hence, all quantities for the third direction (index 3) are separated. The PT claims that $T_{13} = T_{23} = T_{33} = 0$, hence, we solve Eqs. (16)-(18) for E_{13} , E_{23} and E_{33} . Keep in mind that the stiffness tetrad has the major symmetry, thus, the subsequent components are identically equal which leads to simplifications.

$$C_{3313} = C_{1333} \quad C_{3323} = C_{2333} \quad C_{1323} = C_{2313}$$

Further on, we introduce following abbreviations a_{ijkl} for a more compact notation.

$$a_{1313} = C_{3323}^2 - C_{2323}C_{3333}, \quad a_{2313} = C_{1323}C_{3333} - C_{3313}C_{3323}, \quad a_{3313} = C_{2323}C_{3313} - C_{1323}C_{3323},$$

$$a_{1323} = C_{1323}C_{3333} - C_{3313}C_{3323}, \quad a_{2323} = C_{3313}^2 - C_{1313}C_{3333}, \quad a_{3323} = C_{1313}C_{3323} - C_{1323}C_{3313},$$

$$a_{1333} = C_{2323}C_{3313} - C_{1323}C_{3323}, \quad a_{2333} = C_{1313}C_{3323} - C_{1323}C_{3313}, \quad a_{3333} = C_{1323}^2 - C_{1313}C_{2323}.$$

The third and fourth index of these abbreviations refer to the indices of the strain component while the first and second index are used for summation. Next to that a normalisation of the correction term Θ is introduced.

$$\Theta = C_{3333}a_{3333} - 2C_{1323}C_{3313}C_{3323} + C_{2323}C_{3313}^2 + C_{1313}C_{3323}^2$$

This term is used due to differences between 3D and plane states which are resulting from constraints of the assumptions of PT and PE. The following results upon solving Eqs. (16)-(18).

$$E_{13} = -\frac{1}{2\Theta} (a_{1313}C_{13\alpha\beta} + a_{2313}C_{23\alpha\beta} + a_{3313}C_{33\alpha\beta}) E_{\alpha\beta} \quad (19)$$

$$E_{23} = -\frac{1}{2\Theta} (a_{1323}C_{13\alpha\beta} + a_{2323}C_{23\alpha\beta} + a_{3323}C_{33\alpha\beta}) E_{\alpha\beta} \quad (20)$$

$$E_{33} = -\frac{1}{\Theta} (a_{1333}C_{13\alpha\beta} + a_{2333}C_{23\alpha\beta} + a_{3333}C_{33\alpha\beta}) E_{\alpha\beta} \quad (21)$$

Inserting Eqs. (19)-(21) into Eq. (15) leads to three fourth-order tensors which are the corrections of the stiffness tetrad.

$$A_{\alpha\beta\gamma\delta}^{13} = C_{\alpha\beta 13} (a_{1313}C_{13\gamma\delta} + a_{2313}C_{23\gamma\delta} + a_{3313}C_{33\gamma\delta})$$

$$A_{\alpha\beta\gamma\delta}^{23} = C_{\alpha\beta 23} (a_{1323}C_{13\gamma\delta} + a_{2323}C_{23\gamma\delta} + a_{3323}C_{33\gamma\delta})$$

$$A_{\alpha\beta\gamma\delta}^{33} = C_{\alpha\beta 33} (a_{1333}C_{13\gamma\delta} + a_{2333}C_{23\gamma\delta} + a_{3333}C_{33\gamma\delta})$$

The superscript index $i3$ here refers to the corresponding strain measures. These three tensors can be used to build a general correction tensor.

$$\mathbb{A} = \mathbb{A}^{13} + \mathbb{A}^{23} + \mathbb{A}^{33} \quad (22)$$

In index notation this tensor is represented as follows.

$$A_{\alpha\beta\gamma\delta} = a_{i3k3}C_{\alpha\beta k3}C_{i3\gamma\delta}$$

A direct notation is possible, also.

$$\mathbb{A} = a_{i3k3} (\mathbb{C} : \mathbf{e}_k \otimes \mathbf{e}_3) \otimes (\mathbf{e}_i \otimes \mathbf{e}_3 : \mathbb{C}) \quad (23)$$

Finally, it follows the representation of the stiffness tetrad for the PT.

$$\mathbb{C}^{\text{PT}} = \mathbb{C} - \frac{1}{\Theta} \mathbb{A} \quad \iff \quad C_{\alpha\beta\gamma\delta}^{\text{PT}} = C_{\alpha\beta\gamma\delta} - \frac{1}{\Theta} a_{i3k3} C_{\alpha\beta k3} C_{i3\gamma\delta} \quad (24)$$

With this corrected stiffness tetrad HOOKE's law under a PT takes subsequent form.

$$\begin{aligned}
\mathbf{T}^{\text{PT}} &= \mathbb{C}^{\text{PT}} : \mathbf{E}^{\text{PT}} = \left[\mathbb{C} - \frac{1}{\Theta} \mathbb{A} \right] : \mathbf{E}^{\text{PT}} \\
\Downarrow \\
T_{\alpha\beta}^{\text{PT}} &= C_{\alpha\beta\gamma\delta}^{\text{PT}} E_{\gamma\delta}^{\text{PT}} = \left[C_{\alpha\beta\gamma\delta} - \frac{1}{\Theta} a_{i3k3} C_{\alpha\beta k3} C_{i3\gamma\delta} \right] E_{\gamma\delta}^{\text{PT}}
\end{aligned} \tag{25}$$

3.2 Plane Strain State

For the PE we begin with Eq. (7). Up next, the third direction (index 3) is separated from this set of equations, like it was done before. Subsequent relations result.

$$E_{\alpha\beta} = 2S_{\alpha\beta 13} T_{13} + 2S_{\alpha\beta 23} T_{23} + S_{\alpha\beta 33} T_{33} + S_{\alpha\beta\gamma\delta} T_{\gamma\delta} \tag{26}$$

$$E_{13} = 2S_{1313} T_{13} + 2S_{1323} T_{23} + S_{1333} T_{33} + S_{13\alpha\beta} T_{\alpha\beta} \tag{27}$$

$$E_{23} = 2S_{2313} T_{13} + 2S_{2323} T_{23} + S_{2333} T_{33} + S_{23\alpha\beta} T_{\alpha\beta} \tag{28}$$

$$E_{33} = 2S_{3313} T_{13} + 2S_{3323} T_{23} + S_{3333} T_{33} + S_{33\alpha\beta} T_{\alpha\beta} \tag{29}$$

The PE claims that $E_{13} = E_{23} = E_{33} = 0$, hence, we solve Eqs. (27)-(29) for T_{13} , T_{23} and T_{33} . Keep in mind that the compliance tetrad has the major symmetry (like the stiffness tetrad), thus, following components are identically equal which leads to simplifications.

$$S_{3313} = S_{1333} \quad S_{3323} = S_{2333} \quad S_{1323} = S_{2313}$$

Further on, some abbreviations for a more compact notation are introduced.

$$b_{1313} = S_{3323}^2 - S_{2323} S_{3333} \quad b_{2313} = S_{1323} S_{3333} - S_{3313} S_{3323} \quad b_{3313} = S_{2323} S_{3313} - S_{1323} S_{3323}$$

$$b_{1323} = S_{1323} S_{3333} - S_{3313} S_{3323} \quad b_{2323} = S_{3313}^2 - S_{1313} S_{3333} \quad b_{3323} = S_{1313} S_{3323} - S_{1323} S_{3313}$$

$$b_{1333} = S_{2323} S_{3313} - S_{1323} S_{3323} \quad b_{2333} = S_{1313} S_{3323} - S_{1323} S_{3313} \quad b_{3333} = S_{1323}^2 - S_{1313} S_{2323}$$

We furthermore introduce a normalisation of the correction term.

$$\Phi = S_{3333} b_{3333} - 2S_{1323} S_{3313} S_{3323} + S_{2323} S_{3313}^2 + S_{1313} S_{3323}^2$$

It results the solution of Eqs. (27)-(29)

$$T_{13} = -\frac{1}{2\Phi} (b_{1313} S_{13\alpha\beta} + b_{2313} S_{23\alpha\beta} + b_{3313} S_{33\alpha\beta}) T_{\alpha\beta} \tag{30}$$

$$T_{23} = -\frac{1}{2\Phi} (b_{1323} S_{13\alpha\beta} + b_{2323} S_{23\alpha\beta} + b_{3323} S_{33\alpha\beta}) T_{\alpha\beta} \tag{31}$$

$$T_{33} = -\frac{1}{\Phi} (b_{1333} S_{13\alpha\beta} + b_{2333} S_{23\alpha\beta} + b_{3333} S_{33\alpha\beta}) T_{\alpha\beta} \tag{32}$$

Inserting Eqs. (30)-(32) into Eq. (26) leads to three fourth-order tensors which are the corrections of the compliance tetrad.

$$B_{\alpha\beta\gamma\delta}^{13} = S_{\alpha\beta 13} (b_{1313} S_{13\gamma\delta} + b_{2313} S_{23\gamma\delta} + b_{3313} S_{33\gamma\delta})$$

$$B_{\alpha\beta\gamma\delta}^{23} = S_{\alpha\beta 23} (b_{1323} S_{13\gamma\delta} + b_{2323} S_{23\gamma\delta} + b_{3323} S_{33\gamma\delta})$$

$$B_{\alpha\beta\gamma\delta}^{33} = S_{\alpha\beta 33} (b_{1333} S_{13\gamma\delta} + b_{2333} S_{23\gamma\delta} + b_{3333} S_{33\gamma\delta})$$

The superscript index $i3$ here refer to the corresponding stress measures. These three tensors are used to build a correction tensor for plane strain state.

$$\mathbb{B} = \mathbb{B}^{13} + \mathbb{B}^{23} + \mathbb{B}^{33} \tag{33}$$

In index notation this tensor is represented as follows.

$$B_{\alpha\beta\gamma\delta} = b_{i3k3} S_{\alpha\beta k3} S_{i3\gamma\delta}$$

A direct notation is possible, also.

$$\mathbb{B} = b_{i3k3} (\mathbb{S} : \mathbf{e}_k \otimes \mathbf{e}_3) \otimes (\mathbf{e}_i \otimes \mathbf{e}_3 : \mathbb{S}) \tag{34}$$

Finally, it follows the representation of the compliance tetrad for the plane strain state as

$$\mathbb{S}^{\text{PE}} = \mathbb{S} - \frac{1}{\Phi} \mathbb{B} \iff S_{\alpha\beta\gamma\delta}^{\text{PE}} = S_{\alpha\beta\gamma\delta} - \frac{1}{\Phi} b_{i3k3} S_{\alpha\beta k3} S_{i3\gamma\delta} \tag{35}$$

With this corrected compliance tetrad, inverse HOOKE's law under a plane strain state takes subsequent form.

$$\begin{aligned}
 \mathbf{E}^{\text{PE}} &= \mathbb{S}^{\text{PE}} : \mathbf{T}^{\text{PE}} = \left[\mathbb{S} - \frac{1}{\Phi} \mathbb{B} \right] : \mathbf{T}^{\text{PE}} \\
 \Updownarrow \\
 E_{\alpha\beta}^{\text{PE}} &= S_{\alpha\beta\gamma\delta}^{\text{PE}} T_{\gamma\delta}^{\text{PE}} = \left[S_{\alpha\beta\gamma\delta} - \frac{1}{\Phi} b_{i3k3} S_{\alpha\beta k3} S_{i3\gamma\delta} \right] T_{\gamma\delta}^{\text{PE}}
 \end{aligned} \tag{36}$$

4 Matrix Representation

4.1 Normalized 6D Basis

We have seen that the plane stiffnesses and compliances can be obtained from solving three scalar equations, with successive backward substitution. Another approach is to consider sub-matrices in the matrix-vector notation of HOOKE’s law. But care must be taken: For the usual rules of algebra to hold, the basis needs to be normalized. This leads to the so called MANDEL-notation (index \square^{M}), see for example Brannon (2018) Sects. 26.2 and 26.3, Helnwein (2001) or Cowin and Mehrabadi (1992). The normalization was popularized by Mandel (1965), but has been used much earlier by LORD KELVIN, cf. Thomson (1856). Since all involved second-order tensors are symmetric, we introduce a symmetrized basis $\mathbf{B}_{\Gamma} \forall \Gamma \in \{1, \dots, 6\}$.

$$\begin{aligned}
 \mathbf{B}_1 &= \mathbf{e}_1 \otimes \mathbf{e}_1 & \mathbf{B}_4 &= \mathbf{e}_3 \otimes \mathbf{e}_3 \\
 \mathbf{B}_2 &= \mathbf{e}_2 \otimes \mathbf{e}_2 & \mathbf{B}_5 &= \frac{1}{\sqrt{2}} (\mathbf{e}_1 \otimes \mathbf{e}_3 + \mathbf{e}_3 \otimes \mathbf{e}_1) \\
 \mathbf{B}_3 &= \frac{1}{\sqrt{2}} (\mathbf{e}_1 \otimes \mathbf{e}_2 + \mathbf{e}_2 \otimes \mathbf{e}_1) & \mathbf{B}_6 &= \frac{1}{\sqrt{2}} (\mathbf{e}_2 \otimes \mathbf{e}_3 + \mathbf{e}_3 \otimes \mathbf{e}_2)
 \end{aligned} \tag{37}$$

Herein we have introduced capital greek indices having the values 1 . . . 6. The indices of the tensor components ij are substituted with them (Γ) as follows.

$$\{11 \leftrightarrow 1, 22 \leftrightarrow 2, 12 \leftrightarrow 3, 33 \leftrightarrow 4, 13 \leftrightarrow 5, 23 \leftrightarrow 6\}$$

This basis is orthogonal due to the normalizing factor $1/\sqrt{2}$.

$$\mathbf{B}_{\Gamma} : \mathbf{B}_{\Lambda} = \delta_{\Gamma\Lambda} \quad \forall \Gamma, \Lambda \in \{1, \dots, 6\} \tag{38}$$

Our ordering deviates from the VOIGT ordering. It is such that the in- and out-of-plane components of the 1-2-plane have the indices 1 . . . 3 and 4 . . . 6, respectively. Comparing coefficients with the $\mathbf{e}_i \otimes \mathbf{e}_j$ -basis we can now write a compact form.

$$\mathbf{E} = E_{ij} \mathbf{e}_i \otimes \mathbf{e}_j \quad \forall i, j \in \{1, \dots, 3\} \tag{39}$$

$$= E_{\Lambda}^{\text{M}} \mathbf{B}_{\Lambda} \quad \forall \Lambda \in \{1, \dots, 6\} \tag{40}$$

In case of the strain tensor, the components appear as follows.

$$E_1^{\text{M}} = E_{11} \quad E_4^{\text{M}} = E_{33} \tag{41}$$

$$E_2^{\text{M}} = E_{22} \quad E_5^{\text{M}} = \sqrt{2} E_{13} \tag{42}$$

$$E_3^{\text{M}} = \sqrt{2} E_{12} \quad E_6^{\text{M}} = \sqrt{2} E_{23} \tag{43}$$

The same factors apply when going from T_{ij} to T_{Γ}^{M} . Regarding the stiffness and compliance tensors, we can also find a compact expression.

$$\mathbb{C} = C_{ijkl} \mathbf{e}_i \otimes \mathbf{e}_j \otimes \mathbf{e}_k \otimes \mathbf{e}_l \quad \forall i, j, k, l \in \{1, \dots, 3\} \tag{44}$$

$$= C_{\Gamma\Lambda}^{\text{M}} \mathbf{B}_{\Gamma} \otimes \mathbf{B}_{\Lambda} \quad \forall \Gamma, \Lambda \in \{1, \dots, 6\} \tag{45}$$

The components $C_{\Gamma\Lambda}^{\text{M}}$ appear as follows, while $C_{\Gamma\Lambda}^{\text{M}} = C_{\Lambda\Gamma}^{\text{M}}$ holds.

$$\begin{array}{cccccc}
 C_{11}^{\text{M}} = C_{1111} & C_{12}^{\text{M}} = C_{1122} & C_{13}^{\text{M}} = \sqrt{2} C_{1112} & C_{14}^{\text{M}} = C_{1133} & C_{15}^{\text{M}} = \sqrt{2} C_{1113} & C_{16}^{\text{M}} = \sqrt{2} C_{1123} \\
 & C_{22}^{\text{M}} = C_{2222} & C_{23}^{\text{M}} = \sqrt{2} C_{2212} & C_{24}^{\text{M}} = C_{2233} & C_{25}^{\text{M}} = \sqrt{2} C_{2213} & C_{26}^{\text{M}} = \sqrt{2} C_{2223} \\
 & & C_{33}^{\text{M}} = 2C_{1212} & C_{34}^{\text{M}} = \sqrt{2} C_{1233} & C_{35}^{\text{M}} = 2C_{1213} & C_{36}^{\text{M}} = 2C_{1223} \\
 & & & C_{44}^{\text{M}} = C_{3333} & C_{45}^{\text{M}} = \sqrt{2} C_{3313} & C_{46}^{\text{M}} = \sqrt{2} C_{3323} \\
 & & & & C_{55}^{\text{M}} = 2C_{1313} & C_{56}^{\text{M}} = 2C_{1323} \\
 & & & & & C_{66}^{\text{M}} = 2C_{2323}
 \end{array} \tag{46}$$

The same holds for \mathbb{S} .

4.2 Matrix-Representation of Hooke's Law

HOOKE's law can now be written as follows.

$$\begin{aligned} \begin{bmatrix} T_1^M \\ T_2^M \\ T_3^M \\ T_4^M \\ T_5^M \\ T_6^M \end{bmatrix} &= \begin{bmatrix} C_{11}^M & C_{12}^M & C_{13}^M & C_{14}^M & C_{15}^M & C_{16}^M \\ & C_{22}^M & C_{23}^M & C_{24}^M & C_{25}^M & C_{26}^M \\ & & C_{33}^M & C_{34}^M & C_{35}^M & C_{36}^M \\ \hline & & & C_{44}^M & C_{45}^M & C_{46}^M \\ & & & & C_{55}^M & C_{56}^M \\ & & & & & C_{66}^M \end{bmatrix} \begin{bmatrix} E_1^M \\ E_2^M \\ E_3^M \\ E_4^M \\ E_5^M \\ E_6^M \end{bmatrix} \\ &= \begin{bmatrix} \mathbb{C}_{UL}^M & \mathbb{C}_{UR}^M \\ \mathbb{C}_{LL}^M & \mathbb{C}_{LR}^M \end{bmatrix} \begin{bmatrix} \mathbf{E}_{ip}^M \\ \mathbf{E}_{op}^M \end{bmatrix} \quad \mathbb{C}_{UR}^M = [\mathbb{C}_{LL}^M]^T \end{aligned} \quad (47)$$

For the compact form of Eq. (47) we have introduced the subscripts *UL* for upper left, *UR* for upper right, *LL* for lower left, *LR* for lower right, *ip* for in-plane, and *op* for out-of-plane. We can also write this law in terms of components.

$$T_\Gamma^M = C_{\Gamma\Lambda}^M E_\Lambda^M \quad (48)$$

$$E_\Gamma^M = S_{\Gamma\Lambda}^M T_\Lambda^M \quad \text{with} \quad S_{\Gamma\Lambda}^M = [C_{\Gamma\Lambda}^M]^{-1} \quad (49)$$

Note that $S_{\Gamma\Lambda}^M$ is the usual matrix inverse. In case of a PE or a PT we have either $E_4^M = 0, E_5^M = 0, E_6^M = 0$ (PE) or $T_4^M = 0, T_5^M = 0, T_6^M = 0$ (PT). Therefore, the in-plane components of T (PE) or E (PT) are obtained by restricting \mathbb{C} in HOOKE's law to the components of the upper left 3×3 block matrix \mathbb{C}_{UL}^M or by restricting \mathbb{S} in the inverse HOOKE's law to the components of the upper left 3×3 block matrix \mathbb{S}_{UL}^M , respectively. We denote this restriction by \mathfrak{P} , where "P" stands for orthogonal projection onto a subspace.

$$\mathfrak{P}(\mathbb{C}) = \begin{bmatrix} C_{11}^M & C_{12}^M & C_{13}^M \\ & C_{22}^M & C_{23}^M \\ \text{sym} & & C_{33}^M \end{bmatrix} \mathbf{B}_\Gamma \otimes \mathbf{B}_\Lambda = C_{\Gamma\Lambda}^M \mathbf{B}_\Gamma \otimes \mathbf{B}_\Lambda \quad \forall \Gamma, \Lambda \in \{1, \dots, 3\} \quad (50)$$

If we pad the kernel or Null space, \mathfrak{P} is an 8th order tensor.

$$\mathfrak{P} = \frac{1}{2} (\delta_{\Theta\Gamma} \delta_{\Lambda\Delta} + \delta_{\Theta\Delta} \delta_{\Lambda\Gamma}) \mathbf{B}_\Theta \otimes \mathbf{B}_\Lambda \otimes \mathbf{B}_\Gamma \otimes \mathbf{B}_\Delta \quad \forall \Theta, \Lambda, \Gamma, \Delta \in \{1, \dots, 3\} \quad (51)$$

The projection is obtained as a scalar contraction $\mathfrak{P} :: \mathbb{C}$. We can then restrict attention to the in-plane components, which can easily be inverted.

$$\text{PE:} \quad \begin{bmatrix} T_1^M \\ T_2^M \\ T_3^M \end{bmatrix} = \begin{bmatrix} C_{11}^M & C_{12}^M & C_{13}^M \\ & C_{22}^M & C_{23}^M \\ \text{sym} & & C_{33}^M \end{bmatrix} \begin{bmatrix} E_1^M \\ E_2^M \\ E_3^M \end{bmatrix} \leftrightarrow \begin{bmatrix} E_1^M \\ E_2^M \\ E_3^M \end{bmatrix} = \begin{bmatrix} C_{11}^M & C_{12}^M & C_{13}^M \\ & C_{22}^M & C_{23}^M \\ \text{sym} & & C_{33}^M \end{bmatrix}^{-1} \begin{bmatrix} T_1^M \\ T_2^M \\ T_3^M \end{bmatrix} \quad (52)$$

$$\text{PT:} \quad \begin{bmatrix} E_1^M \\ E_2^M \\ E_3^M \end{bmatrix} = \begin{bmatrix} S_{11}^M & S_{12}^M & S_{13}^M \\ & S_{22}^M & S_{23}^M \\ \text{sym} & & S_{33}^M \end{bmatrix} \begin{bmatrix} T_1^M \\ T_2^M \\ T_3^M \end{bmatrix} \leftrightarrow \begin{bmatrix} T_1^M \\ T_2^M \\ T_3^M \end{bmatrix} = \begin{bmatrix} S_{11}^M & S_{12}^M & S_{13}^M \\ & S_{22}^M & S_{23}^M \\ \text{sym} & & S_{33}^M \end{bmatrix}^{-1} \begin{bmatrix} E_1^M \\ E_2^M \\ E_3^M \end{bmatrix} \quad (53)$$

Thus, in terms of the 3D stiffness C_{ij}^M , the 3D compliance $S_{ij}^M = [C_{ij}^M]^{-1}$ and the projection \mathfrak{P} we have the following realtions.

$$\text{PE:} \quad \begin{aligned} C_{ij}^{2D^M} &= (C_{ij}^M) = C_{ULij}^M \\ S_{ij}^{2D^M} &= \left[\mathfrak{P} \left([S_{ij}^M]^{-1} \right) \right]^{-1} = [C_{ULij}^M]^{-1} \end{aligned} \quad \forall i, j \in \{1, 2, 3\} \quad (54)$$

$$\text{PT:} \quad \begin{aligned} S_{ij}^{2D^M} &= \mathfrak{P} (S_{ij}^M) = S_{ULij}^M \\ C_{ij}^{2D^M} &= \left[\mathfrak{P} \left([C_{ij}^M]^{-1} \right) \right]^{-1} = [S_{ULij}^M]^{-1} \end{aligned} \quad \forall i, j \in \{1, 2, 3\} \quad (55)$$

It is no surprise that the plane stress stiffness is not equal to the plane strain stiffness, which is due to subsequent disparity.

$$\mathbb{S}_{UL}^M \neq [\mathbb{C}_{UL}^M]^{-1} \tag{56}$$

The latter is a consequence of the entries in the upper right (resp. lower left block) matrices. Due to the particular ordering for the plane states, these are not zero, even if the material is isotropic. Therefore, the projection \mathfrak{P} and the inversion are not commutative. Note that \mathfrak{P} is more than a projector with zero eigenvalues. We actually imply that we go from a six-dimensional to a three-dimensional space, in the sense of [Gurtin and Murdoch \(1975\)](#). Otherwise, the inverse is not defined, or one would need the pseudoinverse. Also, the plane states allow to restrict only to three non-zero components either for \mathbf{E} or \mathbf{T} , which would make HOOKE’s law a mapping between spaces of different dimensions. The latter is not invertible, which is why we restrict to the plane components. Since the out-of-plane components depend linearly on the in-plane-components, they can be obtained as secondary or derived quantities.

$$\text{PE: } \mathbf{T}_{\text{op}}^M = \begin{bmatrix} T_4^M \\ T_5^M \\ T_6^M \end{bmatrix} = [\mathbb{C}_{LL}^M] \begin{bmatrix} E_1^M \\ E_2^M \\ E_3^M \end{bmatrix} = [\mathbb{C}_{LL}^M] [\mathbb{C}_{UL}^M]^{-1} \begin{bmatrix} T_1^M \\ T_2^M \\ T_3^M \end{bmatrix} \tag{57}$$

$$\text{PT: } \mathbf{E}_{\text{op}}^M = \begin{bmatrix} E_4^M \\ E_5^M \\ E_6^M \end{bmatrix} = [\mathbb{S}_{LL}^M] \begin{bmatrix} T_1^M \\ T_2^M \\ T_3^M \end{bmatrix} = [\mathbb{S}_{LL}^M] [\mathbb{S}_{UL}^M]^{-1} \begin{bmatrix} E_1^M \\ E_2^M \\ E_3^M \end{bmatrix} \tag{58}$$

Such an approach has been used for in the context of homogenization by [Eidel et al. \(2019\)](#) for an anisotropic material, but with the VOIGT ordering $\{11,22,33,23,13,12\}$, such that the indices 2,3,4 form the 3×3 block-matrix for plane states in the \mathbf{e}_2 - \mathbf{e}_3 -plane, and without normalizing the basis. They consider a PT state, hence they map all values outside this block matrix in the compliance matrix to zero (see Eq. 4 in [Eidel et al. \(2019\)](#)).

4.3 Properties of the 2D Stiffnesses and Compliances

The matrix-vector-notation may be useful for numeric calculations. For symbolic calculations, it is slightly more convenient to solve the three equations as presented in Sect. 3.

We have seen that in PEs the form $\mathbf{T} = \mathbb{C}:\mathbf{E}$ and in the PTs the form $\mathbf{E} = \mathbb{S}:\mathbf{T}$ of HOOKE’s law is advantageous when going from 3D to 2D, since then one can simply restrict attention to the components of the upper left block matrix of \mathbb{C}^M or \mathbb{S}^M , presuming the MANDEL notation with the appropriate index assignment. The simplicity of the matrix-vector notation allows to identify some properties:

- the plane stiffness is positive homogeneous of degree 1 in terms of the 3D stiffness
- as a consequence of Cauchy’s interlacing theorem (see, e.g., [Hwang \(2004\)](#)), for a plane stress state the eigenvalues of the plane stiffness tensor are smaller than the eigenvalues of the 3D stiffness tensor: $(\lambda^{\text{PT}} \leq \lambda^{\text{3D}}) \implies$ stiffness is reduced
- for a plane strain state the eigenvalues of the plane compliance tensor are smaller than the eigenvalues of the 3D compliance tensor: $(\eta^{\text{PE}} \leq \eta^{\text{3D}}) \implies$ stiffness is increased

5 Simplifications induced by Material Symmetries

This section is dedicated to the application of Eqs. (12) and (14). Therefore, an isotropic material is analyzed under PT and PE first and then a material with trigonal symmetry is analyzed. The application to other symmetry classes (e.g. cubic, orthotropic, monoclinic) is straight-forward.

5.1 Isotropy

In this section we want to show that Eq. (24) and Eq. (35) are the correct representations of the elasticity and compliance tetrad for the PT and the PE, respectively. Therefore, we assume an isotropic and homogeneous material under small deformations at first.

The stiffness tetrad has then two independent components C_{1111} and C_{1122} . The components of the stiffness tetrad \mathbb{C} are as follows.

$$\begin{array}{lll}
 C_{1111} = C_{1111} & C_{1122} = C_{1122} & C_{1133} = C_{1122} \\
 C_{2211} = C_{1122} & C_{2222} = C_{1111} & C_{2233} = C_{1122} \\
 C_{3311} = C_{1122} & C_{3322} = C_{1122} & C_{3333} = C_{1111} \\
 C_{2323} = \frac{1}{2}(C_{1111} - C_{1122}) & C_{1313} = \frac{1}{2}(C_{1111} - C_{1122}) & C_{1212} = \frac{1}{2}(C_{1111} - C_{1122}) \\
 C_{3232} = \frac{1}{2}(C_{1111} - C_{1122}) & C_{3131} = \frac{1}{2}(C_{1111} - C_{1122}) & C_{2121} = \frac{1}{2}(C_{1111} - C_{1122}) \\
 C_{3223} = \frac{1}{2}(C_{1111} - C_{1122}) & C_{3113} = \frac{1}{2}(C_{1111} - C_{1122}) & C_{2112} = \frac{1}{2}(C_{1111} - C_{1122}) \\
 C_{2332} = \frac{1}{2}(C_{1111} - C_{1122}) & C_{1331} = \frac{1}{2}(C_{1111} - C_{1122}) & C_{1221} = \frac{1}{2}(C_{1111} - C_{1122})
 \end{array}$$

All other components are zero. With this definition of \mathbb{C} we can calculate \mathbb{C}^{2D} for a PT after Eq. (24) and insert this tetrad into Eq. (12) to determine the expressions for the stresses under a PT. This results in subsequent constitutive relations.

$$\begin{aligned}
 T_{11}^{PT} &= \left[C_{1111} - \frac{C_{1122}^2}{C_{1111}} \right] E_{11}^{PT} + \left[C_{1122} - \frac{C_{1122}^2}{C_{1111}} \right] E_{22}^{PT} \\
 T_{12}^{PT} &= \frac{1}{2} [C_{1111} - C_{1122}] E_{12}^{PT} \\
 T_{21}^{PT} &= \frac{1}{2} [C_{1111} - C_{1122}] E_{12}^{PT} \\
 T_{22}^{PT} &= \left[C_{1122} - \frac{C_{1122}^2}{C_{1111}} \right] E_{11}^{PT} + \left[C_{1111} - \frac{C_{1122}^2}{C_{1111}} \right] E_{22}^{PT}
 \end{aligned} \tag{59}$$

The term $-\frac{C_{1122}^2}{C_{1111}}$ is the correction term of the components in the normal directions for a PT to guarantee that the stresses in the third direction are zero. For this example the tetrad \mathbb{C}^{PT} has the following components.

$$\begin{array}{ll}
 C_{1111}^{PT} = C_{1111} - \frac{C_{1122}^2}{C_{1111}} & C_{1122}^{PT} = C_{1122} - \frac{C_{1122}^2}{C_{1111}} \\
 C_{2211}^{PT} = C_{1122} - \frac{C_{1122}^2}{C_{1111}} & C_{2222}^{PT} = C_{1111} - \frac{C_{1122}^2}{C_{1111}} \\
 C_{1212}^{PT} = \frac{1}{2}(C_{1111} - C_{1122}) & C_{2112}^{PT} = \frac{1}{2}(C_{1111} - C_{1122}) \\
 C_{1221}^{PT} = \frac{1}{2}(C_{1111} - C_{1122}) & C_{2121}^{PT} = \frac{1}{2}(C_{1111} - C_{1122})
 \end{array}$$

These components are not zero and afterwards, with Eqs. (19)-(21) someone can calculate the strains resulting in the third direction. These are:

$$E_{13} = 0 \qquad E_{23} = 0 \qquad E_{33} = -\frac{C_{1122}}{C_{1111}} (E_{11}^{PT} + E_{22}^{PT})$$

Up next, the same procedure is performed for the PE. Eq. (14) will be followed by subsequent expressions.

$$\begin{aligned}
 E_{11}^{PE} &= \frac{C_{1111}}{C_{1111}^2 - C_{1122}^2} T_{11}^{PE} - \frac{C_{1122}}{C_{1111}^2 - C_{1122}^2} T_{22}^{PE} \\
 E_{12}^{PE} &= \frac{1}{C_{1111} - C_{1122}} T_{12}^{PE} \\
 E_{21}^{PE} &= \frac{1}{C_{1111} - C_{1122}} T_{12}^{PE} \\
 E_{22}^{PE} &= \frac{C_{1111}}{C_{1111}^2 - C_{1122}^2} T_{22}^{PE} - \frac{C_{1122}}{C_{1111}^2 - C_{1122}^2} T_{11}^{PE}
 \end{aligned} \tag{60}$$

Through the inversion of the compliance tetrad by applying the MANDEL scheme Brannon (2018) the corresponding stiffness tetrad \mathbb{C}^{PE} is derived without a correction term for the stiffness tetrad (This result is expected, cf. Sect. 4.2.). The components of the

stiffness tetrad for the PE are:

$$\begin{aligned}
 C_{1111}^{\text{PE}} &= C_{1111} & C_{1122}^{\text{PE}} &= C_{1122} \\
 C_{2211}^{\text{PE}} &= C_{1122} & C_{2222}^{\text{PE}} &= C_{1111} \\
 C_{1212}^{\text{PE}} &= \frac{1}{2}(C_{1111} - C_{1122}) & C_{2112}^{\text{PE}} &= \frac{1}{2}(C_{1111} - C_{1122}) \\
 C_{1221}^{\text{PE}} &= \frac{1}{2}(C_{1111} - C_{1122}) & C_{2121}^{\text{PE}} &= \frac{1}{2}(C_{1111} - C_{1122})
 \end{aligned}$$

The other components are zero. And from Eqs. (30)-(32) the stresses resulting in the third directions for a PE are determined.

$$T_{13} = 0 \qquad T_{23} = 0 \qquad T_{33} = \frac{C_{1122}}{C_{1111} + C_{1122}} (T_{11}^{\text{PE}} + T_{22}^{\text{PE}})$$

The results of this section are in accordance with the specific literature, e.g. [Altenbach et al. \(2018\)](#); [Chaboche and Lemaitre \(1990\)](#); [Bertram and Glüge \(2015\)](#), and serve as verification for derived equations, consequently.

5.2 Trigonal

In this section a trigonal material is analyzed under a PT and a PE. The stiffness tetrad of a trigonal material contains six independent components C_{1111} , C_{1122} , C_{1133} , C_{3333} , C_{1123} and C_{2323} which are arranged as follows.

$$\begin{array}{lll}
 C_{1111} = C_{1111} & C_{1122} = C_{1122} & C_{1133} = C_{1133} \\
 C_{2211} = C_{1122} & C_{2222} = C_{1111} & C_{2233} = C_{1133} \\
 C_{3311} = C_{1133} & C_{3322} = C_{1133} & C_{3333} = C_{3333} \\
 C_{2323} = C_{2323} & C_{1313} = C_{2323} & C_{1212} = \frac{1}{2}(C_{1111} - C_{1122}) \\
 C_{3232} = C_{2323} & C_{3131} = C_{2323} & C_{2121} = \frac{1}{2}(C_{1111} - C_{1122}) \\
 C_{3223} = C_{2323} & C_{3113} = C_{2323} & C_{2112} = \frac{1}{2}(C_{1111} - C_{1122}) \\
 C_{2332} = C_{2323} & C_{1331} = C_{2323} & C_{1221} = \frac{1}{2}(C_{1111} - C_{1122}) \\
 C_{1123} = C_{1123} & C_{2223} = -C_{1123} & C_{1312} = C_{1123} \\
 C_{1132} = C_{1123} & C_{2232} = -C_{1123} & C_{1321} = C_{1123} \\
 C_{2311} = C_{1123} & C_{2322} = -C_{1123} & C_{1213} = C_{1123} \\
 C_{3211} = C_{1123} & C_{3222} = -C_{1123} & C_{2113} = C_{1123}
 \end{array}$$

The components of the tetrad which are not mentioned are zero. For the PT the following expressions for the stresses results from Eq. (12).

$$\begin{aligned}
 T_{11}^{\text{PT}} &= \left[C_{1111} - \frac{C_{1133}^2}{C_{3333}} \right] E_{11}^{\text{PT}} + \left[C_{1122} - \frac{C_{1133}^2}{C_{3333}} \right] E_{22}^{\text{PT}} \\
 T_{12}^{\text{PT}} &= [C_{1111} - C_{1122}] E_{12}^{\text{PT}} \\
 T_{21}^{\text{PT}} &= [C_{1111} - C_{1122}] E_{12}^{\text{PT}} \\
 T_{22}^{\text{PT}} &= \left[C_{1122} - \frac{C_{1133}^2}{C_{3333}} \right] E_{11}^{\text{PT}} + \left[C_{1111} - \frac{C_{1133}^2}{C_{3333}} \right] E_{22}^{\text{PT}}
 \end{aligned} \tag{61}$$

The normal stresses are corrected with the term $-\frac{C_{1133}^2}{C_{3333}}$ and the shear stress is doubled. After this Eq. (24) can be used to determine the PT stiffness tetrad. This leads to a stiffness tetrad with following nonzero components.

$$\begin{array}{ll}
 C_{1111}^{\text{PT}} = C_{1111} - \frac{C_{1133}^2}{C_{3333}} & C_{1122}^{\text{PT}} = C_{1122} - \frac{C_{1133}^2}{C_{3333}} \\
 C_{2211}^{\text{PT}} = C_{1122} - \frac{C_{1133}^2}{C_{3333}} & C_{2222}^{\text{PT}} = C_{1111} - \frac{C_{1133}^2}{C_{3333}} \\
 C_{1212}^{\text{PT}} = C_{1111} - C_{1122} & C_{2112}^{\text{PT}} = C_{1111} - C_{1122} \\
 C_{1221}^{\text{PT}} = C_{1111} - C_{1122} & C_{2121}^{\text{PT}} = C_{1111} - C_{1122}
 \end{array}$$

Finally, the strains in the third direction can be calculated. Following values for the strains result.

$$\begin{aligned} E_{13} &= -\frac{C_{1123}}{C_{2323}} E_{12}^{\text{PT}} \\ E_{23} &= -\frac{C_{1123}}{2 C_{2323}} \left(E_{11}^{\text{PT}} - E_{22}^{\text{PT}} \right) \\ E_{33} &= -\frac{C_{1133}}{C_{3333}} \left(E_{11}^{\text{PT}} + E_{22}^{\text{PT}} \right) \end{aligned}$$

Due to the anisotropic material, shear strains in the third direction result next to the normal strain. As well, this analyses is done for the PE. Eq. (14) results in subsequent expressions.

$$\begin{aligned} E_{11}^{\text{PE}} &= \left[\frac{C_{3333} (C_{1123}^2 - C_{1111} C_{2323}) + C_{2323} C_{1133}^2}{\bar{C}_1} - \frac{C_{1133}^2}{\bar{C}_2} \right] T_{11}^{\text{PE}} \\ &+ \left[\frac{C_{3333} (C_{1123}^2 + C_{1122} C_{2323}) - C_{2323} C_{1133}^2}{\bar{C}_1} - \frac{C_{1133}^2}{\bar{C}_2} \right] T_{22}^{\text{PE}} \\ E_{12}^{\text{PE}} &= -\frac{2 C_{2323}}{C_{1123}^2 - 2 C_{1111} C_{2323} + 2 C_{1122} C_{2323}} T_{12}^{\text{PE}} \\ E_{21}^{\text{PE}} &= -\frac{2 C_{2323}}{C_{1123}^2 - 2 C_{1111} C_{2323} + 2 C_{1122} C_{2323}} T_{12}^{\text{PE}} \\ E_{22}^{\text{PE}} &= \left[\frac{C_{3333} (C_{1123}^2 + C_{1122} C_{2323}) - C_{2323} C_{1133}^2}{\bar{C}_1} - \frac{C_{1133}^2}{\bar{C}_2} \right] T_{11}^{\text{PE}} \\ &+ \left[\frac{C_{3333} (C_{1123}^2 - C_{1111} C_{2323}) - C_{2323} C_{1133}^2}{\bar{C}_1} - \frac{C_{1133}^2}{\bar{C}_2} \right] T_{22}^{\text{PE}} \end{aligned} \quad (62)$$

Herein we have used subsequent abbreviations.

$$\begin{aligned} \bar{C}_1 &= 2 C_{1111} \left(C_{3333} C_{1123}^2 + C_{2323} C_{1133}^2 \right) \\ &+ C_{3333} \left[C_{2323} \left(C_{1122}^2 - C_{1111}^2 \right) + 2 C_{1122} C_{1123}^2 \right] \\ &- 2 C_{1133}^2 \left(C_{2323} C_{1122} + 2 C_{1123}^2 \right) \\ \bar{C}_2 &= (C_{1111} + C_{1122}) \left(C_{1111} C_{3333} + C_{1122} C_{3333} - 2 C_{1133}^2 \right) \end{aligned}$$

To derive the stiffness tetrad for the PE the VOIGT scheme is applied again to the compliance tetrad and then this tetrad is inverted. The components of the stiffness tetrad for the PE which are not zero are as follows.

$$\begin{aligned} C_{1111}^{\text{PE}} &= \frac{C_{1111} C_{2323} - C_{1123}^2}{C_{2323}} & C_{1122}^{\text{PE}} &= \frac{C_{1122} C_{2323} + C_{1123}^2}{C_{2323}} \\ C_{2211}^{\text{PE}} &= \frac{C_{1122} C_{2323} + C_{1123}^2}{C_{2323}} & C_{2222}^{\text{PE}} &= \frac{C_{1111} C_{2323} - C_{1123}^2}{C_{2323}} \\ C_{1212}^{\text{PE}} &= \frac{2 C_{2323} (C_{1111} - C_{1122}) - C_{1123}^2}{8 C_{2323}} & C_{2112}^{\text{PE}} &= \frac{2 C_{2323} (C_{1111} - C_{1122}) - C_{1123}^2}{8 C_{2323}} \\ C_{1221}^{\text{PE}} &= \frac{2 C_{2323} (C_{1111} - C_{1122}) - C_{1123}^2}{8 C_{2323}} & C_{2121}^{\text{PE}} &= \frac{2 C_{2323} (C_{1111} - C_{1122}) - C_{1123}^2}{8 C_{2323}} \end{aligned}$$

In the last step, the shear and normal stresses in the third direction are calculated after Eqs. (30)-(32).

$$\begin{aligned} T_{13} &= \frac{C_{1123}}{C_{1111} - C_{1122}} T_{12}^{\text{PE}} \\ T_{23} &= \frac{C_{1123}}{C_{1111} - C_{1122}} \left(T_{11}^{\text{PE}} - T_{22}^{\text{PE}} \right) \\ T_{33} &= \frac{C_{1133}}{C_{1111} + C_{1122}} \left(T_{11}^{\text{PE}} + T_{22}^{\text{PE}} \right) \end{aligned}$$

Again, it can be seen that through the anisotropic material, shear stresses in the third direction result.

6 Neglection of reaction stresses in the plane strain case

By a simplified calculation of the plane strain stiffness by projecting the 3D stiffness, i.e. by simply dropping the out-of-plane columns and rows, one neglects the out-of-plane reaction stresses. These can become very large when the material is nearly incompressible. Therefore, the simplified plane stress stiffness can lead to nonconservative estimates, underestimating the actual stresses. This effect can be observed in the homogenization of polymeric materials with a spherulitic microstructure. Inside the spherulites, a crystalline phase with $\nu \approx 0.3$ and an amorphous phase with $\nu \approx 0.499$ are layered. The common in plane strain enforces a considerable out of plane stress in the amorphous phase, which manifests as an apparent stiffness. The increased stiffness is also referred to as the reinforcement or contiguity factor (originally introduced by [Tsai and Pagano \(1968\)](#)), as the oedometric effect or as the confinement effect ([Glüge et al. \(2019\)](#)). If it is not taken into account, the effective stiffness of polymers is usually underestimated.

To quantify the effect of the simplified plane strain stiffness we examined the eigenvalues of an apparent isotropic stiffness in both plane stress and plane strain situations. In isotropic 3D elasticity, it is well known that $\lambda_1 = 3K$ and $\lambda_2 = 2G$ hold true. Here K is the compression modulus and G is the shear modulus of the material. This means that λ_1 corresponds to the resistance to dilatations and λ_2 to the resistance to distortions. The eigenvalues of the stiffness tetrads are given in Tab. 1. Obviously the second eigenvalue is the same for all three states while the first eigenvalue of plane states differs in the following way.

$$\lambda_1^{\text{PT}} = \lambda_1^{\text{3D}} - C_{1122} - 2 \frac{C_{1122}^2}{C_{1111}} \quad (63)$$

$$\lambda_1^{\text{PE}} = \lambda_1^{\text{3D}} - C_{1122} \quad (64)$$

Due to the claim of positive definiteness of all stiffness tetrads it is necessary that $C_{1111} > 0$ holds true. With this restriction and the definition of the eigenvalues (cf. Tab. 1) for all three states we can formulate the following restrictions for the component C_{1122} . Whereby, we perform a normalization with C_{1111} for a better evaluation and introduce the abbreviation $\Psi = C_{1122}/C_{1111}$.

$$\text{3D: } -\frac{1}{2} < \Psi < 1 \quad (65)$$

$$\text{PT: } -\frac{1}{2} < \Psi < 1 \quad (66)$$

$$\text{PE: } -1 < \Psi < 1 \quad (67)$$

Considering these restrictions we plot the first eigenvalue presented in Tab. 1 on the normalized stiffness coefficient Ψ , while normalizing the eigenvalues by C_{1111} as well. All three cases are visualized in Fig. 2, next to the normalized values of steel (stiff material) and a nearly incompressible material. The values are taken from [Bertram and Glüge \(2015\)](#). We can clearly identify a linear dependence in the 3D case and for a plane strain case, while the first eigenvalue is strongly non-linear in C_{1122} in the plane strain case.

We can identify two points of intersection between the 3D- and the PT case, which are at $\Psi = -0.5$ and $\Psi = 0$. Comparing the 3D- and the plane strain case, we find one intersection at $\Psi = 0$. Only in these intersections the plane state stiffness is obtained by dropping rows and columns of the 3D stiffness. Fig. 2 contains exemplary values of steel and a nearly incompressible material for these three states. One can see that the simplified calculation of the plane stiffnesses can only be used for stiff materials but not for a nearly incompressible materials due to the large error.

This is most clearly understood in terms of POISSON's ratio ν . For a nearly incompressible material with $\nu \rightarrow 0.5$ (equal to $\Psi \rightarrow 1$) the error is largest because the true apparent compressive modulus tends to infinity, which is not accounted for by simply dropping rows and columns from the 3D stiffness. The intersection at $\Psi = 0$ corresponds to $\nu = 0$, i.e. the case that $K = 2G/3$, and the interval $-1 < \Psi < 0$ represents auxetic materials with negative POISSON's ratios, i.e. $0 < K < 2G/3$. The second eigenvalue is not changing under the assumptions of plane states. Similar results are obtained by plotting the first eigenvalue and the eigenvalue ratio versus POISSON's ratio, cf. Figure 3. Especially, the right diagram in Fig. 3 shows the growing error when a simplified plane stiffness is obtained in case of a plane strain state. Again, for $\nu \rightarrow 0.5$ the error becomes infinite.

7 Summary

In the forgoing chapters the reduced plane stiffnesses for plane stress and plane strain states are derived, once with tensor algebra and apart from that in vector-matrix notation. Both possibilities have their eligibility:

- In the tensorial notation, the primitive geometric quantities like the normal vector of the plane stress or plane state plane, the directions and planes of material symmetry and the rotations of the symmetry group appear directly in the equations. These

Tab. 1: Isotropic eigenvalues $\lambda_\alpha \forall \alpha \in \{1, 2\}$ of \mathbb{C} , \mathbb{C}^{PT} , and \mathbb{C}^{PE}

	\mathbb{C}	\mathbb{C}^{PT}	\mathbb{C}^{PE}
λ_1	$C_{1111} + 2C_{1122}$	$C_{1111} + C_{1122} - 2 \frac{C_{1122}^2}{C_{1111}}$	$C_{1111} + C_{1122}$
λ_2	$C_{1111} - C_{1122}$	$C_{1111} - C_{1122}$	$C_{1111} - C_{1122}$

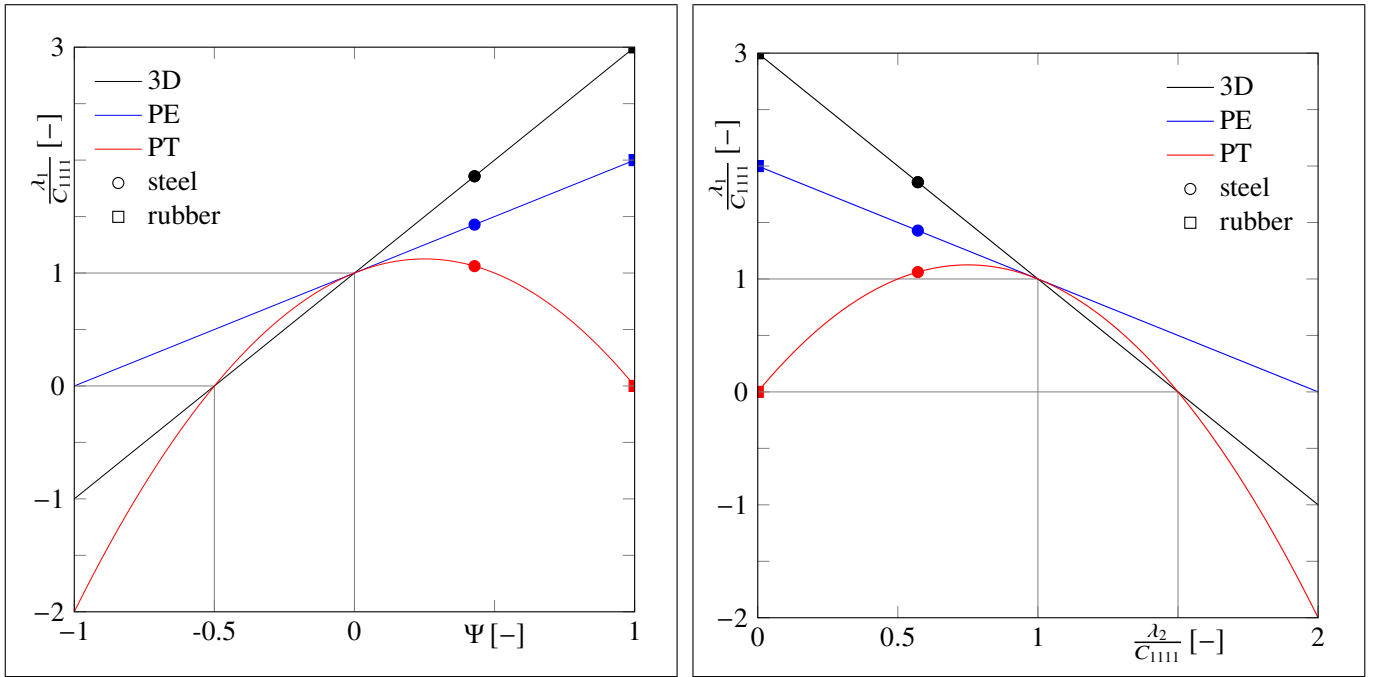


Fig. 2: Normalized first eigenvalue versus Ψ (left) and normalized first versus normalized second eigenvalue (right) for an isotropic material.

are rather obfuscated in the 6×6 matrix notation. For example, if the plane of symmetry does not coincide with the plane stress or plane strain state, it is very hard to give the reduced stiffness directly in matrix form.

- On the other hand, many theorems of linear algebra require a vector-matrix notation *with underlying orthonormal bases*. For example, the fact that the plane stress stiffness is smaller than the plane strain stiffness in terms of eigenvalues follows directly from Cauchy’s interlacing theorem, which requires a matrix representation. Also, the eigenvalues (or Kelvin-moduli) are readily calculated from a matrix representation.

Therefore one should have both representations available, be able to switch between them, and employ them accordingly. From these investigations (eigenvalue analysis) we know that the assumption of the plane stress state leads always to a smaller reduced plane stiffness and the plane strain leads always to an increased plane stiffness for all symmetry classes. This is a consequence of the reaction stresses due to the additional kinematic constraint in the plane strain case.

We limited our explanations to the field of linear elasticity with small deformations. Often, when the plane stress- or plane strain state is used, the material is assumed to be isotropic. However, in many cases the materials may be anisotropic due to the

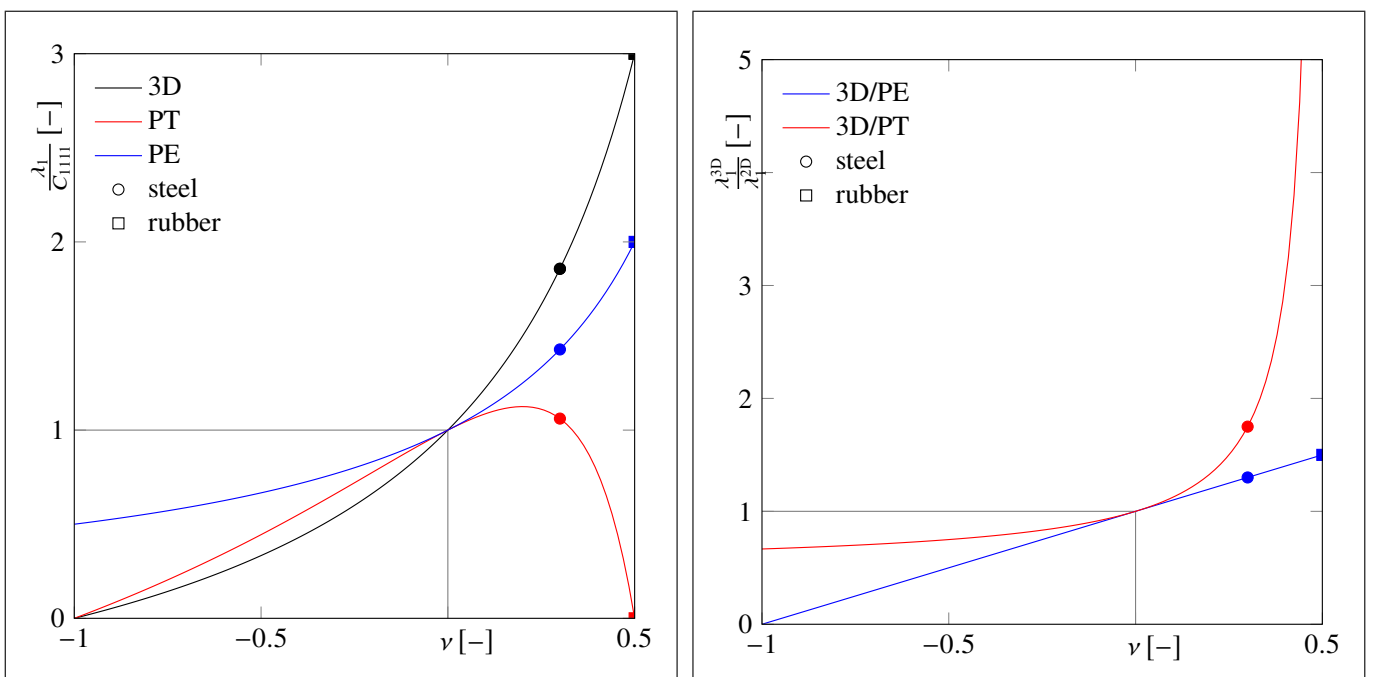


Fig. 3: Normalized first eigenvalue (left) and eigenvalue ratio (right) for an isotropic material, depending on Poisson’s ratio ν

manufacturing process. Nevertheless, it appears that it is not well known how the plane stiffnesses are derived in the anisotropic case. We hope to convince the community that works on reduced-dimensional problems to use the reduced plane stiffnesses also in the anisotropic case, instead of using 3D models. The presented formulations offer the possibility to derive expressions of plane stress and plane strain elements for commercial FE codes like ABAQUS or ANSYS, or derive plate or shell equations for anisotropic materials like rolled steel sheets. However, the present elaboration does not envisage the case of time-variant problematics, i.e. when considering rheonomous material behavior, advanced constitutive relations have to be considered. These may be reduced to a plane formulation by subjecting them to an analogous treatment as presented here. Moreover, we examine the apparent increase of stiffness in case of plane strains due to the plane strain kinematic constraint, and discuss the how the error of simplified plane stiffness depends on the material's compressive behaviour. We conclude that the simplified plane stiffness that is obtained by dropping rows and columns from the 3D stiffness should not be used in the plane strain case when the compression modulus is greater than the bulk modulus. That is, when $\nu > 0.125$.

Acknowledgment and Funding Information

The financial support rendered by the German Research Foundation (DFG) in context of the research training group 'Micro-Macro-Interactions of Structured Media and Particle Systems' (RTG 1554) is gratefully acknowledged. Furthermore, the authors deeply thank the reviewers for their valuable suggestions, which, without a doubt, greatly improved the quality of the present manuscript.

References

- G. B. Airy. IV. On the Strains in the Interior of Beams. *Philosophical Transactions of the Royal Society of London*, 153:49–79, 1863. doi: [10.1098/rstl.1863.0004](https://doi.org/10.1098/rstl.1863.0004).
- H. Altenbach, J. Altenbach, and W. Kissing. *Mechanics of Composite Structural Elements*. Springer Singapore, 2018. doi: [10.1007/978-981-10-8935-0](https://doi.org/10.1007/978-981-10-8935-0).
- G. I. Barenblatt. The formation of equilibrium cracks during brittle fracture. General ideas and hypotheses. Axially-symmetric cracks. *Journal of Applied Mathematics and Mechanics*, 23(3):622–636, 1959. doi: [10.1016/0021-8928\(59\)90157-1](https://doi.org/10.1016/0021-8928(59)90157-1).
- A. Bertram and R. Glüge. *Solid Mechanics. Theory, Modeling, and Problems*. Springer, 2015. doi: [10.1007/978-3-319-19566-7](https://doi.org/10.1007/978-3-319-19566-7).
- R. M. Brannon. *Rotation Reflection and Frame Changes Orthogonal tensors in computational engineering mechanics*. IOP Publishing, 2018. doi: [10.1088/978-0-7503-1454-1](https://doi.org/10.1088/978-0-7503-1454-1).
- S. D. Carothers. XXVI.—Plane Strain in a Wedge, with Applications to Masonry Dams. *Proceedings of the Royal Society of Edinburgh*, 33:292–306, 1914. doi: [10.1017/s0370164600031448](https://doi.org/10.1017/s0370164600031448).
- J.-L. Chaboche and J. Lemaitre. *Mechanics of solid materials*. Cambridge University Press Cambridge, 1990. doi: [10.1017/CBO9781139167970](https://doi.org/10.1017/CBO9781139167970).
- S. C. Cowin and M. M. Mehrabadi. On the identification of material symmetry for anisotropic elastic materials. *The Quarterly Journal of Mechanics and Applied Mathematics*, 40(4):451–476, 11 1987. doi: [10.1093/qjmam/40.4.451](https://doi.org/10.1093/qjmam/40.4.451).
- S. C. Cowin and M. M. Mehrabadi. The structure of the linear anisotropic elastic symmetries. *Journal of the Mechanics and Physics of Solids*, 40(7):1459–1471, 1992. doi: [10.1016/0022-5096\(92\)90029-2](https://doi.org/10.1016/0022-5096(92)90029-2).
- D. S. Dugdale. Yielding of steel sheets containing slits. *Journal of the Mechanics and Physics of Solids*, 8(2):100–104, 1960. doi: [10.1016/0022-5096\(60\)90013-2](https://doi.org/10.1016/0022-5096(60)90013-2).
- B. Eidel, A. Gote, M. Ruby, L. Holzer, L. Keller, and X. Jiang. Estimating the effective elasticity properties of a diamond/ β -sic composite thin film by 3d reconstruction and numerical homogenization. *Diamond and Related Materials*, 97:107406, 2019. doi: [10.1016/j.diamond.2019.04.029](https://doi.org/10.1016/j.diamond.2019.04.029).
- A. Flamant. Sur la répartition des pressions dans un solide rectangulaire chargé transversalement. *CR Acad. Sci. Paris*, 114: 1465–1468, 1892.
- S. Forte and M. Vianello. Symmetry classes for elasticity tensors. *Journal of Elasticity*, 43(2):81–108, 1996. doi: [10.1007/BF00042505](https://doi.org/10.1007/BF00042505).
- R. Glüge, H. Altenbach, I. Kolesov, N. Mahmood, M. Beiner, and R. Androsch. On the effective elastic properties of isotactic polypropylene. *Polymer*, 160:291–302, 2019. doi: [10.1016/j.polymer.2018.10.061](https://doi.org/10.1016/j.polymer.2018.10.061).
- Kh. S. Golovin. One problem in statics of an elastic body (in Russian). *Izvestiya St. Peterburg Prakt. Tekhnol. Inst*, 3:373–410, 1881.
- M. E. Gurtin. The linear theory of elasticity. In S. Flügge, editor, *Handbuch der Physik*, volume Bd. 6, Teile 1-2, pages 1–295. Springer-Verlag, 1972. doi: [10.1007/978-3-662-39776-3_1](https://doi.org/10.1007/978-3-662-39776-3_1).
- M. E. Gurtin and I. A. Murdoch. A continuum theory of elastic material surfaces. *Archive for Rational Mechanics and Analysis*, 57 (4):291–323, 1975. doi: [10.1007/BF00261375](https://doi.org/10.1007/BF00261375).
- P. Helnwein. Some remarks on the compressed matrix representation of symmetric second-order and fourth-order tensors. *Computer Methods in Applied Mechanics and Engineering*, 190(22):2753–2770, 2001. doi: [10.1016/S0045-7825\(00\)00263-2](https://doi.org/10.1016/S0045-7825(00)00263-2).
- S.-G. Hwang. Cauchy's interlace theorem for eigenvalues of hermitian matrices. *The American Mathematical Monthly*, 111(2): 157–159, 2004. doi: [10.1080/00029890.2004.11920060](https://doi.org/10.1080/00029890.2004.11920060).
- C. Kuhn, A. Schlüter, and R. Müller. On degradation functions in phase field fracture models. *Computational Materials Science*, 108:374–384, 2015. doi: [10.1016/j.commatsci.2015.05.034](https://doi.org/10.1016/j.commatsci.2015.05.034).

- M. Levy. Sur l'équilibre élastique d'une plaque rectangulaire. *Comptes Rendus Acad. Sci. Paris*, 129:535–539, 1899.
- A. E. H. Love. *A treatise on the mathematical theory of elasticity*, volume 2. Cambridge University Press Warehouse, 1944.
- J. Mandel. Generalisation de la theorie de plasticite de W. T. Koiter. *International Journal of Solids and Structures*, 1(3):273–295, 1965. doi: [10.1016/0020-7683\(65\)90034-X](https://doi.org/10.1016/0020-7683(65)90034-X).
- J. C. Maxwell. I.—On Reciprocal Figures, Frames, and Diagrams of Forces. *Transactions of the Royal Society of Edinburgh*, 26(1):1–40, 1870. doi: [10.1017/s0080456800026351](https://doi.org/10.1017/s0080456800026351).
- J. H. Michell. On the Direct Determination of Stress in an Elastic Solid, with application to the Theory of Plates. *Proceedings of the London Mathematical Society*, s1-31(1):100–124, 1899. doi: [10.1112/plms/s1-31.1.100](https://doi.org/10.1112/plms/s1-31.1.100).
- C. Miehe, F. Welschinger, and M. Hofacker. Thermodynamically consistent phase-field models of fracture: Variational principles and multi-field FE implementations. *International Journal for Numerical Methods in Engineering*, 83(10):1273–1311, 2010. doi: [10.1002/nme.2861](https://doi.org/10.1002/nme.2861).
- J. F. Nye. *Physical Properties of Crystals: Their Representation by Tensors and Matrices*. Oxford science publications. Clarendon Press, 1985.
- P. P. Teodorescu. One hundred years of investigations in the plane problem of the theory of elasticity. *Applied Mechanics Reviews*, 17(3):175–186, 1964.
- W. Thomson. Elements of a mathematical theory of elasticity. *Philosophical Transactions of the Royal Society of London*, 146:481–498, 1856.
- T. C. T. Ting. *Anisotropic Elasticity: Theory and Applications*. Oxford University Press, 1996.
- T. C. T. Ting. Generalized Cowin-Mehrabadi theorems and a direct proof that the number of linear elastic symmetries is eight. *International Journal of Solids and Structures*, 40(25):7129–7142, 2003. doi: [10.1016/S0020-7683\(03\)00358-5](https://doi.org/10.1016/S0020-7683(03)00358-5).
- S. W. Tsai and N. J. Pagano. *Invariant Properties of Composite Materials*. Defense Technical Information Center, 1968.
- W. Voigt. *Lehrbuch der Kristallphysik: (mit Ausschluss der Kristalloptik)*. B.G. Teubners Sammlung von Lehrbüchern auf dem Gebiete der mathematischen Wissenschaften ; Bd. XXXIV. B.G. Teubner, 1910. doi: [10.1007/978-3-663-15884-4](https://doi.org/10.1007/978-3-663-15884-4).
- M. Weber, R. Glüge, and A. Bertram. Distance of a stiffness tetrad to the symmetry classes of linear elasticity. *International Journal of Solids and Structures*, 2018. doi: [10.1016/j.ijsolstr.2018.08.021](https://doi.org/10.1016/j.ijsolstr.2018.08.021).
- H. Weyl. *The Classical Groups: Their Invariants and Representations*. Princeton mathematical series. Princeton University Press, 1939.
- H. Wittel, D. Jannasch, J. Voßiek, and C. Spura. Stirnräder mit Evolventenverzahnung. In *Roloff/Matek Maschinenelemente*, pages 825–878. Springer Fachmedien Wiesbaden, 2017. doi: [10.1007/978-3-658-17896-3_21](https://doi.org/10.1007/978-3-658-17896-3_21).
- Q. S. Zheng and J. P. Boehler. The description, classification, and reality of material and physical symmetries. *Acta Mechanica*, 102:73–89, 1994. doi: [10.1007/BF01178519](https://doi.org/10.1007/BF01178519).

RVE-size Estimation and Efficient Microstructure-based Simulation of Dual-Phase Steel

Frederik Scherff^{1,3*}, Jessica Gola^{2,3}, Sebastian Scholl³, Kinshuk Srivastava³, Thorsten Staudt³, Dominik Britz², Frank Mücklich², and Stefan Diebels¹

¹ Universität des Saarlandes, Lehrstuhl für Technische Mechanik, Campus A4.2, 66123 Saarbrücken, Germany

² Universität des Saarlandes, Lehrstuhl für Funktionswerkstoffe, Campus D3.3, 66123 Saarbrücken, Germany

³ AG der Dillinger Hüttenwerke, Werkstraße 1, 66763 Dillingen, Germany

Abstract: Dual-phase steel shows a pronounced structure-property correlation, caused by its internal structure consisting of a soft ferrite matrix and embedded hard martensite regions. Due to its high strength combined with high ductility, dual-phase steel is particularly suitable for energy-absorbing and strength-relevant sheet metal applications, but its use as heavy plate is also desirable. Due to the complex microstructure, microstructure-based simulation is essential for a realistic simulation of the mechanical properties of dual-phase steel. This paper describes two important points for the microstructure-based simulation of dual-phase steel. First a method for the straightforward experimental estimation of the RVE size based on hardness measurements prior to tomography preparation is presented and evaluated. Secondly, a method for the efficient meshing of these microstructures, based on material definition at the integration points of a finite element model, is developed.

Keywords: dual-phase steel, RVE size, FEM, 3D tomography, MatIP

1 Introduction

Steel is one of the most widely used structural materials; for example, in 2017 its production amount exceeded the production amount of all plastics by a factor of more than five (PlasticsEurope (2017)). According to this large production amount, there is also a large variety of different steel classes, which differ in their exact internal structure and their properties. One of these classes is dual-phase steel, characterized by a two-phase microstructure of hard martensite regions embedded in a soft ferrite matrix. Due to its microstructure, the mechanical properties of dual-phase steel are defined by high strength and high ductility at the same time (Tasan et al. (2015)). Due to this performance profile, it is classically used in energy-absorbing, strength-relevant sheet metal components (Brands et al. (2016); Tarigopula et al. (2008)). At the same time, however, efforts to use dual-phase steel also in heavy plate products, for example in pipelines, are increasing (Ishikawa et al. (2015); Ji et al. (2014); Li et al. (2011)). The strong structure-property correlation of dual-phase steel makes microstructure-based simulations an important method for improving its mechanical properties and for adapting them to a specific application. The most important microstructural parameters influencing the properties of dual-phase steel are the quantity, shape and distribution of the martensite regions in the ferrite (Das and Chattopadhyay (2009); Davies (1978); Kang et al. (2007); Kim and Lee (2000); Tasan et al. (2015)). For this reason, simulations are used within the framework of the finite element method (FEM, (Zienkiewicz and Taylor (1977))) that explicitly include both phases of the dual-phase steel in the analysis. Simulations based on the real structure of the dual-phase steel have the advantage that they include the entire phase structure in the analysis. Therefore, no structural properties relevant for the macroscopic material properties are unintentionally neglected. By modelling the ferrite and martensite as discrete areas of the mesh, all microstructural details can be taken into account. Therefore simulations based on the real structure usually show a good agreement with the corresponding experiments (Dong et al. (2010); Katani et al. (2013); Marvi-Mashhadi et al. (2012); Paul (2013); Ramazani et al. (2014, 2013)).

For a microstructure based simulation, a 3D reconstruction of the material is required that is large enough to be representative for the material in terms of shape, distribution and connectivity. In the field of materials science, 3D reconstructions based on real structure of various, usually multi-phase materials are used to investigate the 3D microstructure. Tomography enables the microstructural characterization of a defined sample volume in contrast to two-dimensional surface characterization. Thus, important information about the formation and evolution of the phases can be obtained, which allows conclusions to be drawn about the properties of the material (Ohser and Mücklich (2000)). There are different methods that allow 3D reconstruction of a metallic material. Established methods that can be used to image large volumes include X-ray microcomputed tomography (μ CT) (Desplentere et al. (2005); Yan et al. (2014); Zhou et al. (2018)) or serial sectioning tomography (Alkemper and Voorhees (2001); Keehan et al. (2008); Lasagni et al. (2007); Li et al. (1998); Mücklich et al. (2018); Roland et al. (2015)). At μ CT the sample is irradiated with X-rays from many different directions and thus a three-dimensional image of the inner microstructure of the sample is computed (Buzug (2008)). In serial sectioning tomography a large number of two-dimensional microscopic images of the sample is recorded by removing a thin layer of the sample between the individual images. The two-dimensional

images are then digitally combined to reconstruct the three-dimensional structure of the examined sample volume. A light optical serial sectioning tomography uses a light optical microscope to capture the image and the material is removed by mechanical polishing (Alkemper and Voorhees (2001); Li *et al.* (1998); Mücklich *et al.* (2018)). In case small cutting distances are required, a serial sectioning tomography can be performed using a focused ion beam (FIB) in a scanning electron microscope (SEM) (Burnett *et al.* (2016); Keehan *et al.* (2008); Lasagni *et al.* (2007); Li *et al.* (1998); Zhong *et al.* (2019)). However, not all 3D reconstruction methods are suitable for all metals, especially low alloyed, low carbon steels as investigated here. In case of steel, most transformation products are mostly iron, therefore showing a low atomic density contrast. A methodology that uses the material density contrast for the image acquisition, as the CT, can not be used. In addition, the resolution of CT depends on the observed volume. Very high resolutions can be achieved with small volumes. However, the resolution decreases with increasing volume of the sample (Fischer *et al.* (2011); Bauza *et al.* (2018)). Common FIB/SEM devices produce tomographies with a volume too small for the steels under consideration here (Brands *et al.* (2016); Mücklich *et al.* (2018)), but this issue can be overcome in specialized devices by adding a laser (Echlin and Pollock (2008)) or using other ion sources such as xenon (Burnett *et al.* (2016)) instead of gallium to increase the volume. In addition to the classical SEM images also other signals (e.g. EDS or EBSD) can be used for tomographies (Brands *et al.* (2016)). Another approach combines the advantages of classical serial sectioning tomography with images in SEM or EBSD (Uchic *et al.* (2016)). In comparison, the method of serial sectioning in combination with light microscopic images is widely used for steels. By contrasting the microstructures by etching, the different structure components can be separated (Britz *et al.* (2016)). For this reason, light optical serial sectioning tomography is still one of the most widely used methods for the production of large size steel tomography. Tomographies of two-phase steels with an edge length of 100-150 μm have already shown that the phases separated on 2D images have a high connectivity in 3D (Mücklich *et al.* (2015)).

The estimation of the size of the representative volume element (RVE) poses a particular challenge for simulations based on microstructures. The RVE describes the area of the microstructure that is just large enough to contain all relevant information about the microstructure (Hill (1963); Kanit *et al.* (2003); Tasan *et al.* (2014b)). A section of the microstructure with the size of the RVE thus shows the same microstructural properties at any point of the material. These properties additionally do not change for larger structural sections. Simulations on microstructure sections smaller than the RVE cannot reproduce the real macroscopic properties due to the scattering of the microstructure geometry depending on the location of the sampling. On one hand, simulations on microstructure sections larger than the RVE, on the other hand, require significantly more computing time and higher memory loads than necessary for simulation on a RVE due to the unnecessarily large geometry. The estimation of the RVE size is therefore a crucial point in the process of microstructure-based simulation. Nevertheless, the estimation of the RVE size is often carried out not at all (Katani *et al.* (2013); Paul (2013)) or only by time-consuming methods (Brands *et al.* (2016)). For these methods, a 3D tomography is carried out and it is compared to other tomographies of the same material or to the geometric parameters of a bigger micrograph of the sample. In this way, it can be determined, if the section is as big as or bigger than the RVE. If this is not the case, a new, bigger tomography has to be prepared. Therefore, methods to estimate the RVE's size before tomography preparation are desirable to save cost and time.

Tomographies with the size of a RVE often consist of tens of millions of voxels. This enormous size, coupled with the complex shape of the microstructure, poses difficulties for the simulation (Brands *et al.* (2016); Calcagnotto *et al.* (2010)). Due to the large number of elements, the computing time and the required amount of main memory considerably increases. In addition, unstructured geometry conforming meshing to reduce the number of elements of the FE mesh compared to the voxels of the tomography is very complex and only to a limited extent effective. In order to avoid these problems, simulations are often carried out only on the basis of two-dimensional structures in order to reduce the number of elements of the FE mesh and, in addition, the effort required to obtain the microstructure (Kadkhodapour *et al.* (2011); Paul (2013); Tasan *et al.* (2014b,a)). However, it has been shown that such two-dimensional simulations are not capable of correctly mapping the real material behavior (Diehl *et al.* (2016); Ramazani *et al.* (2013); Tasan *et al.* (2014a); Zeghadi *et al.* (2007)). As a result, three-dimensional simulations are indispensable despite the problems described. For this reason, straightforward methods of data reduction are needed to reduce the required computing time and memory load while preserving the microstructure information.

In the article two essential things for the correct microstructure-based simulation of dual-phase steel are presented. Due to the importance of the RVE, a straightforward experimental method for estimating the size of the RVE before the preparation of a tomography is described. It is based on the evaluation of different hardness indentations of the material. For an estimation of the RVE size based on the 3D microstructure, the first guess of the RVE size determines the size of the required tomography. Especially for an unexperienced experimentalist this procedure is trial-and-error and may require to take several time-consuming tomographies. Choosing the region of interest to large or to small will lead to additional time and costs with this method. This gives the main advantage of the proposed method based on hardness measurements, as it is easy and cheap to investigate even larger numbers of different hardness imprints for the estimation of the size of the RVE. The numerical simulation on the one hand and the determination of the relevant geometric parameters of the three-dimensional structure on the other hand serve as validation. The second topic of the work is the efficient numerical modeling based on the microstructure and its 3D tomographic representation. A data reduction approach based on material definition at the integration points of the finite element model is presented. The paper is structured as follows: In Sect. 2, the dual-phase steel under consideration in the study is presented and the experimental basics of the work, the tomography preparation and the process of performing the hardness measurements, are explained. Sect. 3 deals with the numerical implementation. In addition to the general FE implementation of the simulation, the developed data reduction method is described here. In Sect. 4 and Sect. 5, the results of the RVE size estimation and the data reduction are subsequently presented and evaluated. Sect. 6 summarizes the presented work and classifies it into the context of

modern microstructure-based simulations.

2 Material and experimental Methods

2.1 Dual-Phase steel

In this study a sample of a thermo-mechanically rolled dual-phase steel plate with a carbon content of approximately 0.06 wt% and a carbon equivalent of approximately 0.38 wt% was used. The microstructure consists of a ferritic matrix and a martensitic second phase. In Fig. 1 a light optical image using 500 \times resolution after modified Beraha etching according to (Britz *et al.* (2016)) and an electron microscopic image of one second phase object after electrolytic etching are shown. The second phase exhibits in an equiaxed shape, slightly stretched in rolling direction. The second phase objects in the electron microscopic image show a martensitic structure.

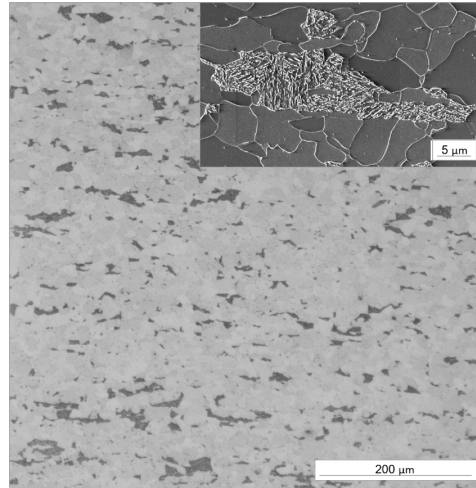


Figure 1: Light optical image of the Beraha etched sample with an electron microscopy image in the top right corner. In the light optical image, only the second phase is clearly contrasted (dark). In the SEM the substructure of the second phase becomes clear and also the grain boundaries of the ferrite are recognizable.

2.2 3D-Tomography

The setup presented by M \ddot{a} ijcklich *et al.* was used to produce a light microscopy serial sectioning tomography of the two-phase steel (M \ddot{u} cklich *et al.* (2015)). The tomography was performed on a modified setup based on a *Leica TXP* target preparation machine for the material removal and a digital light optical microscope (LOM) *VHX 2000* for imaging. This allows a semi-automatic execution of the working steps in one setup. For the production of the tomography data the sample was first fixed to the sample holder of the *TXP* machine with the embedding material *DEMOTec15+*. Then the following steps polishing, etching and image acquisition were repeated several hundred times in order to obtain a representative volume. The material removal was performed using a neoprene cloth and the polish suspension *MasterPrep* with diamond particles in an average diameter of 0.05 μm was used within the *TXP* machine. The material removal per cut was adjusted by the contact pressure of 30 N, the rotation speed of the polishing disk of 400 RPM and the polishing time of 3 min using 2 ml polishing suspension. A modified Beraha etching according to Britz *et al.* was used to contrast the microstructure (Britz *et al.* (2016)). With this etching it is possible to contrast the second phase regions stronger than the grain boundaries of the ferritic matrix, so that an optical separation of the second phase regions from the matrix was achieved (Britz *et al.* (2016)).

Thus, the different phases in microscope images can be segmented by threshold and the images can be converted into binary images by means of image processing programs, Fig. 2. A 3D tomographic reconstruction of the microstructure is obtained by reconstructing the z -position of the binarized images. For the reconstruction of the volume there were 426 images with 424×928 pixels and a pixel size of $409 \text{ nm} \times 409 \text{ nm}$ available after the pictures were taken. These pictures were first z -positioned with the program *Thermo Scientific Amira*[®] and then aligned. The alignment of the images was done using fixed markings on the sample, which were placed on the sample before the tomography process. These markings were also used to determine the original z -position after the material removal per cut. The binary images were generated by threshold segmentation in *Amira*. For this standard filters like shading correction and denoising were used. Artifacts and errors as well as all objects that were only visible in one image were deleted using binary operations. To provide isotropic voxels for the reconstruction, the binary image stack was interpolated to a z distance of 409 nm. Fig. 3 shows the 3D reconstruction of the sample.

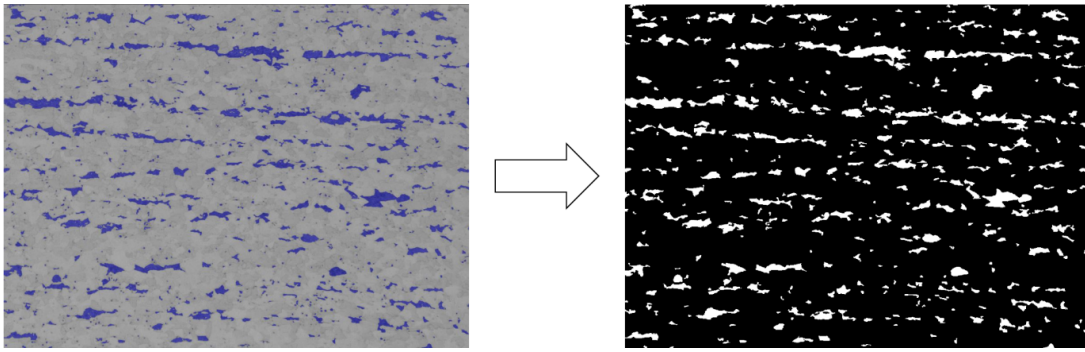


Figure 2: Exemplary representation of light optical images with selected second phase areas (left) and binary image after threshold segmentation (right) that is used for the reconstruction of the microstructure.

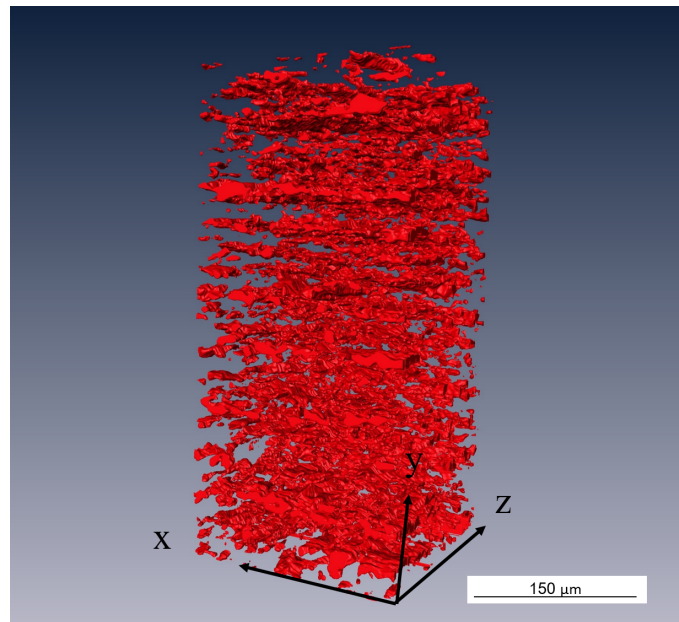


Figure 3: Visualization of the 3D reconstruction of the image stack.

2.3 3D parameter-based RVE size estimation

As an assumption, the 3D microstructure contains all necessary information about different structural components. Many parts of this 3D structure can be identified by determining parameters from 2D sections using stereological relationships (Ohser and Mücklich (2000)). However, parameters such as the connectivity of the phases can only be determined in 3D and a 2D analysis is not adequate, especially for such fissured phases. For this reason an evaluation of the RVE of the tomography was additionally determined by its 3D parameters. In order to find the RVE size cubic volume elements in different sizes were cropped and their characteristic 3D geometric parameters were measured using the program *Mavi*. For that purpose the parameters volume density, surface density, Euler density and particle density were examined for their spreading of the mean value. The quantities and their explanation are shown in Tab. 1. The first three quantities are implemented in *Mavi* and can be calculated from the fully reconstructed tomographies. For the particle density each individual second phase object in the set was counted and the number was divided by the whole volume. The Euler number from the Euler density is a measure of the connectivity of an object of a phase in a multi-phase material that consists of different objects. The calculation examines whether an object has a concave or convex curved surface or whether the surface is a saddle surface (Russ and Dehoff (2000)).

For the RVE estimation cubes with ten different edge lengths between 15 μm and 150 μm were selected. For each size four cubes are cropped from one large experimental data set and their 3D parameters were measured. The center point of the cubes remains at the same position for all sizes. For the estimation of the RVE, the mean value and the standard deviation of all 3D parameters were determined for the four cubes.

2.4 Indent-based RVE size estimation

In general, hardness describes the resistance of a material to the penetration by another object (Bargel *et al.* (2009)). In the present paper the hardness test according to Vickers (Bargel *et al.* (2009); Deutsches Institut für Normung (2006)) was used to estimate the RVE size. In the Vickers hardness measurement, an equilateral square diamond pyramid with an opening angle of 136° is pressed into the sample with a defined force F . After the unloading the diagonals d_1 and d_2 of the remaining imprint are

Table 1: Name and meaning of the volume-based parameters used for evaluation.

parameter	explanation
volume density	Ratio of the total volume of all second phase objects to the total volume of the tomography.
surface density	Ratio of the total surface of all second phase objects to the total surface of the tomography.
Euler density	Ratio of Euler number of the objects observed (difference between object number N and connectivity (object connections C)) to the total volume of the tomography
particle density	Ratio of the number of second phase objects to the total volume of the tomography.

measured and the hardness HV is determined to

$$HV = 2F \sin\left(\frac{136^\circ}{2}\right) \left(\frac{2}{d_1 + d_2}\right)^2, \quad (1)$$

where F is given in kilopond, d_1 and d_2 in millimeters. When specifying the hardness value, the test force is given by default, e. g. 160 $HV_{0.5}$ for a hardness value of 160, which was determined with a force of 0.5 kp. In theory, with varying test load used the imprint diameter changes while the hardness value remains constant (Strnad and Jakab-Farkas (2014)). Therefore, in the case of a completely homogeneous material, both very small and very large hardness imprints should result in the same hardness value with varying test loads.

Based on this assumption, a method for estimating the RVE size was developed in this study in order to overcome the disadvantages of the time-consuming methods described in Sect. 1. The functional principle is shown in Fig. 4. Each hardness imprint has a certain zone of influence, which is deformed by the imprint. A very small hardness imprint has correspondingly a very small zone of influence. Thus it is possible that the zone of influence lies entirely in a purely ferritic area or in a predominantly martensitic area of the microstructure. Due to this, very small hardness imprints show a high scattering in an inhomogeneous material. Above a certain indentation size, the zone of influence is just large enough to cover the size of an RVE. Starting from this indentation size, the spread of the hardness values decreases considerably, as a representative volume of the structure is examined at any time. In particular, the scattering for even larger imprints no longer decreases further, since a larger zone of influence contains no new microstructure information. Based on this hypothesis, a total of 121 hardness measurements were performed on the cross section¹ of the steel with loads ranging from 0.05 kp to 30 kp, see Tab. 2.

Table 2: Number of indents per load level

load [kp]	0.05	0.1	0.2	0.5	1	3	5	10	20	30
number [-]	36	25	16	9	16	9	4	4	1	1

The distance between two hardness imprints is chosen as at least three times the imprint diameter according to the norm for Vickers hardness measurements (Deutsches Institut für Normung (2006)).

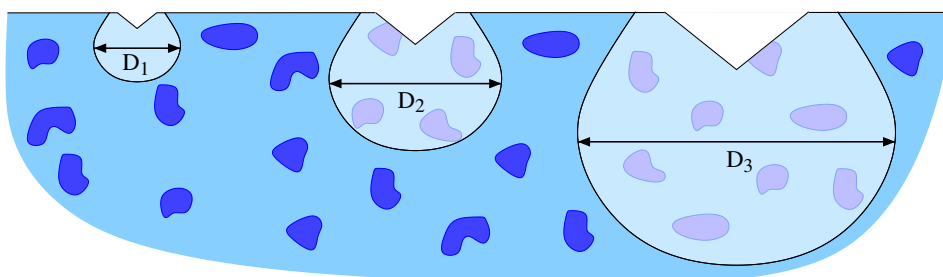


Figure 4: Schematic representation of three hardness imprints and their zones of influence. The size of the influence zone D is well below the RVE size on the left, in the middle in the area of the RVE size and well above it on the right.

3 Numerical Methods

Before the results of the methods for the estimation of the RVE size are discussed, an overview over the numerical methods used in the presented work are given in the following section. At first, the general implementation of the material behaviour in the context of FEM is explained. Then, the method developed for data reduction, i.e. material definition at the integration point, is presented.

¹Section spanned by the transverse direction and the normal direction.

3.1 General numerical implementation

The material is described by an elastoplastic material model. In addition, the examination is focused on the small strain range. Hooke's law is used for the elastic part of the model. Consequently, the relation between the engineering stress $\boldsymbol{\sigma}$ and the engineering strain $\boldsymbol{\varepsilon}$ reads

$$\boldsymbol{\sigma} = 2\mu(\boldsymbol{\varepsilon} - \boldsymbol{\varepsilon}_p) + \lambda \text{tr}(\boldsymbol{\varepsilon} - \boldsymbol{\varepsilon}_p) \mathbf{I}, \quad (2)$$

with the plastic part of the engineering strain $\boldsymbol{\varepsilon}_p$ and the Lamé parameters μ and λ . The plastic part model is described by a standard J_2 von Mises plasticity model (Mises (1913)) and isotropic, linear hardening. This results in a yield condition

$$g = \|\boldsymbol{\sigma}_D\| - \sqrt{\frac{2}{3}}(\sigma_y - K\alpha), \quad (3)$$

with the deviatoric part $\boldsymbol{\sigma}_D$ of the engineering stress tensor, the initial yield strength σ_y , the hardening modulus K and the flow parameter α . As small strains are considered, an additive decomposition of the strain tensor into its elastic and plastic part

$$\boldsymbol{\varepsilon} = \boldsymbol{\varepsilon}_e + \boldsymbol{\varepsilon}_p \quad (4)$$

is applied. The evolution of the plastic strain follows an associated flow rule

$$\dot{\boldsymbol{\varepsilon}}_p = \gamma \frac{\partial g}{\partial \boldsymbol{\sigma}}, \quad (5)$$

with the plastic multiplier γ .

The abovementioned material behaviour is implemented as an FEM model with the help of the open source C++ program library *deal.II* (Arndt et al. (2016); Bangerth et al. (2007)). Starting point is the balance of momentum for a body Ω with boundary Γ in its weak form in the stationary case

$$\int_{\Omega} \text{grad}(\delta \mathbf{u}) : \boldsymbol{\sigma}(\mathbf{u}) \, \forall = \int_{\Gamma} \delta \mathbf{u} \cdot \mathbf{t} \, a, \quad (6)$$

with the gradient operator $\text{grad}(\cdot)$, the test function $\delta \mathbf{u}$ and the Neumann boundary condition \mathbf{t} . The solution is then iteratively calculated with Newton's method. In this context, a high variability of the implemented code with respect to possible extension is achieved by calculating the required derivation of the balance of momentum not analytically, but by means of a numerical tangent (Goldschmidt (2015); Scherff (2019); Scherff et al. (2016)). Plasticity is treated by the Radial Return Method (Bednarczyk et al. (2008); Simo and Taylor (1985); Simo and Hughes (2000); Wilkins (1963)). Finite differences are applied for the calculation of the derivative of the yield condition with respect to the plastic increment for the sake of variability.

Although the analysis is limited to small macroscopic strains, large strains can theoretically occur within the microstructure. Therefore, in a previous study (Scherff (2019)), a Neo-Hooke model for finite deformation was used to investigate whether this has an impact. As expected, within the microscopic stress field relative deviations between the small strain model and the large strain model of up to 10% were observed. Nevertheless it could be shown that the small strain model leads to negligibly small deviations well below 1% for the macroscopic stress-strain relationship under uniaxial tension. Therefore, the small strain model is applicable in the use case under consideration.

The parameters used for the single ferrite and martensite phase were determined with the help of nanoindentation tests, see Scherff (2019). They are given in Tab. 3. As shown in Scherff (2019), the simulation model described above is capable to reproduce the real behavior of the investigated dual-phase steel under uniaxial load with high accuracy.

Table 3: Material parameters used in this study for the ferrite and martensite phase.

	ferrite	martensite
μ [GPa]	89.5	91.7
λ [GPa]	173.7	141.0
K [GPa]	1.70	2.96
σ_y [MPa]	401	1081

3.2 Data reduction

As the microstructures under consideration in tomography consist of a very large number of voxels, many millions of degrees of freedom are generated in classical hexahedral meshing by assigning a single voxel to a single hexahedral element. As a result, the computing time required to solve the system and the memory required for storage increases immensely. Since such

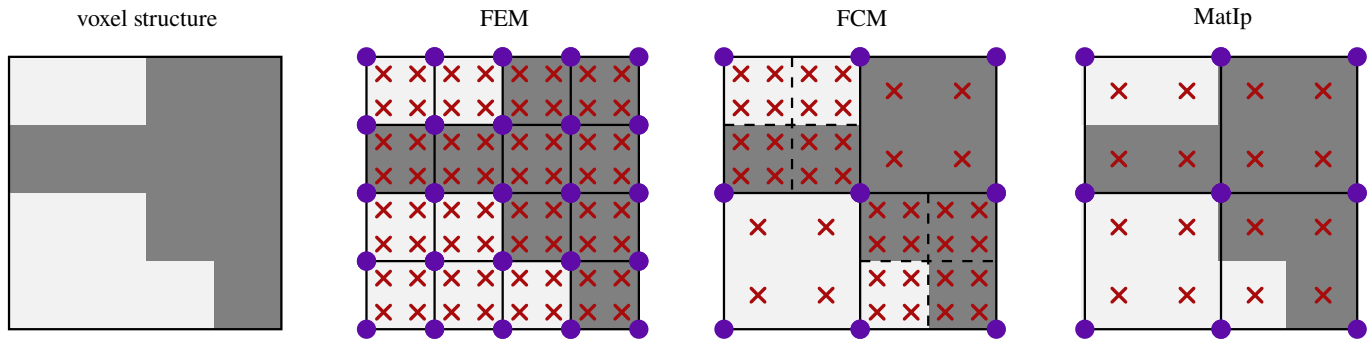


Figure 5: Meshing of a two-component voxel structure by classical FEM, FCM and MatIp (q2fe1). Element nodes are represented by violet dots, integration points by red crosses, element edges by black lines and sub-element edges of the FCM by dashed black lines.

calculations can usually no longer be carried out in an acceptable time on usual workstations, in addition to estimating the RVE size, data reduction is of great importance in the presented work. The aim is to reduce the required number of elements for meshing the microstructure, and thus computing time and working memory load, as far as possible, while maintaining all relevant structural information at the same time. Material definition at the integration point (MatIp) was used for this purpose. The idea of MatIp is based on Gauss Point Oversampling (Zohdi and Wriggers (2004)) and especially on the Finite Cell Method (FCM, (Düster et al. (2008); Parvizian et al. (2007))). The basic idea of FCM is to mesh the geometry under consideration in a strongly coarser way, so that several voxels are assigned to one element. The mesh then includes the geometry under consideration as well as parts of its surrounding. In order to integrate the system equation over these elements, sub-elements are introduced, which make it possible to carry out the integration over elements with homogeneous material. Inspired by this procedure, MatIp was implemented within the framework of this paper. Also in this case several voxels of the structure are combined to one element, whereby one voxel is assigned to exactly one integration point. Instead of standard Gaussian integration points, a grid of equidistant integration points, corresponding to the homogenous voxel size of the tomography, is applied. Accordingly, when calculating stress and treating plasticity, separate material parameters are used at each integration point, depending on whether it is a ferrite or martensite integration point. In contrast to FCM, it is not necessary to use sub-elements to integrate elements with mixed material. While complex geometries with homogeneous material are coarsened in the FCM including their surrounding, leading to a tensile strength of zero in parts of the mesh, good results are achieved with MatIp even with classical integration in comparison to the calculation in full resolution due to the relatively small differences in tensile strength between ferrite and martensite. Here, the order of the integration polynomials and the order of the shape functions can vary depending on the chosen method. For identification purposes, the number of integration points and the order of the shape functions are specified. For example q2fe1-MatIp means material definition at the integration point with linear shape function and two integration points per spatial direction in the element. In this case, one element corresponds to eight voxels of tomography. In order not to influence the volume fraction of martensite by unequal integration weights, equidistant integration points with constant weights were implemented. In Fig. 5 the difference between normal meshing, FCM and MatIp is schematically shown for a two-dimensional geometry. The shown MatIp meshing represents the entire microstructure in the FE mesh, while at the same time achieving a straightforward reduction in the number of elements and degrees of freedom. Further details of MatIp are discussed in Scherff (2019).

It is important to mention, that generally the FCM shows considerably good results with respect to convergence of the solution and accuracy of the results on the microscopic level (Düster et al. (2008); Parvizian et al. (2007)), even for complicated geometries and use cases. These advantages are, however, at the expense of complex and elaborate implementation. At this point the presented method shows its efficiency, with a straightforward and time saving implementation, for the investigated class of applications.

4 Results and Discussion - RVE Size

4.1 Experimental Results

The hardness measurements carried out result in the distribution shown in Fig. 6. As expected, the low hardness classes $HV0.05$ and $HV0.1$ with correspondingly small hardness imprints show a very high spread of the hardness values. From $HV0.2$ on, the spread drops significantly. For higher hardness classes, the spread remains at the same level. More precisely, the standard deviation of the hardness values of initially 20% decreases to under 3% starting with the $HV0.2$ imprint and the spread between maximum and minimum hardness decreases from 70% to under 9% of the mean value. Both values are within the range of measurement accuracy. Consequently, the RVE size is within the range of a $HV0.2$ imprint's zone of influence. The further reduction of the spread from $HV5$ upwards is mainly due to a reduced number of imprints due to the high size of the imprints, also see Tab. 2. A $HV0.2$ indentation corresponds to an imprint diameter of about $d_{\text{imprint}} = 50 \mu\text{m}$ at the present mean hardness. However, the size of the zone of influence is not clearly defined, which prevents a clear statement on RVE size at this point. However, the minimum distance between two hardness imprints according to the norm (Deutsches Institut für Normung (2006)) offers a clue. To ensure that the influence zones of two indentations do not overlap, this distance is three times the indentation diameter, $d_{\text{norm}} = 3 d_{\text{imprint}}$. The size of the influence zone therefore lies between a minimum edge length of one single imprint diameter and a maximum edge length of three times the imprint diameter, i.e. between $50 \mu\text{m}$ and $150 \mu\text{m}$. This assumption is

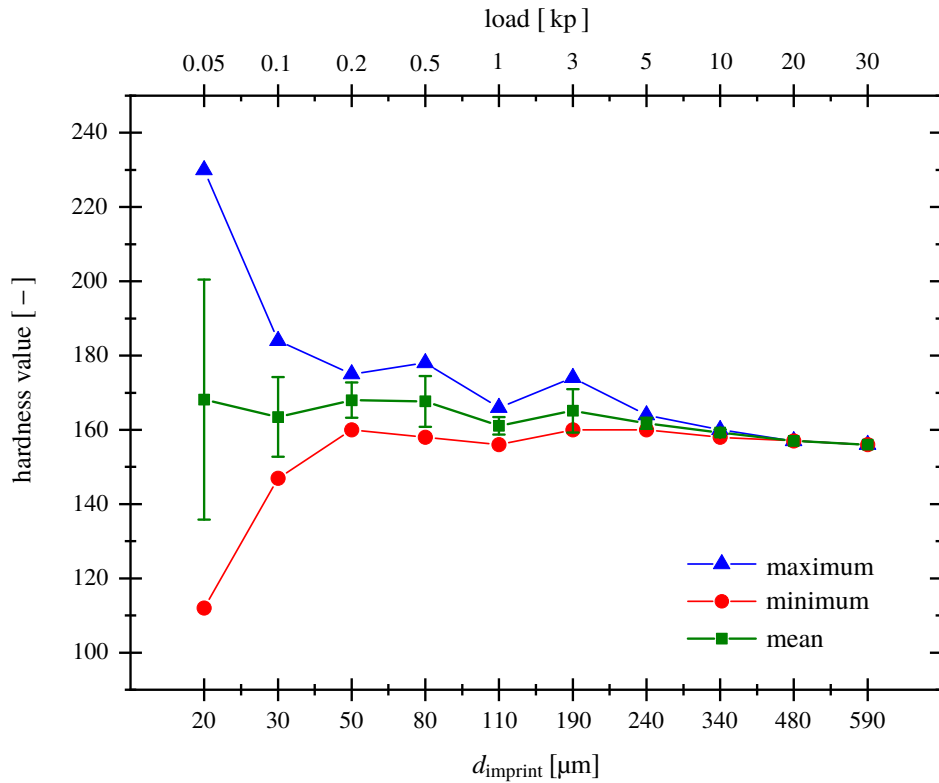


Figure 6: Maximum, minimum and mean value with standard deviation of the hardness values for different test loads.

evaluated below and the exact value is determined.

4.2 Evaluation of the RVE size estimation

To numerically evaluate the experimental RVE estimation, a tomography was prepared of a dual-phase steel, as shown in Sect. 2.2. Its size in each spatial direction is above the specified maximum RVE size of $150 \mu\text{m}$ edge length. The tomography is divided into smaller blocks of the same size and tensile tests are simulated on the individual blocks. The procedure is carried out for blocks with an edge length approximately in the range of the single, double and triple imprint diameter. The size classes thus cover the previously estimated RVE size range. Their extent is shown in Fig. 7 in relation to a two-dimensional section of the tomography. The edge lengths are $52 \mu\text{m}$, $105 \mu\text{m}$ and $157 \mu\text{m}$ instead of $50 \mu\text{m}$, $100 \mu\text{m}$ and $150 \mu\text{m}$ for reasons of efficient meshing². Based on the simulations, the average stress value at 5% total strain $R_{t5.0}$ is determined for each block. The spread of $R_{t5.0}$ within a size class is then considered as a function of the block size. Fig. 8 shows a similar trend for $R_{t5.0}$ as Fig. 6 shows for the hardness. The spread of the hardness decreases much faster at the beginning, but the overall hardness also scatters more strongly than $R_{t5.0}$. The spread decreases from about 50 MPa for $52 \mu\text{m}$ edge length to less than 10 MPa for $157 \mu\text{m}$ edge length, which is in the range of real macroscopic tensile tests. Fig. 8 thus proves the assumption that the RVE size corresponds approximately to three times

²Due to the underlying data structure, meshes with edge lengths of (x^{2y}) elements, with x as low as possible, can be better parallelized



Figure 7: Two-dimensional representation of the three considered block sizes in comparison to the tomography.

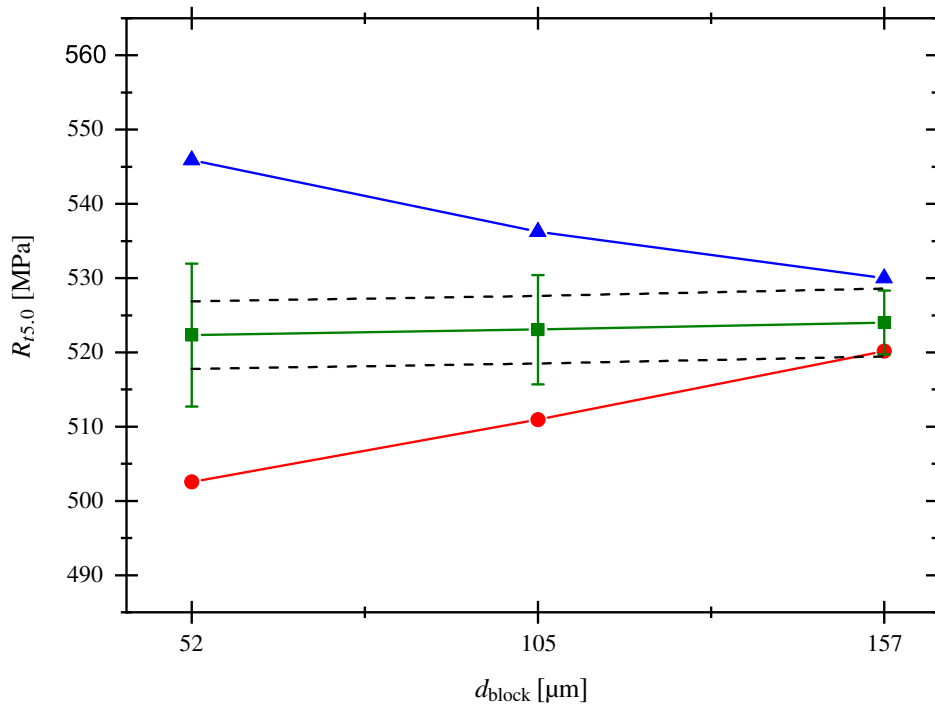


Figure 8: Maximum (blue), minimum (red) and mean value with standard deviation (green) of $R_{t5.0}$ for the different block sizes. The standard deviation of macroscopic tensile tests on the investigated steel is given in black.

the diameter of the hardness imprint for which the spread becomes sufficiently low. The investigated steel therefore has an RVE edge length of about $150 \mu\text{m}$.

Fig. 8 shows another characteristic of the microstructure besides the validation of the RVE size estimation. The ensemble mean of the three size classes remains at approximately the same level. As a result, the structure studied is ergodic. In the context considered here, ergodicity means the equality of the ensemble mean of a property over a sufficiently large number of unrepresentatively small sections with the mean over a representative large volume (Ostoja-Starzewski (2007)). This leads to relevant advantages for the simulation and also for future tomographies. On the one hand, the required memory decreases significantly with sequential simulation of several small structures instead of one large structure, on the other hand, the experimental effort also decreases. Due to the ergodicity, it is not necessarily required to tomograph a coherent block in RVE size. A volume that contains a sufficient number of smaller blocks may be sufficient. However, this statement cannot easily be generalized to other microstructures. In particular for strongly heterogeneous microstructures or microstructures with very high connectivity of the second phase, it can be assumed that this statement does not apply or does only apply to a limited extent.

The RVE was additionally estimated using the 3D structural parameters as described in Sect. 2.3. The results are presented in Fig. 9. For small edge lengths a large spread of the 3D parameters can be seen. From approx. $80 \mu\text{m}$ edge length the spread remains at the same level for all four 3D parameters. This implies that the size of the RVE, with respect to the geometry, is in the range of $80 \mu\text{m}$. The Euler density, which is a parameter for characterizing the connectivity, shows a constant profile from a slightly lower edge length of $60 \mu\text{m}$ on. However, to be sure that the volume is representative, all parameters should be considered at the same time. Thus the found result of the RVE-size based on 3D parameters corresponds to the RVE-size based on mechanical properties determined above, especially considering the generally higher relative spread of the geometry parameters.

5 Results and Discussion - Data Reduction

5.1 Impact of data reduction

In this section, the results of the implemented data reduction method are presented, both in terms of the reduction of computing time and memory usage as well as its accuracy. The load case here is always uniaxial tension in the transverse direction of the steel. The uniaxial tension test is considered here, as it is the universal standard test used in industry in this context, in contrast to other tests like shear, torsion or compression tests. To compare the variants of MatIp, finite elements with two, four, eight and sixteen integration points or voxels per spatial direction are considered. The number of integration points or voxels per spatial direction per element is referred to in the following as the reduction order. All simulations are performed with linear shape functions. The reduction orders 4 and 8 are additionally calculated with quadratic and cubic shape functions. To evaluate the reduction effect, a tensile test is simulated on one exemplary structural section. The section has an edge length of $52 \mu\text{m}$ or 128 vx and contains a total of $2,097,152 \text{ vx}$. During the simulation, the computing time and the memory utilization are recorded to compare the values. The goal in each case is to reduce the computing time and the memory utilization as much as possible without changing the result through the reduction. A full-resolution simulation with classical conforming hexahedral meshing

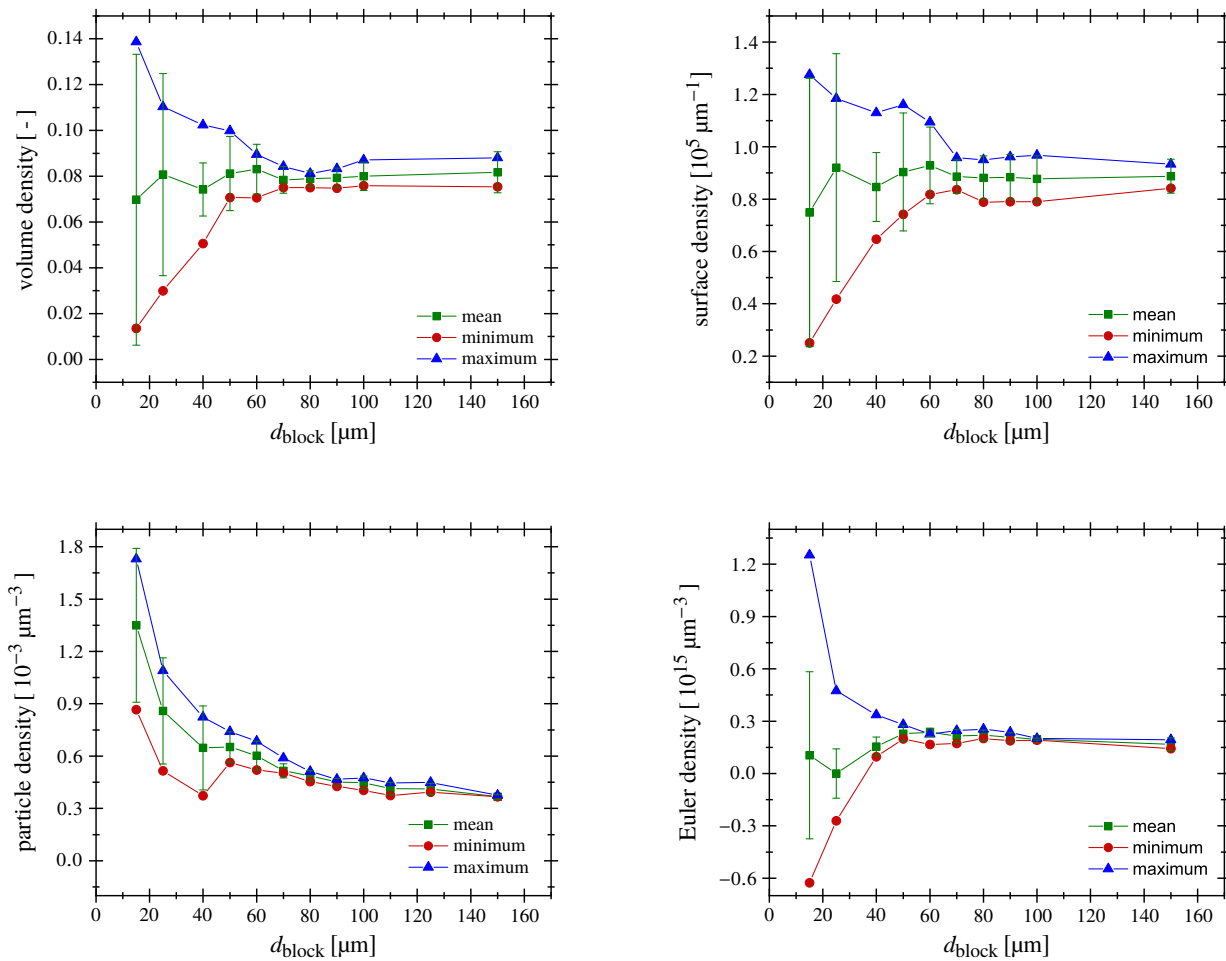


Figure 9: Maximum, minimum and mean value with standard deviation of the volume density (top left), surface density (top right), particle density (bottom left) and Euler density (bottom right) for different block sizes.

and linear shape functions serves as a reference.

Tab. 4 shows the computing time t_{sim} , the maximum memory usage l_m , the total number of degrees of freedom n_{dof} and the number of voxels per element n_{ve} of the different simulations. In the following, the term *element order* is used as an abbreviation for the order of the element's shape function. If the element order remains the same, the number of elements of the mesh and the number of degrees of freedom decrease with increasing order of reduction, resulting in a reduction of the computing time. At element order 1, the computing time decreases by a factor of 9 for the reduction order 2, for the reduction order 4 even by a factor of 34. For the reduction order 8 the computing time decreases only insignificantly, for the order 16 not at all anymore. The reason for this is that the quality of the approximation of the displacement field by the integration function drops considerably due to the high number of different integration points for higher reduction orders. This increases the computing time by a higher effort of time for the solution of the equation system. Memory usage shows a similar trend. Here, the memory load for the reduction orders 2 and 4 decreases by a factor of 7 and 12, respectively. For higher orders, the memory load even begins to increase slightly again. There are two reasons for this. On the one hand, the amount of data stored at the integration point remains constant, because the total number of integration points is not influenced by MatIp. Therefore, a plateau in the memory load is to be expected with increasing reduction order. On the other hand, the type of the underlying parallelization of the model in *deal.II* results in an increased memory load with high reduction orders. Each processor stores not only the data of the elements belonging to its domain, but also the data of all elements directly adjacent to it. With the large number of elements in full resolution or lower reduction orders, this doubling does not have much impact. In high reduction orders, however, there are only a few elements with a high number of integration points. Thus this element doubling has a strong influence and the memory load rises again starting from reduction order 8. A further trend that is evident, as expected, is that memory utilization and computing time increase with increasing element order at constant reduction order. Fig. 10 shows the stress strain diagrams for the simulations with different reduction orders compared to the simulation in full resolution. For a better comparison, Fig. 11 additionally shows the corresponding $R_{75,0}$ values. MatIp leads, especially with a high reduction order of 8 or 16, to a certain virtual hardening of the material. The martensite integration points influence the element stiffness more strongly than desired. This effect is partly compensated by the additional degrees of freedom with higher order of approach, as can be seen from the course of $R_{75,0}$ for the different variants of MatIp with reduction order 4 and 8. A preferred variant of MatIp can be determined

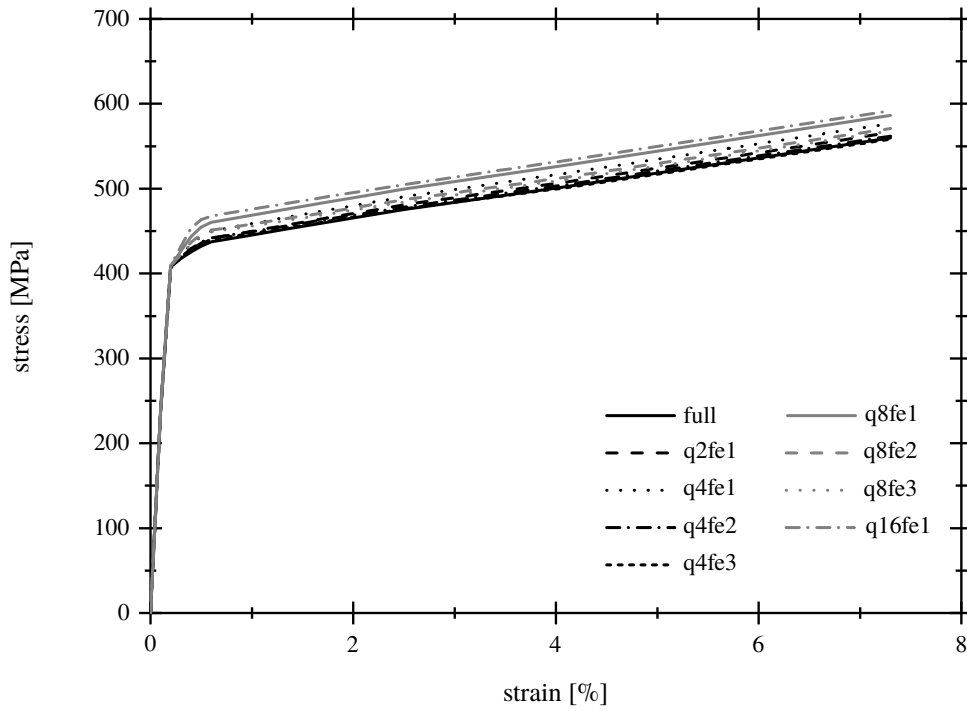


Figure 10: Stress strain diagrams for simulation in full resolution and various MatIp reduction orders.

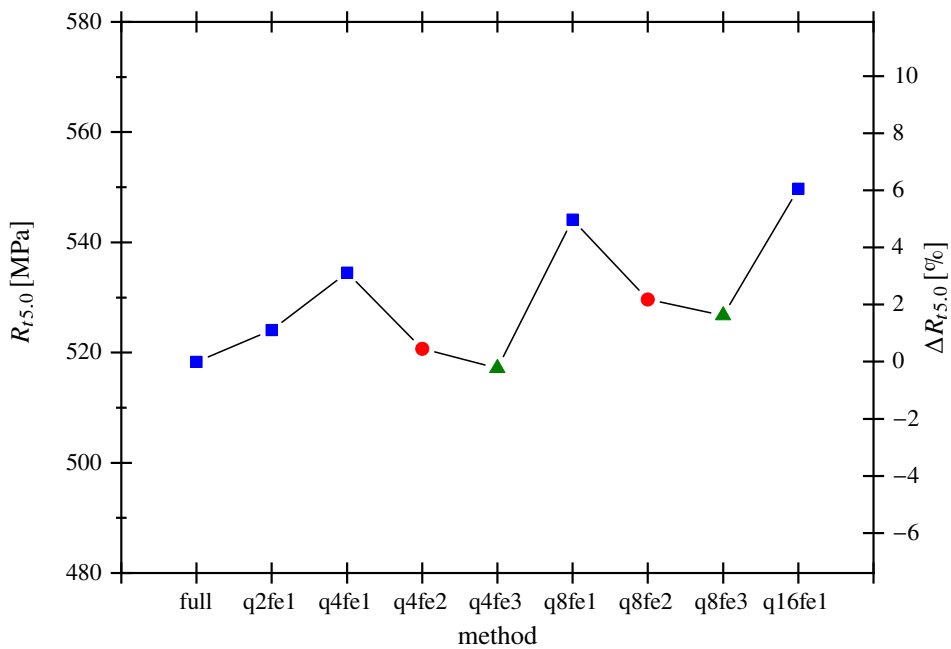


Figure 11: $R_{t,5,0}$ for simulation in full resolution and various MatIp reduction orders. Different element orders are marked with different symbols and colors. The lines are given to illustrate the trend in $R_{t,5,0}$, between the different reduction orders.

Table 4: Comparison of computing time, memory load, number of degrees of freedom and number of voxels per element for MatIp with the simulation in full resolution. In the term $qXfeY$, X gives the reduction order and Y the order of the element's shape function.

	t_{sim} [min]	l_m [GB]	n_{dof} [-]	n_{ve} [-]
full resolution	286.7	34.3	6,440,067	1
q2fe1	32.3	4.9	823,875	8
q4fe1	8.4	2.8	107,811	64
q4fe2	74.4	6.9	823,875	64
q4fe3	648.8	28.2	2,738,019	64
q8fe1	5.9	3.4	14,739	512
q8fe2	27.6	3.9	107,811	512
q8fe3	127.0	6.6	352,947	512
q16fe1	5.9	5.5	2,187	4,096

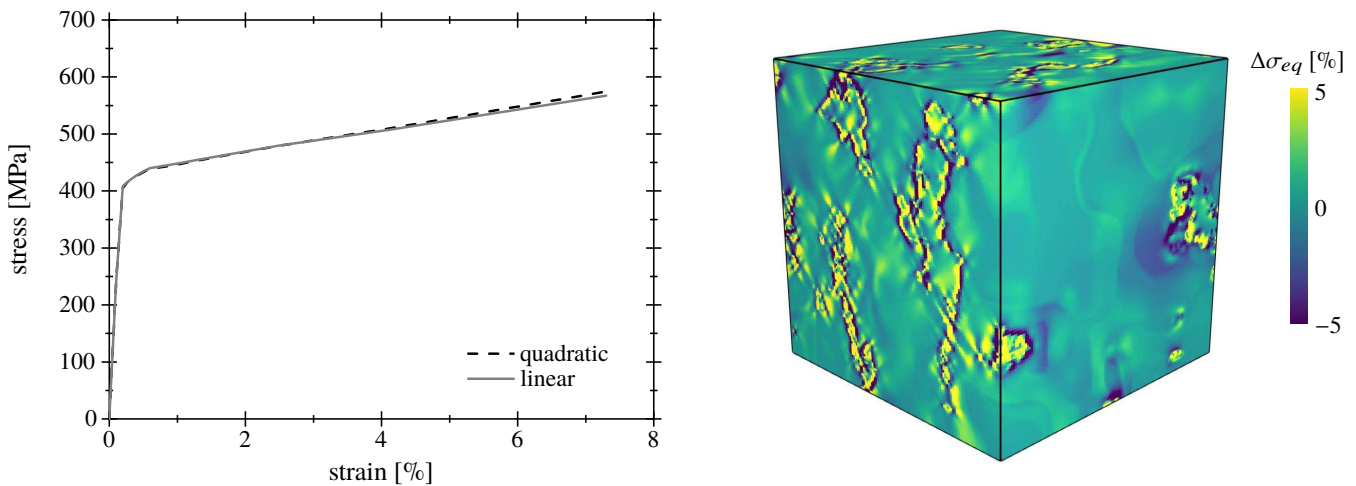


Figure 12: Stress strain diagram for a simulation with linear and quadratic shape functions (left) and the relative difference between the 3D von Mises equivalent stress fields at the end of the simulation (right). For the sake of visualization, the relative difference is limited to a range of $\pm 5\%$.

by combined consideration of the mechanical behavior and the computing time. When considering the difference in the stress level, only the reduction orders 2 and 4 show a sufficiently small deviation. When on the other hand the calculation time is considered, the variants with a higher element order show themselves to be insufficient. This reduces the analysis to q2fe1 and q4fe1 as reduction methods. The variant q2fe1 has a stress value closer to the simulation in full resolution, but requires about four times the computing time of q4fe1. Since q4fe1 also generates only a small deviation of about 3%, this variant is considered the most reasonable solution for most use-cases, as this stress difference is in the range of the spread of normal uniaxial tension tests. However, depending on the application and the desired level of accuracy, q2fe1 can also be used effectively.

The present investigation is limited to the macroscopic level. Even if the deviations due to MatIp are small on the macroscopic level as shown here, local deviations may occur. These can be of importance in the initiation of cracks, for example if the model is extended to damage. For an analysis of the local deviations, see Scherff (2019) for details.

5.2 Verification

In the following, the developed data reduction method will be verified. This happens in two steps. Firstly, a simulation in full resolution with quadratic shape functions shows that the used reference is valid. Secondly, MatIp is compared with a simulation with a geometry conforming mesh.

In the discussions in Sect. 5.1 the result of the simulation in full resolution served as reference value. Each voxel was thus assigned to a linear hexahedral element of the mesh. However, since linear elements tend to locking effects, a further simulation was carried out. In this simulation, the structure was meshed with hexahedral finite elements with quadratic shape functions in the sense of p-refinement. The aim of this is the verification of the originally used reference simulation³. The results of this simulation are presented in Fig. 12 in comparison to the simulation with linear shape functions. When considering the stress strain diagrams, the two simulations show no relevant difference, for example the difference in $R_{7,5,0}$ is 0.7%. Only at higher elongations

³As the simulation with quadratic shape functions produces a memory load of more than 300 GB, a high performance computing server was utilized instead of the workstation used in the rest of the work.

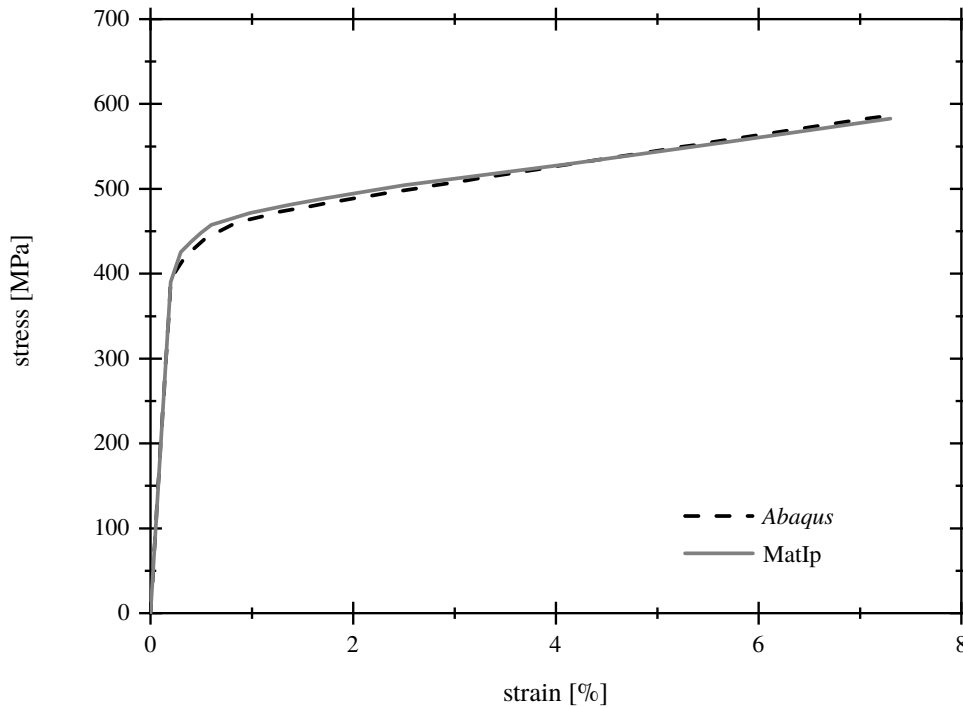


Figure 13: Stress strain diagram for a simulation with MatIp-*deal.II* and with *Abaqus*.

the curves begin to drift very slightly apart. If, however, the field of stress is considered in detail instead, this statement must be limited. Here, too, the difference between linear and quadratic shape functions is negligibly small for the majority of the structure. Around 95% of the structure shows a difference below 5%, more than 70% even a difference below 1%. However, a small area, especially the boundary layer between ferrite and martensite, shows relevant differences. These differences range for a few elements up to almost 55%. Overall, these outliers have no influence on the final result in the macroscopic stress strain diagram. In the context considered in this paper, with the stress strain diagram as target and with an elastic-plastic material model, the simulation with linear shape functions is therefore a valid reference. Limitations must, however, be placed on that conclusion to the extent that the differences observed in the microstructure may be of significance in future investigations. Especially when considering damage effects, they can serve as crack initiators. But since the principal distribution of the stress maxima in linear and quadratic calculations is still identical and only their height differs, the influence cannot yet be estimated.

As mentioned in Sect. 1, the geometry conforming meshing of microstructures is also an option. For this purpose, a section with $96 \times$ edge length of the considered microstructure was meshed with tetrahedral elements using the program *Simpleware ScanIP*[®], a software package for three-dimensional image processing and segmentation of tomographies. In the sense of an efficient simulation, the $884,736 \times$ of the tomography could be meshed with about 320,000 tetrahedral elements through structure smoothing. Since the simulation program based on *deal.II* used in this paper is only designed for hexahedral elements, the geometry conforming mesh was investigated in a simulation with *Simulia Abaqus FEA*[®]. The result is then compared with a simulation with MatIp. Thus, in addition to comparing the types of meshing, this study also compares the developed FE code with an established commercial FE program. The other parameters of the simulation, like material model, material parameters and boundary conditions, were chosen in *Abaqus* analogous to the self-developed code implemented in *deal.II*. The resulting stress-strain diagrams of the two simulations are shown in Fig. 13. The two stress strain diagrams show a very large accordance. The only difference is a small deviation at the start of yield, otherwise both curves are approximately identically. In addition, both simulations required approximately the same computing time per CPU core. This shows a significant secondary advantage of the implemented FE code with MatIp compared to the commercial program *Abaqus*. The parallelized open source implementation allows the use of any number of processor cores⁴. The license model of *Abaqus* also allows an arbitrarily high level of parallelization, but in real-world use it is generally limited due to the number of licenses owned. Overall, the result of the implemented simulation routine and meshing method can thus be verified and its advantage over commercial FEM software can be shown.

6 Conclusion

Two important points for the efficient and realistic microstructure-based simulation of dual-phase steel were implemented in the paper. On the one hand, a straightforward experimental method for estimating the size of the RVE was established, and, on the other hand, MatIp was developed as a method for efficient meshing of microstructures.

A large number of hardness measurements with different test loads and thus different imprint diameters were carried out. With

⁴For the utilized program library *deal.II* linear scaling of parallelization is shown for calculations with more than 16,000 CPU cores (Bangerth et al. (2012))

the hypothesis that the spread of these hardness values strongly decreases for indentation diameters whose influence zone lies in the range of the RVE size, the RVE size of the dual-phase steel under consideration with regard to the mechanical properties could be estimated to about 150 μm for the investigated dual-phase steel. Based on this, a 3D tomography was prepared and sections of different sizes were examined. Numerical simulations on these sections were able to prove the estimated RVE size. Similarly, the investigation of the geometric parameters of the microstructure revealed an RVE size with respect to the geometric parameters in the same size range. Hence, by comparing the proposed method with two other established methods for determining the RVE size, we could confirm our assumptions, at least for the class of material under consideration in this study.

Since microstructures usually consist of millions of voxels, a method for data reduction in hexahedral meshing was developed. By defining the material at the integration point instead of for each element as a whole, the simulation time could be reduced by a factor of 30 and the memory load by a factor of 12 compared to the full resolution simulation. To verify the simulation, a comparison simulation with p-refinement and a simulation of a geometry conforming mesh of the structure were performed. Both showed a high agreement to the simulation with MatIp.

The RVE size estimation now makes it possible to determine the appropriate size of a tomography before it is produced, thus simplifying the manufacturing process. A microstructure determined in this way can then be meshed by MatIp and used for the realistic and very efficient simulation of dual-phase steel on the basis of its microstructure. Further investigations on the suitability of the implemented simulation process and MatIp in consideration of damage effects will have to be carried out in the future.

Acknowledgment

The authors thank Prof. Dr. Dietrich Klakow and his department *Sprach- und Signalverarbeitung* at *Universität des Saarlandes* for readily providing access to his high performance computing server for the calculation of the simulation described in Sect. 5.2.

References

- J. Alkemper and P. W. Voorhees. Quantitative serial sectioning analysis. *Journal of Microscopy*, 201(3):388–394, 2001.
- D. Arndt, W. Bangerth, D. Davydov, T. Heister, L. Heltai, M. Kronbichler, M. Maier, J.-P. Pelteret, B. Turcksin, and D. Wells. The deal.II library, version 8.5. *J. Num. Math.*, 24:135–141, 2016.
- W. Bangerth, R. Hartmann, and G. Kanschat. deal.II – a General Purpose Object Oriented Finite Element Library. *ACM Trans. Math. Softw.*, 33(4):24/1–24/27, 2007.
- W. Bangerth, C. Burstedde, T. Heister, and M. Kronbichler. Algorithms and Data Structures for Massively Parallel Generic Adaptive Finite Element Codes. *ACM Trans. Math. Softw.*, 38(2):14:1–14:28, 2012.
- H. Bargel, P. Cardinal, H. Hilbrans, G. Schulze, and G. Wurzel. *Werkstoffkunde*. Springer-Lehrbuch. Springer, 2009.
- M. B. Bauza, J. Tenboer, M. Li, A. Lisovich, J. Zhou, D. Pratt, J. Edwards, H. Zhang, C. Turch, and R. Knebel. Realization of Industry 4.0 with high speed CT in high volume production. *CIRP Journal of Manufacturing Science and Technology*, 22: 121–125, 2018.
- B. Bednarczyk, J. Aboudi, and S. Arnold. The equivalence of the radial return and Mendelson methods for integrating the classical plasticity equations. *Computational Mechanics*, 41(5):733–737, 2008.
- D. Brands, D. Balzani, L. Scheunemann, J. Schröder, H. Richter, and D. Raabe. Computational modeling of dual-phase steels based on representative three-dimensional microstructures obtained from EBSD data. *Archive of Applied Mechanics*, 86(3): 575–598, Mar 2016.
- D. Britz, A. Hegetschweiler, M. Roberts, and F. Mücklich. Reproducible Surface Contrasting and Orientation Correlation of Low-Carbon Steels by Time-Resolved Beraha Color Etching. *Materials Performance and Characterization*, 5(5):553–563, 2016.
- T. Burnett, R. Kelley, B. Winiarski, L. Contreras, M. Daly, A. Gholinia, M. Burke, and P. Withers. Large volume serial section tomography by xe plasma fib dual beam microscopy. *Ultramicroscopy*, 161:119 – 129, 2016.
- T. M. Buzug. *Computed Tomography: From Photon Statistics to Modern Cone-Beam CT*. Springer Berlin Heidelberg, 2008.
- M. Calcagnotto, D. Ponge, E. Demir, and D. Raabe. Orientation gradients and geometrically necessary dislocations in ultrafine grained dual-phase steels studied by 2D and 3D EBSD. *Materials Science and Engineering: A*, 527(10):2738–2746, 2010.
- D. Das and P. P. Chattopadhyay. Influence of martensite morphology on the work-hardening behavior of high strength ferrite-martensite dual-phase steel. *Journal of Materials Science*, 44:2957–2965, 06 2009.
- R. G. Davies. Influence of martensite composition and content on the properties of dual phase steels. *Metallurgical Transactions A*, 9(5):671–679, May 1978.
- F. Desplentere, S. Lomov, D. Woerdeman, I. Verpoest, M. Wevers, and A. Bogdanovich. Micro-CT characterization of variability in 3D textile architecture. *Composites Science and Technology*, 65(13):1920–1930, 2005.
- Deutsches Institut für Normung. *Metallische Werkstoffe – Härteprüfung nach Vickers*. DIN EN ISO 6507, Berlin, 2006.
- M. Diehl, P. Shanthraj, P. Eisenlohr, and F. Roters. Neighborhood influences on stress and strain partitioning in dual-phase microstructures. *Meccanica*, 51(2):429–441, Feb 2016.

- H.-F. Dong, J. Li, Y. Zhang, J. Park, and Q.-X. Yang. Numerical simulation on the microstress and microstrain of low Si-Mn-Nb dual-phase steel. *International Journal of Minerals, Metallurgy, and Materials*, 17(2):173–178, Apr 2010.
- A. Düster, J. Parvizian, Z. Yang, and E. Rank. The finite cell method for three-dimensional problems of solid mechanics. *Computer Methods in Applied Mechanics and Engineering*, 197(45-48):3768–3782, 2008.
- M. Echlin and T. Pollock. Femtosecond Laser Serial Sectioning: A New Tomographic Technique. In *8th. World Congress on Computational Mechanics*, 2008.
- M. Fischer, A. Stieben, H. Quade, and W. Bleck. 3D Metallography of a Multiphase steel. In *Tagungsband zum 26. Aachener Stahlkolloquium – Werkstofftechnik*, pages 37–48, 2011.
- F. Goldschmidt. *Modellierung und Simulation von Klebeverbindungen mit gradierten mechanischen Eigenschaften*. PhD thesis, Universität des Saarlandes, Saarbrücken, 2015.
- R. Hill. Elastic properties of reinforced solids: Some theoretical principles. *Journal of the Mechanics and Physics of Solids*, 11(5):357–372, 1963.
- N. Ishikawa, K. Yasuda, H. Sueyoshi, S. Endo, H. Ikeda, T. Morikawa, and K. Higashida. Microscopic deformation and strain hardening analysis of ferrite-bainite dual-phase steels using micro-grid method. *Acta Materialia*, 97:257–268, 2015.
- L. K. Ji, H. L. Li, H. T. Wang, J. M. Zhang, W. Z. Zhao, H. Y. Chen, Y. Li, and Q. Chi. Influence of Dual-Phase Microstructures on the Properties of High Strength Grade Line Pipes. *Journal of Materials Engineering and Performance*, 23(11):3867–3874, Nov 2014.
- J. Kadkhodapour, A. Butz, S. Ziaei-Rad, and S. Schmauder. A micro mechanical study on failure initiation of dual phase steels under tension using single crystal plasticity model. *International Journal of Plasticity*, 27(7):1103–1125, 2011.
- J. Kang, Y. Ososkov, J. D. Embury, and D. S. Wilkinson. Digital image correlation studies for microscopic strain distribution and damage in dual phase steels. *Scripta Materialia*, 56(11):999–1002, 2007.
- T. Kanit, S. Forest, I. Galliet, V. Mounoury, and D. Jeulin. Determination of the size of the representative volume element for random composites: Statistical and numerical approach. *International Journal of Solids and Structures*, 40(13-14):3647–3679, 2003.
- S. Katani, S. Ziaei-Rad, N. Nouri, N. Saeidi, J. Kadkhodapour, N. Torabian, and S. Schmauder. Microstructure Modelling of Dual-Phase Steel Using SEM Micrographs and Voronoi Polycrystal Models. *Metallography, Microstructure, and Analysis*, 2(3):156–169, Jun 2013.
- E. Keehan, L. Karlsson, H. K. D. H. Bhadeshia, and M. Thuvander. Three-dimensional analysis of coalesced bainite using FIB tomography. *Materials Characterisation*, 59:877–822, 01 2008.
- S. Kim and S. Lee. Effects of martensite morphology and volume fraction on quasi-static and dynamic deformation behavior of dual-phase steels. *Metallurgical and Materials Transactions A*, 31(7):1753–1760, Jul 2000.
- F. Lasagni, A. Lasagni, E. Marks, C. Holzapfel, F. Mücklich, and H. Degischer. Three-dimensional characterization of 'as-cast' and solution-treated AlSi12(Sr) alloys by high-resolution FIB tomography. *Acta Materialia*, 55(11):3875–3882, 2007.
- M. Li, S. Ghosh, T. N. Rouns, H. Weiland, O. Richmond, and W. Hunt. Serial Sectioning Method in the Construction of 3-D Microstructures for Particle-Reinforced MMCs. *Materials Characterization*, 41(2):81–95, 1998.
- R. Li, X. Zuo, Y. Hu, Z. Wang, and D. Hu. Microstructure and properties of pipeline steel with a ferrite/martensite dual-phase microstructure. *Materials Characterization*, 62(8):801–806, 2011.
- M. Marvi-Mashhadi, M. Mazinani, and A. Rezaee-Bazzaz. FEM modeling of the flow curves and failure modes of dual phase steels with different martensite volume fractions using actual microstructure as the representative volume. *Computational Materials Science*, 65:197–202, 2012.
- R. v. Mises. *Mechanik der festen Körper im plastisch-deformablen Zustand*. *Nachrichten von der Gesellschaft der Wissenschaften zu Göttingen, Mathematisch-Physikalische Klasse*, 1913:582–592, 1913.
- F. Mücklich, M. Engstler, D. Britz, J. Barrirero, and P. Rossi. Why we need all dimensions to solve both very old and very new questions in materials at the micro-, nano- and atomic scales. *Practical Metallography*, 52(9):507–524, 2015.
- F. Mücklich, M. Engstler, D. Britz, and J. Gola. Serial Sectioning Techniques – a Versatile Method for Three-Dimensional Microstructural Imaging. *Practical Metallography*, 55(8):569–578, 2018.
- J. Ohser and F. Mücklich. *Statistical Analysis of Microstructures in Materials Science*. John Wiley & Sons, 2000.
- M. Ostoja-Starzewski. *Microstructural randomness and scaling in mechanics of materials*. Chapman and Hall, 2007.
- J. Parvizian, A. Düster, and E. Rank. Finite cell method: h- and p-extension for embedded domain problems in solid mechanics. *Computational Mechanics*, 41(1):121–133, 2007.
- S. K. Paul. Real microstructure based micromechanical model to simulate microstructural level deformation behavior and failure initiation in DP 590 steel. *Materials & Design*, 44:397–406, 2013.
- PlasticsEurope. Weltweite und europäische Produktionsmenge von Kunststoff in den Jahren von 1950 bis 2016 (in Millionen Tonnen). <https://de.statista.com/statistik/daten/studie/167099/umfrage/weltproduktion-von-kunststoff-seit-1950/>, 2017. (05.11.2018).
- A. Ramazani, K. Mukherjee, H. Quade, U. Prahl, and W. Bleck. Correlation between 2D and 3D flow curve modelling of DP steels using a microstructure-based RVE approach. *Materials Science and Engineering: A*, 560:129–139, 2013.

- A. Ramazani, Z. Ebrahimi, and U. Prael. Study the effect of martensite banding on the failure initiation in dual-phase steel. *Computational Materials Science*, 87:241–247, 2014.
- M. Roland, A. Kruglova, G. Gaiselmann, T. Brereton, V. Schmidt, F. Mücklich, and S. Diebels. Numerical simulation and comparison of a real Al–Si alloy with virtually generated alloys. *Archive of Applied Mechanics*, 85(8):1161–1171, Aug 2015.
- J. C. Russ and R. T. Dehoff. *Practical Stereology*. Springer US, 2000.
- F. Scherff. *Modellierung der Gefüge-Eigenschafts-Korrelation bei Dualphasenstahl*. PhD thesis, Universität des Saarlandes, Saarbrücken, 2019.
- F. Scherff, F. Goldschmidt, S. Scholl, and S. Diebels. High-resolution simulation of microstructures in dual-phase steel. *PAMM*, 16(1):391–392, 2016.
- J. Simo and R. Taylor. Consistent tangent operators for rate-independent elastoplasticity. *Computer Methods in Applied Mechanics and Engineering*, 48(1):101–118, 1985.
- J. C. Simo and T. J. Hughes. *Computational Inelasticity*, volume 7 of *Interdisciplinary applied mathematics*. Springer Science & Business Media, 2000.
- G. Strnad and L. Jakab-Farkas. Improving the accuracy of low-load Vickers microhardness testing of hard thin films. *Procedia Technology*, 12:289–294, 2014.
- V. Tarigopula, O. Hopperstad, M. Langseth, A. Clausen, and F. Hild. A study of localisation in dual-phase high-strength steels under dynamic loading using digital image correlation and FE analysis. *International Journal of Solids and Structures*, 45(2): 601–619, 2008.
- C. Tasan, M. Diehl, D. Yan, C. Zambaldi, P. Shanthraj, F. Roters, and D. Raabe. Integrated experimental–simulation analysis of stress and strain partitioning in multiphase alloys. *Acta Materialia*, 81:386–400, 2014a.
- C. Tasan, J. Hoefnagels, M. Diehl, D. Yan, F. Roters, and D. Raabe. Strain localization and damage in dual phase steels investigated by coupled in-situ deformation experiments and crystal plasticity simulations. *International Journal of Plasticity*, 63:198–210, 2014b. Deformation Tensors in Material Modeling in Honor of Prof. Otto T. Bruhns.
- C. Tasan, M. Diehl, D. Yan, M. Bechtold, F. Roters, L. Schemmann, C. Zheng, N. Peranio, D. Ponge, M. Koyama, K. Tsuzaki, and D. Raabe. An Overview of Dual-Phase Steels: Advances in Microstructure-Oriented Processing and Micromechanically Guided Design. *Annual Review of Materials Research*, 45(1):391–431, 2015.
- M. Uchic, M. Groeber, M. Shah, P. Callahan, A. Shiveley, M. Scott, M. Chapman, and J. Spowart. An Automated Multi-Modal Serial Sectioning System for Characterization of Grain-Scale Microstructures in Engineering Materials. In M. De Graef, H. F. Poulsen, A. Lewis, J. Simmons, and G. Spanos, editors, *Proceedings of the 1st International Conference on 3D Materials Science*, pages 195–202, Cham, 2016. Springer International Publishing. ISBN 978-3-319-48762-5.
- M. L. Wilkins. Calculation of elastic-plastic flow. Technical report, California Univ Livermore Radiation Lab, 1963.
- C. Yan, L. Hao, A. Hussein, P. Young, and D. Raymont. Advanced lightweight 316L stainless steel cellular lattice structures fabricated via selective laser melting. *Materials & Design*, 55:533–541, 2014.
- A. Zeghadi, F. N’guyen, S. Forest, A.-F. Gourgues, and O. Bouaziz. Ensemble averaging stress–strain fields in polycrystalline aggregates with a constrained surface microstructure – Part 1: anisotropic elastic behaviour. *Philosophical Magazine*, 87(8-9): 1401–1424, 2007.
- X. Zhong, M. G. Burke, P. J. Withers, X. Zhang, X. Zhou, T. L. Burnett, Y. Liu, S. B. Lyon, and S. R. Gibbon. Multi-modal plasma focused ion beam serial section tomography of an organic paint coating. *Ultramicroscopy*, 197:1 – 10, 2019.
- H. Zhou, C. Li, L. Zhang, B. Crawford, A. S. Milani, and F. K. Ko. Micro-XCT analysis of damage mechanisms in 3D circular braided composite tubes under transverse impact. *Composites Science and Technology*, 155:91–99, 2018.
- O. C. Zienkiewicz and R. L. Taylor. *The finite element method*, volume 36. McGraw-Hill London, 1977.
- T. Zohdi and P. Wriggers. *Introduction to Computational Micromechanics (Lecture Notes in Applied and Computational Mechanics)*. Springer-Verlag, Berlin, Heidelberg, 2004.

On a Fast Analytical Approximation of Natural Frequencies for Photovoltaic Modules

Stefan Bergmann¹, Fereshteh Hassani², Zia Javanbakht^{3*}, and Marcus Aßmus¹

¹ Otto von Guericke University, Institute of Mechanics, Universitätsplatz 2, 39106 Magdeburg, Germany

² University of Tabriz, Faculty of Civil Engineering, 29 Bahman Boulevard, Tabriz, Iran

³ Griffith University, School of Engineering and Build Environment, Parklands Dr, Southport 4215, Australia

Abstract: In this paper, an eigenvalue problem is considered, i.e., the free vibration of photovoltaic (PV) modules. This structure was selected for its peculiar layer contrast, which forms an anti-sandwich. The aim was to present an analytical procedure for obtaining the natural frequencies of the PV modules over a range of temperatures. To this end, the layered structure was homogenised into an equivalent single layer for which a closed-form solution is presented using the shear-rigid plate theory. Moreover, the finite element method was applied to simulate the behaviour of the discrete layers in terms of mesh sensitivity. By examining the findings and some benchmark values, it was found that the analytical procedure could provide a range for the results. More specifically, the Reuss-Voigt range covers the possible values for the natural frequencies in the examined temperature range. Moreover, the analytical method can predict the natural frequencies with a good accuracy in the temperature range of -40 to 15°C . In contrast, the computational analysis seemed to provide very good results in return for a modest computational effort. In conclusion, the provided analytical procedure could quickly determine the natural frequencies with a good accuracy in the mentioned range.

Keywords: composite structure, homogenisation, plate theory, finite element method

1 Introduction

Overview. Composite structures, due to their high specific properties, are used in various applications in which the vibration of components is inevitable. Of our interest is the so-called anti-sandwich panels, which can be categorised under laminated composites. An anti-sandwich consists of two stiff skin layers and a soft core layer (Aßmus, 2019; Javanbakht et al., 2019). This typical structure is used in manufacturing photovoltaic (PV) modules (Aßmus et al., 2016).

Dynamic analysis. The dynamic performance of structures is measured by studying their vibrational behaviour. The inherent dynamic property of a structure reveals itself under initial excitation (free vibration). The behaviour of the system in this state depends on the natural frequencies of the system, which is obtained from a modal analysis. This information is used to investigate more complex responses, e.g., forced excitation (cyclic/harmonic loads) or transient analysis (damped system under impact) (Meirovitch, 2001).

Damage control/detection. The results of the dynamic analyses can be used in either *damage control* or *damage detection* in PV modules. In the former case, the information is used for fine-tuning the geometric and material parameters during the design process in order to restrict the dynamic response. In the latter context, studying the dynamic behaviour could reveal the extent of damage in the PV modules. For instance, the resonance ultrasonic vibrations method is used as a non-destructive test to detect microcracks (Dallas et al., 2007). In terms of damage control, both *structural* and *functional* failure modes are possible, and thus are required to be covered in the investigations.

Structural failure. Structural damage could happen under either static or dynamic loading. Photovoltaic modules experience most of the static loads during operation; a general solution for arbitrary loading condition is presented in (Aßmus et al., 2017a). More broadly, the dynamic response of the PV modules becomes significant under both pre-operating conditions (transportation-induced vibrations during shipping (Reil et al., 2010) or during installation) and under service (vortex shedding from wind impact (Aßmus and Köhl, 2012)); experimental studies have shown that resonance could occur in such conditions (Aßmus et al., 2011) and cause failure in the module.

Functional failure. Dynamic loads could damage the functionality of the electrical components in PV modules, e.g., broken interconnect ribbons, solar cell fracture or solder bond failure are possible, see (Ferrara and Philipp, 2012; Köntges et al., 2014; Wohlgemuth, 2020) for various failure modes of this type. It seems that dynamic loads cause more functional damage than

* E-mail address: zia.javanbakht@gmail.com

structural. For instance, a higher failure rate of the electrical circuits was reported under dynamic loads due to the loss of solder contact (Koch et al., 2010).

Design requirements. The dynamic response of PV modules should be improved to alleviate any harmful stimuli. This is done by some design alterations, which could provide some additional protection against vibration. For example, it was shown that using silicone encapsulants, instead of ethylene vinyl acetate (EVA) copolymer, could better protect the solar cells under dynamic loads (Mickiewicz et al., 2011). Therefore, standardised approaches are emerging in the literature to address the design requirements.

Current standardised approach. The International Electrotechnical Commission (IEC) imposes the minimum design requirements on the PV modules that are manufactured in Europe—the UK implementation of these are published in British Standards. The British code for terrestrial PV modules—BS EN 61215-1-2:2017 (equivalent to IEC 61215) (British Standards, 2017a) and BS EN 61215-2:2017 (British Standards, 2017b) for crystalline silicon modules, and BS-EN-61646:2008 (equivalent to IEC 61646) (British Standards, 2008) for thin-film modules—only demand a static load testing (uniform load) and a hail test (spherical ice ball impact) as minimum design qualifications. Nevertheless, more attention was directed towards the dynamic properties of the PV modules and their regularisation in the recent years. For example, the transportation testing procedure of IEC 62759:2015 (British Standards, 2015) demands a dynamic loading test according to IEC 62782:2016 (British Standards, 2016) along with humidity freeze and thermal cycling. As the first step, the regulated design requirements are indispensable. However, the behaviour of PV modules should be further understood—especially under unconventional circumstances. To this end, a combination of analytical, numerical, and experimental methods are used.

Experimental efforts. In terms of physical experiments, natural frequencies are obtained under various conditions. An outdoor setup was used in (Weiss et al., 2009) where the deflection of a panel was monitored under wind excitation. Fundamental frequency of 9 and 12 Hz was obtained by means of Fourier Transformation. Moreover, an indoor acoustic test resulted in the range of 14.6–24.6 Hz for the natural frequencies of various PV modules including the outdoor test sample. It seemed that the acoustic test provided more consistent results. A similar attempt was made in (Aßmus et al., 2011) where by combining experiments and finite element (FE) simulations, a range of 14.7–27.2 was reported for the fundamental frequency of various PV modules. In (Pingel et al., 2009), the shaking table test was used to simulate the vibrations during transportation (5–500 Hz); it resulted in a resonance frequency in the range of 1–15 Hz. It was also shown that reducing the wafer thickness would increase the failure rate of the PV modules under dynamic loads. In (Kilikeviciene et al., 2019), it was experimentally shown that the impact of hail could cause microcracking in PV modules and render them ineffective in terms of power generation. An experimental setup for harsh weather conditions was introduced in (Visniakov et al., 2015), which considered induced frequencies up to 40 Hz; it was found that the low frequency loads, which represent windy conditions, could cause damage to the crystalline structure of the PV cells and reduce the performance of the modules. Therein, a fundamental frequency of 7.2 Hz was obtained experimentally while the FE simulation resulted in 6.69 Hz. In (Kilikevicius et al., 2016), a similar setup was used to carry out an *operational modal analysis*, which resulted in a fundamental frequency of about 16 Hz. In this study, it was again affirmed that low-frequency studies could be used to simulate the excitations due to various wind speeds. Moreover, the damping characteristics of the PV modules were considered in the experiments. It is worth mentioning that the variation in the geometry and material property of the PV modules as well as the environmental parameters has resulted in a rather wide range of reported frequencies in the literature.

Computational efforts. The experimental efforts are valuable and necessary but they cannot cover all the possible cases; moreover, they are expensive and time-consuming. Computational methods could, at least partially, reduce such costs—especially when combined with analytical methods. For instance, FE analyses were carried out to obtain the mechanical/thermo-mechanical response (Dietrich et al., 2010; Aßmus et al., 2011; Sander et al., 2013; Beinert et al., 2019) of PV modules. The free vibration of PV modules was simulated using the FE method in (Dallas et al., 2007; Visniakov et al., 2015; Kilikevicius et al., 2016). A multi-scale FE analysis was carried out to study the distribution and orientation of microcracking in PV modules. In this study, both of the functional and structural damage of PV modules were considered in coupled elastic-electric analyses. More specialised approaches, such as the extended Layer-Wise Theory (XLWT) (Naumenko and Eremeyev, 2014), are used as the basis of more computationally effective analyses, see (Aßmus et al., 2017b,c).

Aim. All the aforementioned efforts were ideally seeking a balanced approach between complexity and computational cost. Most of the studies were focused on the static loading conditions and the majority of dynamic studies were limited to experimental setups. Herein, the aim is to provide a simple approximation method for the fundamental natural frequency of the PV modules. To this end, an analytical formulation of the homogenised structure is set up and solved. It is hypothesised that the high contrast of material properties might affect the accuracy of the results. Moreover, a computational prototype was developed to complement the study. The current work is restricted to glass-encapsulant-glass structures with structural symmetry in the thickness direction. However, it can be extended to other anti-sandwich structures.

Outline In the following sections, the homogenisation procedure of the PV modules is elaborated. Then, the shear-rigid plate theory is revisited to obtain the closed-form solution for the eigenvalue problem of PV modules. Finally, a computational prototype is analysed in terms of sensitivity of the results to mesh density and temperature change. Then, the results are benchmarked

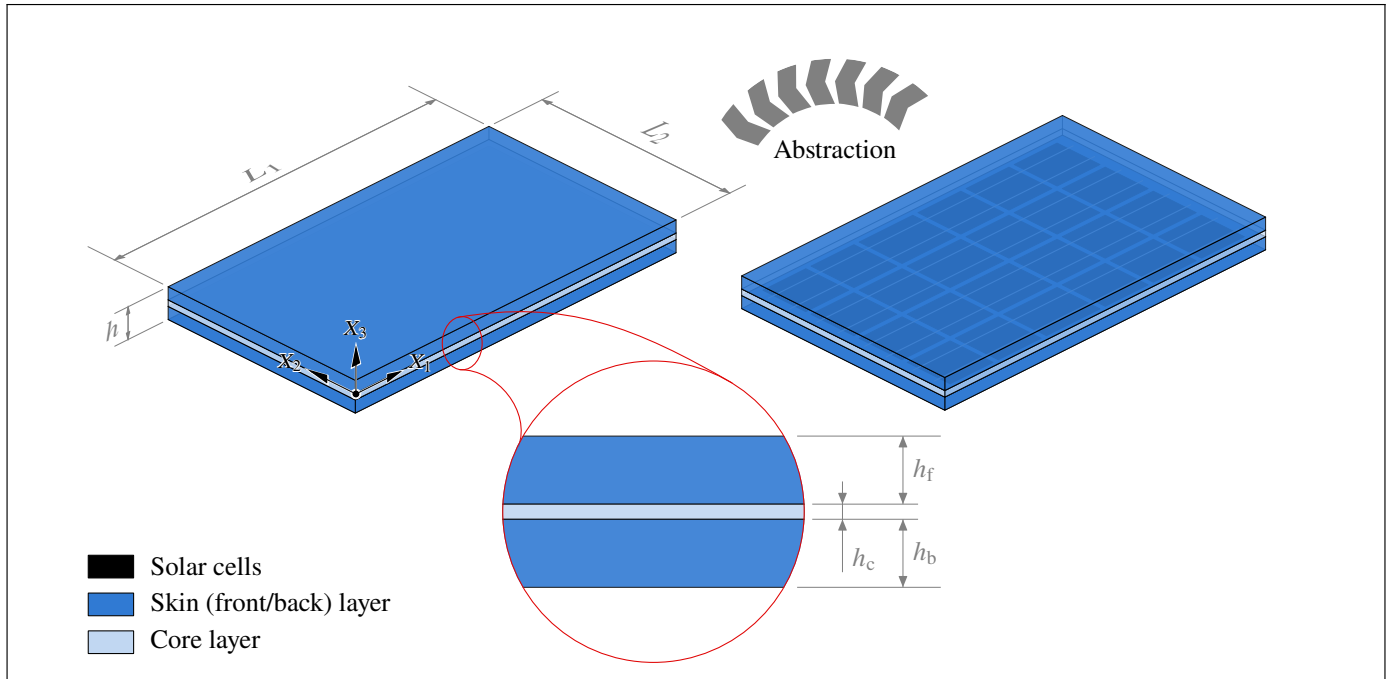


Fig. 1: Abstraction of the geometry and the resulting dimensions for a PV module

against some reported values from the literature and discussed. The final section concludes the findings and suggests some research pathways.

2 Homogenisation of Photovoltaic Modules

2.1 Simplifying the Physical Structure

Geometry. The physical structure of a silicon PV module is illustrated in Fig. 1. Solar cells are embedded in a polymeric core layer, which is covered by front and back skin layers. The contribution of the embedded metallic solar cells to the overall bending and membrane stiffnesses of the laminate can be neglected (Naumenko and Eremeyev, 2014). Thus, a symmetrical anti-sandwich laminate can adequately represent the mechanical behaviour of a PV module. The dimensions of the PV module is $L_1 \times L_2 \times h$ where the overall thickness h is the sum of the thickness of the front (h_f), back (h_b), and core (h_c) layers. In this study, a symmetrical structure is assumed for the PV module whose dimensions are listed in Tab. 1. The front or back layer in a symmetrical photovoltaic module is addressed as a skin layer, e.g., the h_s represents the thickness of the skin ($h_s = h_f = h_b$).

Boundary Conditions. In Fig. 2, the cross-section of a PV module is illustrated. The embedding (often aluminium) frame holds the laminate by a soft sealant. This fixture allows for small rotations, and thus a moment-free constraint can represent this arrangement. Mathematically, this is equivalent to a plate that is simply-supported along the edges:

$$\forall X_1 \in [0, L_1] : \begin{cases} w(X_1, 0) = w(X_1, L_2) = 0 \\ M_2(X_1, 0) = M_2(X_1, L_2) = 0 \end{cases}, \quad (1a)$$

$$\forall X_2 \in [0, L_2] : \begin{cases} w(0, X_2) = w(L_1, X_2) = 0 \\ M_1(0, X_2) = M_1(L_1, X_2) = 0 \end{cases}, \quad (1b)$$

where w is the deflection (displacement along X_3 -axis) of the plate midplane; M_1 and M_2 are the bending moments acting on the planes with normals X_1 and X_2 , respectively.

Tab. 1: Geometric parameters

Layer(s)	L_1 [mm]	L_2 [mm]	h_k [mm]
Skin	1620	810	3.2
Core	1620	810	1.0

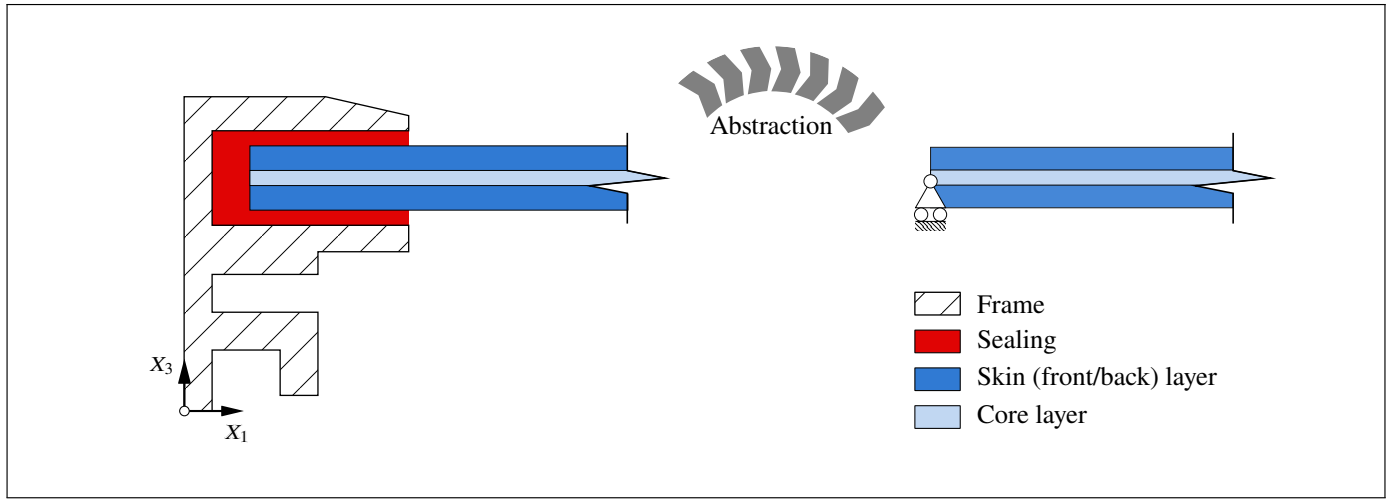


Fig. 2: Cross section view of typical bedding of a PV laminate in a frame and mechanical analogue

2.2 Material Properties

The skin layers of PV modules (front/back layers) are made of glass while the core layer is the EVA polymer, see Tab. 2. The outer layers are denser than the core layer $\rho_s/\rho_c \approx 2.69$ but more importantly, a high contrast of order about $E_s/E_c \approx 10^4$ is observed for their elastic moduli. The Poisson’s ratios $\nu_s/\nu_c \approx 0.73$ denotes similar values for the skin and core layers.

BS standards for both crystalline and thin-film modules (British Standards, 2017b, 2008) require thermal cycling from -40 to 85°C for no more than 6 hours. The module temperatures can vary in natural weathering between -20°C (alpine) and $+60^\circ\text{C}$ (desert), which is well covered the mentioned range. While the material properties of the skin layers (glass) and the solar cells (polycrystalline silicon) can be deemed temperature-independent, the thermal sensitivity of the polymeric encapsulant cannot be ignored, see (Aßmus et al., 2016).

In the current study, the Poisson’s ratio and mass density of the EVA were assumed to be temperature-independent and the respective room temperature properties were used, see Tab. 2. In contrast, the elastic modulus of the EVA is specified as a function of temperature. Using the discrete data that is provided in Tab. 3, the following piecewise linear interpolations were obtained for the elastic modulus of the core layer:

$$E_c(\theta) = \begin{cases} -16.05\theta + 377.046 & \text{for } -40 \leq \theta \leq 23 \\ -0.12974\theta + 10.8778 & \text{for } 23 \leq \theta \leq 80 \end{cases}, \tag{2}$$

where θ is the ambient temperature and $E_c(\theta)$ returns the elastic modulus of the core in N/mm^2 , see Fig. 3. It is worth mentioning that increasing the temperature from -40 to $+80^\circ\text{C}$ reduces the elastic modulus to 0.05% of its initial value. This reduction happens in a very high rate up to $+23^\circ\text{C}$ but after this point, continues with less intensity. Moreover by increasing the temperature, the E_c/E_s ratio approaches zero, and thus the elastic modulus contrast is magnified. For instance, at the highest temperature, the elastic modulus of the skin becomes about $1.4 \cdot 10^5$ times that of the core layer.

2.3 Voigt and Reuss Bounds

The Voigt (Voigt, 1910) and Reuss (Reuss, 1929) bounds are the results of iso-strain and iso-stress assumptions, respectively. It is assumed that various phases of the material undergo the same strain in the former case whereas in the latter case, every phase experiences the same stress, see Fig. 4. In order to simplify the problem, working with a homogeneous medium is preferred. The properties of such smeared continuum is based on its constituents, which are the layers of the PV modules in the current context. The so-called rule of mixture and the inverse rule of mixture (Javanbakht et al., 2020a,b) could be used to obtain various homogenised properties:

$$\square_V = \sum_{i=1}^n \xi^{(i)} \square^{(i)}, \tag{3a}$$

$$\square_R = \left[\sum_{i=1}^n \frac{\xi^{(i)}}{\square^{(i)}} \right]^{-1}, \tag{3b}$$

Tab. 2: Room-temperature material properties

Layer(s)	Material	E_k [N/mm^2]	ν_k [-]	ρ_k [kg/m^3]
Skin	Glass	$73 \cdot 10^3$	0.30	2500
Core	EVA	7.90	0.41	930

Tab. 3: Temperature-dependent material parameters of the EVA encapsulant; adapted from (Eitner, 2011)

θ [°C]	-40	+23	+80
E_c [N/mm ²]	1019.04	7.90	0.52

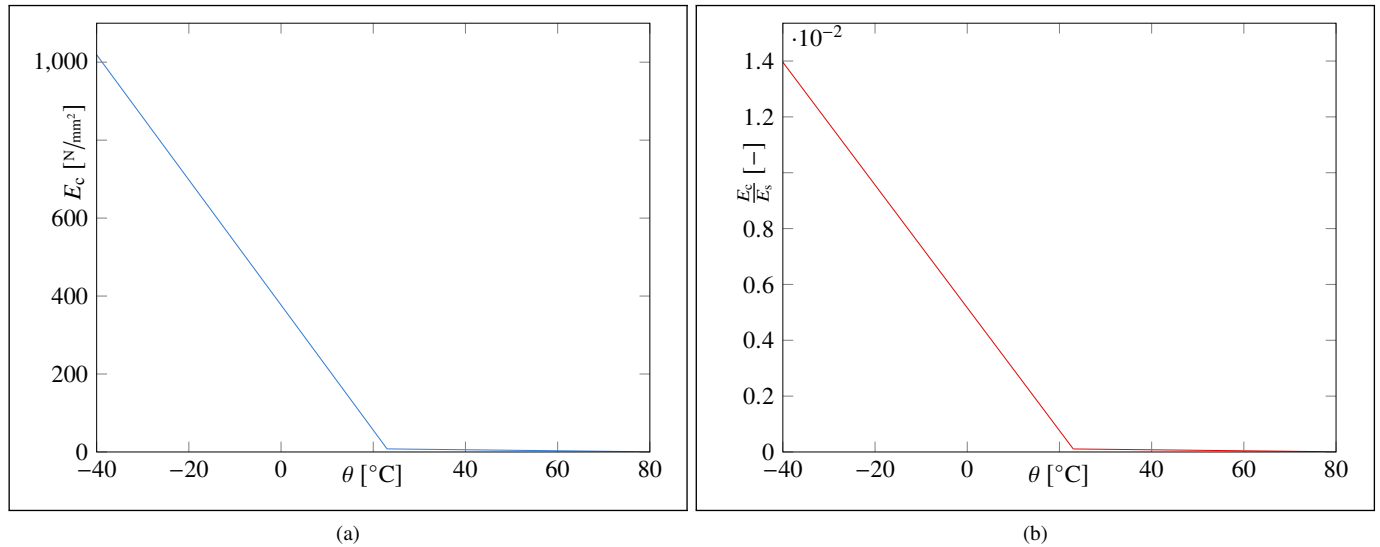


Fig. 3: Temperature-dependent properties: (a) elastic modulus of the core, and (b) core to skin relative elastic modulus

with $\square \in \{E, \nu, \rho\}$ denotes the material property of interest, and the (\square_V) and (\square_R) subscripts denote the pertaining Voigt and Reuss bounds, respectively; n is the number of phases in the material, $\zeta^{(i)}$ is the volume fraction of the phase, and $\square^{(i)}$ is the material property of the i -th phase.

The Voigt and Reuss bounds respectively represent the upper and lower bounds for the homogenised material properties. In terms of PV modules, these bounds correspond to the direction along the layers (Voigt bound) and the direction perpendicular to the layers (Reuss bound), see Fig. 4. Thus, the homogenisation process replaces the layered structure of the PV modules by an anisotropic homogenised medium. In the following section, the homogenised material properties (elastic modulus, Poisson's ratio, and mass density) are expressed in terms of the layer thicknesses of the PV module.

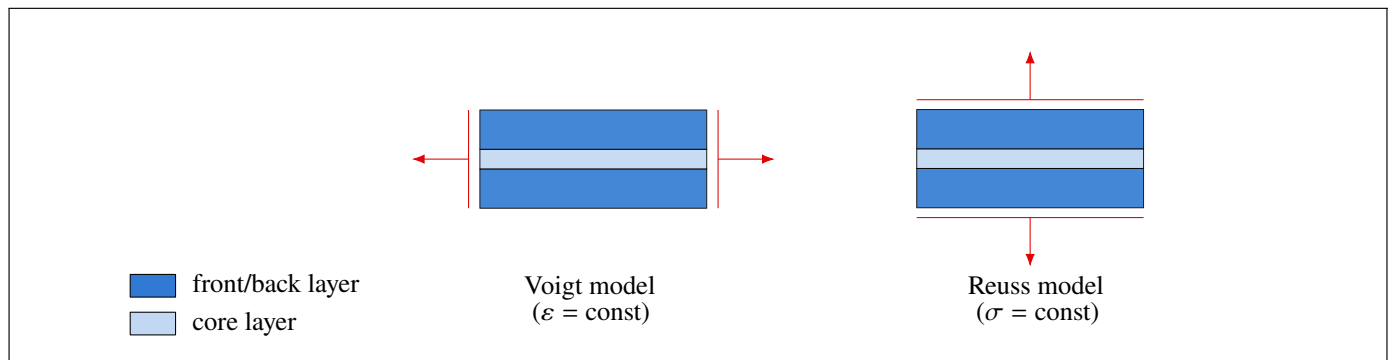


Fig. 4: Underlying assumptions of bounds used for homogenization of photovoltaic composite structure

3 Eigenfrequency Analysis

3.1 Shear-rigid Plate Theory for a Homogenised Medium

Assumptions. In the foregoing section, the effective mechanical properties of a layered structure is obtained as a single equivalent layer. Thereby, instead of any advanced layer-wise theories (Aßmus et al., 2017c; Aßmus, 2019), any single-layer plate theory could be used for determining the natural frequencies. The selection of an appropriate plate theory poses two main considerations:

1. Slenderness hypothesis (with regards to shear rigidity), which decides between a shear-rigid or shear-deformable theories. The thinness of a structural element can be quantitatively measured by defining the slenderness (s) of a body (see Fig. 8):

$$s := \frac{h}{L_{\min}} \quad \text{with } L_{\min} := \min\{L_1, L_2\} \quad \text{and} \quad h := \sum h_k, \quad (4)$$

which for a shear-rigid theory, is limited to $s < 0.1$ (Altenbach, 2008) or more restrictive values such as $s < 0.05$ (Ugural, 2010). Taking into account the geometric data from Tab. 1, $s \approx 9.25 \cdot 10^{-3}$ results, which underlines the assumption.

2. Geometrical linearity or nonlinearity of the problem; in the former case, the nonlinear geometrical terms are neglected, and thus a zero strain is imposed at the mid-surface (Ugural, 2010). In engineering practice, geometrical linearity is ensured by imposing a limit on the maximum deflection, e.g., deflections smaller than the empirical values of $w_{\max} < 0.5H$ (Birman, 2011) or $w_{\max} < 0.2H$ (Altenbach, 2008). However, a limitation (much smaller than 10°) must be applied to the rotations too (Reddy, 2006), i.e., for a complete linear geometry, small strain and small rotations must be guaranteed.

Considering the thinness of the PV modules and restricting the study to first order deformations, the Kirchhoff-Love plate theory is deemed reasonable. By adopting the engineering approach (as opposed to the direct approach) towards the formulation of such thin walled structures, all considerations are reduced to a reference surface, i.e., the mid-surface. Namely, the assumption of plane stress state degenerates the 3D continuum to a 2D counterpart. In this regard, Kirchhoff-Love hypotheses (Kirchhoff, 1850; Reddy, 2006) are adopted, which assume that the transverse normals

- remain straight after deformation,
- are rigid, and
- remain perpendicular to the mid-surface after deformation.

Herein, the following additional assumptions are made:

- geometrical linearity:
 - infinitesimal cross section rotations, and
 - infinitesimal strains;
- physical linearity: material behaviour is linear elastic;
- material homogeneity: all material points have the same physical properties; and
- material isotropy: there is no preferred direction for physical properties.

Formulation. Considering the aforementioned simplifications, the eigenvalue problem of an isotropic plate is restated for a homogenised medium. In the course of this procedure, an overbar ($\bar{\square}$) denotes the respective effective material property, i.e., it can be either Voigt (\square_V) or Reuss (\square_R) homogenised values. The governing partial differential equation of thin plates in canonical form is

$$\bar{K}\Delta\Delta w(X_1, X_2, t) + \bar{\rho}h\ddot{w}(X_1, X_2, t) = 0 \quad \text{with} \quad \bar{K} = \frac{\bar{E}h^3}{12(1-\bar{\nu}^2)}, \quad (5)$$

where \bar{K} is the flexural rigidity of the homogenised plate, w is the deflection of the plate midplane, t is time, and ($\Delta := \nabla \cdot \nabla$) is the Laplace operator. First, the Bernoulli approach is used to multiplicatively separate the temporal (T) and spatial (W) components:

$$w(X_1, X_2, t) = W(X_1, X_2)T(t), \quad (6)$$

which must satisfy Eq. (5), and thus

$$\Delta\Delta W(X_1, X_2) - \lambda^4 W(X_1, X_2) = 0, \quad \text{with} \quad \lambda^4 := \frac{\bar{\rho}h\omega^2}{\bar{K}}, \quad (7a)$$

$$\ddot{T}(t) + \omega^2 T(t) = 0, \quad (7b)$$

where ω is the angular frequency of the vibration. Consequently, the oscillation equation takes the following form:

$$\frac{\bar{K}\Delta\Delta W(X_1, X_2)}{\bar{\rho}hW(X_1, X_2)} = -\frac{\ddot{T}(t)}{T(t)} = \omega^2. \quad (8)$$

The time dependency can be represented by the harmonic ansatz $T = A \sin(\omega t + \alpha)$ where α is a constant denoting the phase shift. Consequently, the temporal component of Eq. (6) is obtained:

$$w(X_1, X_2, t) = W(X_1, X_2) \sin(\omega t + \alpha). \quad (9)$$

The spatial component is the solution of the classic NAVIER problem (a simply supported plate at all edges under a distributed load), i.e., a double Fourier series:

$$W(X_1, X_2) = \sum_{m=1}^M \sum_{n=1}^N W_{mn} \sin\left(\frac{m\pi}{L_1} X_1\right) \sin\left(\frac{n\pi}{L_2} X_2\right), \quad (10)$$

where W_{mn} is the amplitude of the eigenmode shape mn whose magnitude can be scaled arbitrarily; moreover, m and n are the number of mode shape half-waves along the X_1 and X_2 axes, respectively. Finally, substituting this solution into Eq. (7a) results in

$$f_{mn} = \frac{\pi}{2} \left(\frac{m^2}{L_1^2} + \frac{n^2}{L_2^2} \right) \sqrt{\frac{\bar{K}}{\bar{\rho}h}}, \quad \forall m, n = \{1, 2, 3, \dots\}, \quad (11)$$

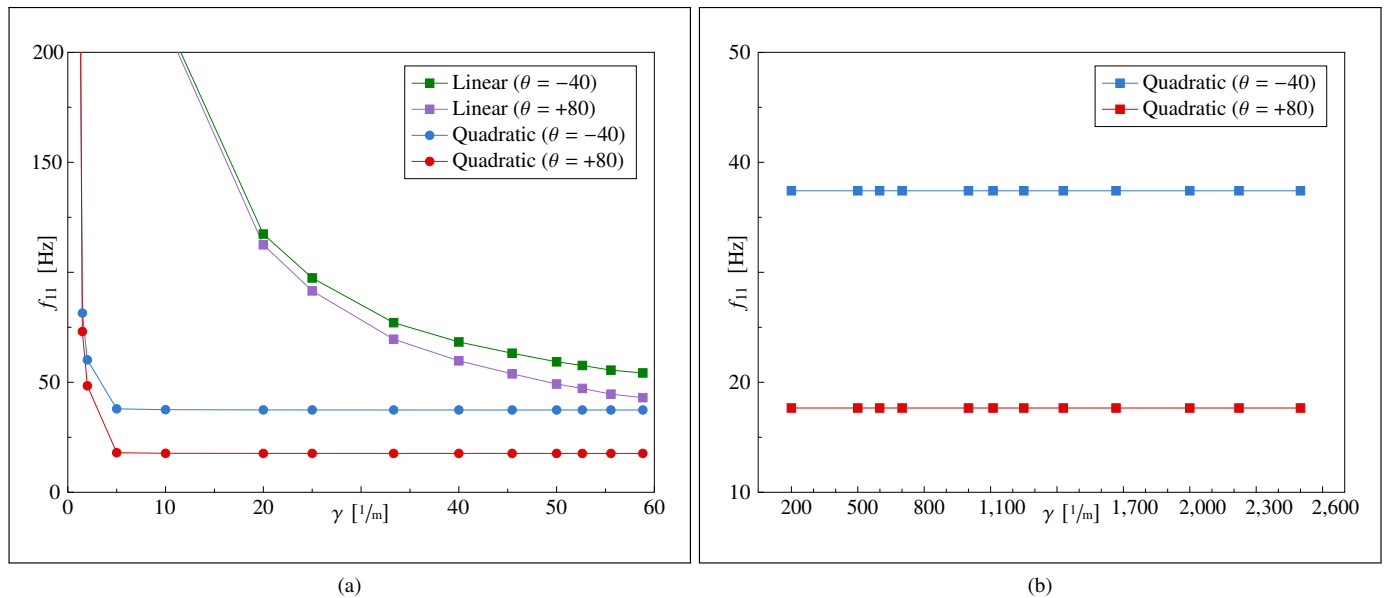


Fig. 5: Convergence study of linear and quadratic elements for two temperature extremes: (a) in-plane mesh sensitivity, and (b) through-thickness mesh sensitivity.

where f_{mn} is the natural frequency of the mode with $m \times n$ half-waves. Note that the angular frequency is related to its linear counterpart (f) via $\omega = 2\pi f$.

In order to compare the results of the closed-form (f_{mn} , $\forall m, n \in \{1, 2, 3\}$) and the computational solution (f_i , $\forall i \in \{1, \dots, 9\}$), the pseudo index r is defined as

$$r := \begin{cases} \frac{m \cdot n}{m} + (m - 1) & \text{if } m = 1 \\ \frac{m \cdot n}{m} + (m + 1) & \text{if } m = 2, \\ \frac{m \cdot n}{m} + (m + 3) & \text{if } m = 3 \end{cases}, \quad \forall n \in \{1, 2, 3\}. \quad (12)$$

The transformation into a sorted sequence f_i follows the $f_i : f_r < f_{(r+1)}$ convention.

3.2 Computational Model

A 3D FE model was prototyped using the MSC MARC/MENTAT commercial FE package (Javanbakht and Öchsner, 2017, 2018). A python script was used to populate the models for the convergence and parametric studies. The former provides a nominated model that is used to obtain the natural frequencies in the Results section. Note that the same geometrical parameters and material properties in Tables 1–3 were used. Moreover, the real geometry of the boundary, i.e., the frame, and the solar cells were not considered in the computational models, see Figs. 1 and 2. However, solid elements were used to represent each layer discretely.

Convergence study. In order to remove the sensitivity of the results to the size of elements, the convergence of the fundamental frequency was studied. Since 3D elements were used in the FE prototype, discretisation of the elements in the X_1 - X_2 plane (planar), and then along the X_3 axis (through-thickness) was considered. To this end, the planar element mesh density (γ) is defined as (Javanbakht et al., 2017a,b)

$$\gamma := \frac{1}{\ell}, \quad (13)$$

where ℓ is the length of the square element in the x - y plane. Linear (8-node isoparametric) and quadratic (20-node isoparametric) elements were nominated for the analyses. The planar refinement of mesh was carried out uniformly over several mesh densities ($\gamma = 1 - 58.82$) while no element subdivisions were carried out in the thickness direction. As depicted in Fig. 5a, the quadratic elements outperformed their linear counterparts and realised a quick convergence for mesh densities above 10. It was found that the linear elements required a higher mesh density to obtain an adequate h-type convergence. In this particular application, quadratic elements seemed to obtain a p-type convergence (Hellen and Becker, 2013) by moderate mesh densities. Moreover, the convergence rate seemed to be almost insensitive to the material contrast at different temperature extremes. In this step, the mesh density of 52.63 1/m was selected to study the sensitivity of the quadratic elements in the thickness direction.

In the thickness direction, mesh densities ($\gamma = 200 - 2500$) were considered over which no considerable sensitivity was observed, see Fig. 5b. Finally, the planar mesh density of 52.63 1/m and the through-thickness mesh density of 1250 1/m was selected to carry out the parametric study.

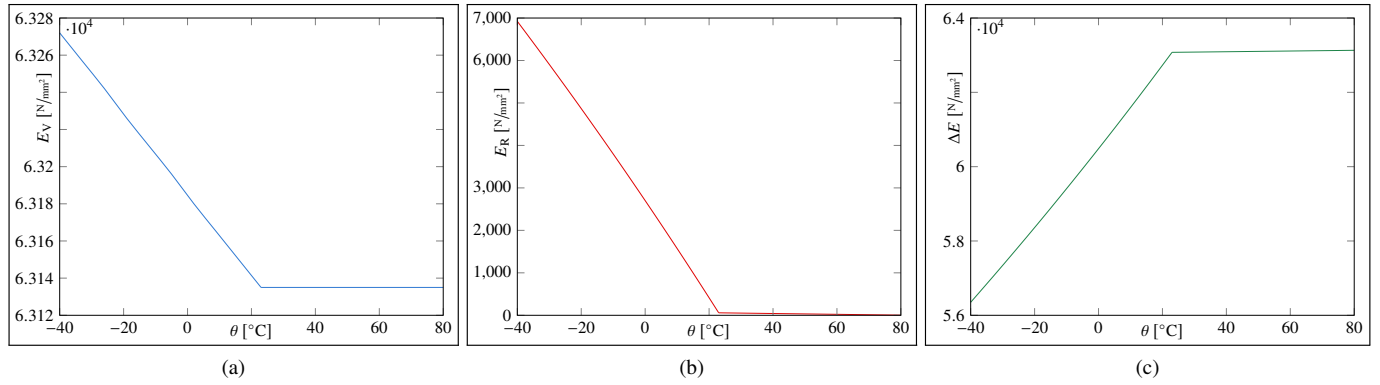


Fig. 6: Bounds of the elastic modulus of the composite behaviour at various temperatures: (a) Voigt bound, (b) Reuss bound, and (c) Voigt-Reuss difference.

4 Results and Discussion

4.1 Homogenisation

The bounds for a layered PV module are obtained using the Eqs. (3a) and (3b). Namely for a unit area of a PV module, the volumes of various layers are taken to calculate the volume fractions of skin and core layers. Consequently, the elastic moduli are obtained as follows:

$$E_V(\theta) = 1/h [2h_s E_s + h_c E_c(\theta)], \quad (14a)$$

$$E_R(\theta) = \frac{h E_c(\theta) E_s}{2h_s E_c(\theta) + h_c E_s}. \quad (14b)$$

The graphical representation of these equations is presented in Fig. 6. It can be seen that as a result of the homogenisation process, the material properties along the principal directions are quite different. The degree of anisotropy for the elastic modulus could be simply represented by the $\Delta E = E_V - E_R$ difference (Aßmus et al., 2020). By increasing the temperature from -40 to $+23^{\circ}\text{C}$, the bandwidth increases from $5.635 \cdot 10^4$ to $6.307 \cdot 10^4$ N/mm^2 and remains about the same value by further increasing the temperature, see Fig. 6c. Namely, at lower temperatures, the smaller bandwidth for elastic modulus indicates a better approximation for its range of possible values. However, from about the room temperature upwards there is only a slight increase in the bandwidth.

In terms of temperature-independent properties, the Voigt and Reuss bounds for Poisson's ratio are

$$\nu_V = 1/h [2h_s \nu_s + h_c \nu_c] = 0.3149, \quad (15a)$$

$$\nu_R = \frac{h \nu_c \nu_s}{2h_s \nu_c + h_c \nu_s} = 0.3113, \quad (15b)$$

for which the parameters of Tab. 2 were used. The bandwidth of the Poisson's ratio estimates is $3.6 \cdot 10^{-3}$, which indicates a very good approximation. Similarly, the Voigt and Reuss bounds for effective mass density are obtained:

$$\rho_V = 1/h [2h_s \rho_s + h_c \rho_c] = 2287.83 \text{ kg/m}^3, \quad (16a)$$

$$\rho_R = \frac{h \rho_c \rho_s}{2h_s \rho_c + h_c \rho_s} = 2035.61 \text{ kg/m}^3. \quad (16b)$$

The bandwidth of the mass density is 252.22 kg/m^3 , which indicates a reasonable approximation.

4.2 Natural Frequencies and Mode Shapes

Mode shapes. The first nine mode shapes of the smeared composite is illustrated in Fig. 7a and the respective room-temperature computational results are depicted in Fig. 7b. It is evident that the proposed analytical procedure results in the same mode shapes as the computational model. In the FE model, the layers of PV module were modelled discretely and compared to the analytical procedure, the numerical effort does not seem to have any apparent advantages in detecting the mode shapes. Additionally, the Lanczos algorithm was used for the numerical solution of the eigenvalue problem, which is prone to produce spurious eigenvalues (Cullum and Willoughby, 2002). Thus, the analytical solution seems to be a better alternative in this sense. Nevertheless, the visual comparison of the mode shapes serves as a preliminary validation for both methods.

Natural frequencies. The Kirchhoff-Love plate theory for the homogenised medium was used to obtain the natural frequencies of the PV modules, see Tab. 4. Moreover, following a discrete modelling of the layers, the computational results are also presented in the same table. The obtained natural frequencies from both methods are related to their counterpart by Eq. (12). In order to develop a better understanding, two temperature extremes of -40°C and 80°C were considered along with the conventional room temperature of 23°C . All the values of the Voigt homogenisation demonstrated a negligible change at various temperatures. On the contrary, the Reuss bound showed a decrease by almost two orders of magnitude at all temperatures. This behaviour can be

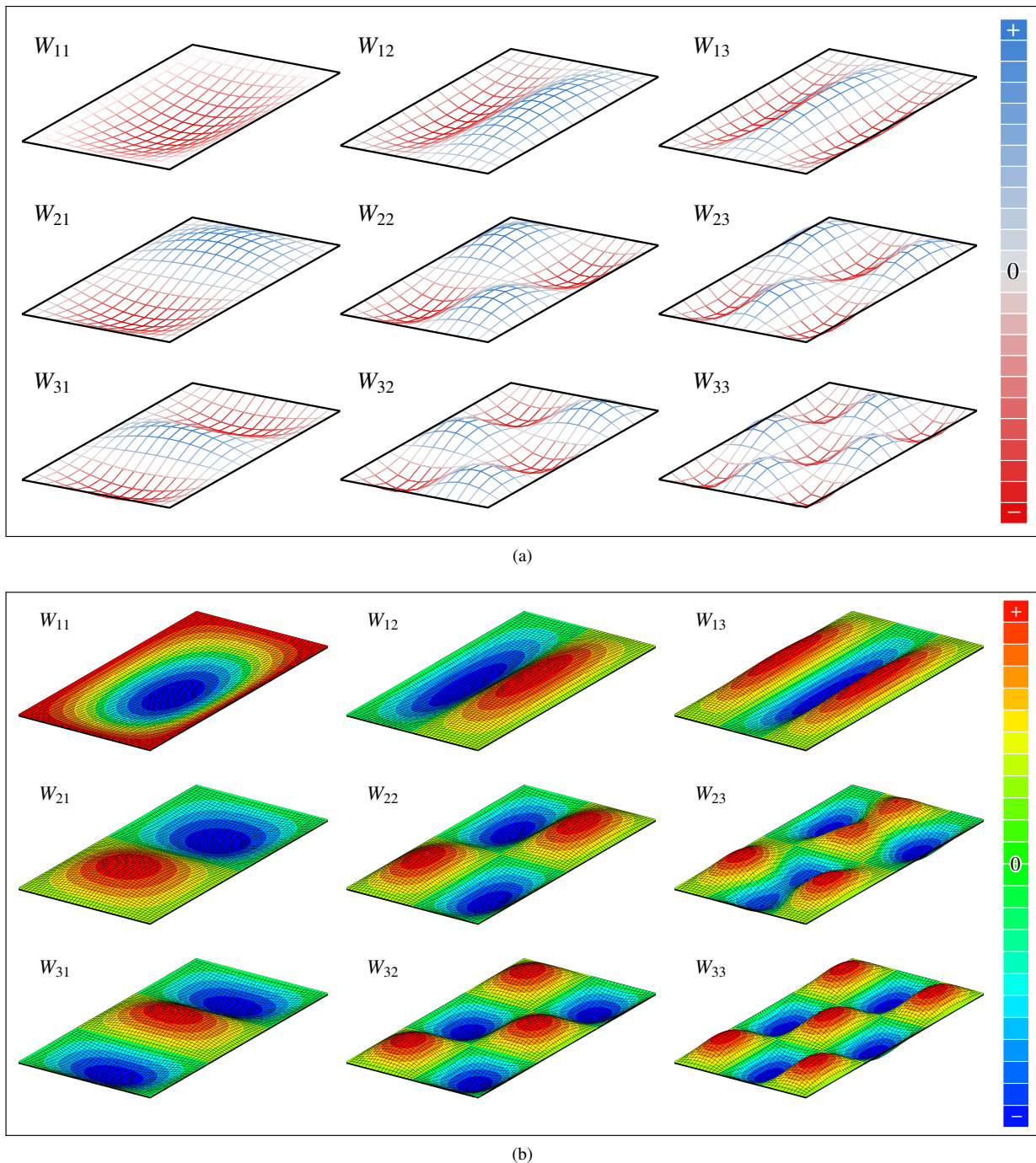


Fig. 7: Nine mode shapes of the photovoltaic module: (a) results of analytical solution, and (b) results of the computational solution at room temperature

attributed to the high contrast of mechanical properties, see Fig. 6c. Meanwhile, the computational results showed a decrease in the natural frequencies as the temperature increased up to $+23^{\circ}\text{C}$ where higher modes seemed to suffer a sharper decrease. Further increase in temperature resulted in additional decrease in the natural frequency, which became milder at higher frequencies. It can be concluded that while the Voigt bound seems to be insensitive to the material properties, the Reuss bound strongly reacts to the change of properties. The FE results followed the Voigt bound up to $+15^{\circ}\text{C}$ after which declined towards the Reuss bound. This behaviour can be attributed to the increase of the material contrast at higher temperatures.

Fundamental frequency. In Fig. 8, the results of the analytical solution and the computational model are illustrated for the fundamental frequency. As stated earlier, the Voigt bound seems to be insensitive to material contrast whereas the Reuss bound is more sensitive in that sense. The Voigt and Reuss bounds mark a wide range for the possible results. Namely, the computational results of the current study are in good agreement within the Reuss-Voigt range. More specifically, for the temperatures below 23°C , the Voigt bound matches the numerical results. By increasing the temperature, the computational results deviate from the Voigt bound. Nevertheless, the analytical bounds confirm that the results are within the acceptable range.

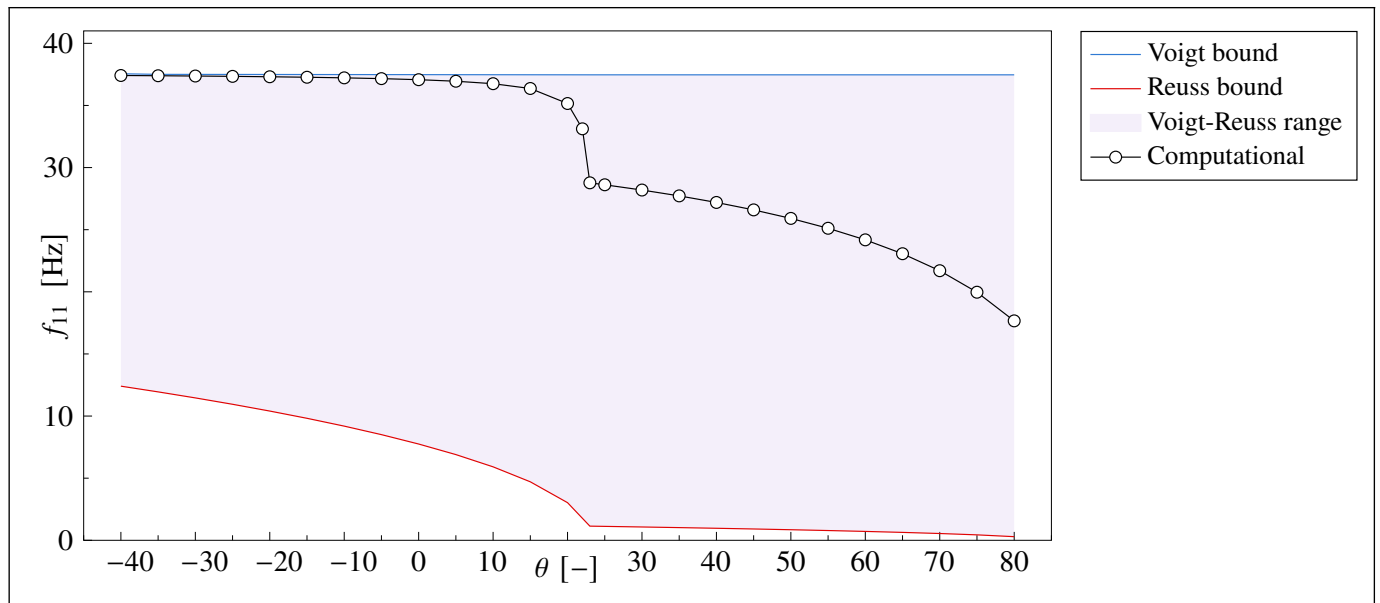


Fig. 8: Fundamental frequency results and the analytical bounds.

5 Final Remarks

Conclusion. The aim of the current study was to obtain a fast solution for the natural frequencies of PV modules. Although the analytical solution was not able to pinpoint the exact values of the fundamental frequencies over the whole temperature range, it provided a very good solution for the temperature range of -40 to 15°C . More specifically, the Voigt-Reuss range seemed to contain both experimental and computational results. In contrast, the provided computational model was able to provide more accurate results while demanding a sensible computational cost. The FE models were also able to mildly capture the effect of material contrast as a result of temperature change. The fundamental frequency of the examined PV module ranged between 17.66 – 37.41 Hz by decreasing the temperature. The value of 28.77 Hz was obtained for the room temperature fundamental frequency.

As many experimental efforts provide ranges for the natural frequencies rather than exact points, the introduced analytical method could be used to obtain a valid range for the results. On the other hand, if the computational procedure is preferred, the mesh sensitivity study recommends the use of quadratic elements and discrete modelling of the layers in order to alleviate the issue of high material property contrast.

Contributions. The major contributions of the current work can be listed as follows:

1. A new analytical procedure was suggested to obtain a range for the fundamental natural frequencies of PV modules or

Tab. 4: Obtained natural frequencies from the analytical solution combined with the Voigt (f^V), and Reuss (f^R) homogenisation schemes versus the results of the computational modelling (f^C)

Homogenisation scheme	Mode (mn)								
	11	21	31	12	22	32	13	23	33
Analytical results									
$f_{mn}^V(-40^{\circ}\text{C})$ [Hz]	37.55	60.08	97.64	127.68	150.21	187.76	277.89	300.42	337.97
$f_{mn}^V(+23^{\circ}\text{C})$ [Hz]	37.46	59.94	97.41	127.38	149.86	187.32	277.24	299.72	337.18
$f_{mn}^V(+80^{\circ}\text{C})$ [Hz]	37.46	59.94	97.41	127.38	149.86	187.32	277.24	299.72	337.18
$f_{mn}^R(-40^{\circ}\text{C})$ [Hz]	12.41	19.85	32.25	42.18	49.62	62.028	91.80	99.25	111.65
$f_{mn}^R(+23^{\circ}\text{C})$ [Hz]	1.14	1.82	2.96	3.88	4.56	5.69	8.43	9.11	10.26
$f_{mn}^R(+80^{\circ}\text{C})$ [Hz]	0.29	0.47	0.76	0.99	1.17	1.46	2.16	2.34	2.63
Computational results									
$f_{mn}^C(-40^{\circ}\text{C})$ [Hz]	37.41	59.49	96.58	126.97	148.38	184.34	273.67	294.45	329.34
$f_{mn}^C(+23^{\circ}\text{C})$ [Hz]	28.77	42.12	62.77	78.46	88.81	106.07	146.88	156.37	172.37
$f_{mn}^C(+80^{\circ}\text{C})$ [Hz]	17.66	26.93	42.26	54.52	63.65	78.87	115.60	124.70	139.89

possibly other anti-sandwich panels.

2. A clear computational procedure was described that can handle the high material contrast issue and produce more accurate results.
3. An analytical approximation was provided for the fundamental frequency of the PV modules in the temperature range of -40 to 15°C .

Outlook. The current study can be extended by conducting a parametric study to cover various sizes of commercial PV modules; considering the damping characteristics of the structure by considering the enclosing frame in the computational procedure or introducing a damping coefficient in the analytical procedure. Temperature-controlled experiments would also be beneficial for the validation of the extreme behaviours.

References

- H. Altenbach. Analysis of homogeneous and non-homogeneous plates. In René de Borst and Tomasz Sadowski, editors, *Lecture notes on composite materials*, volume 154 of *Solid mechanics and its applications*, pages 1–36. Springer, Dordrecht, 2008. ISBN 978-1-4020-8771-4.
- M. Aßmus. *Structural Mechanics of Anti-Sandwiches: An Introduction*. Springer Briefs in Continuum Mechanics. Springer, Cham, Switzerland, 2019. doi: [10.1007/978-3-030-04354-4](https://doi.org/10.1007/978-3-030-04354-4).
- M. Aßmus and M. Köhl. Experimental investigation of the mechanical behavior of photovoltaic modules at defined inflow conditions. *Journal of Photonics for Energy*, 2(1):1–11, 2012. doi: [10.1117/1.JPE.2.022002](https://doi.org/10.1117/1.JPE.2.022002).
- M. Aßmus, S. Jack, K.-A. Weiss, and M. Koehl. Measurement and simulation of vibrations of PVmodules induced by dynamic mechanical loads. *Progress in Photovoltaics: Research and Applications*, 19(6):688–694, 2011. doi: [10.1002/pip.1087](https://doi.org/10.1002/pip.1087).
- M. Aßmus, K. Naumenko, and H. Altenbach. A multiscale projection approach for the coupled global–local structural analysis of photovoltaic modules. *Composite Structures*, 158:340–358, 2016. doi: [10.1016/j.compstruct.2016.09.036](https://doi.org/10.1016/j.compstruct.2016.09.036).
- M. Aßmus, S. Bergmann, J. Eisenträger, K. Naumenko, and H. Altenbach. Consideration of non-uniform and non-orthogonal mechanical loads for structural analysis of photovoltaic composite structures. In H. Altenbach, R. V. Goldstein, and E. Murashkin, editors, *Mechanics for Materials and Technologies*, volume 46 of *Advanced structured materials*, pages 73–122. Springer International Publishing, Cham, 2017a. doi: [10.1007/978-3-319-56050-2_4](https://doi.org/10.1007/978-3-319-56050-2_4).
- M. Aßmus, S. Bergmann, K. Naumenko, and H. Altenbach. Mechanical behaviour of photovoltaic composite structures: A parameter study on the influence of geometric dimensions and material properties under static loading. *Composites Communications*, 5:23–26, 2017b. doi: [10.1016/j.coco.2017.06.003](https://doi.org/10.1016/j.coco.2017.06.003).
- M. Aßmus, K. Naumenko, and H. Altenbach. Mechanical behaviour of photovoltaic composite structures: Influence of geometric dimensions and material properties on the eigenfrequencies of mechanical vibrations. *Composites Communications*, 6(-): 59–62, 2017c. doi: [10.1016/j.coco.2017.10.003](https://doi.org/10.1016/j.coco.2017.10.003).
- M. Aßmus, R. Glüge, and H. Altenbach. On the analytical estimation for isotropic approximation of elastic properties applied to polycrystalline cubic silicon used at solar cells. *Technische Mechanik*, 40(2):120–133, 2020. doi: [10.24352/UB.OVGU-2020-020](https://doi.org/10.24352/UB.OVGU-2020-020).
- A. J. Beinert, P. Romer, M. Heinrich, M. Mittag, J. Aktaa, and H. Neuhaus. Thermomechanical evaluation of new PV module designs by fem simulations. In *36th European Photovoltaic Solar Energy Conference and Exhibition*, pages 783–788, 2019. doi: [10.4229/EUPVSEC20192019-4BO.11.1](https://doi.org/10.4229/EUPVSEC20192019-4BO.11.1).
- V. Birman. *Plate structures*, volume 178 of *Solid mechanics and its applications*, 0925-0042. Springer, Dordrecht, 2011. ISBN 9789400717145.
- British Standards. Thin-film terrestrial photovoltaic (PV) modules - Design qualification and type approval: (IEC 61646:2008), 2008.
- British Standards. Photovoltaic (PV) modules - Transportation testing: Part 1: Transportation and shipping of module package units (IEC 62759-1:2015), 2015.
- British Standards. Photovoltaic (PV) modules - Cyclic (dynamic) mechanical load testing: (PD IEC/TS 62782:2016), 2016.
- British Standards. Terrestrial photovoltaic (PV) modules - Design qualification and type approval: Part 1-2: Special requirements for testing of thin-film cadmium (IEC 61215-1-2:2016), 2017a.
- British Standards. Terrestrial photovoltaic (PV) modules - Design qualification and type approval: Part 2: Test procedures (IEC 61215-2:2016), 2017b.
- J. K. Cullum and R. A. Willoughby. *Lanczos algorithms for large symmetric eigenvalue computations*, volume 41 of *Classics in applied mathematics*. Society for Industrial and Applied Mathematics, Philadelphia, 2002. ISBN 0898715237.
- W. Dallas, O. Polupan, and S. Ostapenko. Resonance ultrasonic vibrations for crack detection in photovoltaic silicon wafers. *Measurement Science and Technology*, 18(3):852–858, 2007. ISSN 0268-1242. doi: [10.1088/0957-0233/18/3/038](https://doi.org/10.1088/0957-0233/18/3/038).
- S. Dietrich, M. Pander, M. Sander, S. H. Schulze, and M. Ebert. Mechanical and thermomechanical assessment of encapsulated solar cells by finite-element-simulation. In Neelkanth G. Dhare, John H. Wohlgemuth, and Kevin Lynn, editors, *Reliability of Photovoltaic Cells, Modules, Components, and Systems III*, volume 7773 of *SPIE Proceedings*, page 77730F. SPIE, 2010. doi: [10.1117/12.860661](https://doi.org/10.1117/12.860661).

- U. Eitner. *Thermomechanics of Photovoltaic Modules*. PhD-thesis, Martin-Luther-Universität Halle-Wittenberg, 2011. URL <http://nbn-resolving.de/urn:nbn:de:gbv:3:4-5812>.
- C. Ferrara and D. Philipp. Why do PV modules fail? *Energy Procedia*, 15:379–387, 2012. doi: [10.1016/j.egypro.2012.02.046](https://doi.org/10.1016/j.egypro.2012.02.046).
- T. Hellen and A. A. Becker. *Finite element analysis for engineers*. NAFEMS, Glasgow, 2013. ISBN 9781874376989.
- Z. Javanbakht and A. Öchsner. *Advanced Finite Element Simulation with MSC Marc*. Springer International Publishing, Cham, 2017. ISBN 978-3-319-47667-4. doi: [10.1007/978-3-319-47668-1](https://doi.org/10.1007/978-3-319-47668-1).
- Z. Javanbakht and A. Öchsner. *Computational Statics Revision Course*. Springer International Publishing, Cham, 2018. ISBN 978-3-319-67461-2. doi: [10.1007/978-3-319-67462-9](https://doi.org/10.1007/978-3-319-67462-9).
- Z. Javanbakht, W. Hall, and A. Öchsner. The effect of partitioning on the clustering index of randomly-oriented fiber composites: a parametric study. *Defect and Diffusion Forum*, 380:232–241, 2017a. ISSN 1662-9507. doi: [10.4028/www.scientific.net/DDF.380.232](https://doi.org/10.4028/www.scientific.net/DDF.380.232).
- Z. Javanbakht, W. Hall, and A. Öchsner. The effect of substrate bonding on characterization of thin elastic layers: A finite element study. *Materialwissenschaft und Werkstofftechnik*, 48(5):456–462, 2017b. ISSN 09335137. doi: [10.1002/mawe.201700035](https://doi.org/10.1002/mawe.201700035).
- Z. Javanbakht, M. Aßmus, K. Naumenko, A. Öchsner, and H. Altenbach. On thermal strains and residual stresses in the linear theory of anti-sandwiches. *Journal of Applied Mathematics and Mechanics*, 99(8):1, 2019. doi: [10.1002/zamm.201900062](https://doi.org/10.1002/zamm.201900062).
- Z. Javanbakht, W. Hall, and A. Öchsner. An element-wise scheme to analyse local mechanical anisotropy in fibre-reinforced composites. *Materials Science and Technology*, pages 1–13, 2020a. ISSN 0267-0836. doi: [10.1080/02670836.2020.1762296](https://doi.org/10.1080/02670836.2020.1762296).
- Z. Javanbakht, W. Hall, A. S. Virk, J. Summerscales, and A. Öchsner. Finite element analysis of natural fiber composites using a self-updating model. *Journal of Composite Materials*, page 002199832091282, 2020b. ISSN 0021-9983. doi: [10.1177/0021998320912822](https://doi.org/10.1177/0021998320912822).
- K. Kilikeviciene, J. Matijosius, A. Kilikevicius, M. Jurevicius, V. Makarskas, J. Caban, and A. Marczuk. Research of the energy losses of photovoltaic (pv) modules after hail simulation using a newly-created testbed. *Energies*, 12(23):4537, 2019. doi: [10.3390/en12234537](https://doi.org/10.3390/en12234537).
- A Kilikevicius, A Cereska, and K Kilikeviciene. Analysis of external dynamic loads influence to photovoltaic module structural performance. *Engineering Failure Analysis*, 66:445–454, 2016. ISSN 13506307. doi: [10.1016/j.engfailanal.2016.04.031](https://doi.org/10.1016/j.engfailanal.2016.04.031).
- G. Kirchhoff. Über das Gleichgewicht und die Bewegung einer elastischen Scheibe. *Journal für die reine und angewandte Mathematik (Crelles Journal)*, 1850(40):51–88, 1850. doi: [10.1515/crll.1850.40.51](https://doi.org/10.1515/crll.1850.40.51).
- S. Koch, J. Kupke, D. Tornow, M. Schoppa, S. Krauter, and P. Grunow. Dynamic mechanical load tests on crystalline silicon modules. In *25th European Photovoltaic Solar Energy Conference and Exhibition*, pages 3998–4001, 2010. doi: [10.4229/25THEUPVSEC2010-4AV.3.11](https://doi.org/10.4229/25THEUPVSEC2010-4AV.3.11).
- S. Köntges, M. Kurtz, C. Packard, U. Jahn, K. A. Berger, and K. Kato. *Performance and reliability of photovoltaic systems: Subtask 3.2: Review of failures of photovoltaic modules : IEA PVPS task 13 : external final report IEA-PVPS*. International Energy Agency, Photovoltaic Power Systems Programme, Saint Ursen, Switzerland, 2014.
- L. Meirovitch. *Fundamentals of vibrations*. McGraw-Hill, Boston, USA, 2001.
- R. Mickiewicz, B. Li, D.M.J. Doble, T. Christian, J. Lloyd, A. Stokes, C. Völker, M. Winter, B. Ketola, A. Norris, and N. Shephard. Effect of encapsulation modulus on the response of PV modules to mechanical stress. In *26th European Photovoltaic Solar Energy Conference and Exhibition*, pages 3157–3161, 2011. doi: [10.4229/26THEUPVSEC2011-4CO.7.4](https://doi.org/10.4229/26THEUPVSEC2011-4CO.7.4).
- K. Naumenko and V. A. Eremeyev. A layer-wise theory for laminated glass and photovoltaic panels. *Composite Structures*, 112: 283–291, 2014. doi: [10.1016/j.compstruct.2014.02.009](https://doi.org/10.1016/j.compstruct.2014.02.009).
- S. Pingel, Y. Zemen, O. Frank, T. Geipel, and J. Berghold. Mechanical stability of solar cells within solar panels. In *24th European Photovoltaic Solar Energy Conference and Exhibition*, pages 3459–3463, 2009. doi: [10.4229/24thEUPVSEC2009-4AV.3.49](https://doi.org/10.4229/24thEUPVSEC2009-4AV.3.49).
- J. N. Reddy. *Theory and analysis of elastic plates and shells*. CRC Press, Boca Raton, FL, 2nd ed. edition, 2006. ISBN 9780849384158.
- F. Reil, J. Althaus, W. Vaassen, W. Herrmann, and K. Strohkendl. The effect of transportation impacts and dynamic load tests on the mechanical and electrical behaviour of crystalline PV modules. In *25th European Photovoltaic Solar Energy Conference and Exhibition*, pages 3989–3992, 2010. doi: [10.4229/25THEUPVSEC2010-4AV.3.9](https://doi.org/10.4229/25THEUPVSEC2010-4AV.3.9).
- A. Reuss. Berechnung der Fließgrenze von Mischkristallen auf Grund der Plastizitätsbedingung für Einkristalle. *Zeitschrift für Angewandte Mathematik und Mechanik*, 9(1):49–58, 1929.
- M. Sander, S. Dietrich, M. Pander, M. Ebert, and J. Bagdahn. Systematic investigation of cracks in encapsulated solar cells after mechanical loading. *Solar Energy Materials and Solar Cells*, 111:82–89, 2013. doi: [10.1016/j.solmat.2012.12.031](https://doi.org/10.1016/j.solmat.2012.12.031).
- A. C. Ugural. *Stresses in Beams, Plates, and Shells*. Taylor & Francis, 3rd edition, 2010.
- N. Visniakov, A. Kilikevicius, J. Novickij, A. Grainys, and V. Novickij. Low-cost experimental facility for evaluation of the effect of dynamic mechanical loads on photovoltaic modules. *Eksploatacja i Niezawodnosc - Maintenance and Reliability*, 17(3): 334–337, 2015. ISSN 15072711. doi: [10.17531/ein.2015.3.2](https://doi.org/10.17531/ein.2015.3.2).
- W. Voigt. *Lehrbuch der Kristallphysik (mit Ausschluss der Kristalloptik)*. Teubner, Leipzig, 1910.
- K-A Weiss, M Assmus, S Jack, and M Koehl. Measurement and simulation of dynamic mechanical loads on PV-modules. In Neelkanth G. Dhare, John H. Wohlgemuth, and Dan T. Ton, editors, *Reliability of Photovoltaic Cells, Modules, Components, and Systems II*, SPIE Proceedings, page 741203. SPIE, 2009. doi: [10.1117/12.824859](https://doi.org/10.1117/12.824859).

J. Wohlgemuth. *Photovoltaic module reliability*. Wiley, Hoboken, NJ, USA, 2020. doi: [10.1002/9781119459019](https://doi.org/10.1002/9781119459019).

TECHNISCHE MECHANIK

Scientific Journal for Fundamentals and Applications of Engineering Mechanics
Wissenschaftliche Zeitschrift für Grundlagen und Anwendungen der Technischen Mechanik

Instructions for Authors

TECHNISCHE MECHANIK publishes articles in all fields of mechanics, theoretical as well as applied, including related disciplines, and in particular also articles demonstrating practical applications. The journal publishes full length papers, as well as discussions on papers which have appeared in the journal.

TECHNISCHE MECHANIK is a non-profit (open-access) journal, founded by the Otto-von-Guericke-University. It can be freely downloaded from the website.

Manuscripts have to be written with LaTeX. The most important features of the style guidelines are implemented in the files contained in **tm-article.zip** (download from <http://www.ovgu.de/techmech/>).

Each submitted paper runs through a standard peer review process. Please suggest three international well known reviewers for your paper when you submit it.

Please submit your paper in electronic form by email.

Hinweise für Autoren

Die Zeitschrift TECHNISCHE MECHANIK veröffentlicht Forschungsarbeiten aus dem Gesamtgebiet der Mechanik, d. h. allen Zweigen der theoretischen und angewandten Mechanik einschließlich angrenzender Fachgebiete sowie Diskussionsbeiträge zu in dieser Zeitschrift erschienenen Arbeiten. Die Zeitschrift ist ein open-access Journal das 1980 von der Otto-von-Guericke-Universität gegründet wurde. Alle Artikel können kostenfrei von unserer Webseite herunter geladen werden.

Artikel werden ausschließlich in englischer Sprache veröffentlicht.

Die Manuskripte müssen in LaTeX geschrieben werden. Die wichtigsten Stil-Richtlinien sind in den Dateien umgesetzt, die in **tm-article.zip** (bereit gestellt unter <http://www.ovgu.de/techmech/>) enthalten sind.

Jeder eingereichte Beitrag durchläuft einen standardmäßigen Begutachtungsprozess. Bitte schlagen Sie bei Einreichung des Artikels drei mögliche, international renommierte Gutachter vor.

Bitte reichen Sie Ihren Beitrag elektronisch per E-Mail ein.

Internetadresse / website	http://journals.ub.uni-magdeburg.de/ubjournals/index.php/techmech
E-Mail / email	http://www.ovgu.de/techmech Technische.Mechanik@ovgu.de

Address of the editor:
Institut für Mechanik
Otto-von-Guericke-Universität
Postfach 4120

D-39016 Magdeburg

Tel.: +49-391-67-52459
Sekretariat -58608
Fax: +49-391-67-12439
-12863

e-mail: Technische.Mechanik@ovgu.de
<http://www.ovgu.de/techmech/>

Inhalt / Contents

Preface	40 Jahre Zeitschrift Technische Mechanik 40th anniversary of the journal Technische Mechanik	109
M.-U. Noll, L. Lentz, U. von Wagner	Comparison of the dynamics of a Duffing equation model and experimental results for a bistable cantilever beam in magnetoelastic energy harvesting	111
M. Aßmus, R. Glüge, H. Altenbach	On the Analytical Estimation for Isotropic Approximation of Elastic Properties applied to Polycrystalline Cubic Silicon used at Solar Cells ...	120
L. Spannan, F. Duvigneau, M. Gavila Lloret, C. Daniel, D. Juhre, E. Woschke	A study on harmonic excitation based experimental characterization of damping materials for acoustic simulations	134
V. Rizov, H. Altenbach	Longitudinal Fracture Analysis of an Inhomogeneous Stepped Rod with Two Concentric Cracks in Torsion	149
J. Nordmann, M. Aßmus, R. Glüge, H. Altenbach	On the Derivation of Hooke's Law for Plane State Conditions	160
F. Scherff, J. Gola, S. Scholl, K. Srivastava, T. Staudt, D. Britz, F. Mücklich, S. Diebels	RVE-size Estimation and Efficient Microstructure-based Simulation of Dual-Phase Steel	175
S. Bergmann, F. Hassani, Z. Javanbakht, M. Aßmus	On a Fast Analytical Approximation of Natural Frequencies for Photovoltaic Modules	191